THE UNIVERSITY
of EDINBURGH

Brown Dwarfs and Giant Exoplanets: Bridging Observations and Theory with Statistical Methods

Clémence Cécile Pia Fontanive

Doctor of Philosophy
The University of Edinburgh
May 2019

Abstract

Stellar physics has been widely studied over the last century, with theoretical models for stars robustly tested by decades of observations. In contrast, studies of brown dwarfs and extra-solar giant planets were only possible for the last two decades due to the intrinsically faint luminosity of these objects. As a result, the fundamental properties of substellar objects are still poorly constrained. Formation mechanisms for brown dwarfs and planetary-mass objects remain heavily debated, and atmospheric models widely lack empirical validation at the lowest masses and temperatures. Theoretical models are currently the only available way to infer physical parameters (e.g. mass, temperature) for isolated objects and directly-imaged companions on wide orbits, and are thus widely used by the community in spite of the extremely high uncertainties they carry.

More stringent observational constraints, or new alternative methods, are essential to allow for a further and deeper understanding of brown dwarfs and giant planets. Robust population studies provide invaluable insights into formation processes and empirical trends. Statistical methodologies may thus be used to refine theoretical models and obtain a more complete overview of the properties and statistics of the substellar populations.

This dissertation addresses three problems in the framework of brown dwarfs and giant exoplanets, namely, substellar binary properties, the formation of massive planets and brown dwarfs around stars, and the detection and model-independent masses of direct imaging systems. Chapter 2 presents results from a multiplicity survey investigating the binary statistics of the lowest-mass brown dwarfs. As binarity is a direct outcome of formation, observed trends as a function of mass provide valuable insights into formation processes. In Chapter 3, I conduct

a search for stellar companions to stars with close-in, massive planets, as a test of formation theory for giant planets and brown dwarfs on small orbital separations. Chapter 4 introduces a dedicated tool designed to identify new wide-orbit companions and constrain the orbits of astrometric systems. The method allows for the determination of dynamical masses for directly-imaged companions, a powerful way to circumvent the large uncertainties introduced by models.

The common goal to these projects is to infer new, crucial observational constraints for formation theories or atmospheric models in the substellar regime. This will in turn provide a more comprehensive view of the characteristics and demographics of brown dwarfs and exoplanets.

Lay Summary

Brown dwarfs are very faint astronomical objects, with masses too low to undergo hydrogen fusion in their cores, the driving source of energy sustaining stars. The lowest-mass brown dwarfs share remarkable similarities with giant planets like Jupiter, including similar sizes, weather features observed in their atmospheres, and Earth-like temperatures for the very coolest brown dwarfs. With masses ranging from a few times that of Jupiter to about 8% of the mass of the Sun, brown dwarfs represent the long-sought bridge between stars and planets, filling the crucial gap in mass and temperature between the lowest-mass stars and the most massive planets.

Despite being intrinsically faint and particularly challenging to detect, brown dwarfs appear to be incredibly numerous. These "substellar" objects therefore provide invaluable insights into the fundamental properties of our Galaxy. In addition, isolated brown dwarfs also represent excellent proxies to study planets orbiting other stars than our Sun, known as exoplanets, which are generally extremely difficult to observe directly. Indeed, with no bright stars in their proximity preventing detailed characterisations of their atmospheres, free-floating brown dwarfs offer ideal alternatives to analyse planet-like objects in depth.

Stellar physics has been widely studied over the last century, with theoretical models for stars robustly tested by decades of observations. In contrast, studies of brown dwarfs and extra-solar planets were only possible for the last two decades, due to the intrinsically faint luminosity of these objects. Despite the abundance of brown dwarfs in the Galaxy, the fundamental properties of the lowest-mass objects are still poorly constrained.

Theoretical models are developed to understand the atmospheres of brown dwarfs and giant planets, and trace the evolution of their properties with time. However, these predictions still struggle to reproduce observed characteristics, due to the small number of benchmark objects available to calibrate the models. Similarly, extensive theoretical simulations attempt to explain the formation and predict the evolution and fate of extra-solar planets and brown dwarfs. Nevertheless, a number of theories and discordant processes are currently envisaged, and formation mechanisms for substellar objects remain heavily debated. More stringent observational constraints, or new alternative methods, are essential to allow for a further and deeper understanding of the brown dwarf and giant planet populations.

Motivated by this goal, this thesis aims at achieving a more complete overview of the intrinsic properties of brown dwarfs and exoplanets. The work presented here centres on the direct detection and characterisation of brown dwarfs and planetary systems, with the objective to explore the demographics of giant planets and ultracool, low-mass brown dwarfs. Population studies are critical for differentiating between competing scenarios, and provide crucial insights into formation theories and empirical trends. Robust statistics of brown dwarfs and planetary systems may thus be used to obtain new observational constraints for theoretical models, that severely lack empirical validation at the lowest masses and temperatures. This will in turn allow for a deeper comprehension of the inherent characteristics of brown dwarfs and exoplanets, providing unprecedented insights into the worlds lying outside our own Solar system.

In Chapter 2, I present a search for binary companions to some very low-mass, isolated brown dwarfs, and constrain the binary frequency and statistical distributions of the coolest known brown dwarfs. Comparing their demographics to those of more massive objects suggests a common formation mechanism for stars and brown dwarfs, yielding valuable information for theoretical models. In Chapter 3, I investigate the role played by stellar companions in the puzzling existence of massive exoplanets and brown dwarfs orbiting stars at very small separations. This study revealed a very high binary occurrence rate for these systems, demonstrating that binarity greatly influences the formation or evolution of these objects. These results allow for unique tests of formation and evolution processes for giant planets and brown dwarf companions to stars.

In Chapter 4, I introduce a new code developed to identify new wide-orbit giant planets and constrain their orbits and masses. This tool allows for the selection of the most promising targets using independent signs of the presence of a planet, and provides reliable constraints on the planet orbits with limited amounts of observational data. This powerful approach is expected to lead to new, key discoveries, and enable a better characterisation and modelling of giant planets and brown dwarfs.

Declaration

I declare that this thesis was composed by myself, that the work contained herein is my own except where explicitly stated otherwise in the text, and that this work has not been submitted for any other degree or professional qualification except as specified. I would like to note the support and guidance of my collaborators, Dr. Beth Biller, Dr. Mariangela Bonavita, Dr. Katelyn Allers, Prof. Ken Rice, Dr. Eric Lopez, Dr. Koraljka Mužić, in obtaining the work shown in this thesis.

Work presented in this thesis has been published, or will be published, as follows:

1. Fontanive C., Biller B., Bonavita M. & Allers K., 2018, MRNAS, 479, 2702. *Constraining the multiplicity statistics of the coolest brown dwarfs: binary fraction continues to decrease with spectral type* (Chapter 2).

2. Fontanive C., Rice K., Bonavita M., Lopez E., Mužić K. & Biller B., 2019, MNRAS, 485, 4967. *A high binary fraction for the most massive close-in giant planets and brown dwarf desert members* (Chapter 3).

3. Fontanive C., Bonavita M., Biller B. & Mužić K., in preparation. *Finding and characterising the orbit of directly-imaged companions with COPAINS* (Chapter 4).

Clémence Fontanive
May 2019

Acknowledgements

I would like to extend thanks to the many people who have made this thesis possible, who cheered me on from various places around the world, and who made my time in Edinburgh some of the best years of my life.

Foremost, I wish to thank my two supervisors, Dr. Beth Biller and Dr. Mariangela Bonavita. I am incredibly grateful to Beth for her endless patience and invaluable wisdom (I will never forget that "*the perfect is the enemy of the good*"). She found the ideal balance for me between rigorous guidance and freedom in my research plans, and has made the four years of my PhD a more fun and enjoyable experience than I could ever have imagined. I would like to thank Mariangela for all the late nights spent with me on various proposals and applications, and for the fond memories I keep of our numerous expeditions. Not many PhDs involve a detour to Machu Picchu after an observing trip in the Atacama desert, or a Californian road trip with a whale watching adventure.

Many thanks go to my collaborators who so generously contributed to the work presented in this thesis. I would like to thank Dr. Katelyn Allers and her contagious enthusiasm, for being such an amazing collaborator and dedicated mentor. I am thankful to Dr. Eric Lopez for making every work trip more cultural and culinary. Most importantly, he has always supported me in my academic goals and has provided me with fantastic chances to pursue these objectives. I also wish to thank Dr. Luigi (Rolly) Bedin, who has been truly supportive of my career from the moment we met. I am extremely grateful for his constant encouragement and profound faith in my work. This thesis would not have been possible without the unwavering guidance and contribution of Prof. Ken Rice and his insightful comments, on both science and life. I also extend my gratitude

to Dr. Koraljka Mužić, whom I had the great pleasure of working with in the last year, for her generosity and passionate attitude.

I would like to thank everyone at the Royal Observatory for creating such a friendly and thriving work environment. In particular, I wish to thank all my fellow PhD students who made my time at the IfA a real pleasure, with special mentions to my office mates, Ben, Rachel, Vasiliy and Raphaël, for keeping me sane in this last year. I cannot begin to express my gratitude to Niall for his endless kindness and support, and more generally for putting up with me. He kept a sense of humour when I had lost mine and never failed to lift my mood. I am also very thankful to Sophie for our unwinding tennis games and lengthy chats around a cup of tea when the weather was too Scottish for us to brave.

Finally, I would like to extend my deepest gratitude to my friends and family for their unwavering belief in my ability to succeed. I thank my mother for her infinite support in whatever I pursue and for indulging my interest in astrophysics. I am extremely grateful to my father for sharing his passion for science with me, and introducing me with so much enthusiasm to the world of astronomy. I owe him my curiosity about the world, and would not have embarked on this path and become an astronomer without him. I am thankful to my siblings, Julia, Renaud and Gauthier, for their (sometimes questionable) humour, for constantly challenging me, and for always being there. I would like to thank my grandmother, Micha, for her inspiring courage, and everyone else in my family for still asking about brown dwarfs and exoplanets at every family reunion.

All men have stars, but they are not the same things for different people.
For some, who are travelers, the stars are guides.
For others they are no more than little lights in the sky.
For others, who are scholars, they are problems...

– Antoine de Saint-Exupéry, *The Little Prince*

Contents

List of Figures

List of Tables

Science tells us our story: astronomy our past and ecology our future.

– Hubert Reeves

1

Introduction: Brown Dwarfs and Extra-Solar Giant Planets

Contents

1.1 The Brown Dwarf-Exoplanet Connection

The sheer number and wide variety of planets in our Solar system have been a strong motivation in the search for planets orbiting other stars, known as exoplanets. Since the discovery of the first extra-solar planet in 1995 (51 Peg b; Mayor & Queloz 1995), almost 4000 exoplanets have been found[1], and thousands more are awaiting confirmation. The majority of these exoplanets were found to have wildly different characteristics and demographics from the planets in our own Solar system. With a diversity of physical properties and system architectures extending far beyond anticipations, it quickly became clear that our Solar system may not be a standard archetype of planetary systems after all.

In parallel to the first exoplanet detection, 1995 was also the year of discovery of a new class of astronomical objects known as brown dwarfs. Brown dwarfs represent the long-sought bridge between stars and planets, filling a crucial gap in mass, spectrum and temperature between the lowest-mass stars and the most massive planets. These objects are especially interesting since they share remarkable similarities and physical properties with giant planets, including comparable sizes to Jupiter and similar spectroscopic and photometric characteristics to massive Jovian planets. In particular, the very lowest-mass brown dwarfs represent excellent analogues to the directly-imaged giant planets, with ultracool temperatures and weather features observed in their atmospheres, making them ideal proxies to study cool exoplanets.

While planets were known to exist from our Solar system, the existence of brown dwarfs was purely theoretical until the discovery of Gliese 229B around a low-mass star by Nakajima et al. (1995) and Oppenheimer et al. (1995). Brown dwarfs were first theorised in the 1960s by Kumar (1963) and Hayashi & Nakano (1963), who predicted a population of faint and cool star-like objects, with masses too low to undergo hydrogen fusion in their cores, the driving source of energy sustaining stars. More than 2000 brown dwarfs are now known[2].

The upper mass limit for brown dwarfs is well agreed on, taken to be the hydrogen-burning limit at $\sim$75 M_{Jup} (roughly 8% of the mass of the Sun), where objects

[1]NASA Exoplanet Archive, `https://exoplanets.nasa.gov`
[2]MLTY Dwarf Archives, `www.DwarfArchives.org`

above that threshold are able to sustain stable hydrogen fusion and are classified as stars. On the other hand, the lower limit of the brown dwarf mass range is still heavily debated. The deuterium-burning limit at $\sim$13 M_{Jup} was historically considered as the boundary between brown dwarfs and planets (Saumon et al. 1996; Lucas & Roche 2000). The discovery in recent years of free-floating objects with effective temperatures comparable to those of giant planets (Cushing et al. 2011; Kirkpatrick et al. 2011; Liu et al. 2011) have gradually reduced the temperature gap between the coolest brown dwarfs ($T_{\rm eff} \sim 250$ K; Luhman 2014) and the planet Jupiter ($T_{\rm eff} \sim 130$ K). Isolated objects with masses as low as a few M_{Jup}, but photometric colours similar to brown dwarfs challenge current formation theories and question this brown dwarf/planet boundary, suggesting an overlap between the masses and temperatures of the lowest-mass brown dwarfs and the most massive planets.

A definition based on formation instead of mass may thus be preferable to differentiate brown dwarfs and planets, as it has been argued by Chabrier et al. (2005) and Schlaufman (2018). In this case, planets would be defined as objects forming in circumstellar discs around stars, while brown dwarfs and stars would arise from the collapse of proto-stellar clouds, with a distinction based on the ability to sustain hydrogen fusion. The lower mass limit for brown dwarfs could then be as low as $\sim$3 M_{Jup} (Kumar 2003; Boyd & Whitworth 2005), the minimum mass for opacity-limited fragmentation in turbulent cloud cores (Silk 1977). The difficulty with a formation-based distinction between brown dwarfs and planets comes from the need to know how objects formed in hindsight in order to classify them. This is especially challenging since the imprints from formation mechanisms on temperature and luminosity are only observable at very early stages and rapidly fade away.

1.2 Properties and Classification

1.2.1 The Luminosity-Mass-Age Degeneracy

Without hydrogen fusion in their core to sustain them, brown dwarfs and giant planets spend their entire lifetime contracting and cooling down, evolving in

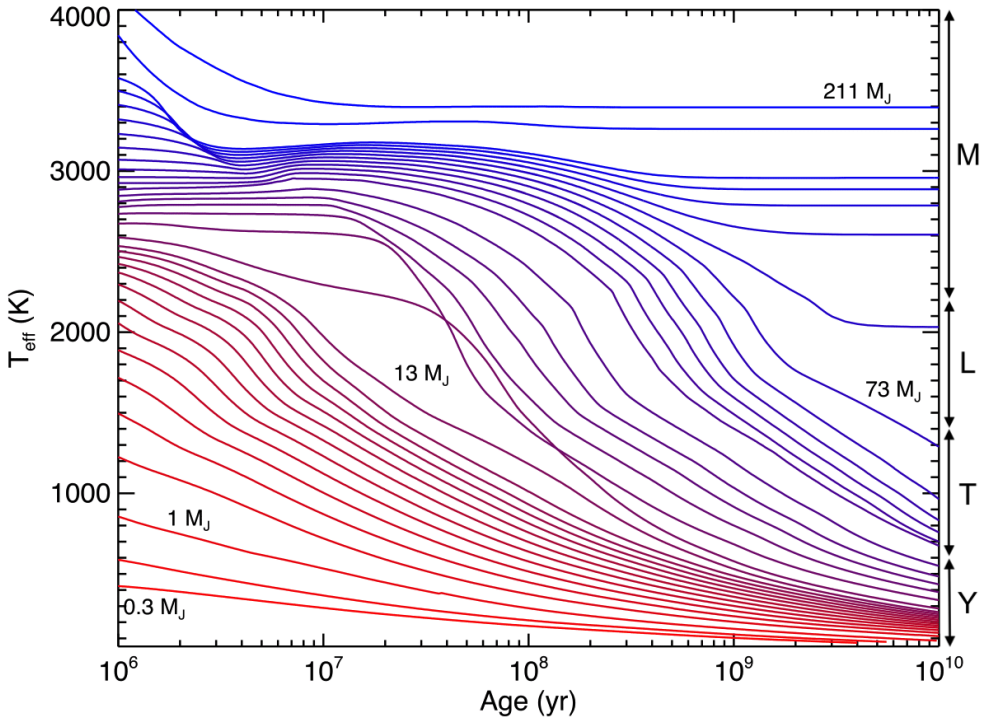

Figure 1.1. Evolutionary model showing the effective temperature $T_{\rm eff}$ as a function of age for stellar (blue), substellar (purple) and planetary-mass (red) objects. The strong age degeneracy of brown dwarfs and giant planets in the mass-temperature relationship is apparent. Corresponding spectral types are marked on the right. While the temperature of low-mass stars only varies by a few 100 K over the first few Myr (pre-main sequence), then remaining relatively constant for 10 Gyr (main sequence), substellar objects steadily cool with time and the effective temperature of brown dwarfs can decrease by over 2000 K in that timescale. Figure from Burrows et al. (1997).

their spectral and photometric appearance as they age (Burrows et al. 2001). This results in a key difference between substellar objects and main sequence stars: while stellar masses can be directly inferred from a star's spectral type, brown dwarfs and giant planets show a temperature-mass-age degeneracy. For example, an object with a measured luminosity L (corresponding to an effective temperature $T_{\rm eff}$) could be an old, massive brown dwarf, or may be a very low-mass younger analogue. Figure 1.1 shows the temperature evolution with age for low-mass stars (blue), deuterium-burning brown dwarfs (purple) and planetary-mass objects below the 13 $M_{\rm Jup}$ deuterium fusion limit (red), illustrating this inherent temperature-mass-age degeneracy in the substellar regime.

Evolutionary models like the one presented in Figure 1.1 were developed to track the evolution of brown dwarfs and their properties depending on their mass (e.g. Chabrier et al. 2000; Baraffe et al. 2003; Burrows et al. 2003; Marley et al. 2007; Saumon & Marley 2008). Using these predictions, measured luminosities of brown dwarfs or exoplanets can be used to infer their masses at any given age, by looking for the relevant evolutionary track in Figure 1.1.

However, significant theoretical uncertainties remain in these evolutionary models, in particular at early stages (Bowler 2016). The limited amount of information available to constrain the underlying chemistry in brown dwarf and exoplanet atmospheres, together with the lack of empirical validation regarding the physical evolution of these atmospheres with time, results in a number of highly uncertain and discrepant sets evolutionary models (see Section 1.5). Furthermore, precise age measurements can be extremely challenging, in particular for field stars isolated from known moving groups (associations of stars sharing common origins and kinematics), resulting in additional uncertainties in model-dependent mass estimates (Jeffries 2014; Soderblom et al. 2014). Because theoretical models are currently the only available tool to infer physical parameters for most directly-imaged companions and isolated objects, evolutionary tracks are nevertheless widely used by the community, in spite of the large uncertainties they carry.

1.2.2 Spectral Sequence

Like stars, brown dwarfs and cool giant planets are classified according to their spectral morphology, which is directly related to the effective temperature $T_{\rm eff}$. The lower temperatures and new spectral absorption features observed in substellar objects led to the introduction of a new classification scheme, extending the OBAFGKM stellar classification system (Cannon & Pickering 1901) to the new L, T and Y spectral classes (Kirkpatrick 2005; Cushing et al. 2011). Brown dwarfs typically start their lives with a late-M or early-L spectrum, and evolve through L, T and eventually Y spectral types as they cool down (Kirkpatrick et al. 1999; Kirkpatrick 2005; see Figure 1.1).

Understanding the atmospheres of brown dwarfs and cool giant planets is crucial to constrain their evolution and comprehend their complex appearances. The

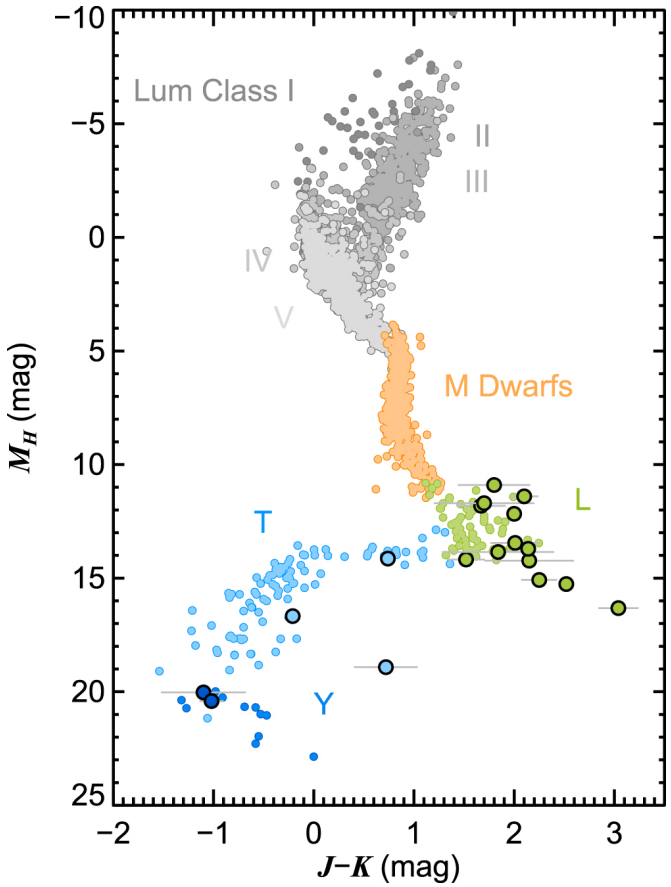

Figure 1.2. Colour-magnitude diagram of MLTY substellar objects compared to OBAFGK stars, showing the NIR $J-K$ colours against absolute H-band magnitude. Directly-imaged companions are marked by bold circles. Figure from Bowler (2016).

relatively cool temperatures of these objects allow for a chemical equilibrium to occur, which enables the formation of molecules. Moreover, condensates can form at these low temperatures, adding intricate clouds, bands and haze structures to the problem, in addition to observed photometric variability (Artigau et al. 2009; Radigan et al. 2012; Apai et al. 2013; Biller et al. 2013b; Vos et al. 2019). These temperature-dependent atmospheric properties result in significant changes in colours and photometric aspects as a function of spectral type. Figure 1.2 shows the positions in the near-infrared (NIR) colour–magnitude diagram of MLTY objects. OBAFGK stars are shown in grey. Directly-imaged companions, marked by bold circles, typically have redder colours than field brown dwarfs for the same spectral types (Faherty et al. 2013), extending the brown dwarf sequences to redder and fainter magnitudes in Figure 1.2.

1.2.2.1 M Dwarfs

While most M dwarfs are low-mass stars, some late-type M objects may be hot, massive brown dwarfs. Because of the constant cooling and age degeneracy of substellar objects described above, only very young brown dwarfs can have an M spectral type (Bailey 2014). The optical M stellar spectral classification (Boeshaar 1976) was extended by Kirkpatrick et al. (1991) to include spectral types up to M9, corresponding to objects with effective temperatures down to around 2200 K. Kirkpatrick et al. (2010) later defined spectral standards based on the NIR spectral region.

M-dwarf spectra are distinguished by the presence of prominent titanium oxide (TiO) and vanadium oxide (VO) bands in the optical. The increasing strengths of these features with later spectral type are used as discriminators between subtypes. Broad water (H_2O) absorption bands are observed in the NIR, which increase in depth with later-type. Additional features such as sodium Na I and potassium K I lines, and iron hydride (FeH) and carbon monoxide (CO) bands are also present in the $1-2.5$ μm region. Figure 1.3 shows the spectral standards for M6 and M8 objects in the red optical and NIR spectral ranges, highlighting some of these spectroscopic features.

1.2.2.2 L Dwarfs

L dwarfs typically extend from $\sim$2200 K for L0 objects to $\sim$1400 K for late-L objects. The L spectral class was defined by Kirkpatrick et al. (1999) based on the optical spectral region, before being outlined in the NIR by Reid et al. (2001) and Geballe et al. (2002). Kirkpatrick et al. (2010) subsequently defined NIR spectral standards for L dwarfs, which are shown in Figure 1.3. The L-dwarf sequence is marked by the weakening with later type of the TiO and VO features in the optical, characteristic of M dwarfs, which eventually disappear by mid-L spectral types (Bailey 2014). Some overlapping features with M stars are observed in the NIR L spectra, such as the H_2O and CO absorption bands, which continue to increase in strength in later-type objects (Figure 1.3). Enhanced hybride bands and alkali lines are also seen in L-type spectra.

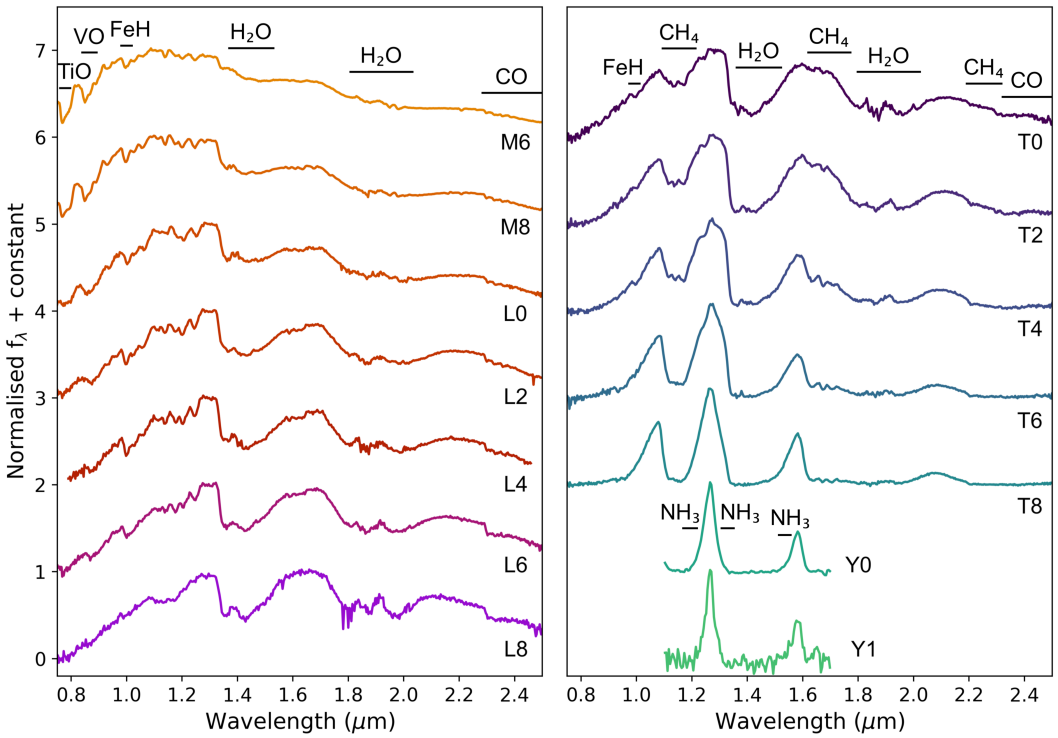

Figure 1.3. NIR spectral standards for the late-M, L, T and Y sequences, in the red optical and NIR spectral regions. All spectra are normalised to unity at 1.27 μm, and offset with constants in increments of 1. The dominant absorption bands present in M-L (left panel), T and Y (right panel) spectra are marked at the top of each sequence, clearly showing the evolution of the main atmospheric properties as brown dwarfs cool down. Data were taken from the SpeX Prism Spectral Libraries[1] for M, L and T dwarfs, and from the Y Dwarf Compendium[2] for Y dwarfs.

The transition from M to L in spectral type is associated with the formation of mineral condensates in the cool photospheres of L-type dwarfs (Burrows & Sharp 1999; Lodders 2002). In chemical equilibrium, species like Ti, VO and various silicates start to condense as effective temperature decreases below ∼2000 K, thus disappearing from gas phase. The formation of condensates produces grain and dust clouds in the visible atmosphere. These clouds, as they become progressively thicker and more opaque, are believed to be responsible for the red NIR colours of L dwarfs in Figure 1.2 (Allard et al. 2001; Marley et al. 2002).

[1]Maintained by A. Burgasser, `http://pono.ucsd.edu/~adam/browndwarfs/spexprism`.
[2]Maintained by M. Cushing, `https://sites.google.com/view/ydwarfcompendium`.

1.2.2.3 T Dwarfs

The T spectral class further extends the classification of low-temperature objects (Burgasser et al. 2002, 2006a; Kirkpatrick et al. 2010), encompassing temperatures from ∼1400 K at the L/T transition to ∼600 K for the coolest, latest-type T dwarfs. T dwarfs are distinguished by the appearance of strong methane (CH_4) absorption bands around 1.6 μm and 2.2 μm (right panel of Figure 1.3). The CH_4 and H_2O bands continue to strengthen through the subtypes, resulting in NIR spectra shaped by triangular peaks in the latest-type T objects. Figure 1.3 shows the NIR spectral standards of the T spectral sequence, clearly illustrating this distinctive characteristic of late-T dwarfs in the NIR region.

The L/T transition is associated with a turnover in abundances between CO and CH_4, occurring at equilibrium temperatures of ∼1400 K (Lodders 2002), making CH_4 the dominant carbon-bearing species in cooler atmospheres. More importantly, the evolution to T spectral types is marked by a dispersal of the clouds present in L-type atmospheres (Allard et al. 2001; Burgasser et al. 2002). This dissipation occurs when dust grains settle deeper in the atmosphere as brown dwarfs cool down. With the clearing of the dust clouds, the opacity floor that the clouds provided is removed. Combined with strong CH_4 features in the NIR that remove over half of the flux at red NIR wavelengths, T dwarfs become increasingly blue compared to L dwarfs, as shown in Figure 1.2 (Marley et al. 2012).

1.2.2.4 Y Dwarfs

The possible existence of even cooler atmospheres, filling the gap between the coldest T dwarfs and Jupiter, was explored in early atmospheric models by Burrows et al. (2003). The theoretical prediction of new spectral features at temperatures below $T_{\rm eff} \sim 600$ K, such as the formation of ammonia molecules (NH_3) or the disappearance of alkali lines, suggested the need for a new spectral class for such ultracool objects (Leggett et al. 2007; Kirkpatrick 2008). The discovery in the following years of a number of extremely faint objects exhibiting comparable features to the latest-T dwarfs, but also showing NH_3 absorption, confirmed the existence of cooler field brown dwarfs and started populating the new Y sequence (Cushing et al. 2011; Kirkpatrick et al. 2012; Tinney et al. 2012).

About 25 Y dwarfs have now been confirmed, with temperatures as low as ∼250 K for the most extreme example (WISE 0855; Luhman 2014).

Y dwarfs show similarly deep H_2O and CH_4 absorption bands as T dwarfs. The appearance of NH_3 absorption features around 1−1.5 μm results in even narrower peaks in the NIR spectra, as shown in Figure 1.3. As brown dwarfs keep cooling, water and then ammonia clouds are expected to form below $T_{\rm eff} \sim 400$ K, as seen in Jupiter (Morley et al. 2012; Leggett et al. 2013). The formation of these cloud decks gives rise to redder NIR colours (Leggett et al. 2017), reversing the trend towards blue colours seen for T dwarfs in Figure 1.2. Non-equilibrium chemistry is also thought to be important for these objects (Leggett et al. 2017).

Ultracool Y dwarf are intrinsically faint, due to their extremely low effective temperatures. As a result, we are currently restricted to the most nearby Y dwarfs, typically within 10 pc from the Sun. Photometric and spectroscopic data are very limited for Y objects, in quantity, quality and spectral coverage. Large disparities are seen among the small sample of Y spectra available, and the atmospheric properties of the very coolest Y dwarfs are not fully understood and remain poorly modelled.

1.2.2.5 Young Brown Dwarfs and Directly-Imaged Companions

Directly-imaged giant planets are typically very young, as younger objects are brighter and thus easier to detect. These young exoplanets are thus less massive than older field counterparts for similar effective temperatures. Since brown dwarfs contract considerably in their first ∼300 Myr (Burrows et al. 2001), the population of young puffy planets has a lower surface gravity than field objects.

Directly-imaged companions are thought to have a delayed transition from cloudy L atmospheres to condensate-free T dwarfs due to their lower surface gravities (Marley et al. 2012; Faherty et al. 2013). The reduced gravity allows clouds to remain at higher altitudes compared to older field dwarfs, where these clouds would have dissipated. With a later removal of the cloud layer, the upper atmospheres of young planetary-mass objects and direct imaging companions remain opaque until cooler temperatures are reached, explaining the extension to fainter magnitudes and redder colours in Figure 1.2.

1.3 Brown Dwarf and Planet Formation Theories

1.3.1 Planet Formation via Core Accretion

Most planets are thought to form via the core accretion (CA) mechanism, including all planets from our Solar system. In the CA formation process, dust grains or pebbles in the protoplanetary disc coagulate and build up to form planetesimals, which in turn accrete to form a rocky core (Pollack et al. 1996; Ida & Lin 2004; Alibert et al. 2005; Lambrechts & Johansen 2012). Cores reaching a critical mass of $\sim$5$-$10 $M_{\oplus}$ subsequently attract a gas envelope and form gas giants (Kennedy & Kenyon 2008). This scenario can therefore successfully explain the formation of a wide range of planets, from small Earth-like planets to large Jovian planets.

Planet formation via CA is generally observed to be dependent on the physical parameters of the host star. For example, more massive stars and discs, as well as longer disc lifetimes, tend to be associated with higher numbers of planets and more massive planets (see Alibert et al. 2011; Mordasini et al. 2012). The formation of massive planets with this mechanism is also believed to be strongly correlated to stellar metallicity, where the most massive planets predominantly form around metal-rich stars (Fischer & Valenti 2005). Planets with masses larger than $\sim$5 $M_{\rm Jup}$ are thus very challenging to form via CA around Sun-like stars (Matsuo et al. 2007), with a steep drop in number and a strong metallicity dependence seen in the formation of higher-mass planets (Jenkins et al. 2017).

Theoretical simulations show that planetesimal accretion primarily occurs within a few AU from the star (Alibert et al. 2005). The formation of Jovian planets of several $M_{\rm Jup}$ beyond 20$-$100 AU is challenging to explain with a CA formation because of the very long timescales involved (Kennedy & Kenyon 2008). This process typically takes about 1$-$10 Myr in the optimal regions of protoplanetary discs, comparable to disc lifespans. In contrast, the formation of a massive gas giant beyond a few tens of AU would take significantly longer than the lifetime of the disc. The existence of high-mass exoplanets at large orbital separations, like the population of wide directly-imaged giant planets around very young stars ($\sim$few Myr old), is therefore difficult to reconcile with this theory.

1.3.2 Planet Formation via Gravitational Disc Instability

An alternative way to form giant planets around stars is through gravitational instability (GI) in a protoplanetary disc. In this process, an unstable disc collapses under its own gravity and fragments to form massive planetary or brown dwarf companions on wide orbits (Cameron 1978; Boss 1997). Disc fragmentation requires fairly massive discs, and preferentially occurs in the cool, outer regions of protoplanetary discs (Rafikov 2005). Theoretical calculations (Kratter et al. 2010; Forgan & Rice 2011) and numerical simulations (Stamatellos 2013; Hall et al. 2017) predict the formation of companions with masses larger than $\sim$4 M_{Jup}, and mostly in the brown dwarf regime, from separations of a few tens to hundreds of AU.

GI is thus likely to be responsible for the formation of the most massive exoplanets, and in particular the population of wide giant planets and brown dwarf companions detected with direct imaging. This process also occurs very rapidly, typically on timescales shorter than 0.1$-$1 Myr (Forgan & Rice 2013), significantly faster than the longevity of protoplanetary discs ($\sim$few Myr; Richert et al. 2018). Extremely young planets imaged in the gaps of their discs (see Figure 1.4) could therefore be explained with this mechanism.

Nevertheless, a number of issues remain with this formation theory. The massive discs required for instabilities to be triggered ($>$ 0.1$-$0.3 $M_{\odot}$; Stamatellos & Whitworth 2009) are not compatible with current observations (e.g. Mann & Williams 2009). In addition, appropriate cooling conditions need to be fulfilled for fragments to cool fast enough to form bound objects (Bell et al. 1997). These settings are generally challenging to reproduce in theoretical simulations for realistic environments. As a result, the GI formation mechanism is also problematic in the hot innermost regions of discs (within $\sim$10$-$30 AU separation) where the local cooling times are overly long compared to the dynamical timescale of the formation process (Rafikov 2005). Furthermore, magnetic fields are found to stabilise protoplanetary discs and prevent the growth of fragments after the collapse of a clump (Hennebelle & Teyssier 2008; Price & Bate 2009). Combined with the scarcity of wide and massive companions uncovered in direct imaging surveys, these difficulties suggest that GI rarely occurs and is unlikely to be the dominant process for planet formation (Janson et al. 2012a; Vigan et al. 2017).

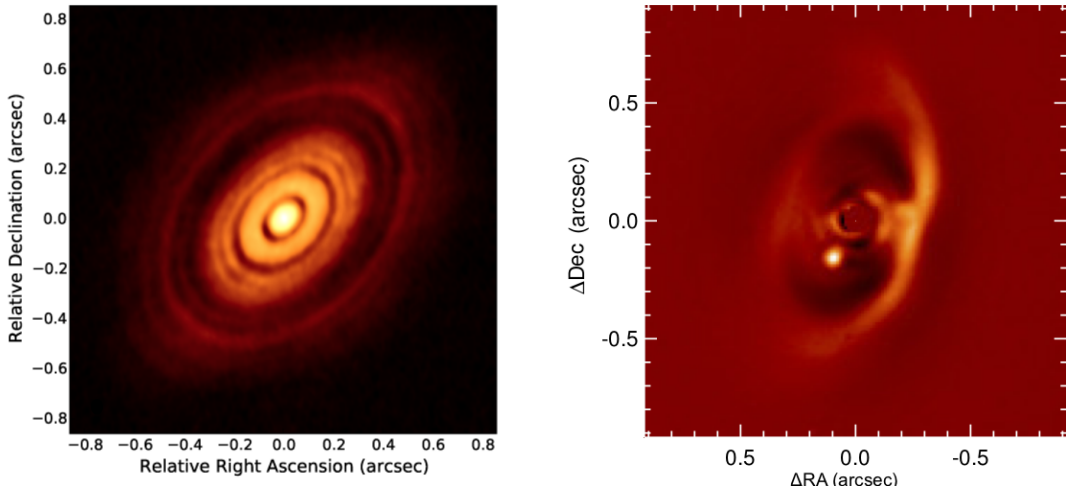

Figure 1.4. Left: ALMA image of the protoplanetary disc around the 1 Myr old HL Tau, discovered by ALMA Partnership et al. (2015). The concentric gaps in the disc could indicate the presence of emerging planets. Figure from Dipierro et al. (2015). **Right:** VLT / SPHERE observations of the proto-planet PDS 70b identified by Keppler et al. (2018) at 22 AU, in the gap of the protoplanetary disc around the 5.4 Myr old star PDS 70. Figure from Müller et al. (2018).

1.3.3 Forming Brown Dwarfs like Stars

While some brown dwarf companions might form around stars via GI, most brown dwarfs are believed to form in isolation through a similar mechanism to stars, via the gravitational collapse of a molecular cloud (Hoyle 1953; Hunter 1962). The main challenge in the theoretical modelling of brown dwarf formation via a star-like formation process is to circumvent the problems associated with the Jean's mass in the formation of very low-mass objects. The Jean's mass is the minimum mass required for an interstellar gas clouds to collapse under its own gravity (Jeans 1902), which is generally orders of magnitudes larger than a brown dwarf in typical star-forming environments (Padoan & Nordlund 2004). A way to decrease the Jean's mass in the natal gas, or to limit mass accretion after the onset of collapse, is thus required to prevent objects from becoming stars. A number of different models have been proposed for brown dwarf formation and the primary contenders are detailed below. It is important to note that these processes are not mutually exclusive and that brown dwarfs are likely the result of several coexisting and complementary mechanisms rather than a unique one (Whitworth et al. 2007).

1.3.3.1 The Ejection Scenario

One of the earliest theories developed for brown dwarf formation is the ejection scenario, a process suggested by Boss (2001) and Reipurth & Clarke (2001). In this model, brown dwarfs are premature stellar embryos which are disrupted by other cluster members and dynamically expelled from their natal cluster at very early stages. The accretion is thus cut off before the embryos reach the minimum mass required to undergo stable hydrogen fusion and become stars, creating substellar objects.

A number of tight subsellar binaries were discovered in the field in the early 2000s, most of which have separations < 10 AU (Close et al. 2003; Burgasser et al. 2003, 2006b; Liu et al. 2006). This prevalence of very close binaries was initially considered as evidence for this scenario, in which only the tightest binaries can survive an ejection event (Reipurth & Clarke 2001; Bate et al. 2002). However, surveys in young nearby associations have uncovered in the last decade a number of wider (> 20 AU) binary pairs with low binding energies (Kraus et al. 2006; Close et al. 2007; Konopacky et al. 2007; Todorov et al. 2010). Although more recent simulations have achieved less violent disruptions, allowing some wider systems to survive, the existence of a significant population of wide binaries suggests that the involvement of ejection is not a necessary component of the birth of brown dwarfs (Bate 2009).

1.3.3.2 The Turbulent Fragmentation Model

Brown dwarfs may also form via turbulent fragmentation of molecular clouds (Padoan & Nordlund 2002). This mechanism produces very low-mass prestellar cores after fragmentation of the gas cloud under turbulent compression due to strong magnetic shocks. The presence of a magnetic field modifies the local gas density and decreases the Jean's mass. If the density is sufficiently high, the cores then become gravitationally unstable and collapse to form low-mass stars, brown dwarfs and even planetary-mass objects (Padoan & Nordlund 2004).

Simulations show that if self-gravitating objects can form with masses as low as $\sim$1 M_{Jup}, most of the produced fragments tend to continue to accrete mass

from their surrounding medium, eventually reaching and passing the point of the hydrogen-fusion threshold (Boss 2001; Bate et al. 2003). The formation of brown dwarfs therefore appears difficult to achieve in large quantities with these models, which also require a particularly high density to bypass the usual Jean's mass requirements and allow for low-mass fragments to collapse.

1.3.3.3 Fragmentation of Massive Prestellar Cores

In a variation of the turbulent fragmentation model, brown dwarfs may also form through the collapse and fragmentation of more massive cores (Whitworth et al. 2007; Bonnell et al. 2008). In this scenario, molecular cloud fragmentation produces large, high-mass prestellar cores ($\sim$1$-$10 $M_{\odot}$) that display nonlinear density structures (Whitworth et al. 2007). The cores then undergo dynamical fragmentation themselves as they collapse, generating clusters of protostars with a range of masses. The protostellar embryos formed subsequently accrete mass through self-gravity, with a distribution largely amplified by any existing density substructure (Bonnell et al. 2008). A combination of competitive accretion and dynamical interactions will lead to the formation of a variety of stars, as well as substellar objects with masses below the hydrogen-burning limit.

These models provide viable mechanisms to explain the existence of very wide binary systems observed at young ages. Unfortunately, the range of admissible initial conditions for numerical simulations is large and poorly constrained, as discussed in Whitworth et al. (2007). This theory has been advocated on theoretical grounds but further information is required to make it more realistic.

1.3.3.4 Photo-erosion of Prestellar Cores

Another possibility involving the photo-erosion of proto-stellar cores was suggested by Hester et al. (1996) and Whitworth & Zinnecker (2004). In this scenario, a newly-formed cluster of massive OB stars ionises the surrounding gas, exciting a large H II region. The outer layers of a nearby prestellar core with a mass of a few $M_{\odot}$ will then be eroded by the ambient ionising radiation when it becomes embedded in the H II region. The eroded core is left with a significantly truncated

mass, which may be below the hydrogen-burning limit (Whitworth & Zinnecker 2004). The object that will subsequently be formed from that core may then remain inside the substellar regime, making it a brown dwarf. This theory is supported by the observations of globulettes (small and dense conglomerations of gas) within H II regions (Haikala et al. 2017), thought to be the result of such an evaporation process.

The photo-erosion theory allows for the formation of low-mass objects for a wide range of initial conditions. However, it is generally found to be highly inefficient as it requires the formation of a very massive prestellar core to form a single brown dwarf (Whitworth & Goodwin 2005). In addition, this mechanism requires the vicinity of massive OB stars. Since isolated brown dwarfs are found in low-mass star-forming regions with no OB stars like Taurus (e.g. Luhman et al. 2017), this scenario is unlikely to be the dominant process for brown dwarf formation.

1.4 Detection Methods

1.4.1 Indirect Detection Techniques

The majority of known exoplanets and substellar companions to stars were detected via indirect detection methods, which search for a signal based on the effect of the companion on its host star, rather than detecting the planet itself. So far, the most efficient techniques for planet detection have been the Doppler radial velocity and photometric transit methods, which have led to the discovery of $\sim$20% and $\sim$75% of known exoplanets, respectively. In particular, radial velocity and transiting surveys have demonstrated the existence of a vast population of massive and short-separation exoplanets that are not found in our Solar system.

Figure 1.5 shows the demographics of known companions to stars, colour-coded by detection method. Transiting systems (orange) are mostly concentrated within 0.1 AU, while radial velocity (light blue) and microlensing (green) companions extend out to $\sim$5 AU. Only direct imaging (dark blue) is sensitive to separations beyond 10 AU. The concepts behind each technique, as well as their performances, advantages and limitations are discussed in the following sections.

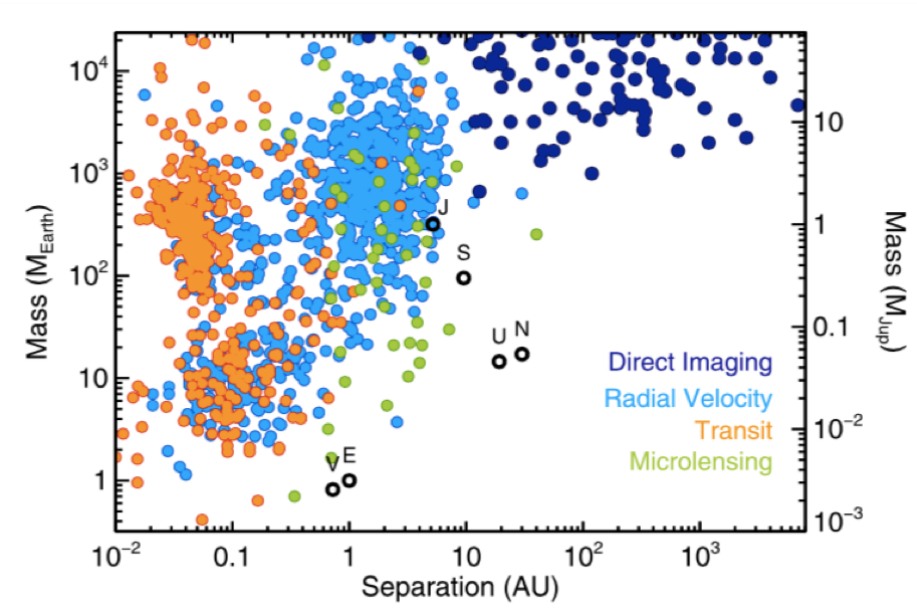

Figure 1.5. Masses and separations of companions to stars discovered via various detection methods. Some of the Solar system planets are also shown for comparison. The brown dwarf desert can be seen in the shortfall of massive, short-separation systems in the top left corner. Figure from Bowler (2016).

The major, puzzling feature from Figure 1.5 that is not the result of observational biases or limitations is the shortfall of massive, close-in planetary and brown dwarf companions, in the upper left corner. This attribute is known as the brown dwarf desert (Marcy & Butler 2000; Grether & Lineweaver 2006; Ma & Ge 2014) and is still not fully understood. It represents a significant deficit of brown dwarf companions within a few AU observed around Sun-like stars, relative to the higher incidence of lower-mass planets and more massive stellar companions on similar orbital configurations, and compared to the larger number of wide-orbit brown dwarfs. The brown dwarf desert is further discuss below, in the context of various detection methods.

1.4.1.1 Radial Velocity

The presence of an unseen companion causes a star to wobble around the centre of mass of the system under the gravitational influence of the secondary companion. The radial velocity (RV) detection method consists of measuring the Doppler shift in the spectrum of a star caused by this movement of the star along the line

of sight. The identification of periodic variations in the reflex velocity of the star can be used to reveal the existence of the companion and characterise its orbit.

The Doppler spectroscopy technique was successfully used by Mayor & Queloz (1995) to detect the first exoplanet identified around a main sequence star, 51 Peg b, a Jupiter-mass planet on a 4.23-day orbit. New RV systems are now regularly reported and over 700 exoplanets have been confirmed to date via this method (NASA Exoplanet Archive), including some multi-planet systems (e.g. Lovis et al. 2011; Fischer et al. 2012; Lo Curto et al. 2013).

The shape of the obtained radial velocity curve allows for the measurement of the velocity semi-amplitude, orbital period, eccentricity, argument of periastron and time of periastron passage, providing an excellent characterisation of the orbital properties of the system. If the mass of the star is known, these parameters can in turn be used to calculate a minimum mass for the companion. Because only the component of the star's movement that lies along the line of sight is detected with this approach, only the projected component of the mass M_2 can be inferred. This lower mass limit, $M_2 \sin i$, is dependent on the inclination i of the orbital plane, which cannot be determined from radial velocity data alone. Observations from a complementary method (e.g. transit, see below) must be used to constrain the system's orbital inclination and obtain a true mass for the companion.

The effect of a companion on its star increases with smaller orbital separation and larger companion mass. As a result, the RV approach is most sensitive to close-in and massive planets, such as hot Jupiters (Jovian planets on orbits of a few days like 51 Peg b). The precision of RV measurements has drastically improved from about 10 m s^{-1} in 1995 to less than 1 m s^{-1} with the commissioning of the HARPS spectrograph in 2003 (Mayor et al. 2003). The achieved accuracy of RV data can now probe small exoplanets of a few Earth masses within $\sim$0.1$-$1 AU, as well as gas giants out to Jupiter-like orbits (see Figure 1.5). While more distant companions could theoretically be detected with this precision level, RV observations must cover one complete orbit to robustly measure the period, and require a coverage spanning multiple orbital periods in order to confirm the true nature of candidates. Consequently, RV surveys remain for now limited to short-period planets (within a few AU), as several decades of observations would be required to identify wider-orbit companions.

As the amplitude of RV signatures is amplified for higher companion masses, massive giant planets and brown dwarfs ($M_2 \gtrsim 10$ M_{Jup}) on separations shorter than several AU should be easily detectable with the Doppler spectroscopy method. However, very few brown dwarf desert members are detected in radial velocity programs. Since the lack of such companions is not a consequence of observational limitations, the brown dwarf desert is believed to be a real feature.

The major drawback of the RV detection technique is that it is mostly limited to old, quiet stars with numerous spectral lines. The noise from the strong photospheric activity of young stars conceals the signals induced by small companions, making young targets unsuitable for this method. While the fast rotation of massive stars impedes the detection of exoplanets via Doppler spectroscopy, dynamical perturbations on stellar pulsations can also be used to discover exoplanets. In a comparable manner to the radial velocity approach, the pulsation timing method has uncovered multiple planetary companions around pulsars (rapidly and stably rotating neutron stars) by precisely tracking the arrival of their radio pulses (Wolszczan & Frail 1992; Konacki & Wolszczan 2003).

1.4.1.2 Photometric Transit

As a planet passes across the face of a star, it blocks out some of the star's light, causing a drop in the stellar photometric flux. The transit method relies upon carefully monitoring the brightness of a star in order to observe periodic dips in the light curve due to a transiting companion.

Based on the shape of the stellar light curve, the transit technique measures the physical radius of the transiting companion, and determines the orbital inclination i of the system. Follow-up observations with radial velocity therefore provide a measurement of the true mass by removing the inclination dependence from the RV minimum mass. The combination of radius and true mass also yields density estimates for exoplanets. Furthermore, a transit offers a unique chance to study the atmosphere of a short-period planet without resolving the system. During the transit, radiation from the star is transmitted through the planet's atmosphere and the spectral imprint from the planet can be probed via transmission spectroscopy (Sing et al. 2015, 2016). Similarly, the atmospheric

composition of a planet can be observed at occultation from the emission spectrum, as thermal radiation and reflected light from the planet disappear and reappear in the stellar spectrum (Knutson et al. 2014; Evans et al. 2017).

The main difficulty with the transit approach is that it requires systems to be in fortuitous orbital alignment with the Earth for a planet to pass directly in front of its star, as viewed from the Earth. Only a small fraction of systems exhibit transits, and the probability of observing a transit decreases steeply with larger orbital separation. As a result, the observing strategy adopted in transit surveys usually consists in observing large patches of sky, in order to monitor the photometry of many stars at once.

The flood of new planets that emanated from the development of large ground-based projects (e.g. WASP; Pollacco et al. 2006) and space-based programs (e.g. CoRot; Barge et al. 2008) rapidly demonstrated the success of the transit technique. In particular, the Kepler space mission (Borucki et al. 2010) has contributed to the most significant advances in exoplanet detection in the last decade. With the identification of over 2500 confirmed exoplanets between the main and extended missions, and as many candidates awaiting confirmation, the Kepler planets represent the vast majority of currently-known exoplanets. The most notable transit discovery to date is the TRAPPIST-1 system, which hosts 7 Earth-like planets with masses from 0.1 to 1.2 Earth masses within 0.06 AU (Gillon et al. 2016, 2017). The recent launch of the TESS space telescope (Ricker et al. 2015) is expected to lead to the discovery of many more transiting systems.

The duration of a transit increases with larger orbital separation, while the transit probability rapidly decreases beyond periods of a few days. As a full transit event must be observed to be characterised, and preferably over multiple orbits to be confirmed, the transit method is primarily biased towards very short-period planets (mostly within 0.1 AU) like hot Jupiters. Because the amount of star light blocked, and thus the depth of the light curve dip, is proportional to the radius of the planet, transit events from larger planets and brown dwarfs are easier to observe. Again, brown dwarf desert inhabitants should therefore be easily detectable via this approach. Nonetheless, the substellar regime remains poorly populated compared to lower-mass companions on separations probed by transit programs (Figure 1.5).

One of the biggest challenges faced in transiting surveys is the high false positive rates observed in light curve data (O'Donovan et al. 2006). For example, an eclipsing stellar companion can mimic the photometric transit of a low-mass substellar or planetary companion. Similarly, the passage in the line of sight of an unrelated star cannot be distinguished from the transit of a bound companion over a single event. In addition, cases in which the primary star is an unresolved binary, or where a closely-separated background object blends with the target, will lead to overestimates of the planetary radii. Extensive follow-up observations (with the same or another detection method) are thus crucial to confirm the bonafide nature and physical properties of transit candidates.

1.4.1.3 Microlensing

The gravitational microlensing detection technique is based on predictions from Einstein's theory of general relativity (Einstein 1936). When a massive foreground body passes across the line of sight of a star, the gravitational field of the foreground object bends the light emitted by the star, and acts as a lens to intensify its apparent brightness. If the lensing body is a planet-hosting star, the planets will also gravitationally deviate the light of the background star as they in turn pass in front of it as seen from the Earth. In doing so, the planetary companions will create perturbations in the light curve of the magnified background star over the duration of the lensing event. These anomalous features can be isolated from the primary signal to infer the presence of these planets and determine their properties.

In order to maximise the chances of finding elusive microlensing phenomena, surveys target regions of the sky with very high densities of stars, specifically in the direction of the Galactic bulge. The ground-based OGLE (Udalski 2003) and MOA (Bond et al. 2001) projects have been the most prolific microlensing campaigns so far. Over 70 exoplanets have been uncovered via gravitational microlensing, in addition to a dozen companions in the brown dwarf mass range. Discovered planets have separations ranging from 0.2 AU to 18 AU, with a wide spread of masses extending from Earth-mass planets to massive gas giants near and above the deuterium-burning limit (see Figure 1.5). A number of free-floating

(or extremely widely-separated) planetary-mass objects have also been detected via microlensing (e.g. Mróz et al. 2018).

Microlensing is the only method capable of discovering planets at distances up to several kpc, thus probing a possibly different exoplanet population than other discovery techniques, closer to the Galactic centre. The main merits of the gravitational lensing approach is its sensitivity to very small Earth-mass planets from ground-based observations. With an optimal efficiency for exoplanets or brown dwarfs on intermediate orbital separations from their stars ($\sim$1$-$10 AU), this technique is also nicely complementary to other detection methods in the planet separation space (Figure 1.5).

Nevertheless, the probability of observing a planet-lensing event is incredibly low ($\sim 10^{-8}$ per star; Tsapras 2018). This makes discovery rates rather low, even with extensive survey coverage and monitoring. Furthermore, microlensing discoveries are based on single and unique detection events. As a result, no follow-up observations or further characterisation of identified planets are possible past the microlensing event. In addition, there is a degeneracy in the interpretation of the physical parameters that can be inferred from the lensing signal, which cannot be disentangled without additional observations and characterisation of the planet host (Han 2005).

1.4.1.4 Astrometry

In a complementary manner to the RV method which relies on stellar movements along the line of sight, the wobble of a star due to the gravitational tug of an orbiting planet can also be observed in the plane of the sky. Astrometry consists of measuring the precise position of a star on the sky. The presence of an exoplanet can be determined by searching for nonlinear changes in the apparent sky-position of its host star, and characterising the orbital perturbations induced by the planet.

All orbital parameters can theoretically be inferred from the astrometric motion of a planet host, including unequivocal and direct determinations of the system's orbital inclination and the true mass of the companion. Astrometry therefore provides a powerful method for the discovery and characterisation of extra-solar planets, regardless of the system's alignment. In addition, positional

measurements are not highly affected by the strong atmospheric variations of young stars and this approach is mostly immune to stellar activity. The detectability of astrometric signals increases with larger orbital separation and planet mass, while it decreases with increasing stellar mass and distance from the Earth (Perryman et al. 2014). The astrometric detection method is thus sensitive to nearby, long-period massive companions, overlapping with the parameter space covered by direct imaging programs in Figure 1.5.

While a few brown dwarf binaries have been identified through astrometric variability (Dupuy & Liu 2012), only one exoplanet discovery has been claimed so far (Muterspaugh et al. 2010). The detection of planetary companions to stars via astrometry remains challenging due to the limited quality of the available data. The precision required to detect signatures of orbital motions induced by planetary companions, of typical amplitudes smaller than one milli-arcsecond, sits at the limit of the capabilities of current ground and space-based telescopes (Malbet & Sozzetti 2018). Nonetheless, astrometry has already been successfully used to complement other detection methods. For example, *Gaia* and *Hipparcos* astrometric data have been considered in combination with radial velocity and direct imaging observations to determine the masses of known planets (e.g. Sahlmann et al. 2011; Brandt et al. 2018; Dupuy et al. 2019).

The new ESA astrometry-dedicated *Gaia* survey (Gaia Collaboration et al. 2016, 2018b) monitors the sky positions of billions of stars to unprecedented accuracy levels. By the end of the mission, *Gaia* is expected to detect thousands of massive (> 1 M_{Jup}), long-period Jovian planets through the reflex motion of planet-bearing stars (Perryman et al. 2014). This will greatly propel the contribution of astrometry to the detection of extra-solar planets in the coming years.

1.4.2 Direct Imaging

Direct imaging is the only detection method that provides observations of an exoplanet or brown dwarf itself. With the unique opportunity to obtain direct photometric and spectroscopic observations of substellar objects, direct imaging allows for a direct probe of ultracool atmospheres. This detection technique is necessary to study the unexplored, outer regions of planetary systems, and

has played a critical role in the detection of wide and cool giant planets. This new population of exoplanets has provided us with tremendous insights into the demographics and architectures of exoplanetary systems, inspiring novel formation and evolution theories. Direct imaging has also enabled the discovery of isolated and binary brown dwarfs, including some key planetary-mass objects. Spectroscopic characterisation of these systems has offered us the first glimpse into the statistical and physical properties of ultracool brown dwarfs, advancing our fundamental understanding of planetary atmospheres.

1.4.2.1 Companions to Stars

While thousands of exoplanets have been uncovered via the indirect detection methods described in the previous section, none of these planets can be directly studied and analysed. By capturing the thermal emission of self-luminous companions themselves, direct imaging provides unparalleled information about the physical properties of giant planets. However, the direct observation of an exoplanet is an extremely challenging task and is tremendously impeded by the close vicinity of its bright host star. Due to the intrinsic faintness of such cool objects, a young Jupiter-like planet is typically $10^4 - 10^8$ times fainter than its star (Biller 2014), and the situation is further complicated by the small angular distances separating the planets and their stars on the sky.

The last decade has seen the emergence of new high-contrast adaptive optics (AO) systems and the advent of specialised coronagraphs to block out the stellar light on dedicated planet-finding instruments. Combined with innovative observing strategies and pioneering post-processing techniques, the search for extra-solar planets with direct imaging has rapidly evolved in the past ten years (Bowler 2016). Using 8-m class telescopes, a first generation of high-contrast imagers led to the detection of the first directly-imaged exoplanets. Figure 1.6 shows the HR 8799 system (Marois et al. 2008, 2010) identified with the Keck/NIRC2 and Gemini/NIRI instruments, and the β Pic b planet (Lagrange et al. 2010) discovered using NACO at the Very Large Telescope (VLT). The HR 8799 planetary system contains four gas giants with masses of $5-10$ M_{Jup}, on projected separations between 14 AU and 68 AU, and remains the only directly-imaged

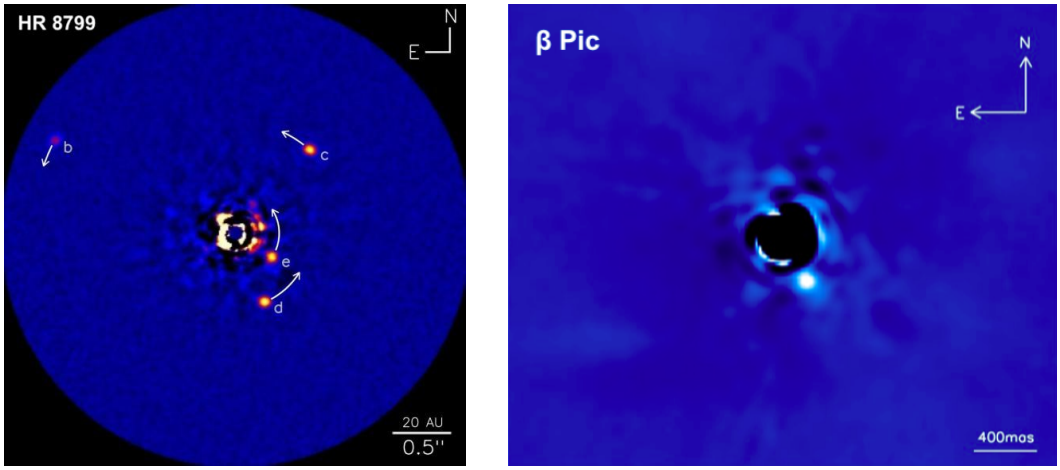

Figure 1.6. **Left:** the directly-imaged planetary system around HR 8799, showing the four giant planets discovered by Marois et al. (2008) and Marois et al. (2010). This image was taken with the NIRC2 instrument at the W. M. Keck Observatory in Hawaii. Image credit: Jason Wang and Christian Marois. **Right:** direct imaging observations of the β Pic b planet identified by Lagrange et al. (2010) with the VLT/NACO instrument. Image from Lagrange et al. (2010).

multi-planet system known to date. The young giant planet orbiting β Pic has an estimated mass of around 11 M_{Jup} at a projected separation of $\sim$10 AU.

A large number of completed programs, including the Gemini NICI Planet-Finding Campaign (Liu et al. 2010; Biller et al. 2013a; Nielsen et al. 2013), the NACO Large Program at VLT (Chauvin et al. 2015; Vigan et al. 2017), the International Deep Planet Survey (IDPS; Vigan et al. 2012; Galicher et al. 2016), as well as ongoing projects like the Gemini Planet Imager (GPI; Macintosh et al. 2014) Exoplanet Survey and the SHINE survey with VLT/SPHERE (Chauvin et al. 2017) steadily increased the census of wide companions. A dozen directly-imaged exoplanets with masses below the deuterium-burning limit have now been confirmed around main sequence stars, and roughly twice as many companions with masses in the brown dwarf mass range are known. Despite these discoveries, many of these surveys yielded null detections. The main statistical results that emanated from these studies were that massive planets are exceedingly rare on wide orbits (Bowler 2016).

Direct imaging is restricted to companions on wide orbital separations ($\gtrsim$ 5$-$10 AU), where companions can be resolved by the instrument inner working angle, and the faint signals emitted by the planets or brown dwarfs can be recovered

behind the flux of the host stars. Directly-imaged companions extend from separations of a few AU to hundreds or thousands of AU (see Figure 1.5), therefore probing a population completely inaccessible to the radial velocity and transit detection methods. Direct imaging is also applicable to a large variety of stars, and surveys have targeted all types of hosts, from low-mass M dwarfs to massive A stars.

While imaging provides unique probes into the atmospheric characterisation of exoplanets via photometry and in some cases spectroscopy, it only allows for the measurement of the planet's luminosity and the system's relative astrometry. Masses for direct imaging planets and brown dwarfs must therefore be extrapolated from the observed photometry, relying on highly uncertain theoretical models as discussed in Section 1.5. The large separations of directly-imaged companions also mean that these systems have very long orbital periods, usually of at least several decades. As a result, the orbital coverage of available data is generally insufficient to observe a significant fraction of the orbital motion. Orbital constraints and dynamical mass measurements are thus unattainable for the direct imaging population without multiple decades of monitoring, or additional information from alternative methods. For example, Snellen & Brown (2018) and Dupuy et al. (2019) recently refined the mass of β Pic b by combining imaging observations with radial velocity and astrometric data.

Direct imaging programs also suffer from high false positive rates from background interlopers. A second epoch of observation is needed to confirm that a candidate is gravitationally bound to the primary star. The baseline required to confirm physical association scales with the proper motion of the target and typically varies from several months to a few years. Despite the very wide orbits of directly-imaged companions, selected candidates can therefore be confirmed through common proper motion analyses in time spans much shorter than the orbital periods of the systems.

Theoretical models predict that brown dwarfs and cool giant planets are substantially more luminous at the earliest stages of their evolution. Young stars thus provide the highest chance of detecting a low-mass companion, before it cools down and becomes too faint to be observed. Nearby stars are also preferable, in order to optimise the resolvable orbital separation of systems. For these reasons,

young moving groups, with ages of 10−300 Myr and located within 100 pc, offer ideal and accessible age-calibrated targets. The precise knowledge of stellar ages is especially important as it removes the age degeneracy in the mass estimation of companions.

Finally, the ability to observe extremely young giant planets means that direct imaging has the potential to capture planets being born, like the protoplanet PDS 70 b (Keppler et al. 2018; Müller et al. 2018) observed in the gap of its protoplanetary disc (see Figure 1.4). Observing forming planets provides crucial information towards our understanding of planet formation, and these types of observations can be used to discriminate between competing formation theories.

1.4.2.2 Isolated Objects

Most isolated brown dwarfs known to date have been discovered through wide-field photometric surveys such as the Two Micron All Sky Survey (2MASS; Skrutskie et al. 2006), Sloan Digital Sky Survey (SDSS; York et al. 2000) or Deep Near Infrared Survey of the Southern Sky (DENIS; Epchtein et al. 1997). These programs acquire photometric data in multiple bandpasses, and brown dwarfs are searched for and identified through their broadband near-infrared and infrared colours, at wavelengths where such cool objects are brightest. With the launch of the *Wide-Field Infrared Survey Explorer* (*WISE*; Wright et al. 2010), over 2000 brown dwarfs have now been identified via wide-field imaging surveys, with spectral types down to early-Y (Cushing et al. 2011; Kirkpatrick et al. 2011, 2012; Luhman 2014).

Wide-field imaging offers the advantage of covering large areas of the sky, increasing the chances that the obtained images contain brown dwarfs. However, the large field of view provided is at the expense of deep images, therefore limiting the possibility of detecting cooler and fainter sources. In these programs, brown dwarf candidates are selected based on their broadband photometry. Because of the high contamination rates in wide-band surveys, many of the candidates selected for their red colours turn out to be reddened background objects. Spectroscopic follow-up observations are usually required to confirm the substellar nature of identified candidates.

Spectroscopic confirmation is typically done through the fitting of spectral templates to the observed spectrum of a brown dwarf candidate. Spectral fitting requires high-resolution spectroscopic data, with measurements taken over a sufficiently large wavelength range. This can be difficult to achieve for extremely faint or distant targets. Other methods, looking for defining characteristics in specific spectral signatures (e.g. lithium, Pozio 1991; Kirkpatrick 2008; methane, Burgasser et al. 2000; Kirkpatrick 2005; water, Allers et al. 2007; Allers & Liu 2010), have been developed to identify bonafide brown dwarfs and estimate spectral types without the need for high-resolution spectroscopy.

The large compilation of brown dwarfs identified in the Galactic field, as well as members of star-forming regions and young associations, has provided us with a comprehensive overview of the observational properties of brown dwarfs. This detailed understanding of substellar characteristics has allowed us to considerably refine atmospheric and evolutionary models for brown dwarfs and planetary-mass objects. Observational constraints have also provided stringent tests for formation theories in a previously unexplored mass regime. However, theoretical models still struggle to reproduce outliers of the observed populations, and a number of issues remain in trying to reconcile observations and theories (see Section 1.5).

1.4.2.3 Companions to known Brown Dwarfs

With no bright stars next to them, isolated brown dwarfs offer ideal proxies to study ultracool, planet-like atmospheres in detail. While the best exoplanet analogues are particularly hard to find as free-floating objects, because of their extreme dimness, this issue can be circumvented by searching for them as companions to known brown dwarfs. In this alternative way to search for the coolest brown dwarfs, high-resolution imaging is used to target previously-confirmed brown dwarfs and search for substellar companions orbiting them (Biller et al. 2011; Cushing et al. 2011; Gelino et al. 2011). This significantly increases the sensitivity of surveys by taking much deeper images. Focusing on a narrower region of the sky also strongly reduces the contamination rate.

Although this method is limited by the binary fraction of substellar objects, known to be relatively low compared to stellar multiplicity rates (Duchêne &

Kraus 2013), numerous binary systems have already been uncovered through high-contrast searches (Burgasser et al. 2006b; Biller et al. 2011; Gelino et al. 2011; Liu et al. 2012; Todorov et al. 2014; Huélamo et al. 2015). Most of these systems have tightly-separated components with near-equal masses (Allen 2007; Burgasser et al. 2007). Photometric candidates, identified with ground-based laser guide star adaptive optics (LGS-AO) or from space using the *Hubble Space Telescope* (*HST*), are often confirmed by establishing common proper motion with the primary, and subsequently characterised and classified via spectroscopic observations.

A handful of companions with masses in the planetary regime (5−15 M_{Jup}) have been discovered with direct imaging, by targeting higher mass brown dwarfs (Chauvin et al. 2005; Todorov et al. 2010; Gauza et al. 2015), or by resolving late-T and Y dwarfs into two lower-mass components (Liu et al. 2011, 2012; Dupuy et al. 2015). Notably, Chauvin et al. (2004, 2005) imaged the very first planetary-mass companion identified with high-contrast imaging, 2M1207b, preceding the discovery of the first wide-orbit giant exoplanets orbiting a main sequence star (Marois et al. 2008, 2010). This 5 M_{Jup} companion was found to orbit a young 25 M_{Jup} brown dwarf at a large separation of 41 AU. The unusually low mass ratio and wide orbit of the system made it stand out from the overall distributions of brown dwarf binaries in the field (Allen 2007; Burgasser et al. 2007). The abnormally red colours of the underluminous L-type secondary were also the first observational indications that young planetary-mass companions could differ in their appearances from the population of older and more massive field brown dwarfs (Skemer et al. 2011).

The first prototypes of the L (GD 165B; Becklin & Zuckerman 1988; Kirkpatrick et al. 1993), T (Gl 229B; Nakajima et al. 1995; Oppenheimer et al. 1995) and Y (WD 0806-661B; Luhman et al. 2011) spectral classes were all identified as directly-imaged companions to low-mass stars and brown dwarfs. By offering the first probes into novel and cooler atmospheres, these findings initiated a new generation of investigations and scientific discoveries. The search for low-mass companions to known brown dwarfs thus offers a promising pathway to complete the currently sparse Y-dwarf sequence, possibly extending it to even lower temperatures.

1.5 Constraining Theoretical Models

As mentioned repeatedly throughout this chapter, a number of problems persist in the theoretical modelling of brown dwarfs and giant exoplanets. Despite the abundance of brown dwarfs discovered in the Solar neighbourhood, the fundamental properties of substellar objects are still poorly constrained. Atmospheric and evolutionary models struggle to reconcile theoretical predictions with the photometric information (e.g. luminosity, colours) and measured physical properties (e.g. mass, surface gravity) of observed systems. In particular, the characteristics of the scarce population of ultracool Y dwarfs, as well as peculiar atmospheric features seen in the rare directly-imaged planets, remain challenging to reproduce with current models.

In parallel, formation processes for brown dwarfs and planetary-mass objects are also heavily debated. A number of conflicting mechanisms have been proposed, and the connection between the coolest brown dwarfs and giant exoplanets is still not understood. Empirical tests fail to discriminate between proposed scenarios, as a result of the lack of constraints on the statistical properties of isolated brown dwarfs. The demographics of exoplanets (e.g. distributions of mass, separation, eccentricity) cannot be explained with a unique and self-consistent formation picture. Some specific features, like the existence of brown dwarf desert members or the presence of giant planets on extremely wide orbits, are also problematic regarding formation and evolution theories, in terms of the extreme conditions required or the timescales involved.

This section explores areas in the framework of observational exoplanet and brown dwarf science that can be studied to achieve a more complete overview of the intrinsic properties of the substellar populations. In order to improve our understanding of these objects' atmospheres and formation, I consider the following paths forward:

- increasing sample sizes,
- precise mass and distance measurements,
- improving population statistics for both brown dwarfs and giant exoplanets.

These approaches offer promising pathways to obtain new, crucial empirical constraints for theoretical models, some of which are addressed in detail in this thesis. By improving our perspective of the substellar demographics and system architectures, these prospects can provide a more comprehensive picture of planetary atmospheres, and enhance our fundamental understanding of brown dwarf and planet formation and evolution.

1.5.1 Increasing Samples Sizes

The major challenge faced in the theoretical modelling of brown dwarfs and giant planets is the lack of empirical validation available, especially at the lowest masses and temperatures. The limited number of known wide-orbit giant planets, free-floating planetary-mass objects or ultracool Y dwarfs, strongly impedes our understanding and characterisation of these populations.

While over a thousand M and L brown dwarfs ($T_{\rm eff} \sim 1400-3000$ K) are known, only a few hundred T dwarfs ($T_{\rm eff} \sim 600-1400$ K) have been discovered, and less than 25 Y dwarfs ($T_{\rm eff} < 600$ K) have been confirmed so far. The planetary-mass brown dwarf WISE 0855 has an effective temperature of ∼250 K, making it the coolest known object outside of our Solar system (Luhman 2014). Nevertheless, a crucial gap persists in mass and temperature between brown dwarfs and the planet Jupiter, with an effective temperature of $T_{\rm eff} \sim 130$ K. The discovery of new analogues to WISE 0855 would help complete the bridge between the substellar and planetary populations, providing new vital benchmarks for testing evolutionary and atmospheric models at such cool temperatures. It is therefore highly important to continue pushing the limits of our knowledge to lower temperatures and pursue the ongoing efforts searching for colder atmospheres (e.g. Tinney et al. 2018).

As a direct consequence of the small number of individual benchmark objects available, statistical studies of brown dwarf populations also suffer from small sample sizes at the low-mass end of the substellar regime. Binary properties, observed mass functions and space densities all provide key constraints for theoretical simulations of formation and dynamical evolution. With poor observational constraints placed on the demographics and statistics of the lowest-

mass brown dwarfs, our understanding of their history and destiny remains ambiguous and highly incomplete (Bardalez Gagliuffi et al. 2019). Larger samples sizes are again required to obtain a better diagnostic of formation processes and evolutionary mechanisms, and be able to predict the fate of the lowest-mass free-floating objects.

Likewise, only a handful of companions below the deuterium-burning limit have been uncovered around stars in direct imaging programs. Despite the remarkable efforts that have been invested in the development of new observing technologies and image processing techniques, the occurrence of wide giant planets appears to be intrinsically low, and most surveys still result in null detections (Biller et al. 2007; Lafrenière et al. 2007; Nielsen & Close 2010; Vigan et al. 2012; Biller et al. 2013a; Rameau et al. 2013; Galicher et al. 2016; Vigan et al. 2017). Larger numbers of detections are essential to enable a better characterisation and understanding of the directly-imaged exoplanets, and obtain a clearer picture of their formation patterns.

Target selection is a challenging process in direct imaging surveys, due to the limited information available about these poorly constrained populations. It is therefore critical to conceive new, innovative approaches for target selection in these campaigns, and increase the chances of detections compared to the essentially blind searches completed so far. For example, some direct imaging programs have focused on stars exhibiting long-term radial velocity accelerations, using independent indications of the presence of a perturbing companion to select the most promising targets (Kasper et al. 2007; Janson et al. 2009; Crepp et al. 2012b; Rodigas et al. 2016). While these surveys have led to the detection of several low-mass stellar and brown dwarf companions, this approach has not been successful yet at uncovering companions in the planetary mass domain. This is likely a result of the projection effect in the RV signal, which limits the sensitivity of the selection method to more massive companions. In addition, Doppler spectroscopy observations are unfeasible for very young, active stars, which biases this strategy towards older and thus more massive companions. Alternative approaches are thus still required to increase the current census of directly-imaged exoplanets and allow for a more complete overview of their properties and demographics.

1.5.2 Measurements of Physical Properties

1.5.2.1 Dynamical Masses

Mass is the most fundamental parameter governing a planet's basic characteristics, from its formation history and fate, to its atmospheric features and chemical environment. Unfortunately, very few direct measurements of physical properties are currently available for isolated substellar objects or widely-separated companions to stars. Most mass estimates for free-floating brown dwarfs and wide giant planets are instead derived from models by comparing observable properties to theoretical predictions.

The evolutionary grids used to characterise these objects from spectroscopic and photometric observations are highly dependent on initial conditions. Series of models associated with the outcome of various formation mechanisms have been implemented. The "hot-start" evolutionary models (Burrows et al. 1997; Baraffe et al. 2003; Saumon & Marley 2008) intend to emulate planet formation via disc gravitational instability, while the "cold-start" models (Marley et al. 2007; Fortney et al. 2008) are meant to reflect the core accretion picture. The "warm-start" scenario (Spiegel & Burrows 2012) was introduced in an attempt to blur these formation channels with intermediate initial entropies. These various models lead to significant differences in the expected brightness of substellar objects, in particular at young ages. In addition, the cooling curves characterised by the evolutionary models also depend on the physics and chemistry considered in the underlying atmospheric models, resulting in further uncertainties at later evolutionary stages (Saumon & Marley 2008; Marley & Robinson 2015).

Furthermore, the inherent luminosity-mass-age relationship of brown dwarfs and planetary-mass objects means that two of those three parameters must be known in order to constrain the third one. Stellar and substellar ages are especially difficult to determine accurately for targets isolated from known moving groups or well-defined associations (Jeffries 2014; Soderblom et al. 2014). As model-dependent masses are extremely sensitive to this quantity, age uncertainties extensively dominate the error in the inferred values for any given model, adding to the overall uncertainties from the models themselves.

Mass estimates for directly-imaged planets and isolated brown dwarfs are consequently heavily model-dependent and highly uncertain (Bowler 2016). Alternative methods to determine masses are thus critical to circumvent the large uncertainties introduced by theoretical models, but also to allow for empirical calibrations of evolutionary tracks. Dynamical mass measurements provide ideal ways to bypass and refine evolutionary models. While the vast majority of substellar objects are not amenable to direct mass measurements, binary systems provide ideal archetypal systems to infer dynamical masses and constrain theoretical models.

Closely-separated brown dwarf binaries allow for the measurement of dynamical masses, which can be determined through long-term orbital monitoring (e.g. Close et al. 2007; Liu et al. 2008; Dupuy et al. 2009, 2014; Dupuy & Liu 2017). Age-calibrated systems with dynamical masses have revealed that commonly-used evolutionary models tend to underestimate the luminosity of brown dwarfs at field ages (from several hundred Myr to a few Gyr), causing systematic errors of 15−25% in model-derived masses at these ages (Dupuy et al. 2014, 2015). These consequential offsets further argue for the necessity of larger samples of dynamical masses in the substellar regime in order to accurately characterise the known population of brown dwarfs. Mass-calibrated binary components have also enabled a direct determination of the age distribution of brown dwarfs in the field (Dupuy & Liu 2017), which is essential to reduce the error budget of model-inferred masses for the field population.

Recently, the first dynamical masses of wide planetary and substellar companions to stars were derived by combining data obtained with direct imaging, radial velocity and astrometry (Brandt et al. 2018; Calissendorff & Janson 2018; Dupuy et al. 2009). The determination of model-independent masses for new brown dwarfs and planets yields invaluable measurements of physical properties for pivotal benchmark systems. Such information in turn provides crucial empirical validations for atmospheric and evolutionary models, that severely lack observational constraints at the lowest masses and temperatures. As mass is a fundamental component encoded in the formation history of any astronomical object, mass determinations also provide key testable fingerprints of planet and brown dwarf formation processes.

1.5.2.2 Precise Distances

Another crucial parameter for investigating basic physical properties is the distance of an object. Precise distances are essential to connect measured properties to intrinsic characteristics (e.g. apparent to absolute magnitude), and therefore to compare observations to theoretical predictions.

Atmospheric and evolutionary models struggle to reproduce the brightness and photometric colours of the lowest-mass and coolest brown dwarfs in the field (Schneider et al. 2016; Leggett et al. 2017). Similarly, large disparities in photometric properties are seen between observations and theory for the population of young giant planets and free-floating planetary-mass objects (Faherty et al. 2013). Measurements of accurate distances allow for robust analyses of inherent properties through the determination of absolute fluxes and unbiased spectral energy distributions. The knowledge of absolute quantities for key benchmark objects is critical to test and calibrate theoretical models, making precise distance measurements a necessary step to improve characterisation and modelling of low-mass objects (e.g. Kirkpatrick et al. 2019; Best et al. in prep.).

Precise distance estimates can also be used to compare the appearance of individual objects to well-calibrated colour-magnitude diagrams. In particular, the identification of outliers along the standardised locus can probe secondary attributes of these substellar objects. For example, overluminous sources may be indicative of unresolved binarity (Manjavacas et al. 2013; Tinney et al. 2014; Kirkpatrick et al. 2019). Likewise, excessively red or blue colours can trace a deviant surface gravity or metallicity, or be evidence for diverse atmospheric features like clouds (Knapp et al. 2004; Chiu et al. 2006; Cruz et al. 2007, 2009).

Volume-limited samples are also necessary for any robust statistical studies of populations. Defining high-confidence space volumes can only be achieved through measurements of distances. Current observations of substellar mass functions and space densities are in tension with model predictions (Burgasser 2004; Allen et al. 2005; Pinfield et al. 2006; Kirkpatrick et al. 2012). Precise distance estimates for large sets of brown dwarfs are thus required to obtain a comprehensive portrait of the local substellar population. The study of well-defined and complete samples in space allows for the development and testing

of formation and evolution theories, and provides a rich source of empirical constraints for theoretical simulations (e.g. Kirkpatrick et al. 2019).

Parallaxes are the most direct measures of distance for stellar and substellar objects. With the extensive sky coverage of large astrometric missions (e.g. *Gaia*, *Hipparcos*), most stars in the solar neighbourhood and nearby moving groups or star-forming regions have reliable parallax measurements. The majority of brown dwarf and planetary companions to nearby stars are therefore distance-calibrated, and observed parameters can robustly be bridged to intrinsic properties for these systems. Isolated brown dwarfs, on the other hand, are generally too faint to be detected by these broad surveys and very few substellar objects are included in these astrometric catalogues.

Spectrophotometric distances (based on expected relations between absolute magnitude and spectral type or apparent photometry) are often the only viable way to estimate distances for intrinsically faint objects. However, significant disagreements have been found between model-derived spectrophotometric distances and parallactic measurements (e.g. Kirkpatrick et al. 2011, 2012), and the former estimates are often viewed as unreliable (Cushing et al. 2011; Liu et al. 2011). Some dedicated programs aim at deriving trigonometric parallaxes for brown dwarfs, such as the Hawaii Infrared Parallax Program (Dupuy & Liu 2012; Liu et al. 2016) or the Brown Dwarf Kinematics Project (Faherty et al. 2012; see also Dupuy & Kraus 2013; Manjavacas et al. 2013, 2019; Martin et al. 2018; Kirkpatrick et al. 2019 for other compilations of parallactic distances). Despite these remarkable efforts, the typical precision reached in these observationally-expensive campaigns ($\sim$10 mas uncertainty in parallax) results in substantial uncertainties in the underlying distances, and large inconsistencies remain between programs for the faintest targets (e.g. Beichman et al. 2014).

1.5.3 Population Statistics

Population studies are critical for differentiating between conflicting theories. Robust statistics of brown dwarf populations and planetary systems provide invaluable insights into formation scenarios and empirical trends, and may be used to obtain new, crucial observational constraints for theoretical simulations.

1.5.3.1 Demographics of Giant Exoplanets

Understanding the demographics of exoplanets is a prerequisite to the development of observationally-derived formation and migration models. In terms of exoplanet populations, observed systemic architectures of statistical samples may be used to put formation and evolution theories to test. These include any observed property from occurrence rates and distributions of orbital elements (e.g. mass, separation, eccentricity, orbital alignment), to higher-order multiplicity and correlations to stellar properties.

The primary observational constraints that theoretical models aim at reproducing are the measured occurrence rates of giant planets, and their variations with orbital separation and planet mass. The frequency of hot Jupiters around Solar-like stars is thought to be around 0.5−1% (Howard et al. 2010; Mayor et al. 2011). The occurrence of giant planets on separations of 5−10 AU increases to 10−20% for FGK stars (Cumming et al. 2008; Mayor et al. 2011), before dropping to $< 4\%$ at distances of tens to hundreds of AU for the directly-imaged population (Bowler 2016). In terms of planet mass, the occurrence of giant planets is observed to drop above companion masses of $\sim$4 M_{Jup} (Santos et al. 2017), and this decrease extends past the deuterium-burning limit, marking the appearance of the brown dwarf desert. However, the speculative assumptions made to correct for observational biases in surveys are generally obtained from theoretical predictions (Howard et al. 2010). Derived values are therefore not fully empirical and additional observational constraints are still needed to rigorously remove remaining model dependencies.

These observed characteristics are also seen to be dependent on stellar properties. Giant planet frequency is found to strongly increase with host star metallicity (Santos et al. 2004; Fischer & Valenti 2005). This is often viewed as evidence that core accretion is the dominant process for giant planet formation, as this mechanism shows a manifest metallicity dependence in the formation of very massive planets (Ida & Lin 2004; Mordasini et al. 2012). In addition, the frequency of giant planets is observed to scale with stellar mass, with an occurrence rate $< 2\%$ for M-dwarfs (Bonfils et al. 2013), then steadily increasing up to host masses of $\sim$2 $M_{\odot}$, followed by a rapid drop beyond 2.7 $M_{\odot}$ (Reffert et al. 2015). All these traits provide crucial information for the theoretical modelling

of planet formation, and must be taken into account in order to achieve a robust theoretical outcome, representative of the observed statistical populations (Alibert et al. 2011; Mordasini et al. 2012).

Some studies have also constrained the occurrence of close-in planets in binary star systems (Eggenberger et al. 2007; Adams et al. 2012; Ginski et al. 2012), finding that stellar binarity tends to inhibit planet formation (Roell et al. 2012; Bergfors et al. 2013; Kraus et al. 2016). Interestingly, the most massive short-period giant planets ($\gtrsim$ 4 M_{Jup}) appear to be preferentially orbiting components of multiple star systems (Zucker & Mazeh 2002; Eggenberger et al. 2004), pointing towards distinct formation channels, differently affected by the presence of massive binary companions. On the other hand, searches for circumbinary planets (orbiting two stars) obtained statistical results consistent with the distribution of companions around single stars for Jovian planets up to 15 M_{Jup} and separations of tens to hundreds of AU (Asensio-Torres et al. 2018). This suggests that the efficiency of massive planet formation in circumbinary discs is comparable to that of wide giant planets in standard circumprimary environments.

1.5.3.2 Brown Dwarf Binary Properties

As binarity is a direct outcome of formation, the multiplicity statistics (binary fraction, mass ratio and separation distributions) of substellar populations can serve as a key diagnostic of formation processes, and help identify dominant formation channels. Differences in binary statistics with primary mass have crucial implications for theoretical models. Probing distinct stages in the life of brown dwarfs is also critical to disentangle between primordial formation and subsequent dynamical evolution.

There is evidence that stellar binary pairs with lower-mass primaries decline in number, have closer separations and higher mass ratios (Duquennoy & Mayor 1991; Raghavan et al. 2010). These trends are also observed to continue across the substellar boundary (Kraus & Hillenbrand 2012), with field brown dwarfs found to be less prevalent than their stellar analogues, predominantly on tight orbits ($<$ 10 AU), and highly concentrated near equal-mass systems (Allen 2007; Burgasser et al. 2007). These tendencies may even persist throughout the brown

dwarf mass range, with later-type systems observed to be even rarer and more compact (Aberasturi et al. 2014).

The apparent smooth transition in binary statistics between the stellar and brown dwarf regimes argues for a common formation mechanism between the two domains (Whitworth et al. 2007), providing robust clues on the primary formation patterns for brown dwarfs. However, multiplicity studies of the faintest objects are generally limited by small samples or low resolution (Bardalez Gagliuffi et al. 2019). Larger sample sizes and more complete studies are required to confirm whether these trends persist down to the very coolest late-T and Y dwarfs, or if a bimodal population exists at the lowest masses, indicative of a change in the dominant formation process for these systems. Constraining the binarity of the latest-type brown dwarfs in the field is thus essential to allow for unprecedented tests of formation theories of the lowest-mass objects.

Observed disparities between primordial binary properties and the evolved field population provide valuable insights into both initial conditions and evolution processes. Biller et al. (2011) demonstrated the existence of a significant population of wide binaries ($>$ 20 AU) in young star-forming regions. Such systems are inconsistent with a violent formation process like the ejection scenario (Bate 2009). These findings also present a conundrum since this wide population is not found around older field brown dwarfs (Close et al. 2003). The lack of wide binaries in the field could suggest that the widest companions observed at young ages will likely get disrupted by interactions with passing stars, allowing us to predict the fate of these weakly-bound young binaries (Allers 2012). More robust statistical studies in extremely young regions are required to further constrain substellar multiplicity right after birth, and investigate a possible dependence on environment (i.e. cluster density; Close et al. 2007). This will in turn enable a more realistic modelling of brown dwarf formation and evolution.

Additional tests for formation and evolution models can be made by comparing theoretical predictions of eccentricity distributions to the observed ones. For example, simulations of brown dwarf binary formation around a star via disc instability (Stamatellos & Whitworth 2009) predict higher eccentricities than observed. In contrast, theoretical outcome from simulations of turbulent cloud fragmentation (Bate 2009) agree well with the observed statistical distributions

of brown dwarf binaries (Dupuy & Liu 2011), and such an analysis can be used to favour one family of models over others.

1.5.4 Outline of Chapters 2-4

The work presented in this thesis explores the demographics of brown dwarfs and giant exoplanets in various configurations, with the aim to obtain new empirical constraints for simulations of formation processes, and the development of atmospheric and evolutionary models.

In Chapter 2, I present a binary survey for late-T and Y brown dwarfs in the field. I introduce a new Bayesian statistical tool and place the first statistically robust constraints on the multiplicity properties of the coolest brown dwarfs. I demonstrate that the lowest-mass brown dwarfs extend the trends observed in their more massive counterparts, allowing me to trace their formation through their multiplicity statistics.

In Chapter 3, I provide a test of formation and evolution processes for the most massive close-in giant exoplanets and brown dwarfs. Using direct imaging observations and the *Gaia* DR2 catalogue, I show that the majority of these systems are found in multiple-star systems, indicating that binarity plays a crucial role in the existence of short-period massive planets and brown dwarf desert inhabitants.

Chapter 4 describes a new code developed to select promising targets in direct imaging searches, based on proper motion accelerations in large-scale astrometric catalogues. The tool allows for the orbital characterisation of identified systems and can provide reasonable dynamical mass measurements for directly-imaged companions, with minimal orbital coverage from direct imaging observations.

This thesis has contributed to a more comprehensive understanding of the brown dwarf and giant planet populations, providing crucial constraints on their demographics and testable fingerprints of their formation, in addition to an encouraging new selection method for direct imaging surveys and the prospect of key measurements of physical properties for directly-imaged companions.

Published in Fontanive et al. 2018, MNRAS, 79, 2702.

2

Constraining the Multiplicity Statistics of the Coolest Brown Dwarfs

Contents

2.1 Introduction

There is evidence that binary frequency in the Galactic field decreases as a function of spectral type. Over 70% of massive B and A-type stars are observed in binary or hierarchical systems (Kouwenhoven et al. 2007; Peter et al. 2012). This fraction decreases to 50−60% for Solar-type stars (Duquennoy & Mayor 1991; Raghavan et al. 2010) and around 30−40% of M-stars are found in multiple systems (Fischer & Marcy 1992; Delfosse et al. 2004; Janson et al. 2012b). Surveys probing old (1−10 Gyr) brown dwarfs from the field (Close et al. 2003; Burgasser et al. 2006b; Gelino et al. 2011; Huélamo et al. 2015) observed a substantially lower binary rate (∼10−20%) than in the stellar population, extending the trend of a decreasing binary fraction with later spectral type seen in the stellar regime. As stellar binary frequency decreases with decreasing primary mass, the semi-major axis distribution peaks at closer separations and mass ratios shift towards unity.

These trends appear to continue across the boundary between stars and substellar objects and to persist throughout the brown dwarf mass regime (Duchêne et al. 2007; Kraus et al. 2012; Duchêne & Kraus 2013). Indeed, brown dwarf binaries are found to be less prevalent than their stellar analogues, are predominantly found on tightly-bound orbits, with an observed peak in separation around ∼4 AU, and are highly concentrated near equal-mass systems, with over 75% of systems having mass ratios $q \equiv M_2/M_1 \geq 0.8$ (Allen 2007; Burgasser et al. 2007). Surveys investigating binary properties of late-M and L dwarfs in the field (Reid et al. 2001; Close et al. 2002, 2003) found binary fractions around 15−20%. These searches also revealed that L dwarfs have fewer binary companions detected on separations > 10 AU than M-type field objects. Burgasser et al. (2003, 2006b) probed T-dwarfs with spectral types spanning from T0−T8 and measured binary rates of ∼10%, with all identified systems having separations < 5 AU and mass ratios > 0.8. These results confirm the idea of a decreasing binary fraction within the brown dwarf mass regime and suggest a more compact and symmetric substellar binary population at later spectral types (Huélamo et al. 2015).

Binary statistics of the latest-type (⩾ T8), coolest brown dwarfs ($T_{\rm eff} < 800$ K) are still poorly constrained, mainly because the majority of late-T and Y ultracool

dwarfs were only discovered in recent years (Cushing et al. 2011; Kirkpatrick et al. 2011, 2012; Mace et al. 2013; Pinfield et al. 2014). Five brown dwarf binaries with primary spectral types of T8 or later have been discovered so far (see Gelino et al. 2011; Liu et al. 2011, 2012; Dupuy et al. 2015). Two of these systems (W1217+1626 and W1711+3500; Liu et al. 2012) have unusually wide separations (8−15 AU) and surprisingly low mass ratios ($q \sim 0.5$). It is not clear whether these discoveries signal a change in binary properties at the lowest masses or consist of peculiar systems, thus not representative of the true binary population of ultracool dwarfs. Most formation scenarios for brown dwarfs only allow very tight binaries ($<$ 10 AU separation) to survive to field ages (e.g. ejection scenario, Reipurth & Clarke 2001; turbulent fragmentation, Padoan & Nordlund 2004; disc fragmentation and binary disruption, Goodwin & Whitworth 2007). The existence of wide field binaries such as those discovered by Liu et al. (2012) is difficult to explain via such mechanisms, but such systems may simply be uncommon.

In this chapter, we present a search for low-mass companions to some of the coolest brown dwarfs in order to place the first constraints to date on the binary properties of the latest-type T and Y dwarfs in the field. Our multiplicity search is also an attempt to confirm whether wide, low mass ratio systems are indeed more common around $\geqslant$ T8 dwarfs than around their more massive, earlier-type counterparts. Section 2.2 describes the probed sample and our observations. The search for companions is detailed in Section 2.3 and the achieved sensitivity limits are presented in Section 2.4. In Section 2.5 we introduce additional samples of T5−T7.5 and $\geqslant$ T8 brown dwarfs from the multiplicity surveys in Gelino et al. (2011) and Aberasturi et al. (2014). The latter subset is used to extend the size of our observed sample and set more robust statistical constraints on binary fraction for $\geqslant$ T8 brown dwarfs, while the former serves as a comparison with earlier spectral types. A thorough statistical analysis of binary properties is detailed in Section 2.6 for the observed and additional samples. We provide an assessment of the multiplicity properties of mid-T to Y field brown dwarfs in Section 2.7, where we discuss our interpretation of the obtained results and compare them to earlier-type stellar and substellar objects. Finally, we summarise the main results of our project in Section 2.8.

2.2 Sample and Observations

2.2.1 Sample Selection

Our sample consists of 12 nearby sources ($d < 30$ pc) identified as isolated field objects in prior searches for brown dwarfs (Kirkpatrick et al. 2011, 2012; Mace et al. 2013) via the *Wide-Field Infrared Survey Explorer* (*WISE*; Wright et al. 2010). With reported spectral types of T8 or later and estimated masses $\lesssim$ 40 M_{Jup} (see Section 2.2.3), these objects are some of the coolest and lowest-mass known brown dwarfs in the Solar neighbourhood. The observed targets are listed in Table 2.1. The full *WISE* designations are given in the table in the form WISE Jhhmmss.ss±ddmmss.s. We abbreviate source names to the short form Whhmm±ddmm hereafter. All targets were observed with the Wide Field Camera 3 (WFC3) on the *Hubble Space Telescope* (*HST*).

2.2.2 HST/WFC3 Imaging

A common problem encountered in direct imaging searches for brown dwarfs is the high contamination rates observed in most photometric surveys. The broadband colours of brown dwarfs can be very similar to those of reddened stars in the near-infrared (NIR) and a large number of selected candidates turn out to be background interlopers. True substellar objects may however be distinguished from background stars through specific spectral characteristics like molecular bands (e.g. Stumpf et al. 2010). In particular, brown dwarfs have a strong water absorption feature observed at 1.35−1.45 μm (McLean et al. 2003). This H_2O spectral signature is found in all objects with spectral types $\geqslant$ M6, with a deeper absorption observed in later-type objects. Spectra of reddened stars lack this water absorption feature and this attribute can thus be used to identify brown dwarfs and differentiate them from background stars (see Allers & Liu 2010).

The WFC3/IR F139M filter on *HST* is sensitive to this water absorption band and, combined with the F127M filter, provides a unique probe into this substellar characteristic. Brown dwarfs are indeed expected to appear fainter in the F139M water band, while reddened stars will not exhibit any absorption. Comparing

photometry in the two adjacent *HST* filters therefore provides a robust detection method for brown dwarfs, especially for late-type T and Y dwarfs that show particularly deep water absorption features. For this reason, targets in this study were observed with the F127M and F139M bands on WFC3, covering the 1.27 μm peak observed in late-type brown dwarfs and the H_2O absorption band found around 1.4 μm in substellar spectra, respectively.

Observations were taken between October 2012 and September 2013 with the IR channel of the WFC3 instrument on *HST* (Snapshot Program 12873, PI Biller). With a field of view of $123'' \times 136''$, the 1024×1024 pixel array of the IR channel has a plate scale of $0\farcs13$ pixel^{-1}. At the estimated distances of our targets, this resolution allows us to probe companions down to separations in the range 0.96−3.38 AU. Images were taken in MULTIACCUM mode with two 349.233 s exposures along a two-point $\sim 0\farcs6$ line dither pattern in each filter, providing a total exposure time of 698.466 s in both filters. All observations were performed so that the targets were roughly located at the centre of the field of view of the camera. The pipeline processed flat-field images were used as input in the MultiDrizzle software (Fruchter & Hook 2002) to correct for geometric distortion, perform cosmic ray rejection and combine all dithered images into a single and final master frame.

The original Snapshot proposal contained a total of 33 science targets, with one orbit per target, from which 13 were executed. From the 13 sources observed, one target (WISE J085716.25+560407.6) was missed due to wrong telescope pointing, providing us with a final sample of 12 objects. Dupuy et al. (2015) discovered that the brown dwarf WISE J014656.66+423410.0 is a close near-equal mass binary with a projected separation of $0\farcs0875$ (0.93 AU). However, the binary is not resolved in our *HST* observations due to the large pixel scale of the WFC3/IR camera, and is thus treated as an unresolved single source in our multiplicity analysis. A log of observations is given in Table 2.1.

We used the PhotUtils Python package to perform aperture photometry on the primaries in the F127M images. The PhotUtils *CircularAperture* and *aperture_photometry* modules were called in Python to extract the photometry, adopting a $0\farcs4$ aperture radius. Following the procedure in Schneider et al. (2015), we estimated the background level and its uncertainty by applying the

Table 2.1. Log of *HST* observations, F127M photometry and F139M limiting magnitude.

Object ID	Short Name	Obs. Date	F127M		F139M	
		(UT)	t (s)	Phot. (mag)	t (s)	Phot. (mag)
WISE J014656.66+423410.0	W0146+4234	2013 Jun 24	698.465	20.01 ± 0.03	698.465	> 26.5
WISE J014807.30−720259.0	W0148−7202	2012 Oct 30	698.465	18.51 ± 0.03	698.465	> 24.9
WISE J024714.52+372523.5	W0247+3725	2012 Nov 14	698.465	17.65 ± 0.03	698.465	> 24.7
WISE J032120.91−734758.8	W0321−7347	2013 Aug 18	698.465	18.35 ± 0.03	698.465	> 24.9
WISE J033515.01+431045.1	W0335+4310	2013 Jan 01	698.465	19.02 ± 0.03	698.465	> 27.2
WISE J071322.55−291751.9	W0713−2917	2013 Aug 15	698.465	19.33 ± 0.03	698.465	> 25.3
WISE J072312.44+340313.5	W0723+3403	2013 Apr 04	698.465	17.84 ± 0.03	698.465	> 26.9
WISE J073444.02−715744.0	W0734−7157	2013 Sep 23	698.465	19.82 ± 0.03	698.465	> 24.8
WISE J104245.23−384238.3	W1042−3842	2012 Oct 26	698.465	18.39 ± 0.03	698.465	> 25.5
WISE J115013.88+630240.7	W1150+6302	2012 Nov 10	698.465	17.36 ± 0.03	698.465	> 24.9
WISE J151721.13+052929.3	W1517+0529	2013 Jul 22	698.465	18.18 ± 0.03	698.465	> 26.5
WISE J222055.31−362817.4	W2220−3628	2013 Jul 21	698.465	19.84 ± 0.03	698.465	> 26.4

same 0.″4 aperture to 1000 random star-free positions (determined via a 3-σ clip) and took the mean and standard deviation of these measurements as the background and its uncertainty. Magnitudes were calculated on the Vega system using the photometric zero point provided in the *HST*/WFC3 webpages[1] for the F127M filter (23.4932). The same method was applied to estimate the limiting background magnitude at the 5-σ level in the F139M observations (zero point of 23.2093) since all of our targets dropped out entirely in the F139M observations. The obtained photometry for the science targets is presented in Table 2.1.

2.2.3 Primary Mass Estimates

Published information available for all targets was gathered from the literature in order to estimate the masses of our science targets. NIR photometry (Mauna Kea Observatory (MKO) or 2MASS filter system), spectral types and distances are summarised in Table 2.2. Filippazzo et al. (2015) derived bolometric corrections for brown dwarfs at various ages and found a tighter correlation of spectral type with BC_J rather than BC_{K_s} for old mid to late-T dwarfs. This suggests that the former provides a more reliable correction when estimating luminosities for late-type field objects. We thus used J-band photometric data to estimate primary masses. Magnitudes on the MKO-NIR filter system were converted to 2MASS magnitudes using the relations derived in Stephens & Leggett (2004) based on spectral type.

Absolute magnitudes were computed for all targets adopting the distances in Table 2.2. We used parallax measurements from Beichman et al. (2014) or Tinney et al. (2014) when available and the "adopted distances" from table 8 in Kirkpatrick et al. (2012) otherwise. No errors are reported for the distance estimates from Kirkpatrick et al. (2012), derived from the combination of H and $W2$ spectrophotometric distances. The average relative standard deviation of single band distance estimates around the adopted mean for the full list of objects considered in that work is 11.5%. We thus chose relative errors of $\pm$12% on the final distances for these targets. We note that photometric distances assume sources are single, and that the resulting estimates would be invalid in cases of unresolved binaries (e.g. Lachapelle et al. 2015. A Monte-Carlo approach was

[1] `http://www.stsci.edu/hst/wfc3/phot_zp_lbn`

Table 2.2. Observed late-T and Y brown dwarf targets.

Object ID	RA (J2000)	Dec. (J2000)	SpT (NIR)	Distance (pc)	Ref.	J (mag)	H (mag)	Ref.	$\log(L_{\rm bol}/L_\odot)$	Mass ($M_{\rm Jup}$)
W0146+4234[a]	01:46:56.67	+42:34:10.1	T9.0	10.6 ± 1.5	(1)	20.69 ± 0.07	20.30 ± 0.12	(4)	-6.59 ± 0.25	17 ± 6
W0148−7202	01:48:07.30	−72:02:59.0	T9.5	11.0 ± 0.4	(2)	18.96 ± 0.07	19.22 ± 0.04	(5)	-6.05 ± 0.27	29 ± 7
W0247+3725[b]	02:47:14.52	+37:25:23.5	T8.0	17.5 ± 2.1	(3)	18.44 ± 0.17	18.24 ± 0.19	(6)	-5.84 ± 0.17	34 ± 5
W0321−7347	03:21:20.91	−73:47:58.8	T8.0	26.0 ± 3.1	(3)	19.13 ± 0.11	19.06 ± 0.12	(6)	-5.91 ± 0.16	32 ± 5
W0335+4310	03:35:15.01	+43:10:45.1	T9.0	14.3 ± 1.7	(1)	20.07 ± 0.30	19.60 ± 0.26	(6)	-6.50 ± 0.24	19 ± 6
W0713−2917	07:13:22.55	−29:17:51.9	Y0.0	9.4 ± 1.2	(1)	19.64 ± 0.15	> 19.30	(7)	-6.19 ± 0.31	26 ± 7
W0723+3403[b]	07:23:12.44	+34:03:13.5	T9.0	14.0 ± 1.7	(3)	18.21 ± 0.14	> 18.47	(6)	-5.63 ± 0.23	40 ± 8
W0734−7157	07:34:44.02	−71:57:44.0	Y0.0	13.6 ± 1.2	(2)	20.41 ± 0.27	···	(7)	-6.16 ± 0.28	27 ± 7
W1042−3842	10:42:45.23	−38:42:38.3	T8.5	15.4 ± 0.8	(2)	18.98 ± 0.09	19.08 ± 0.11	(6)	-6.18 ± 0.17	26 ± 5
W1150+6302[b]	11:50:13.88	+63:02:40.7	T8.0	10.1 ± 1.2	(3)	17.72 ± 0.08	> 18.01	(5)	-6.03 ± 0.16	29 ± 5
W1517+0529	15:17:21.13	+05:29:29.3	T8.0	22.2 ± 2.7	(3)	18.54 ± 0.05	18.85 ± 0.15	(6)	-5.82 ± 0.16	35 ± 5
W2220−3628	22:20:55.31	−36:28:17.4	Y0.0	7.4 ± 0.9	(1)	20.38 ± 0.17	20.81 ± 0.30	(6)	-6.60 ± 0.31	17 ± 7

Notes. [a] combined photometry for the binary W0146+4234AB (see text).
Magnitudes are on the MKO-NIR filter system except for [b] on the 2MASS filter system. Bolometric luminosities and masses were derived in this work (see text). Masses were estimated adopting uniform age distributions in the range 2−8 Gyr.
References.
Distances: (1) Beichman et al. (2014); (2) Tinney et al. (2014); (3) Kirkpatrick et al. (2012).
Photometry: (4) Dupuy et al. (2015); (5) Kirkpatrick et al. (2011); (6) Mace et al. (2013); (7) Kirkpatrick et al. (2012).

implemented to account for the distance uncertainties. A total of 10^6 distances were drawn from a Gaussian distribution centred on the distance value and with a standard deviation σ set to the error on the distance. Similarly, apparent magnitudes were selected from a Gaussian centred on the measured apparent magnitude values in Table 2.2 and with standard deviations set to the errors on the measured apparent magnitudes. An absolute magnitude was obtained for every apparent magnitude and distance generated and the final absolute J magnitude was set to the mean of the output distribution, with an error set to the standard deviation of the output distribution.

Luminosities were then obtained by applying bolometric corrections to the absolute magnitudes. We used the spectral types in Table 2.2 to estimate bolometric corrections BC_J and associated errors from the relations in Filippazzo et al. (2015) for field objects, assuming errors in spectral type of ± 0.5 subtypes. The relations were extrapolated for spectral types later than T9. The extracted BC_J were used to compute bolometric luminosities L_{bol} and their uncertainties, using the same approach to propagate the uncertainties. The final bolometric luminosity for each target is given in Table 2.2.

Precise ages for our targets are not known and are particularly difficult to obtain. Caloi et al. (1999) found that field stars with high V space velocities (in the direction of Galactic rotation) have minimum ages of 2 Gyr, uniformly distributed up to $\sim$8$-$10 Gyr. Given the typical space velocities of nearby brown dwarfs (Zapatero Osorio et al. 2007), we assumed that a similar distribution in age as in the solar neighbourhood applied to our sample and adopted ages of 2$-$8 Gyr. For each target, we simulated an input of 10^6 Gaussian-distributed luminosities, using the value and associated error calculated previously as the mean and standard deviation of the Gaussian, and drew an age value from a uniform distribution between 2 and 8 Gyr for each luminosity. We then interpolated the drawn luminosity and age values into the Lyon/COND evolutionary models for brown dwarfs (Baraffe et al. 2003) to infer a corresponding mass. The final mass was taken to be the mean of the output distribution and the associated mass uncertainty was set to the standard deviation of the output distribution.

The estimated bolometric luminosities and primary masses for all targets in our sample are shown in Table 2.2. All targets were found to have estimated masses

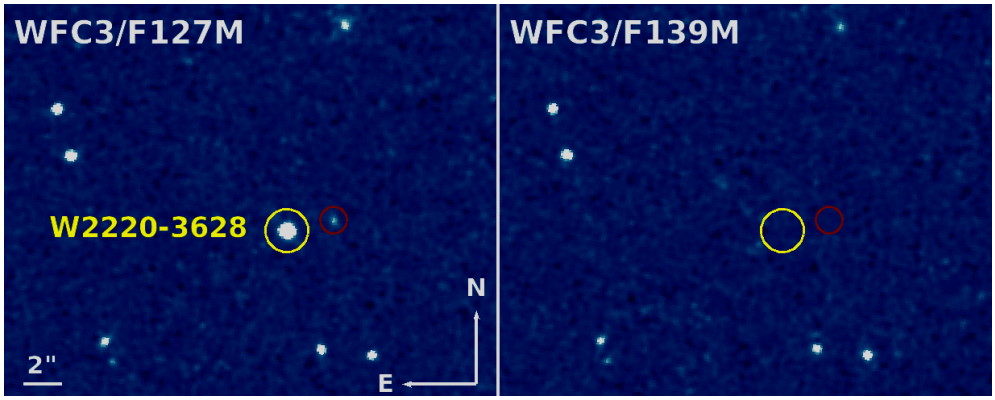

Figure 2.1. WFC3/IR F127M (left) and F139M (right) images of W2220−3628. The science target is in the yellow circle. The identified candidate companion is encircled in red. While most objects in the field of view have roughly similar fluxes in the two bandpasses, the Y dwarf and the selected candidate both exhibit a strong magnitude drop in the water-band F139M filter.

$\lesssim$ 40 M_{Jup} for the adopted ages of 2−8 Gyr, making our sample the largest subset of very late-type and exclusively low-mass brown dwarfs studied as part of a multiplicity search. As the W0146+4234 binary system (Dupuy et al. 2015) is unresolved in our images and is thus treated as a single source in our analysis, we used the combined photometry of the binary components to estimate the mass of an unresolved object with that apparent magnitude.

2.3 Search for Candidate Companions

2.3.1 The Water-Band Detection Method

Images in the WFC3/IR F127M and F139M filters from our core sample were visually inspected to search for sources other than the science targets exhibiting a significant magnitude drop in the latter bandpass. All targets in our sample were found to drop out entirely in the F139M water-band filter as a result of the deep water absorption feature robustly observed at 1.4 μm in substellar spectra, which is particularly strong for late spectral types (Figure 2.1). Assuming a similar or later spectral type for possible companions, potential candidates are expected to drop by the same amount as the primaries and to also be undetected in the F139M band.

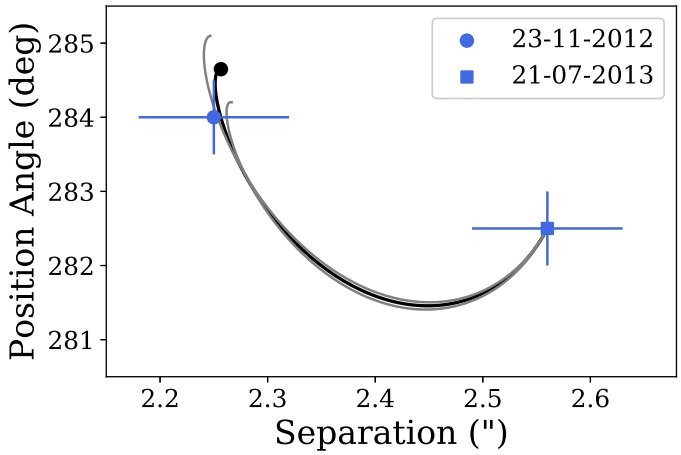

Figure 2.2. Common proper motion analysis of W2220−3628 and the selected candidate. The black solid line represents the motion of a background object relative to the primary, computed using the proper motion and parallax measurements of the science target from Beichman et al. (2014). The grey lines show the same motion using the 1-σ errors on the proper motion and parallax values. The blue symbols mark the measured positions of the candidate relative to the science target in our images (square) and in the past *HST* epoch (circle). The black circle indicates the expected position of a background source at the date of the first epoch. The relative motion of the candidate between the two epochs is consistent with a background object.

2.3.1.1 Candidate Companion around W2220−3628

Only one candidate companion was identified in our sample, found at $2\farcs56 \pm 0\farcs07$ around the Y0 brown dwarf W2220−3628. The candidate was detected in each dithered frame in the F127M band but was not retrieved in the F139M images. Figure 2.1 shows the primary and candidate companion in the final F127M and F139M images, highlighting the significant magnitude drop of both objects in the latter bandpass (right panel). To be considered bonafide companions, candidates must have similar red colours to their primary in addition to a robust sign of water absorption at 1.4 μm. We found no blue source at the position of the candidate in broadband surveys (*WISE*, *Spitzer*). A true companion must also possess common proper motion with the primary. Archival *HST* images of W2220−3628 in the WFC3/IR F125W filter (GO Program 12970, PI Cushing) were compared to our images, providing an 8-month baseline between epochs. Figure 2.2 shows the position of the candidate relative to W2220−3628 in our program (blue square) and in the past *HST* epoch (blue circle). The black circle

shows the expected position of a background object in the first epoch images. With the high proper motion of our science target ($\mu_{\alpha*} = 283 \pm 13$ mas yr^{-1} and $\mu_\delta = -97 \pm 17$ mas yr^{-1}; Beichman et al. 2014), astrometric measurements in the two epochs proved the candidate to be lacking common proper motion with the primary and to be consistent with a background object.

2.3.1.2 Nature of the Background Contaminant

Possible contaminants with the water-band detection method may be background brown dwarfs or mid-M stars showing water absorption at 1.4 μm, or faint galaxies undetected in the F139M band with an emission line covered by the F127M filter. While the past *HST* program used to check for common proper motion with the primary only contained one set of F125W images providing a sufficiently large time baseline to confirm or refute common proper motion for the candidate, additional observations in the F105W and F125W filters were also acquired as part of the same program in June 2013 (one month before observations from our program). We therefore used those images to investigate the photometry and colours of the identified background source. We used the same method as that described in Section 2.2.2 to perform aperture photometry on the primary and selected candidate in the F127M, F105W and F125W images, and estimate the limiting background magnitude in the F139M observations. Magnitudes were calculated on the Vega system using the appropriate photometric zero points provided in the *HST*/WFC3 webpages[1] for each of the considered filters. The obtained photometry for the science target and the background source is presented in Table 2.3. We note that our F105W and F125W photometry for W2220−3628 is in good agreement with the values reported in Schneider et al. (2015) for the same *HST* images (21.638 ± 0.027 mag and 20.997 ± 0.005 mag, respectively).

The F105W−F125W colour of the background source was found to be comparable to that of the science target, suggesting that it could be a late-type brown dwarf. Photometry in the F127M and F139M bandpasses showed the candidate to be dropping by a minimum of 3.12 ± 0.04 mag between the two filters. In Figure 2.3 we computed synthetic F127M−F139M colours for all L and T dwarfs in the

[1] `http://www.stsci.edu/hst/wfc3/phot_zp_lbn`

Table 2.3. *HST* WFC3/IR photometry and colours of W2220−3628 and the background source.

Filters	W2220−3628 (mag)	Background source (mag)
F127M	19.84 ± 0.03	23.29 ± 0.03
F139M	$> 26.41 \pm 0.03$	$> 26.41 \pm 0.03$
F105W	21.64 ± 0.03	24.18 ± 0.03
F125W	21.04 ± 0.03	23.63 ± 0.03
F127M−F139M	$< -6.57 \pm 0.04$	$< -3.12 \pm 0.04$
F105W−F125W	0.60 ± 0.04	0.55 ± 0.04

SpeX prism spectral libraries[1] (grey symbols). We excluded targets with no NIR spectral classification as well as spectra flagged as low-quality data. Flux ratios between the F127M and F139M bandpasses were computed for all available sources by taking into account the transmission value of the two filters at each wavelength and integrating the spectra over the relevant spectral regions. A third order polynomial was fit to the data (black line in Figure 2.3) yielding:

$$\begin{aligned} \text{F127M}-\text{F139M} = 3.719 &- \left(9.127 \times 10^{-1} \times \text{SpT}\right) \\ &+ \left(6.456 \times 10^{-2} \times \text{SpT}^2\right) - \left(1.572 \times 10^{-3} \times \text{SpT}^3\right), \end{aligned} \tag{2.1}$$

where SpT(L0) = 10 and SpT(T8) = 28. The fit was derived for spectral types between L0 and T8 as the SpeX Prism Spectral Libraries do not contain > T8 spectra. The derived relation strongly reflects the strengthened H_2O absorption band along the L and T substellar sequences. Burgasser et al. (2010) compared SpeX and literature classifications for 189 spectra of 178 L and T sources and found standard deviations between classifications of 1.1 subtypes for L dwarfs and 0.5 subtypes for T dwarfs. We thus assumed uncertainties of 1 and 0.5 subtypes for L and T dwarfs, respectively, when deriving the polynomial fit. The mean scatter in the relation in Equation 2.1 is 0.3 mag. We note that there are fewer > T5 objects relative to earlier spectral types and that these objects show a significantly larger scatter in their synthetic colours. Our measured F127M−F139M lower limit for W2220−3628 (blue star) appears to be consistent with the extrapolation of the fit at spectral types later than T8. The lower limit

[1] `http://www.browndwarfs.org/spexprism`

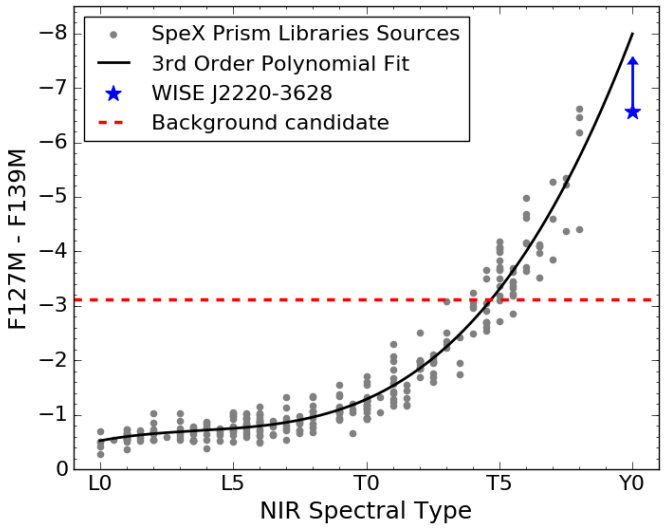

Figure 2.3. Synthetic F127M−F139M colours of L and T dwarfs in the SpeX prism spectral libraries (grey circles) and third order polynomial fit to the data (black line). The minimum colours estimated from the measured photometry of W2220−3628 and the background source are shown by the blue symbol and red line, respectively.

for the F127M−F139M photometry of the background source is shown by the red line in Figure 2.3. The observed drop in the water-band filter suggests a spectral type of ∼mid-T or later for this object to be of substellar nature.

To quantify the likelihood that the background source is a brown dwarf, we calculated the probability of finding a background brown dwarf false positive in our survey, for spectral types varying from T4 to Y0.5. We used published brown dwarf space density values to estimate the probability of observing one such background brown dwarf for various spectral type bins. Space densities were taken from Burningham et al. (2013) for the T6 to T8.5 spectral types and from Kirkpatrick et al. (2012) for $\geqslant$ T9 brown dwarfs. We used the value for the T3−T5.5 space density from Metchev et al. (2008) for T4 to T5.5 objects, assuming a homogeneous distribution of densities across that spectral type range. We used the relation from Dupuy & Liu (2012) between spectral type and absolute magnitude to infer expected 2MASS J absolute magnitudes for each spectral type bin. We then applied a filter transform to convert the obtained J-band magnitudes to absolute F127M and F139M magnitudes for each spectral type, based on a similar method to the one used to compute synthetic F127M−F139M colours.

Table 2.4. Summary of the calculation of the number $N_{\rm exp}$ of background brown dwarf contaminants expected to be found in our survey for spectral types between T4 and Y0.5. The values of M_J for each spectral type were calculated using the relations in M_J versus spectral type derived by Dupuy & Liu (2012). Distances correspond to the range over which an object of given absolute J magnitude is detectable in the F127M images (upper limit) but not in the F139M observations (lower limit), assuming the average detection limits of our survey. See text for references of space density values.

SpT	M_J (mag)	$d_{\rm min}$ (pc)	$d_{\rm max}$ (pc)	Space Density ($\times$ 10^{-3} pc^{-3})	$N_{\rm exp}$
T4−T4.5	14.87	225	600	0.47 ± 0.27	0.017−0.063
T5−T5.5	14.95	139	552	0.47 ± 0.27	0.014−0.051
T6−T6.5	15.50	99	485	0.50 ± 0.28	0.010−0.037
T7−T7.5	16.11	49	381	0.73 ± 0.42	0.007−0.027
T8−T8.5	17.55	18	204	2.63 ± 0.58	0.007−0.011
T9−T9.5	18.41	6	137	1.6	0.002
Y0−Y0.5	20.53	1	52	1.9	0.0001

False positives are background sources detected in our F127M data but dropping out in the F139M observations. As a result, we estimated, based on the derived *HST* absolute magnitudes, the distance ranges in which brown dwarfs of various spectral types are detectable in the former images but not in the latter. We used our average 5-σ detection limits in both sets of observations (25.2 mag in F127M and 25.5 mag in F139M, respectively) to infer the maximum distance at which an object of given absolute magnitude can be detected in the F127M images, and compute the minimum distance required for the object to be undetected in the F139M data. Space densities, absolute 2MASS J magnitudes and the estimated minimum and maximum distances are listed in Table 2.4.

For each spectral type bin, the expected number of contaminant background brown dwarfs is found by considering the volume of a thick spherical shell located within the distance limits in Table 2.4. We then multiplied that volume by the corresponding space density and the fraction of the sky area covered by our program (12 images of $123'' \times 136''$ over 4π sr) to obtain an average number of background brown dwarfs expected to be found in our survey for each spectral type bin. The obtained values are listed in the $N_{\rm exp}$ column in Table 2.4. The expected number of T4−Y0.5 background brown dwarfs in our program detected

in the F127M images but not retrieved in the F139M data was found to be in the range 0.057−0.191, given by the sum of the values in Table 2.4. The identified source is thus rather unlikely to be a background mid-T−Y brown dwarf. We exclude later spectral types as a later-type Y object would need to be very close to be detected (< 50 pc; see Table 2.4) and would likely show high proper motion over the 8-month baseline between epochs, and would thus not be consistent with a background source. As the F139M−F127M colour of this object ruled out the possibility of it being an earlier-type star or brown dwarf, we conclude that it is most likely extra-galactic, although there is a small probability of the contaminant being a background mid-T to Y dwarf. While a large number of extra-galactic reference sources are found in our deep *HST* observations, only one such object was identified in the total sky area covered by our program. The contamination rate from such sources for the water-band detection method is therefore low and does not present a major concern regarding the reliability of our selection technique for substellar companions.

2.3.2 PSF Subtraction

No well-resolved binary pairs were identified in our F127M images. Point spread function (PSF) subtraction was attempted to search for more closely-separated systems with blended PSFs, at separations < 0.″5. The WFC3/IR PSF is severely undersampled by the 0.″13 detector pixel. To mitigate the effect of undersampling, we constructed higher-resolution master frames using the individual F127M dithered frames to recover information lost to undersampling. The pipeline processed flat-field images were used as input in the MultiDrizzle software (Fruchter & Hook 2002) and recombined into a single output frame with a 0.″065 pixel scale, improving the spatial resolution of the final images by a factor of 2.

Tiny Tim models (Krist 1995) are generated from pre-launch simulations and still show large discrepancies when applied to on-orbit WFC3/IR data (see Biretta 2014; Garcia et al. 2015). We therefore generated empirical PSFs from the data and did not attempt synthetic PSF fitting. As the primaries all have roughly similar spectral types (within two subtypes) and are all located near the centre of the detector chip, variations in the PSF due to spatial or spectral variations are expected to be negligible. For each target, we performed PSF subtraction

using the PSFs of all other targets in the sample (excluding the known tight binary W0146+4234AB) to create an empirical PSF model. We extracted sub-images of 40×40 pixels (2.″6×2.″6) centred on the primaries. Each sub-image was background-subtracted and normalised to a peak pixel value of 1. To align two individual PSFs, we performed a progressive grid search to identify the best position. One PSF was moved on a coordinate grid of resolution 0.05 pixel and re-sampled onto the original image grid at each position via a cubic interpolation. The optimal position was taken to be the one that minimised the root mean square difference of the two sub-images. All observed PSFs used to create an empirical PSF were aligned via this method and median-combined to generate a final empirical PSF model for each target in our observed sample.

The observed and empirical PSFs were then aligned using the same fitting routine, after scaling the peak of the empirical PSF to that of the target. PSF subtraction was performed at the position that minimised the root mean square difference of the observed PSF and re-binned empirical PSF. Varying amounts of residual flux were found in the resulting images, with relative intensities ranging from 0.01 to 0.25 of the maximum flux of the data. The amount of residuals was generally found to be correlated to the brightness of the primary relative to the rest of the sample. Observed residuals in the final PSF-subtracted images can be due to either the presence of a secondary source or to discrepancies in the shapes of the individual PSFs of our targets. In the case of an unresolved binary, we expect to find similar residuals when using the individual observed PSFs of our targets as separate PSF models. On the other hand, residuals due to large disparities between observed PSFs should vary based on the PSF used to perform PSF subtraction.

To check the origin of the observed residuals, we also ran the same PSF-subtraction routine for each target using the PSF of every other object in the sample as a single model PSF. We found that targets of similar magnitude generally provided better fits. We did not find any convincing sign of close-in companions in the PSF-subtracted images around any of the targets. The residuals seen with the median empirical PSF models were not consistently recovered with the single PSF models and were due to disparities between the PSFs of objects with larger magnitude differences. Our PSF subtraction technique did not allow us to recover the tight binary W0146+4234AB, which

showed large fluctuations in the residual flux based on the model PSF used for the subtraction. This result is not surprising given the 87.5 mas separation of the binary and the large 130 mas pixel scale of the WFC3/IR channel.

To test the ability of our PSF-subtraction technique to recover close-in candidates, we injected fake companions around the primaries and performed the same PSF subtractions. We used scaled-down versions of the PSFs of other primaries in the sample to simulate companions with magnitude differences in the range 0−5 mag and separations from 0 to 10 pixels (0″ to 0.″65) from the centre of the primary at randomly chosen position angles. For each injected companion we then repeated the same PSF subtractions on the synthetic binaries, using a median and single empirical PSFs, and visually inspected the obtained images. We found that at separations $\geqslant$ 0.″25, observations were background-limited rather than diffraction-limited. Injected companions were retrieved with signal-to-noise ratios (S/N) $\geqslant$ 5 in all PSF-subtracted images provided that the magnitude of the fake companion was within the detection limits of the image (see Section 2.4). At separations in the range 0.″10−0.″25, our PSF-subtraction technique was able to recover companions with Δmag down to $\sim$1−2, with a localised residual flux found at the position angle of the fake companion. Injected companions were consistently retrieved in the image obtained using a median empirical PSF, as well as in over two thirds of the images obtained with single PSF models.

An example of the typical results achieved is shown in Figure 2.4. The top panels show the observed PSF of W0335+4310 before and after PSF subtraction, using a median empirical PSF. In the bottom panels, a fake companion with a magnitude difference of 1.5 was injected at a separation of 0.″1. After running the same PSF subtraction routine on the synthetic binary system, the simulated companion was clearly retrieved. At separations $<$ 0.″1 the amount and position of the residual flux after PSF subtraction were found to vary significantly between the final images for a given target and injected companion. The discrepancies observed were comparable to the disparities obtained after applying PSF subtraction to the original data, with no injected companion, or to the unresolved W0146+4234 binary system. These residuals could therefore not be interpreted as an unambiguous sign of binarity. We note that simulated companions similar to the W0146+4234 secondary component were never detected. Comparable results were achieved around all primaries in the sample.

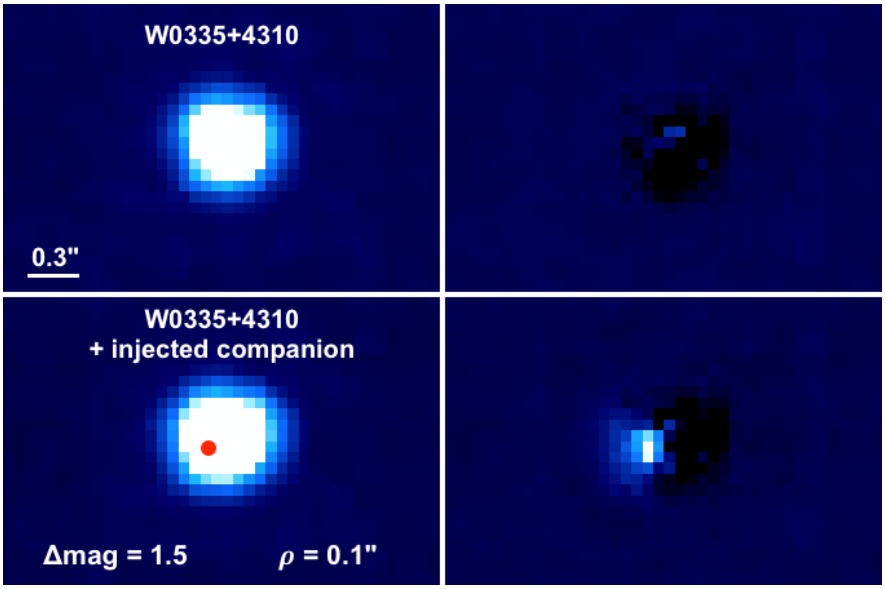

Figure 2.4. Top: W0335+4310 before (left) and after (right) PSF subtraction. PSF subtraction was performed using an empirical PSF constructed with the observed PSFs of all other targets in our sample. **Bottom:** same as top panels with a fake 0.″1 companion with Δmag = 1.5 injected around the science target. The red dot indicates the position at which the companion was injected. The same PSF subtraction routine was applied to fit the synthetic binary. A clear localised residual flux was found at the position angle of the simulated companion after single PSF subtraction.

We conclude that our PSF subtraction method would have allowed us to detect companions at separations from 0.″25 with magnitudes within our detection limits, as well as to uncover closer companions down to 0.″1 with magnitude contrasts $\Delta\text{mag} \lesssim 1-2$. These results are consistent with the contrast curves derived in Section 2.4. The lack of obvious signs of companions in our PSF-subtracted images strongly indicates that our sample did not contain any bonafide companion in these separation and magnitude ranges. As PSF-subtraction for closer-in binaries showed significant discrepancies depending on the PSF used as model, our technique could not confidently rule out the presence of $< 0.''1$ companions in our sample, such as the 0.″0875 W0146+4234 binary (Dupuy et al. 2015) which was not recovered with our PSF-subtraction method.

Table 2.5. Measured F127M contrasts and minimum detectable mass ratios.

Object ID	Δmag (0.″2)	q (0.″2)	Δmag (0.″3)	q (0.″3)	Δmag (0.″5)	q (0.″5)	Δmag (1.″0)	q (1.″0)	Δmag (2.″0)	q (2.″0)	Δmag (5.″0)	q (5.″0)
W0146+4234	0.58	0.68	1.80	0.53	3.93	0.35	3.85	0.36	3.86	0.36	3.95	0.35
W0148−7202	0.84	0.65	2.60	0.37	5.05	0.22	5.36	0.21	5.52	0.20	5.61	0.20
W0247+3725	0.63	0.85	2.11	0.58	4.81	0.29	5.79	0.24	6.13	0.22	6.22	0.22
W0321−7347	1.30	0.81	2.69	0.57	5.25	0.27	5.78	0.24	5.85	0.24	6.01	0.23
W0335+4310	0.79	0.83	2.46	0.57	4.64	0.35	5.08	0.33	5.12	0.33	4.89	0.34
W0713−2917	0.73	0.55	2.09	0.36	4.11	0.24	4.59	0.23	4.38	0.23	4.42	0.23
W0723+3403	0.73	0.75	2.16	0.51	4.90	0.23	5.68	0.20	6.01	0.18	6.08	0.18
W0734−7157	0.87	0.56	2.26	0.35	4.06	0.24	4.33	0.23	4.28	0.23	4.24	0.23
W1042−3842	0.54	0.78	2.32	0.48	5.04	0.31	5.18	0.30	5.38	0.29	5.37	0.29
W1150+6302	0.62	0.80	2.35	0.51	5.03	0.29	5.88	0.25	6.35	0.23	6.43	0.23
W1517+0529	1.11	0.74	2.88	0.49	5.05	0.28	5.45	0.26	5.84	0.24	5.83	0.24
W2220−3628	1.46	0.51	3.02	0.30	4.50	0.23	4.69	0.22	4.48	0.23	4.64	0.23

2.4 Survey Sensitivity Limits

2.4.1 Achieved Contrasts

For each object in the sample, sensitivity limits were computed to establish the full range of detectable companions covered by the survey (Table 2.5). Detection limits were determined from the final F127M images described in Section 2.2.2. The 5-σ noise curves were calculated as a function of radius by computing the standard deviation in circular annuli with 1-pixel widths ($0\farcs13$), centred on the targets. Limits were calculated from a radius of 1 pixel up to 20 pixels before the closest edge of the image. Noise levels were then converted into magnitude contrasts by dividing the obtained noise levels at each separation by the peak pixel value of the targets and converting the obtained flux ratios into magnitude differences. The achieved magnitude contrasts are presented in Figure 2.5. We are complete down to Δmag $\sim$ 2 at $0\farcs3$, and down to Δmag $\sim$ 4 from angular separations of $0\farcs5$ and physical separations of 10 AU.

The results achieved for the injection of simulated companions in Section 2.3.2 are consistent with our measured contrast curves. Fake companions simulated as scaled-down versions of our primaries with contrasts down to our achieved limits were consistently retrieved with S/N $\geqslant$ 5. We therefore conclude that our measured contrast curves provide reliable estimates for the limits of detectable companions.

2.4.2 Limits on Minimum Detectable Companion Masses

The magnitude contrasts Δmag were converted into apparent magnitudes using the measured F127M photometry of our science targets (Table 2.1). We then converted the apparent magnitude limits into corresponding absolute magnitudes using the parallax and spectrophotometric distances from Table 2.2.

The magnitude−mass relationship for brown dwarfs shows a strong age degeneracy. As shown in Figure 2.6, the age chosen to convert our detection limits into minimum detectable masses highly affects the obtained results. For our

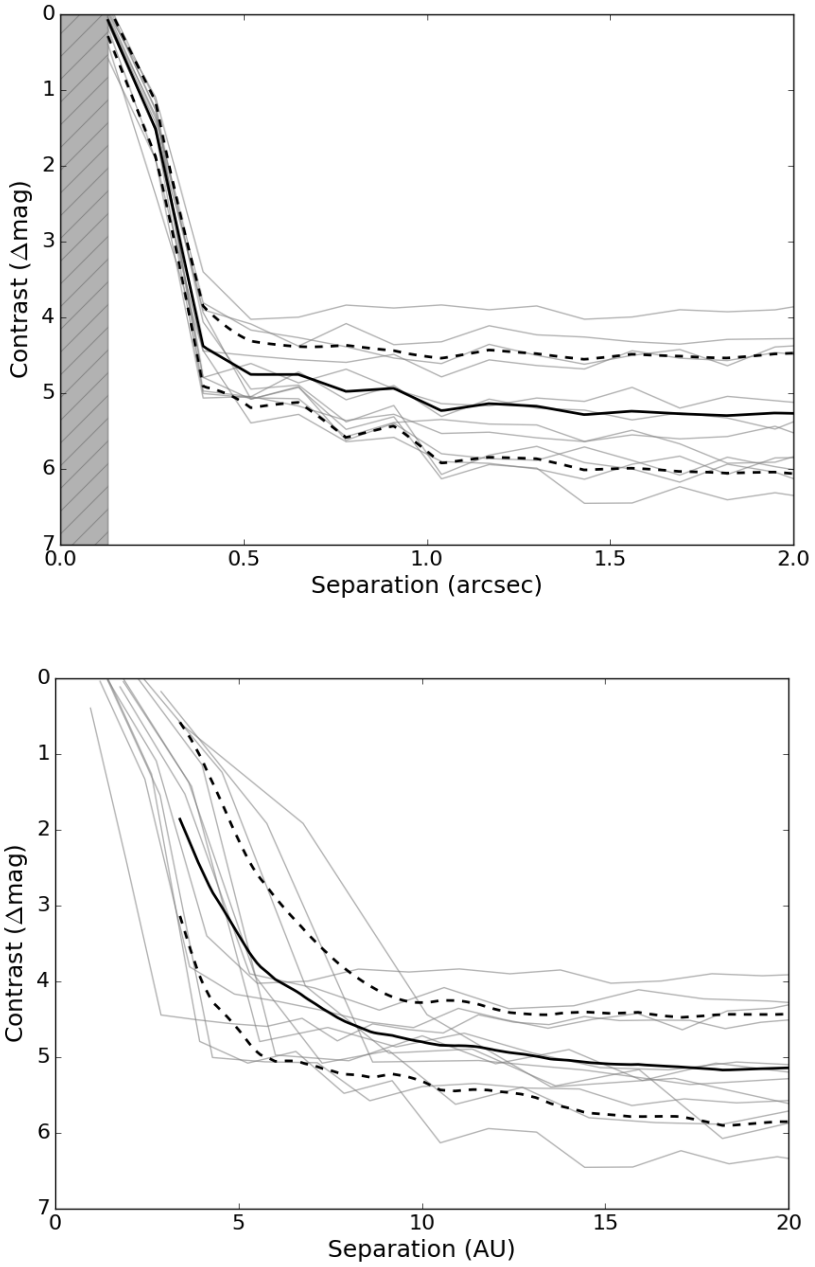

Figure 2.5. Magnitude difference limits at the 5-σ level around our 12 targets in the WFC3/IR F127M observations (grey lines) as a function of angular (top) and physical (bottom) projected separation. The solid black lines show the mean detection levels for the sample and the 1-σ standard deviations around the mean (dotted lines). The shaded region on the left panel represents the pixel scale of the WFC3/IR camera. On the right panel, the mean was calculated starting at the smallest physical separation resolved for all targets.

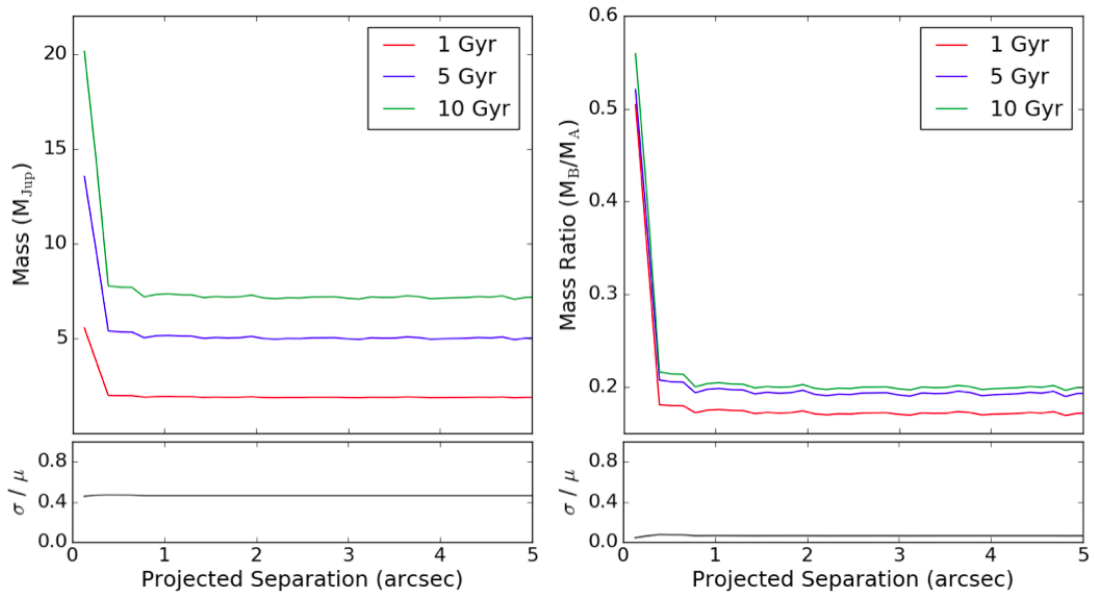

Figure 2.6. Detection limits reached around our target W0148−7202 in terms of minimum detectable masses (left) and mass ratios (right). The magnitude limits for the target (Figure 2.5) were converted to masses using the AMES-COND evolutionary models from Allard et al. (2001) at discrete ages of 1, 5 and 10 Gyr. The primary mass was calculated at each age considered when converting the mass limits into mass ratios. The bottom panels show the relative scatter in the masses and mass ratios between adopted ages of 1, 5 and 10 Gyr. The mass limit curves have a mean relative scatter of 0.49. The same curves in mass ratio space have a mean relative scatter of 0.11, therefore significantly reducing the uncertainty introduced by adopting a discrete age of 5 Gyr.

12 targets, we found an average scatter in the inferred mass limits of 3.7 M_{Jup} when considering discrete ages of 1 Gyr, 5 Gyr and 10 Gyr. This corresponds to a very large mean relative scatter of 0.50 for the lower mass limits reached in our survey. Working with mass ratios, on the other hand, significantly reduces the scatter between various adopted ages. Converting the same mass limits into mass ratio curves, we found a mean relative scatter in mass ratio of only 0.12, therefore crucially reducing the scatter seen in the mass domain for the same discrete ages. Figure 2.6 illustrates this effect for one target from the survey, showing the notably smaller relative scatter obtained in the mass ratio curves (bottom panels). We thus consider mass ratio space rather than companion mass throughout this work and adopted a median age of 5 Gyr to obtain sensitivity limits at the 5-σ detection level.

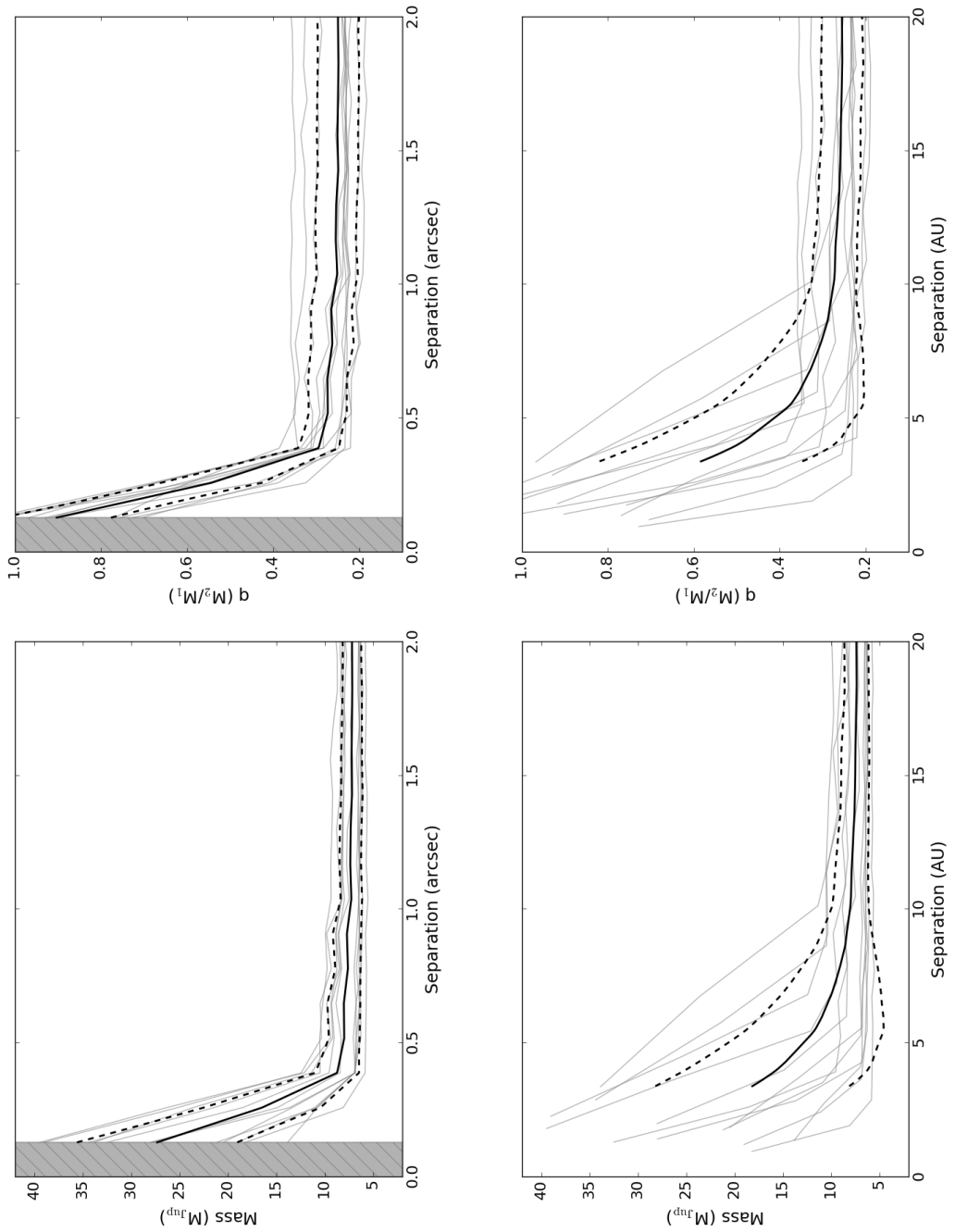

Figure 2.7. Minimum masses and mass ratios detectable around our 12 targets at the 5-σ level as a function of angular and physical projected separation. Magnitude contrasts were converted to masses using the AMES-COND evolutionary models from Allard et al. (2001) at an adopted age of 5 Gyr. Mass limits were converted to mass ratios using the masses calculated in this work and listed in Table 2.2. The solid black lines show the mean detection levels for the sample and the 1-σ standard deviations around the mean (dotted lines). The shaded region represents the pixel scale of the WFC3/IR camera.

We interpolated the absolute magnitude curves into the AMES-Cond evolutionary models Allard et al. (2001) to infer corresponding mass and mass ratio limits at an adopted age of 5 Gyr for all survey objects. The AMES-Cond luminosity isochrones are similar to those from the Lyon/COND models (Baraffe et al. 2003) used to estimate primary masses in Section 2.2.3. As the AMES-Cond models provide photometric data specific to the *HST*/WFC3 filters, not available in the Lyon/COND models, the former are better suited to convert our magnitude limits into masses. The minimum detectable masses and mass ratios around each target are presented in Figure 2.7. We are sensitive to systems with secondary masses $> 5{-}10$ M_{Jup} beyond $0''.5$ assuming ages of 5 Gyr for our targets. In comparison, using ages of 1 Gyr and 10 Gyr yields corresponding limits of $\sim 2{-}5$ M_{Jup} and $\sim 8{-}15$ M_{Jup}, respectively. In terms of mass ratios, we are complete down to $q \sim 0.7$ at $0''.3$ and $q \sim 0.4$ at separations $\geqslant 0''.5$ assuming a median age of 5 Gyr for our sample. These values vary by less than $\sim$12% for ages of $1{-}10$ Gyr and we consider that they are representative of the true detection limits of our survey regardless of the unknown ages of our targets.

2.4.3 Detection Probability Map

The obtained sensitivity curves were used to define a detection probability map for our survey. This provides the probability that a companion at a given physical projected separation ρ and mass ratio q would have been detected in our observed program. The 5-σ mass ratio limits for each target in the sample (see Figure 2.7) were placed using a cubic interpolation onto a grid of separations and mass ratios with a resolution of 0.002 in q and steps of 0.01 in $\log(\rho)$. For every point of the grid, we then identified the number of targets around which a companion of given separation and mass ratio would have been retrieved in our survey. A companion was considered as detectable around a given target if its mass ratio was higher than the detection limit value at the projected separation of the companion. Companions with separations outside the range covered for a given target were counted as undetectable. The number obtained for each cell of the grid was then divided by the total number of objects in our sample, providing a number between 0 and 1 representing the average detection probability in our program for any (ρ, q) pair at the 5-σ detection level.

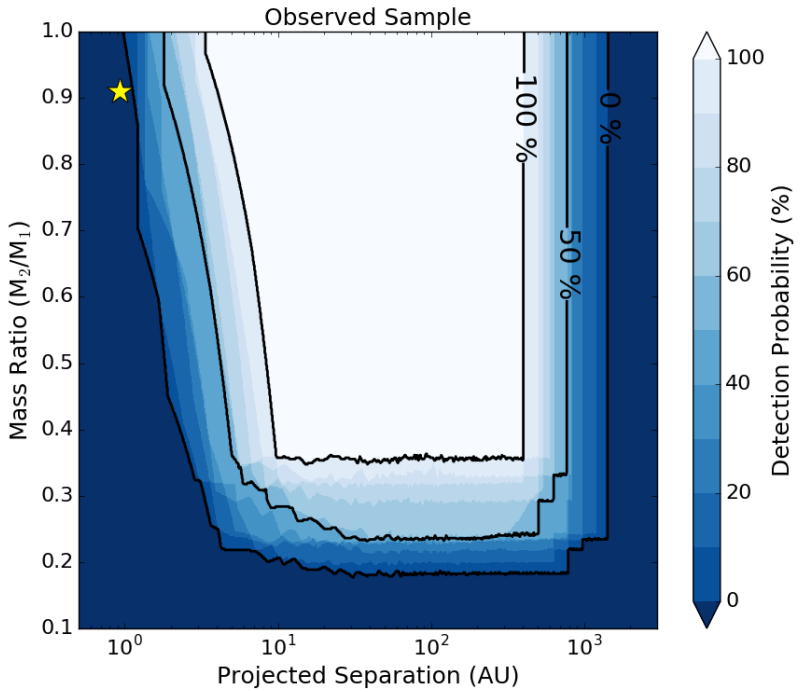

Figure 2.8. Detection probability map for our observed sample using the mass ratio sensitivity limits for our 12 targets. Black contours denote the 0%, 50% and 100% completeness regions at the 5-σ level. The yellow star shows the position of the unresolved W0146+4234 binary discovered in Dupuy et al. (2015), located in the 0% detection region of our survey.

Figure 2.8 shows the resulting detection probability map for our core sample of 12 objects. Companions inside the 100% completeness region are detectable around all targets in the survey. We are not sensitive to any companion in the 0% detection probability region. Using the bolometric luminosity values derived by Dupuy et al. (2015) for the binary components of W0146+4234, we inferred masses of 11 ± 4 M_{Jup} and 10 ± 4 M_{Jup} at an age of 5 ± 3 Gyr for the primary and secondary, respectively, from the Lyon/COND evolutionary models for brown dwarfs (Baraffe et al. 2003). These masses correspond to a mass ratio $q = 0.91 \pm 0.05$. The unresolved W0146−4234AB system is marked by a yellow star in Figure 2.8 and was found to be located outside our sensitivity limits, in the 0% detection probability region.

2.5 Additional Mid and Late-T Samples

In addition to a search for planetary-mass companions, the aim of this survey is to place the first statistically robust constraints to date on the binary properties of ultracool $\geqslant$ T8 brown dwarfs. To improve our statistics, we include in our analysis (Section 2.6) published binary surveys that probed similar spectral type objects. We only consider multiplicity studies containing a minimum of two $\geqslant$ T8 targets, as a single object would introduce more systematics into our analysis than it would improve the overall statistics. As our program also aims at confirming the existence of a statistically significant population of wide ultracool binaries like those discovered by Liu et al. (2012), we excluded surveys that did not search for companions on separations larger than at least a few tens of AU. We do not consider serendipitous discoveries or publications not presenting a full observed sample, as one-off discoveries would strongly bias our results. From the above selection criteria, we retained the binary surveys by Gelino et al. (2011) and Aberasturi et al. (2014), from which we define an "extended" $\geqslant$ T8 sample of 23 targets (including our observed program) and a "comparison" T5$-$T7.5 sample of 24 objects. Both additional subsets are presented below.

2.5.1 Extended Sample of $\geqslant$ T8 Brown Dwarfs

To extend our T8 and later sample size, we consider all objects with spectral types $\geqslant$ T8 from the studies in Gelino et al. (2011) and Aberasturi et al. (2014), doubling the overall size of our sample. All additional targets have similar estimated field ages ($\sim$few Gyr) and distances ($<$ 30 pc) to our core sample. The subset from Gelino et al. (2011) consists of 7 objects and includes a T8.5+T9.5 binary system discovered as part of that multiplicity search. The survey conducted by Aberasturi et al. (2014) includes 4 brown dwarfs with spectral types of T8 or later, none of which was found to be a resolved binary. Using the method described in Section 2.2.3, we estimated the mass of each target from its published J-band photometry. Photometric information, distances and derived properties for the 11 additional sources are presented in Table 2.6.

Table 2.6. Additional sample of $\geqslant$ T8 brown dwarfs.

Object ID	RA (J2000)	Dec. (J2000)	SpT (NIR)	Distance (pc)	J (mag)	H (mag)	Ref.	$\log(L_{\rm bol}/L_{\odot})$	Mass ($M_{\rm Jup}$)
From Gelino et al. (2011)									
WISE J0458+6434A[a,b]	04:58:53.90	+64:34:51.9	T8.5	10.5 ± 1.4	17.50 ± 0.09	17.81 ± 0.13	(1)	-5.93 ± 0.23	31 ± 7
WISE J0750+2725[a]	07:50:03.78	+27:25:44.8	T9.0	15.8 ± 2.0	18.69 ± 0.04	19.00 ± 0.06	(2)	-5.87 ± 0.22	34 ± 8
WISE J1322−2340	13:22:33.66	−23:40:17.1	T8.0	10.4 ± 2.0	17.21 ± 0.10	17.01 ± 0.14	(2)	-5.81 ± 0.21	35 ± 8
WISE J1614+1739[a]	16:14:41.45	+17:39:36.7	T9.0	10.0 ± 2.0	19.08 ± 0.06	18.47 ± 0.22	(2)	-6.43 ± 0.25	20 ± 6
WISE J1617+1807[a]	16:17:05.75	+18:07:14.3	T8.0	15.4 ± 2.0	17.66 ± 0.08	18.23 ± 0.08	(3)	-5.78 ± 0.16	36 ± 7
WISE J1653+4444	16:53:11.05	+44:44:23.9	T8.0	12.1 ± 2.0	17.59 ± 0.03	17.53 ± 0.05	(2)	-5.83 ± 0.18	35 ± 7
WISE J1741+2553	17:41:24.26	+25:53:19.7	T9.0	5.7 ± 2.0	16.48 ± 0.02	16.24 ± 0.04	(2)	-5.78 ± 0.32	36 ± 9
From Aberasturi et al. (2014)									
ULAS J0034−0052[a]	00:34:02.76	−00:52:08.0	T8.5	12.6 ± 0.6	18.15 ± 0.08	18.49 ± 0.04	(4)	-6.02 ± 0.17	29 ± 6
2MASS J0729−3954	07:28:59.47	−39:53:46.3	T8.0	6.0 ± 1.0	15.92 ± 0.08	15.98 ± 0.18	(5)	-5.77 ± 0.19	36 ± 8
2MASS J0939−2448	09:39:35.87	−24:48:38.0	T8.0	10.0 ± 2.0	15.98 ± 0.11	15.80 ± 0.15	(6)	-5.36 ± 0.22	49 ± 9
ULAS J1238+0953[a]	12:38:28.57	+09:53:51.3	T8.5	18.5 ± 4.3	18.95 ± 0.02	19.20 ± 0.02	(7)	-6.03 ± 0.27	29 ± 8

Notes.
Magnitudes are on the 2MASS filter system except for [a] on the MKO-NIR filter system. [b] Primary component only, see text for secondary component and binary properties. Bolometric luminosities and masses were derived in this work. Masses were estimated adopting uniform age distributions in the range 2−8 Gyr.

References.
Distances for targets from Gelino et al. (2011) are the "adopted" distances from table 8 in Kirkpatrick et al. (2012), except for WISE J0458+6434A from Gelino et al. (2011). Distances for targets from Aberasturi et al. (2014) are those listed in Table 1 in that paper. Spectral types and photometry from: (1) Gelino et al. (2011); (2) Kirkpatrick et al. (2011); (3) Burgasser et al. (2011) (4) Warren et al. (2007); (5) Looper et al. (2007); (6) Tinney et al. (2005); (7) Burningham et al. (2008).

Gelino et al. (2011) found that W0458+6434 is a 510 ± 20 mas binary with a Δmag of $\sim$1 in both J and H. At the spectrophotometric distance of 10.5 ± 1.4 pc adopted in Gelino et al. (2011) for the system, the measured angular separation corresponds to a physical projected separation of 5.0 ± 0.4 AU. With spectral types of T8.5 and T9.5 (Burgasser et al. 2012) for the primary and secondary components, respectively, W0458+6434AB is one of the latest-type brown dwarf binaries discovered to date. Gelino et al. (2011) estimated component masses of 15 M_{Jup} and 10 M_{Jup} at an adopted age of 1 Gyr. From the J-band photometry reported for the individual components and applying the method used throughout this work for mass estimation, we derived masses of 31 ± 7 M_{Jup} and 26 ± 7 M_{Jup} for the two binary components assuming a uniform age distribution in the range 5 ± 3 Gyr. These results are in good agreement with the values reported in Gelino et al. (2011) for the slightly older ages adopted here. Our derived component masses yield a mass ratio of $q = 0.84 \pm 0.05$ for the system.

Targets from Aberasturi et al. (2014) were observed with WFC3/IR on *HST* in the F110W, F127M and F164N filters. The F127M bandpass covers the 1.27 μm peak observed in late-T brown dwarfs and is thus more sensitive to search for faint companions (see Aberasturi et al. 2014). We therefore used the *HST*/WFC3 F127M images from this program and the photometry reported in that paper to derive the detection limits of that subset, after performing the same data reduction as for our core sample. Total exposure times of 1197.7 s were obtained for the F127M observations, providing slightly deeper images than our observed program.

The multiplicity search carried by Gelino et al. (2011) was conducted with the infrared camera NIRC2 together with the Laser Guide Star Adaptive Optics system (LGS AO; Wizinowich et al. 2004) on the 10 m Keck II telescope. Images were taken in the H filter and observations are described in the survey paper. The narrow camera (plate scale of $0\farcs009942$ pixel^{-1}) was used for all observations, with the exception of one target (W0750+2725) which was observed with the wide camera ($0\farcs039686$ pixel^{-1}). The Keck/NIRC2 H-band images were reduced using custom Python scripts. For each image, we subtracted a mean dark frame generated from all other dithered positions to remove the sky background. We then applied a bad pixel mask and divided by a flat-field image before stacking all dithered frames.

The sensitivity limits for all additional targets in the extended late-T sample were obtained following the method applied to our core sample, described in Section 2.4. We used the measured WFC3/F127M photometry from Aberasturi et al. (2014) and 2MASS or MKO H-band photometry for the targets from Gelino et al. (2011) together with the corresponding AMES/COND models (Allard et al. 2001) to compute mass detection limits for each object. Sensitivity curves in the Keck images were started at a radius of 4 pixels because of the high noise level inside that radius, except for the target observed with the wide camera, for which we used an initial radius of 1 pixel. The obtained detection limits for each subset are presented in Figure 2.9 in terms of mass ratio as a function of angular and physical projected separation. The regions of the parameter space probed in the two subsets are considerably different as shown in Figure 2.10. While the *HST* observations are deep ($q \sim 0.2-0.3$ at separations > 10 AU) and have a wide field of view ($123'' \times 136''$), the $0\farcs13$ pixel^{-1} plate scale of the WFC3/IR instrument only allows us to probe separations down to 0.8−2.4 AU at the distances of the targets. In comparison, the NIRC2 images have a resolution of $0\farcs01$ pixel^{-1} ($0\farcs04$ pixel^{-1} for the wide camera). The 4-pixel radius at which the contrast curves were started (1 pixel for images acquired with the wide camera) corresponds to projected separations of 0.23−0.63 AU. With a $10'' \times 10''$ field of view and mass ratio limits of $q \sim 0.6$, observations from this subset are not sensitive to wide ($>$ 20−60 AU) or low-mass ($q < 0.5$) companions.

The average detection probability map for the combined sample of 23 objects (observed and extended samples) was derived from the sensitivity limits of all individual targets, following the approach described in Section 2.4.3. The resulting map is shown in Figure 2.11. As a result of the different facilities and instruments used, the combined survey is only complete down to $q \sim 0.75$ and between ∼5−25 AU, the region of the parameter space where all surveys overlap. The binary discovered in Gelino et al. (2011), W0458+6434AB (red star), is located inside the 100% completeness region of the combined survey, meaning that we are sensitive to systems with the physical properties of this system around all targets. The 50% completeness contour shows that systems with separations in the range ∼3−500 AU and mass ratios > 0.3 are detectable around half of the targets in the final sample. The unresolved binary from Dupuy et al. (2015) is located in the 20−30% detection probability region (yellow star).

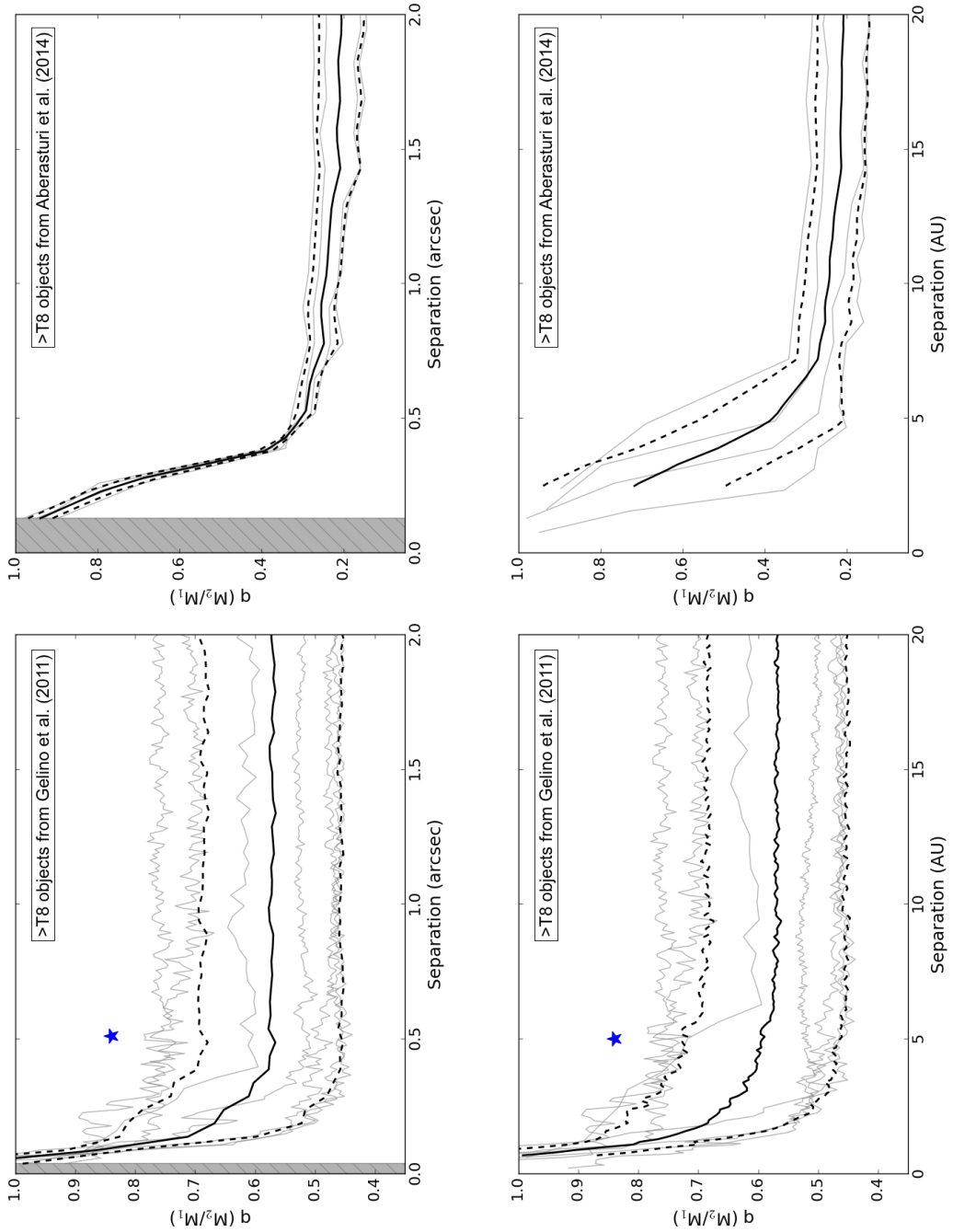

Figure 2.9. Mass ratio sensitivity limits for the additional late-T sample, showing the 7 targets from Gelino et al. (2011) and the 4 targets from Aberasturi et al. (2014). Mass ratio limits were derived using the masses calculated in this work and listed in Table 2.6. The shaded regions represent the radii at which the contrast curves were started. The black solid lines shows the mean sensitivity level for each subset and the 1-σ standard deviation around the mean (dotted lines). The blue star indicates the position of the secondary companion W0458+6434B. The binary companion was masked before computing the contrast curve around the primary W0458+6434A.

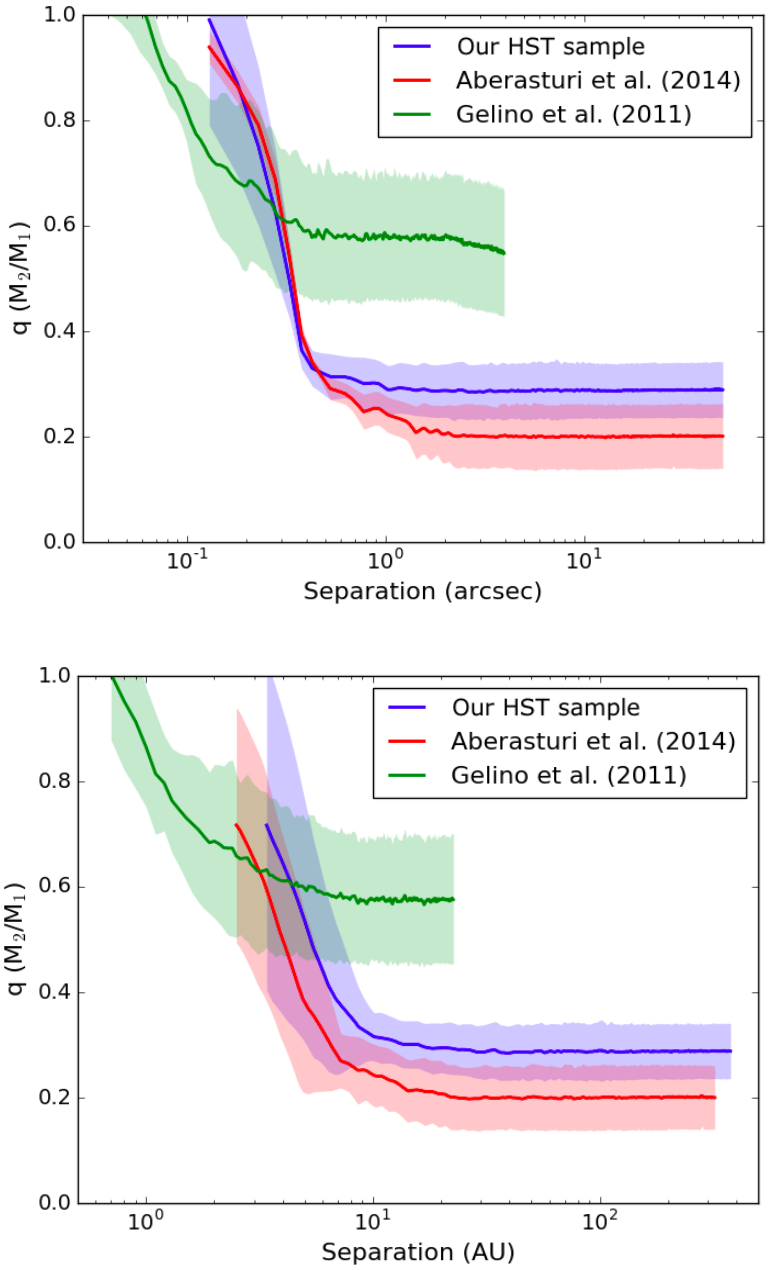

Figure 2.10. Mean mass ratio sensitivities at the 5-σ level for our observed sample and the two subsets from the additional late-T sample, showing the different regions of the parameter space probed by each subset. The shaded areas correspond to the 1-σ standard deviation around the mean (solid line). On the right panel, limits of each subset are only shown for physical separations resolved around all targets in any subset. While the *HST* observations (blue and red curves) probe wide separations and are sensitive to low mass ratios, the Keck images (green) have a smaller inner working angle and may resolve smaller separations.

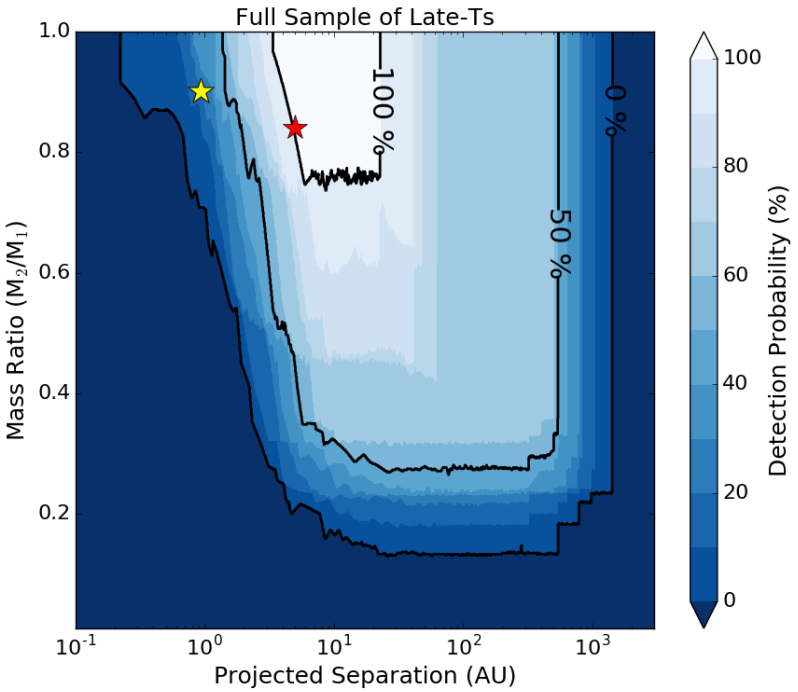

Figure 2.11. Same as Figure 2.8 for the extended sample combining our observed survey with the $\geqslant$ T8 brown dwarfs selected from Gelino et al. (2011) and Aberasturi et al. (2014). Contours denote the 0%, 50% and 100% completeness regions. The red star shows the position of the T8.5+T9 binary discovered in Gelino et al. (2011), W0458+6434AB, using the component masses calculated in this work. The yellow star corresponds to the known W0146+4234 binary, unresolved in our observations.

2.5.2 Comparison Sample of T5−T7.5 Brown Dwarfs

In order to compare our results to the binary properties of earlier-type objects, we also compiled a sample of 24 mid-T (T5−T7.5) brown dwarfs from Gelino et al. (2011) (2 objects) and Aberasturi et al. (2014) (22 objects). The two subsets considered come from the same surveys as the additional late-T sample presented in Section 2.5.1, allowing for a direct comparison of the obtained results. The comparison mid-T sample is presented in Table 2.7. Luminosities and masses were derived following the approach described in Section 2.2.3, adopting uniform age distributions in the range 2−8 Gyr. With earlier spectral types, and thus higher effective temperatures at the same adopted ages, targets from this subset have larger estimated masses ($\sim$40−60 M_{Jup}) than the late-T objects from our observed

Table 2.7. Comparison sample of T5−T7.5 brown dwarfs.

Object ID	RA (J2000)	Dec. (J2000)	SpT (NIR)	Distance (pc)	J (mag)	H (mag)	Ref.	$\log(L_{\rm bol}/L_{\odot})$	Mass ($M_{\rm Jup}$)
From Gelino et al. (2011)									
WISE J1627+3255	16:27:25.64	+32:55:24.1	T6.0	15.4 ± 2.0	16.48 ± 0.04	16.40 ± 0.05	(1)	-5.37 ± 0.12	48 ± 8
WISE J1841+7000A[a,b]	18:41:24.74	+70:00:38.0	T5.0	40.2 ± 4.9	17.24 ± 0.10	17.73 ± 0.10	(2)	-4.91 ± 0.12	61 ± 8
From Aberasturi et al. (2014)									
HD3651B[a]	00:39:18.61	+21:15:12.7	T7.5	11.0 ± 0.1	16.16 ± 0.03	16.68 ± 0.04	(3)	-5.56 ± 0.08	43 ± 7
2MASS J0050−3322	00:50:19.92	−33:22:41.4	T7.0	8.0 ± 1.0	15.93 ± 0.07	15.84 ± 0.19	(4)	-5.67 ± 0.12	39 ± 7
SDSS J0325+0425	03:25:53.11	+04:25:40.0	T5.5	19.0 ± 2.0	16.25 ± 0.14	> 16.08	(5)	-5.08 ± 0.11	57 ± 8
2MASS J0407+1514	04:07:08.94	+15:14:55.4	T5.0	17.0 ± 2.0	16.06 ± 0.09	16.02 ± 0.21	(6)	-5.08 ± 0.11	57 ± 8
2MASS J0510−4208	05:10:35.32	−42:08:08.2	T5.0	18.0 ± 2.0	16.22 ± 0.09	16.24 ± 0.16	(6)	-5.09 ± 0.11	57 ± 8
2MASS J0727+1710	07:27:19.07	+17:09:52.2	T7.0	9.1 ± 0.2	15.60 ± 0.06	15.76 ± 0.17	(7)	-5.42 ± 0.06	47 ± 7
2MASS J0741+2351	07:41:48.96	+23:51:25.9	T5.0	18.0 ± 2.0	16.15 ± 0.10	15.84 ± 0.18	(6)	-5.07 ± 0.11	57 ± 8
2MASS J1007−4555	10:07:32.99	−45:55:13.3	T5.0	15.0 ± 2.0	15.65 ± 0.07	15.68 ± 0.12	(5)	-5.03 ± 0.13	58 ± 8
2MASS J1114−2618	11:14:48.90	−26:18:27.2	T7.5	10.0 ± 2.0	15.86 ± 0.08	15.73 ± 0.12	(8)	-5.40 ± 0.20	47 ± 9
2MASS J1231+0847	12:31:46.74	+08:47:22.3	T5.5	12.0 ± 1.0	15.57 ± 0.07	15.31 ± 0.11	(6)	-5.21 ± 0.08	53 ± 8
SDSS J1346−0031	13:46:46.04	−00:31:51.3	T6.5	14.6 ± 0.5	16.00 ± 0.10	15.46 ± 0.12	(5)	-5.21 ± 0.06	53 ± 7
SDSS J1504+1027	15:04:11.74	+10:27:18.8	T7.0	15.9 ± 2.5	17.03 ± 0.23	> 16.90	(5)	-5.52 ± 0.18	44 ± 8
SDSS J1628+2308	16:28:38.99	+23:08:18.4	T7.0	14.0 ± 4.0	16.45 ± 0.10	16.11 ± 0.15	(4)	-5.43 ± 0.29	46 ± 9
2MASS J1754−1649	17:54:54.56	+16:49:18.1	T5.0	14.3 ± 1.3	15.81 ± 0.07	15.65 ± 0.13	(9)	-5.13 ± 0.09	56 ± 8

Table 2.7. (Continued.)

Object ID	RA (J2000)	Dec. (J2000)	SpT (NIR)	Distance (pc)	J (mag)	H (mag)	Ref.	$\log(L_{\rm bol}/L_\odot)$	Mass ($M_{\rm Jup}$)
SDSS J1758+4633	17:58:05.49	+46:33:17.1	T6.5	12.0 ± 2.0	16.15 ± 0.08	16.25 ± 0.21	(4)	-5.45 ± 0.16	46 ± 8
2MASS J1828−4849	18:28:36.01	−48:49:02.6	T5.5	11.0 ± 1.0	15.18 ± 0.06	14.91 ± 0.07	(8)	-5.13 ± 0.09	56 ± 8
2MASS J1901+4718	19:01:05.89	+47:18:09.9	T5.0	15.0 ± 2.0	15.86 ± 0.07	15.47 ± 0.09	(5)	-5.51 ± 0.13	44 ± 8
SDSS J2124+0100	21:24:14.02	+01:00:02.7	T5.0	18.0 ± 2.0	16.03 ± 0.07	16.18 ± 0.20	(5)	-5.02 ± 0.11	58 ± 8
2MASS J2154+5942	21:54:32.98	+59:42:14.4	T5.0	10.0 ± 1.0	15.66 ± 0.07	15.76 ± 0.17	(5)	-5.38 ± 0.10	48 ± 8
2MASS J2237+7228	22:37:20.47	+72:28:35.3	T6.0	13.0 ± 2.0	15.76 ± 0.07	15.94 ± 0.21	(10)	-5.23 ± 0.14	53 ± 8
2MASS J2331−4718	23:31:23.84	−47:18:28.2	T5.0	13.0 ± 2.0	15.66 ± 0.07	15.51 ± 0.15	(6)	-5.16 ± 0.14	55 ± 8
2MASS J2359−7335	23:59:41.09	−73:35:04.9	T6.5	12.3 ± 1.9	16.17 ± 0.04	16.06 ± 0.07	(1)	-5.43 ± 0.14	47 ± 8

Notes.

Magnitudes are on the 2MASS filter system except for [a] on the MKO-NIR filter system. [b] Primary component of only, see text for secondary component and binary properties. Bolometric luminosities and masses were derived in this work. Masses were estimated adopting uniform age distributions in the range 2−8 Gyr.

References.

Distances for targets from Gelino et al. (2011) are the "adopted" distances from table 8 in Kirkpatrick et al. (2012), except for WISE J1841+7000A from Gelino et al. (2011). Distances for targets from Aberasturi et al. (2014) are those listed in Table 1 in that paper. Spectral types and photometry from: (1) Kirkpatrick et al. (2011); (2) Gelino et al. (2011); (3) Luhman (2007); (4) Dupuy et al. (2015); (5) Looper et al. (2007); (6) Faherty et al. (2009); (7) Vrba et al. (2004); (8) Tinney et al. (2005); (9) Faherty et al. (2012); (10) Mace et al. (2013).

program and the extended sample (< 40 M_{Jup}). Gelino et al. (2011) identified W1841+7000 as a T5+T5 near equal-mass binary with a 2.8 AU projected separation (70 ± 14 mas). We estimated component masses of 61 ± 8 M_{Jup} and 58 ± 8 M_{Jup} adopting an age of 2−8 Gyr and using the photometric measurements for individual components reported in Gelino et al. (2011), implying a mass ratio of $q = 0.95 \pm 0.05$. Aberasturi et al. (2014) found no binary system among the 22 objects selected for this subset.

Like for the additional late-T sample, we used the *HST* WFC3/IR F127M images from the program in Aberasturi et al. (2014) and Keck/NIRC2 H-band data for the two targets from Gelino et al. (2011), applying the same data reduction as in Section 2.5.1. Detection limits for all targets were derived in the same way as for the additional late-T objects and are shown in Figure 2.12. For similar achieved mass limits in each subset from the two programs considered, we obtained slightly better mass ratio sensitivities overall than for the late-T targets as a result of the higher primary masses of the mid-T targets.

The sensitivity limits were finally combined to create a detection probability map (see Section 2.4.3) for the full sample of mid-T brown dwarfs, presented in Figure 2.13. Again, the use of multiple instruments probing different regions of the parameter space resulted in a rather restricted 100% completeness region. The observed binary, W1841+7000AB, was found to be at an 83% detection probability level.

2.6 Measured Binary Properties

Despite a null detection, results from our survey may still be used to place statistical limits on the binary properties for $\geqslant$ T8 field brown dwarfs. The absence of resolved binaries in our observed program is consistent with the current census for the binary properties of the latest-type brown dwarfs. Substellar binary rate is believed to decrease with spectral type within the field population (Allen 2007; Kraus et al. 2012) and multiple systems are hence expected to be rare among the latest-type objects. Multiplicity surveys in the field indicate a clear tendency towards near equal-flux systems. As most field binaries are found to have high mass ratios ($q > 0.8$; Burgasser et al. 2006b), we expect our observed program

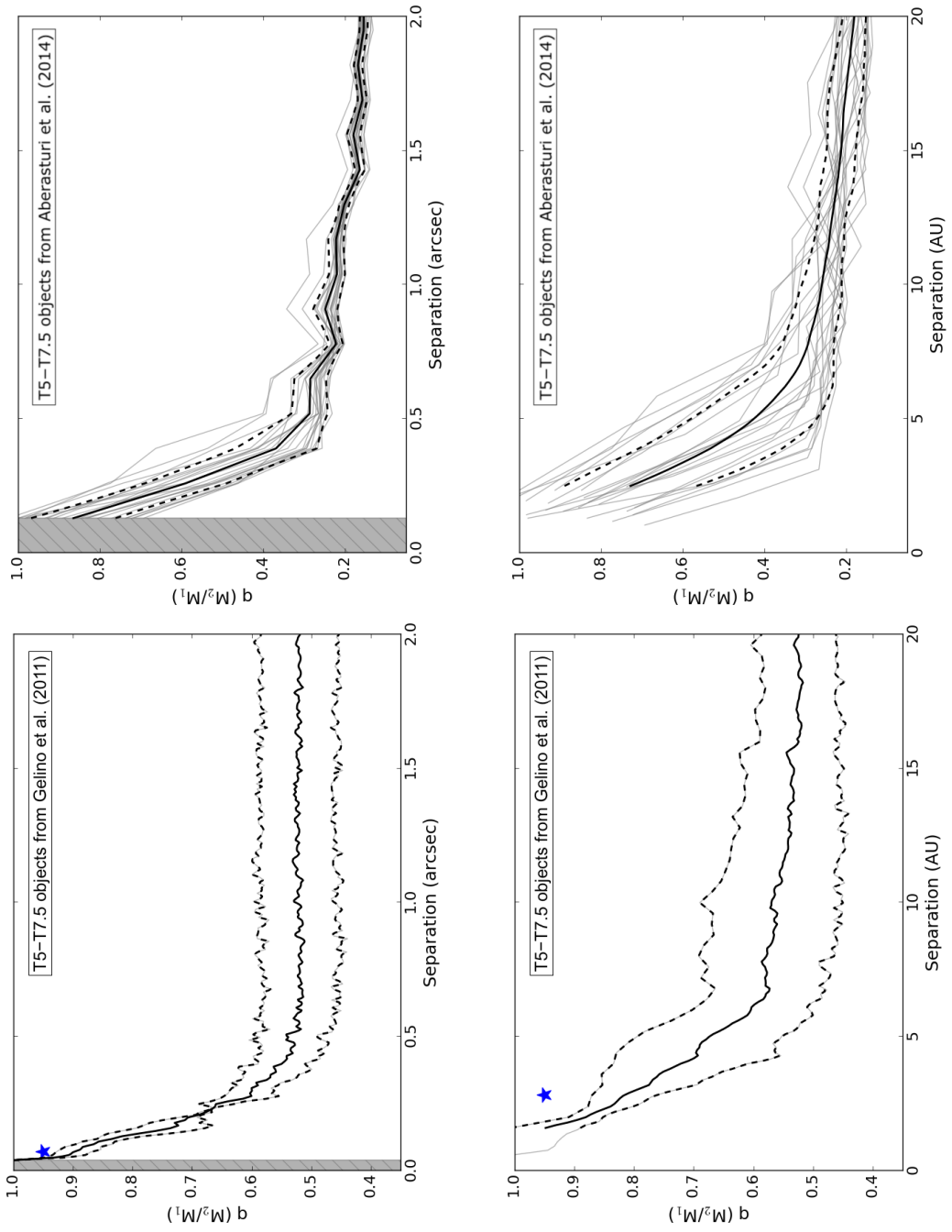

Figure 2.12. Same as Figure 2.9 for the comparison mid-T sample, showing the minimum mass ratios detectable around the 2 targets from Gelino et al. (2011) and the 22 targets from Aberasturi et al. (2014). The blue star indicates the position of the secondary companion W1841+7000B. The binary companion was masked before computing the contrast curve around the primary W1841+7000A.

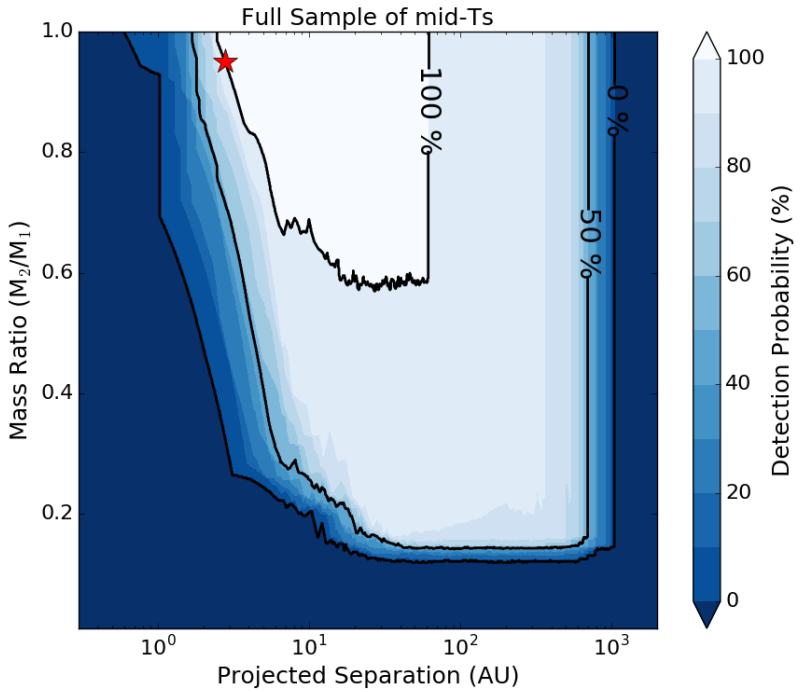

Figure 2.13. Same as Figure 2.8 for the T5−T7.5 sample selected from Gelino et al. (2011) and Aberasturi et al. (2014). Contours denote the 0%, 50% and 100% completeness regions. The red star shows the position of T5+T5 binary discovered in Gelino et al. (2011), W1841+7000AB.

to be sensitive to most binaries beyond ∼5 AU, since we are complete down to $q \sim 0.75$ at 5 AU and $q \sim 0.4$ from 8 AU. Given our survey sensitivity, it is unlikely that we missed a significant number of such systems. However, the observed peak of the separation distribution for field brown dwarfs (∼4 AU; Allen 2007; Burgasser et al. 2007) is close to our resolution limits. We are thus only sensitive to somewhat wide binaries, thought to be uncommon at such late spectral types. While a population of very low mass ratio systems lying below our detection limits seems unlikely, a fraction of close binaries could still remain undetected due to survey incompleteness. This observational bias must be carefully taken into account when investigating the binary properties of our probed targets.

With no new companion detected as part of our study, we cannot place any new constraints on the mass ratio or separation distributions of the latest-type brown dwarf binary systems based on our observed sample. We are however able to constrain the binary frequency of old objects with estimated masses < 40 M_{Jup}

for the separations and mass ratios probed in this study. We used a Markov Chain Monte Carlo (MCMC) approach to estimate the binary fraction most compatible with the observed data, assuming a range of possible distributions of companion populations. The MCMC sampling tool accounts for the survey detection limits and the presumed shapes of companion population distributions, therefore correcting for observational biases. The statistical tool is described in Section 2.6.1 and results from its application to our core program and the extended and comparison samples are presented in Section 2.6.2.

2.6.1 Bayesian Statistical Analysis: MCMC Tool

We developed an MCMC sampling tool designed for Bayesian parameter estimation. The tool was built using the EMCEE (Foreman-Mackey et al. 2013) Python implementation of the affine-invariant ensemble sampler for MCMC proposed by Goodman & Weare (2010). The core of this method is based on Bayesian parameter estimation. Bayes' theorem states:

$$P(\theta \mid D) \propto P(D \mid \theta)\, P(\theta), \tag{2.2}$$

where θ represents the model and D the data. $P(\theta)$, the prior distribution, is the initial probability density of the model. $P(D \mid \theta)$, the likelihood function, gives the probability of the data given the model. $P(\theta \mid D)$, the posterior distribution, is the probability of the model given the data. For any model θ, we are able to calculate the likelihood function, that is, the probability that the data D would have been measured given the hypothesised model. Using Bayes' theorem (Equation 2.2) we may then compute the probability of a hypothesised model being true given the observed data, that is, the posterior distribution.

The MCMC sampling method iteratively generates sequences of samples for each parameter describing the model, calculating the likelihood function for each set of parameters so as to approximate the desired posterior distribution. At each step, the algorithm randomly attempts to move the walkers in the parameter space. Moving to a point in a higher probability density region of the posterior distribution is always accepted. Attempting to move to a less probable point is accepted or rejected based on the current and trial positions. As a result,

while the sampler occasionally visits low probability density regions, it tends to remain in higher probability density parts of the parameter space, returning final output samples representative of the sought posterior distributions for each model parameter. The affine-invariant ensemble diverges from the usual "random walk" Metropolis-Hasting algorithm (Metropolis et al. 1953; Hastings 1970) by using the current positions of all the other walkers in the ensemble to move a given walker. The intuition behind this is that other walkers have already sampled an important part of the parameter space and provide valuable information about the underlying distributions. This significantly improves performances by reducing the time required for the algorithm to identify and explore the most relevant regions of the parameter space, making the affine-invariant MCMC very competitive.

Based on previous substellar multiplicity surveys (e.g. Close et al. 2003; Burgasser et al. 2006b, 2007; Allen 2007), companion populations were assumed to follow a lognormal distribution in projected separation ρ and a power law distribution in mass ratio $q \equiv M_2/M_1$. The MCMC sampler explores four model parameters describing the companion populations:

- ρ_0, the peak of the lognormal distribution in projected separation.
- σ, the standard deviation of the normal distribution in $\log(\rho)$.
- γ, the index of the power law distribution in the mass ratio q.
- f, the binary frequency of a given separation range.

The lognormal distribution in projected separation ρ is given by:

$$P(\rho \mid \mu, \sigma) = \frac{1}{\sqrt{2\pi}\,\sigma\,\rho}\, e^{-[\log_{10}(\rho) - \mu]^2 \,/\, 2\sigma^2}, \tag{2.3}$$

where μ is the mean of the underlying normal distribution in $\log(\rho)$. The mean μ is a function of ρ_0 and σ and is found by solving for the root of $\partial P(\rho)/\partial\rho$ at $\rho = \rho_0$ at any given step. Equation 2.3 may be truncated to be restricted to a defined range of separations.

The mass ratio distribution ranges from 0 to 1 and is described by the equation:

$$P(q \mid \gamma) = (\gamma + 1)\, q^{\gamma}. \tag{2.4}$$

Based on our lack of knowledge of any of these parameters for the very low-mass objects studied in this work, prior distributions were chosen to be flat distributions, set to unity over a chosen range and to zero elsewhere. We defined priors in the ranges 0.3−10 AU for ρ_0, 0.03−1 for σ, 1−12 for γ and 0−1 for f. We assumed no prior knowledge about f so as to explore the full range of possible values. Ranges for the other three model parameters were chosen so as to span a wide enough space to likely cover the expected peak value of each parameter based on previous studies (e.g. Reid et al. 2006; Burgasser et al. 2007), while limiting the region of parameter space to be explored. As null or low number of detections does not allow us to constrain the shapes of the separation and mass ratio distributions, wider ranges for prior probabilities in ρ_0, σ and γ only result in a broader output distribution in f due to the many more possible companion populations tested by the sample. We therefore restrained prior distributions to what we consider plausible regions based on past studies.

Walkers were started in a tight 4-dimensional ball, centred around a chosen point expected to be close to the maximum probability point for each parameter. This approach reduces the risk of walkers getting stuck in low-probability regions of the parameter space. The walkers quickly expanded out to explore and fill the relevant parts of parameter space. The initial positions of the walkers were drawn from Gaussian distributions centred around $\rho_0 = 3$ AU, $\sigma = 0.5$, $\gamma = 4$ and $f = 0.1$, with standard deviations of 0.1 AU, 0.01, 0.1 and 0.01, respectively.

Let N_* be the number of objects in the observed sample and d the number of binaries detected in that sample. For each set of parameters generated by the MCMC tool, a synthetic population of $n = 10^5$ companions is drawn from the lognormal and power law distributions in projected separation and mass ratio, respectively. Each simulated companion (with separation ρ and mass ratio q) is then injected into the detection probability map for the survey (see Section 2.4.3) to get the probability p_i that such a companion would have been retrieved in the observations. Assuming a binary rate f for the sample studied, the total number of companions expected to be detected, k, for the achieved detection limits is given by:

$$k = \sum_{i=1}^{n} (p_i) \times f \times \frac{N_*}{n}. \tag{2.5}$$

The obtained value for k may then be compared to the number of binaries d detected in the observed data in order to estimate the likelihood of the data for a given a set of model parameters. We used Poisson statistics to define the likelihood function $\mathcal{L}$:

$$\mathcal{L}(d \mid k) = \frac{k^d \, e^{-k}}{d!}, \tag{2.6}$$

where k, the mean expected number of detections for the model parameters considered (given by Equation 2.5) is the mean of the Poisson probability mass function. Equation 2.6 thus gives the probability of detecting d companions given that an average of k binaries are expected to be detected if the binary population in the observed sample is described by parameters ρ_0, σ, γ and f.

For a survey with a null detection, the code explores all four population parameters throughout the ranges of allowed values but only really allows for the investigation of the binary frequency f. In that case, the returned posterior probability distribution for the binary fraction may be used to determine an upper limit for f that is most compatible with the observed data, marginalised over the other three model parameters.

In cases where one or more companions are present in the sample studied, the separations and mass ratios of the observed companions may be taken into account in the MCMC code to further constrain the remaining three parameters. This is done by estimating the probabilities of the detected companions being drawn from the model distributions considered at any step. Sensitivity limits must be taken into account when computing these probabilities in order to truly compare the model to the data and account for observational biases. As our detection limits vary throughout the parameter space, the distributions of companions expected to be observed differ from the model distributions. In order to compare the model to our data, we must transform the parameter space of the model to an observed one. The top panel in Figure 2.14 shows the detection probability at every point in the $\rho - q$ space for our observed survey. The middle panel shows the joint model companion distribution assuming model parameters $\rho_0 = 4$ AU, $\sigma = 0.5$ and $\gamma = 3$, truncated at 1.5 AU. The bottom panel shows the same 2-dimensional density function mapped onto the observed parameter space, that is, multiplied by the

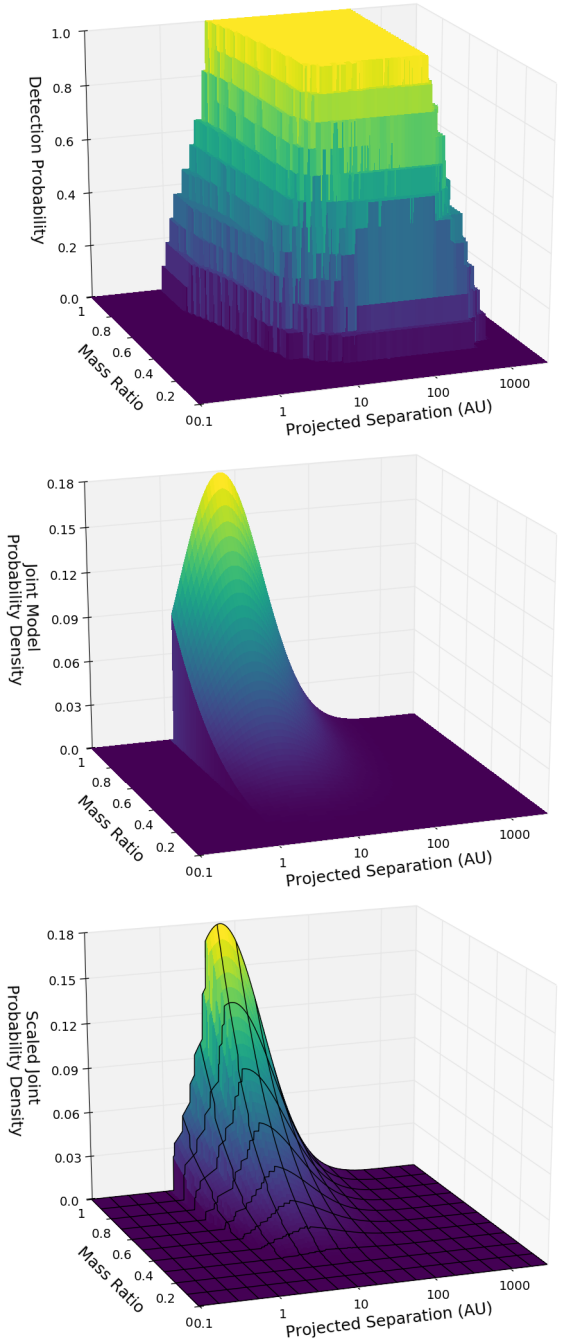

Figure 2.14. Calculation of the probabilities of observing specific binary systems for given model parameters and achieved sensitivity limits. **Top:** Detection probability for our observed sample (same as Figure 2.8) shown in the 3-dimension space. **Middle:** Joint model probability density of companion distribution assuming populations described by $\rho_0 = 4$ AU, $\sigma = 0.5$ and $\gamma = 3$. The separation distribution was truncated at 1.5 AU and 1000 AU. **Bottom:** Same as middle panel scaled by the detection probability from the top panel. This provides the companion distribution expected to be observed for the achieved limits and model parameters considered.

detection probability from the top panel in every point. This provides an expected observed distribution of companions for the model parameters considered, given the achieved detection limits.

The $\log(\rho)$ space is then divided into bins of 0.25 and the q domain into bins of 0.1, as shown by the black lines in the bottom panel of Figure 2.14. The probability of observing any given companion is found by estimating the probability of ρ and q falling in the region enclosing the observed parameters, given by the volume under the scaled density function in that region. The code computes this probability for the projected separation and mass ratio of every companion detected in the observations. The likelihood $\mathcal{L}$ from Equation 2.6 is then multiplied by each of the returned probabilities. The product of all individual probabilities is larger when the observed distributions of companions are well approximated by the scaled model distributions. As a result, this allows the algorithm to favour model distributions from which the observed data were more likely to be drawn, while accounting for detection limits and preventing a bias towards better-sampled regions of the parameter space. The likelihood obtained at each step of the ensemble therefore provides us with the probability of seeing the observed data if the companion population is described by the model parameters considered at that step. The MCMC then uses Bayes' theorem (Equation 2.2) and the provided prior distributions to compute the probability of a set of model parameters given the observed data set. The output posterior distributions generated by the sampler finally return the probability density function for each parameter that is most compatible with the observed data.

2.6.2 Results

2.6.2.1 Observed Sample

The MCMC sampling tool described in Section 2.6.1 was applied to our observed *HST* sample to investigate the brown dwarf binary rate of our survey. At projected separations of 2 AU, we are sensitive to near equal-mass binaries around $\sim$80% of our observed sample, to $q > 0.8$ companions around half of our targets, and down to $q \sim 0.6$ for $\sim$40% for our sample. Given the known preference for high mass ratios in field substellar binaries, we consider 2 AU a suitable lower

limit on the separation range reliably accessible to the observations. As a result, the lognormal distribution in projected separation was truncated so as to only explore the separation range 2−1000 AU.

The code was run with 2×10^3 walkers taking 5×10^3 steps each. We found that ∼50 steps were sufficient for the sampler to expand from the initial positions to a reasonable sampling of the parameter space and to get settled around the maximum density regions. We thus discarded the initial 50 steps of the "burn-in" phase and considered the rest of the samples as representative of the posterior densities. A mean acceptance rate (fraction of steps accepted for each walker) of 0.38 was reached after a few hundred steps. Foreman-Mackey et al. (2013) suggest as a rule of thumb that the acceptance fraction should be between 0.2 and 0.5 and we trust the obtained value to be an acceptable sign of convergence. However, larger samples were required in order to obtain smooth output distributions and be able define confidence intervals for the posterior probability functions. The final number of walkers and steps chosen was found to be a good compromise between the need for a high number of iterations and the expensive associated computing times, while providing a stable acceptance rate within the preferred range.

The null detection of our survey did not allow us to place any new constraints on the separation and mass ratio distributions of $\geqslant$ T8 brown dwarf binaries. We were however able to investigate the binary fraction f of our observed sample. Figure 2.15 shows the posterior probability distribution for the binary frequency f of our survey, given the observations. With no new detected companion in the observed sample, we were only able to place an upper limit on the observed binary rate. We used a highest posterior density approach to determine the boundaries of a Bayesian credible interval for the output posterior distribution. For a given level of credibility α, we can define a credible interval bounded by $f_{\rm min}$ and $f_{\rm max}$ as the shortest interval that contains a fraction α of the probability. This can be thought of as a horizontal line placed over the posterior density intersecting the posterior in $f_{\rm min}$ and $f_{\rm max}$ such that the region between these two values has a probability α. If there is no detection, like in our observed program, the posterior density for f is a one-tail distribution (Figure 2.15) and $f_{\rm min} = 0$. The highest density region approach has the useful property that any point within the interval has a higher probability than any other point of the posterior (for

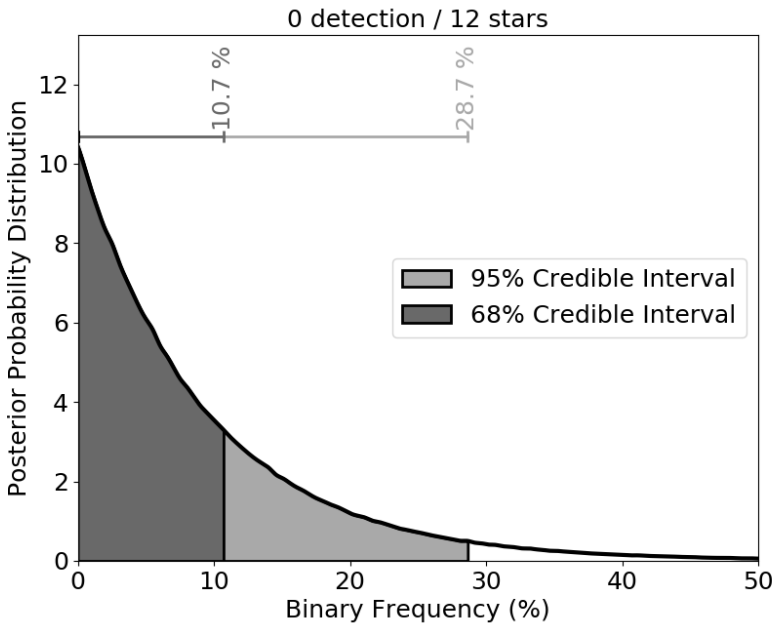

Figure 2.15. Posterior probability distribution of the binary frequency f for our observed sample of 12 targets obtained with the MCMC sampler described in Section 2.6.1. The null detection in the program allows us to place an upper limit of $f < 10.7\%$ (1-σ) on the binary fraction of our survey at separations > 2 AU.

a unimodal distribution), thus providing a collection of the most likely values of the parameter. We consider the $\alpha = 68\%$ and $\alpha = 95\%$ credible intervals, which correspond to 1-σ and 2-σ Gaussian limits, respectively. Using this approach, we inferred a binary frequency of $f < 10.7\%$ ($< 28.7\%$) at the 1-σ (2-σ) confidence level for our observed sample on separations between 2−1000 AU.

2.6.2.2 Extended Sample

To improve our statistics, we performed the same analysis on an extended sample, combining our observed sample with the additional subset of $\geqslant$ T8 objects presented in Section 2.5.1. We used the MCMC sampling tool described in Section 2.6.1 to run the same statistical analysis on the extended sample of 23 objects as that applied to our observed *HST* sample. The detection probability map for the combined survey of late-T brown dwarfs (shown in Figure 2.11) was used as an input for the code. We defined the same prior distributions and initial walker positions as for our observed sample in Section 2.6.2.1. With the slightly

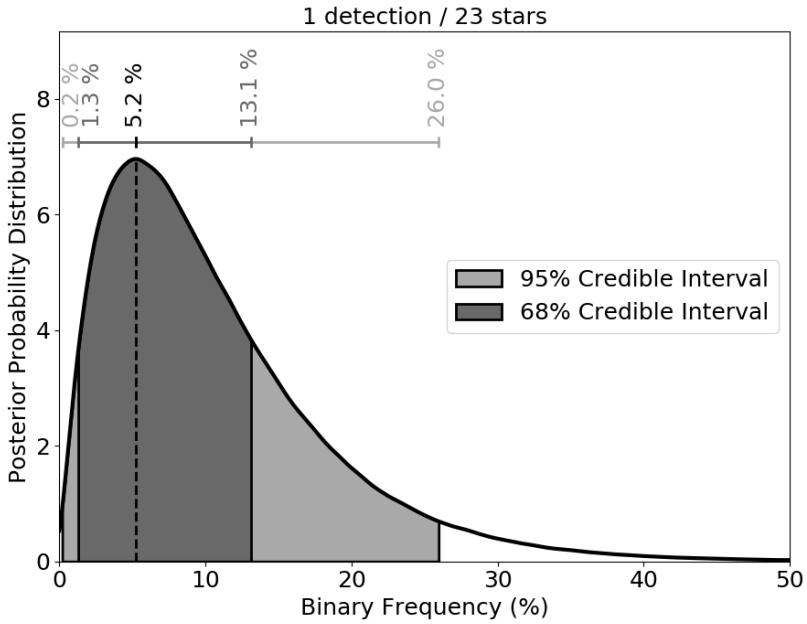

Figure 2.16. Posterior probability distribution of the binary frequency of T8−Y0 brown dwarfs on the separation range 1.5−1000 AU for the extended sample of 23 objects, combining our observed *HST* program and the ⩾ T8 sources from the surveys in Gelino et al. (2011) and Aberasturi et al. (2014). The detection of one companion in the additional subset provides well-defined 1-σ and 2-σ confidence intervals around a most likely value for the observed binary fraction, $f = 5.2\%$.

improved average inner working angle of the additional subset, we are sensitive to smaller separations and thus explored the separation range 1.5−1000 AU for the extended sample. The binary separation measured in Gelino et al. (2011) for W0458+6434AB together with our derived mass ratio for the system were used as additional inputs when computing the likelihood for each set of model parameters. The output posterior probability distribution for the binary rate f is shown in Figure 2.16. While a single detection was still insufficient to reliably constrain the companion distributions in separation and mass ratio, the presence of one binary in the additional subset allowed us to place new limits on the measured binary fraction. The sampler returned a smooth distribution peaking at 5.2%, the most likely value for f given the observed data. Confidence intervals were inferred from the output distribution following the approach described in Section 2.6.2.1, yielding a binary frequency of $f_{\mathrm{T8-Y0}} = 5.2^{+7.9}_{-3.9}$ $(^{+20.8}_{-5.0})\%$ at the 1-σ (2-σ) level for separations > 1.5 AU.

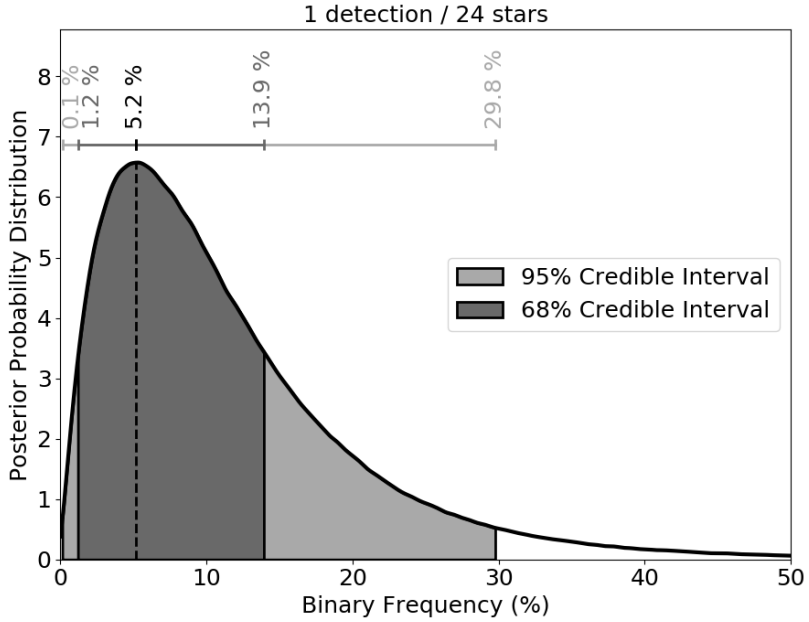

Figure 2.17. Same as Figure 2.16 for the sample of 24 T5−T7.5 brown dwarfs compiled from the surveys in Gelino et al. (2011) and Aberasturi et al. (2014). The obtained distribution is very similar to that obtained for the sample of late-T objects for the same separation range (1.5−1000 AU).

2.6.2.3 Comparison Sample

The MCMC sampling tool detailed in Section 2.6.1 was then run on the mid-T sample presented in Section 2.5.2 in order to compare the results obtained for late-Ts to the mid-T binary population. We used the same input parameters (number of walkers and steps, prior distributions, initial walker positions) as those used for our observed and extended late-T samples to constrain the binary rate over separations of 1.5−1000 AU. The detection probability map shown in Figure 2.13 and the properties the binary system W1841+7000AB were used as inputs to compute the posterior probabilities of the parameters describing the underlying companion population distributions. As for our $\geqslant$ T8 sample, a single detection was not sufficient to confidently constrain the separation and mass ratio distributions. The output posterior distribution for the binary frequency f is shown in Figure 2.17. We inferred a binary fraction of $f_{\mathrm{T5-T7.5}} = 5.2^{+8.7}_{-4.0}\%$ at the 1-σ level ($5.2^{+24.6}_{-5.1}\%$ at the 2-σ level) for T5−T7.5 field brown dwarfs. The results obtained for the $>$ 1.5 AU binary rate of mid-Ts are comparable to those derived for $\geqslant$ T8 brown dwarfs in Section 2.6.2.2 for the same separation range.

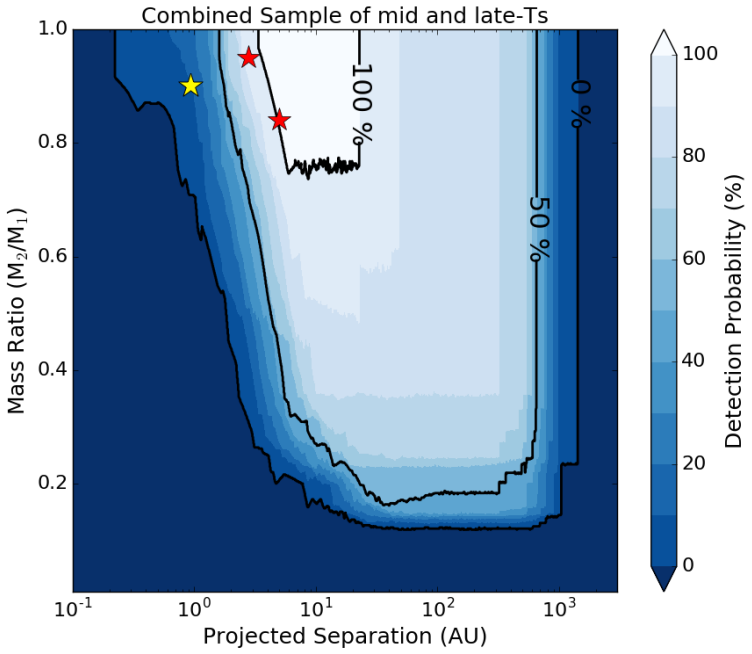

Figure 2.18. Detection probability map for the combined samples of mid and late-T brown dwarfs, compiled from our observed program and the surveys from Gelino et al. (2011) and Aberasturi et al. (2014). Contours denote the 0%, 50% and 100% completeness regions. The red stars show the positions of the two binaries discovered by Gelino et al. (2011), using the component masses calculated in this work. The yellow star corresponds to the known unresolved W0146+4234AB system, located in the 0−10% detection probability region of the full sample.

2.6.2.4 Combined Mid and Late-T Samples

As the binary fractions of our compiled samples of T5−T7.5 and $\geqslant$ T8 brown dwarfs are in excellent agreement, we may combine the two samples so as to more tightly constrain the binary frequency of the $\geqslant$ T5 substellar population. The detection probability map for the full sample of 47 objects is shown in Figure 2.18, together with the respective positions of the two binaries from Gelino et al. (2011) (red stars) and the unresolved binary W0146+4234 (yellow star). Our MCMC tool was used to perform the same statistical analysis on the combined sample as that applied to the individual subsets in previous sections. With a larger sample size and a total of two resolved binary systems, we were able to strengthen the constraints placed separately on mid and late-Ts. The posterior probability distribution for the binary fraction of $\geqslant$ T5 brown dwarfs is presented

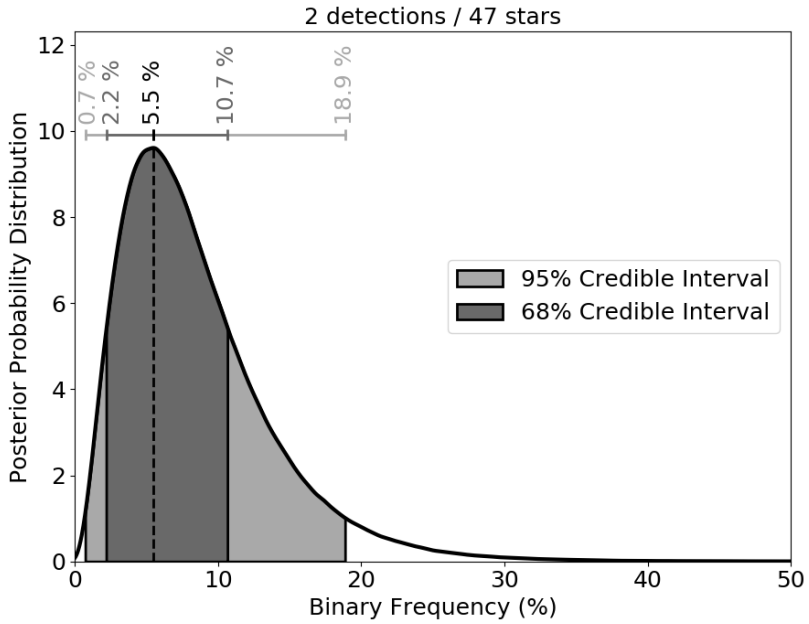

Figure 2.19. Posterior probability distribution of the > 1.5 AU binary frequency of $\geqslant$ T5 brown dwarfs for the combined sample of 47 objects compiled from our program and the surveys in Gelino et al. (2011) and Aberasturi et al. (2014).

in Figure 2.19. We inferred a binary frequency of $f_{\mathrm{T5-Y0}} = 5.5^{+5.2}_{-3.3}(^{+13.4}_{-4.8})$ % at the 1-σ (2-σ) credibility level for the full sample of $\geqslant$ T5 objects on separations 1.5−1000 AU. The peak of the output distribution for f was found to be close to the values obtained for the individual mid and late-T subsets and well within their respective 1-σ credible intervals. The increased sample size and the presence of two binary companions in the final sample provided additional constraints to the MCMC tool, resulting in a sharper output posterior distribution for f and narrower credible intervals than those obtained for the separate samples.

The presence of two companions in the combined sample also allowed us to constrain the parameters describing the separation and mass ratio distributions. The full output from our MCMC analysis is presented in Figure 2.20. The best-fit values for the binary parameters of T5−Y0 brown dwarfs on separations in the range 1.5−1000 AU are: $f_{\mathrm{T5-Y0}} = 5.5^{+5.2}_{-3.3}$%, $\rho_0 = 2.9^{+0.8}_{-1.4}$ AU, $\sigma = 0.21^{+0.14}_{-0.08}$ and $\gamma = 6.1^{+4.0}_{-2.7}$, where the errors correspond to 68% confidence intervals, estimated using the highest density region approach described previously. The power law index γ is the only parameter that was not strongly constrained by the MCMC sampler. While the remaining parameters converged to sharply-defined peaks in

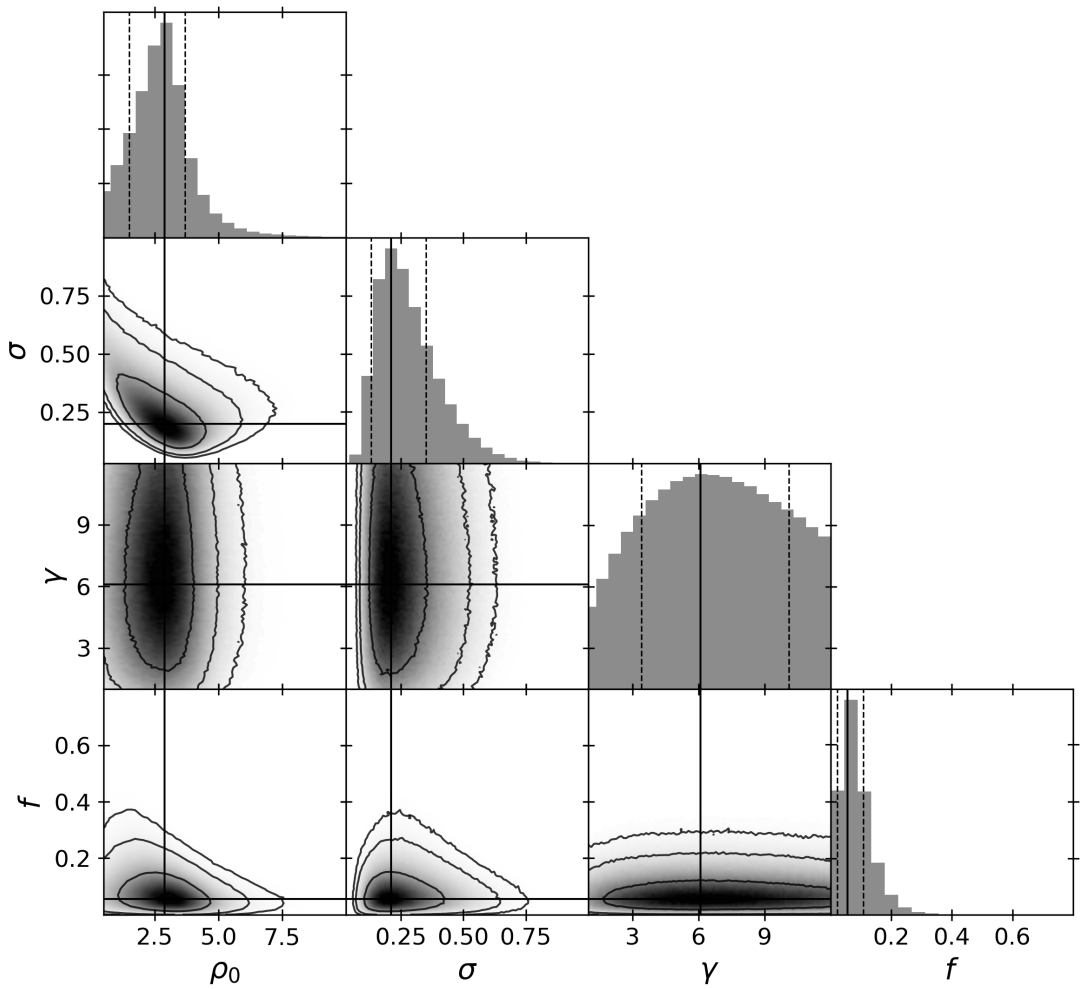

Figure 2.20. Marginalised posterior probability distributions of all binary parameters from our MCMC analysis (diagonal) and correlation among all pairs of parameters (triangle plot). Normalised histograms at the ends of rows are marginalised over all other parameters. In histograms, solid lines show the best-fit values and dashed lines show the 68% (1-σ) credible intervals calculated using a highest density region approach. The black contour lines in the correlation plots correspond to regions containing 68%, 95% and 99% of the posterior.

the posterior distributions, a wider range of possible values was found by the MCMC tool for the power law index, as a result of our attempt to fit a power law through only two data points.

All other MCMC parameters show some covariance in Figure 2.20. In particular, we note that the marginalised posterior distributions for ρ_0 and σ are asymmetric, with ρ_0 having a larger probability density in the lower tail (at values smaller than the best-fit peak value), while σ shows a broader upper tail. This reflects the observational incompleteness at very tight separations and shows that the code successfully attempts to fit a companion population with a significant fraction of unresolved systems. In terms of the correlation between the two parameters, we observe that, as expected, a peak at smaller separations requires a broader width in the lognormal distribution in order to reproduce the observed data. With a best-fit value for ρ_0 at 2.9 AU, our sample is nevertheless found to be more compatible with a peak inside our resolution limits than with a population of preponderantly unresolved systems lying just below the probed separation range. We are sensitive to equal-mass binaries around half of our sample from 1.5 AU and down to $\sim$0.5$-$1 AU for a third of the targets. With resolved binaries at 2.8 AU and 5 AU, respectively, and one unresolved system at 0.93 AU, a peak in separation around $\rho_0 = 0.5-2$ AU should statistically have resulted in the detection of more tightly-bound binaries, which we do not detect despite the achieved sensitivity limits. While this does not exclude the possibility of secondary peak at even smaller separations (e.g. $\sim$0.2 AU), it strongly suggests that we are not seeing the edge of a distribution peaking just outside our completeness region and the resolution limits of direct imaging surveys (typically 1$-$3 AU), as it has been speculated in the literature (e.g. Burgasser et al. 2007).

2.6.2.5 False Negative Analysis and Overall Binary Fraction

Dupuy et al. (2015) found W0146+4234 to be a tight, near-equal mass binary with a projected angular separation of 87.5 ± 2.1 mas, corresponding to a projected physical separation of $0.93^{+0.12}_{-0.16}$ AU. The target was part of the original sample for our *HST* observations but is not resolved in the WFC3 data due to the large plate scale of the IR channel (130 mas pixel^{-1}). As a result, we treated this object as an unresolved single source in our analysis, like all other targets

with no detected companion. We may however use the fact that W0146+4234 is a known binary as a further validation of our results. We can indeed use the posterior distributions from our MCMC analysis to estimate the number of binaries expected to be uncovered or missed within a fixed separation range and check that it is consistent with our observations and additional knowledge of the sample.

We started by estimating the number of companions we expected to detect or miss in our *HST* program in the 2−1000 AU separation range reliably probed by our observations. This was done by selecting 10^5 random walkers and steps from our final MCMC run in Section 2.6.2.4 (Figure 2.20) to draw sets of values for f, ρ_0, σ and γ. This allows for the correlation between the different parameters to be taken into account, which is not possible by drawing values from the marginalised posterior distributions. Following the method implemented in our MCMC tool, we then generated a synthetic population of 10^5 companions based on the drawn ρ_0, σ and γ values. The simulated companions were injected into the detection probability map for our observed sample (see Figure 2.8) to find the probability p_i that each simulated companion would have been retrieved in our data. The probability that a companion remains undetected is then given by $1 - p_i$. As the binary fraction f from the MCMC output was computed from separations of 1.5 AU, this parameter had to be corrected to an equivalent 2−1000 AU binary fraction. The required scaling factor was found by calculating the ratio of the areas under the separation distribution (defined by the drawn ρ_0 and σ values) over the two separation ranges considered (2−1000 and 1.5−1000 AU in this case). We finally used Equation 2.5 with the adjusted binary fraction and the obtained p_i $(1 - p_i)$ values to estimate the number of companions we expected to detect (miss) in our *HST* program from separations of 2 AU.

The obtained results are presented in Table 2.8. We found that for the obtained parameter distributions, a total of ∼0.6 objects out of our 12 targets should be a $>$ 2 AU binary. Taking into account our detection limits, we expected to detect an average of 0.5 systems, and found that we are missing out on less than 0.2 companions. This is consistent with our null detection, suggesting that 0−1 binaries were to be uncovered in our program, and confirms the excellent completeness of our survey on these separations. We then extrapolated our posterior distributions to smaller separations and carried the same analysis for the

Table 2.8. Comparison between predictions from our MCMC output and the observed binary population over various separation ranges. N is the size of the sample considered. The number of companions predicted by the MCMC analysis corresponds to the most likely value and the range given in square brackets represents the 68% confidence interval, using a highest posterior density approach. Cases for which only an upper limit is provided correspond to the 68% highest density region of a one-tail distribution peaking at or near 0.

Sample	N	Separation range	Predictions from MCMC analysis			Observations	
		(AU)	Total expected	Detectable	Undetectable	Detected	Undetected
Observed program	12	0.1−2	0.3 [0.0−0.6]	< 0.1	0.3 [0.0−0.5]	0	$\geqslant 1$
		2−1000	0.6 [0.2−1.2]	0.5 [0.2−1.0]	< 0.2	0	...
T5−Y0 sample	47	0.1−1.5	0.4 [0.0−0.8]	< 0.1	0.3 [0.0−0.7]	0	$\geqslant 1$
		1.5−1000	2.4 [1.2−5.0]	2.2 [1.2−4.5]	0.2 [0.0−0.5]	2	...

separation range 0.1−2 AU, scaling again the drawn binary frequency accordingly. We found that we would have expected up to 0.1 companions to be retrieved at those tight separations for our 12 targets, and that ∼0.3 binaries may remain unresolved (see Table 2.8). This is in good agreement with our null detection at small separations (see Section 2.3.2) and with the presence of the known 0.93 AU binary W0146+4234AB. As we know that W0146+4234 is a binary system and our results do not predict more than 0.3 ± 0.3 companions (68% confidence) in total around our 12 objects within 2 AU, these results suggest that the remaining targets in our sample are unlikely to be binaries.

We performed the same analysis on the combined sample of mid and late-Ts and list our results in Table 2.8. For the full separation range 0.1−1000 AU, the obtained binary parameters predict a total of ∼2.8 binaries among the 47 objects, consistent with the 3 known binaries in the full sample. We found that on the probed separation range (1.5−1000 AU), around 2.4 companions were expected to be retrieved given our sensitivity limits, and around 0.2 likely remain undetected. This is in excellent agreement with the 2 resolved binaries from Gelino et al. (2011) and suggests that we unlikely missed more than 0−1 binaries on these separations. Similarly, at separations < 1.5 AU, less than 0.1 companions were expected to be retrieved, while about ∼0.3 undetected binaries may still lie in the data (Table 2.8). This is again consistent with the lack of detection on these separations and with the presence of the unresolved W0146+4234 binary system at 0.93 AU.

Finally, from this analysis we found a binary rate ranging from 0−4% (68% confidence interval) on the separation range 0.1−1.5 AU for the full sample of 47 targets, with a mean around ∼2%. Assuming that our derived separation and mass ratio distributions hold at such small separations, this brings the overall (0.1−1000 AU separation range) binary fraction of T5−Y0 brown dwarfs to an estimated $f_{\rm tot} = 8 \pm 6\%$ (1-σ level). It is important to emphasise that these values rely entirely on the assumption that the resolved population may be extrapolated onto the unseen part of the parameter space. Looking at separations > 10 AU, we found the wide binary fraction for late-T and Y brown dwarfs to be below ∼1% at the 1-σ level.

2.7 Discussion

2.7.1 The Binary Frequency of Ultracool Brown Dwarfs

Given the broad pixel scale of the WFC3/IR channel and the emerging evidence for preferred tight orbits for late-type binaries (Burgasser et al. 2003, 2006b), we expected $\sim$0$-$2 binaries to be uncovered around the 12 targets probed in our survey. The absence of new discoveries is consistent with the current census for the binary properties of the latest-type brown dwarfs. With the inclusion of additional subsets from Gelino et al. (2011) and Aberasturi et al. (2014), we were able to constrain the binary fraction of $\geqslant$ T8 brown dwarf binaries with separations $>$ 1.5 AU to $f_{\rm T8-Y0} = 5.2^{+7.9}_{-3.9}\%$ at the 1-σ level, placing the first statistically robust constraints to date on the binary frequency of the very coolest ($T_{\rm eff} < 800$ K), lowest-mass (< 40 $M_{\rm Jup}$) known brown dwarfs.

The sample of T5$-$T7.5 brown dwarfs gathered in Section 2.5.2 has a comparable size to the extended $\geqslant$ T8 subset and our statistical analysis uncovered a binary frequency of $f_{\rm T5-T7.5} = 5.2^{+8.7}_{-4.0}\%$ on separations $>$ 1.5 AU at the 1-σ level for this sample. While the results obtained for the mid and late-T samples are statistically consistent, these constraints are based on small number statistics and larger sample sizes are required to confirm and further constrain the substellar multiplicity fraction at such late spectral types. Combining the two samples into a larger $\geqslant$ T5 sample, we were able to more tightly constrain the binary rate of T5$-$Y0 ultracool brown dwarfs at separations of 1.5$-$1000 AU to $f_{\rm T5-Y0} = 5.5^{+5.2}_{-3.3}\%$ at the 1-σ level. Using the outputs of our MCMC analysis, we extrapolated the inferred population distributions down to 0.1 AU to derive an overall binary fraction of $f_{\rm tot} = 8 \pm 6\%$ (1-σ) for T5 to Y0 brown dwarfs.

Our results are consistent with those obtained by Aberasturi et al. (2014) for T5$-$T8.5 objects. For similar population distributions to those used in this work (power law in mass ratio and lognormal in separation) that study set an upper limit on the total binary rate of 17% at the 95% confidence level. This is in good agreement with the 2-σ upper limit ($\sim$20%) derived here for the overall binary rate of $\geqslant$ T5 brown dwarfs at the same confidence level. Opitz et al. (2016) searched for close-in, near-equal mass companions to five Y brown dwarfs (including one

of our science targets, W0713−2917) and found no evidence of binarity down to separations of ∼0.5−1.9 AU. The lack of uncovered binary system in that study is consistent with the binary statistics established here for very late-type T and Y ultracool brown dwarfs.

2.7.2 Decreasing Binary Fraction with Spectral Type

There is evidence that stellar binary pairs with later-type primaries decline in number and have closer separations and more equal mass ratios (Duquennoy & Mayor 1991; Fischer & Marcy 1992; Delfosse et al. 2004; Kouwenhoven et al. 2007; Raghavan et al. 2010). High-resolution imaging surveys in the substellar regime found substantially lower binary rates than in the stellar population, and this decrease of binary fraction with primary mass is also observed to persist throughout the brown dwarf regime. Recent studies probing M field stars (Fischer & Marcy 1992; Bergfors et al. 2010) concluded that M-dwarfs constitute a smooth intermediate stage in binary properties between higher-mass stars and brown dwarfs, and even suggest a trend of decreasing binary fraction with stellar mass within just the M-star spectral range (Janson et al. 2012b). In the substellar regime, Reid et al. (2006) investigated the binary properties of 52 M8−L7.5 ultracool field dwarfs, probing separations down to 1.5 AU, and found an observed binary fraction of 12^{+7}_{-3}%, for an overall, bias-corrected L-dwarf binary frequency of 24^{+6}_{-2}%, assuming a lognormal distribution in separation and a power law in mass ratio. These results are consistent with prior surveys for late-M and L brown dwarfs in the field (15±7% for M8.0−L0.5, Close et al. 2003; 15±5% for M8−L8, Gizis et al. 2003) for separations > 1−3 AU.

Figure 2.21 shows the binary fraction of solar-type stars, low-mass stars and brown dwarfs as a function of spectral type in the Galactic field. While some values in Figure 2.21 only represent an observed binary frequency defined over a certain range of separations or companion masses (open symbols), and may be missing a significant fraction of binaries, the filled symbols are considered to be "overall" binary fractions and clearly highlight the trend of a declining binary rate with spectral type. The separation and mass ratio ranges over which each data point in Figure 2.21 was estimated are plotted in Figure 2.22. Our results (red)

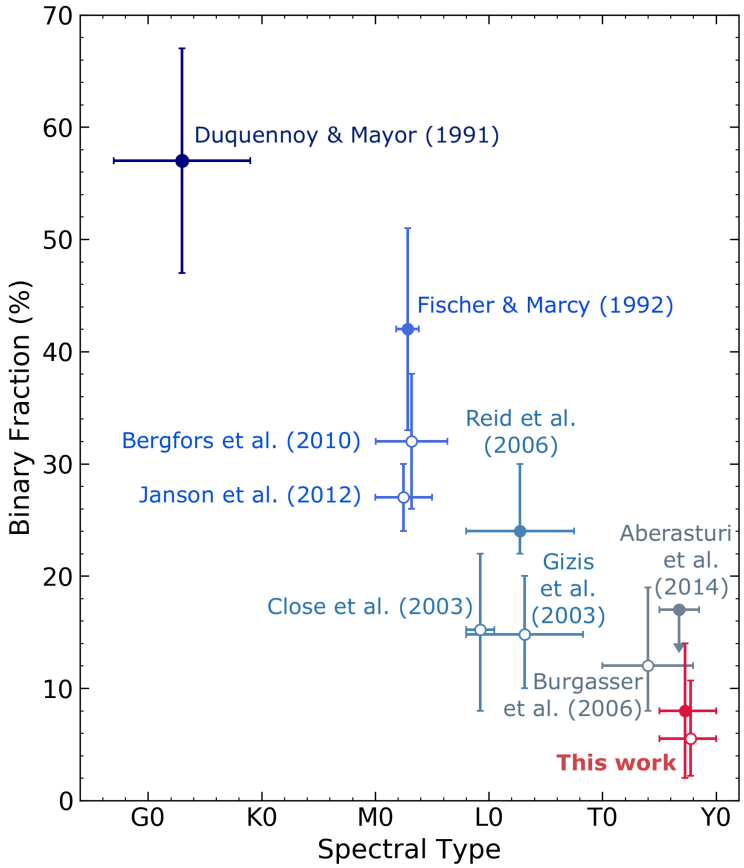

Figure 2.21. Stellar and substellar binary fractions as a function of the spectral type in the Galactic field showing a clear decline in binary frequency with decreasing primary mass. Filled symbols correspond to total binary fractions, estimated over complete ranges of separations and mass ratios. The > 1.5 AU (open symbol) and overall (filled symbol) binary frequencies determined in this work for the T5−Y0 population are shown in red. The data point from Aberasturi et al. (2014) corresponds to the upper limit estimated in that paper for a lognormal distribution in separation and a power law in mass ratio, similar to the distributions considered here. Error bars on binary fractions correspond to 1-σ uncertainties, except for the value from Aberasturi et al. (2014) which corresponds to a 2-σ confidence level (see text). The ranges of separations and mass ratios considered in each survey are plotted in Figure 2.22. Some points were slightly shifted to make the figure clearer.

strongly support the idea that the continuously decreasing binary fraction with decreasing primary mass persists down to the very latest spectral types.

At the lower end of the substellar mass range, Burgasser et al. (2006b) searched for companions to 22 T0−T8 nearby ultracool dwarfs and estimated a bias-corrected binary fraction of 12^{+7}_{-4}% for the observed sample. Of the five binaries detected in that program, we note that two systems were subsequently determined via spectral decomposition to have L-type primary components. As a result, we argue that the strictly-defined T0−T8 binary fraction of that sample (see Figure 2.21) should be lower than the derived value. In addition, only one out of 13 $\geqslant$ T5 targets was identified as a binary, leaving a total of two T0−T4.5 binaries out of seven objects. Although these are small number statistics and are not meaningful without a thorough statistical analysis, this also points towards the idea of a lower binary fraction at later spectral types within the T spectral sequence. Aberasturi et al. (2014) determined total binary fractions of $< 16-25$% (95% confidence level) for T5−T8.5 brown dwarfs, with an upper limit of 17% assuming similar population shapes to those used in this work (lognormal in separation and power law in mass ratio). The uncertainties in the binary fractions from the studies mentioned above were generally defined as Poisson errors, corresponding to 1-σ Gaussian intervals. We must therefore keep in mind that the data point from Aberasturi et al. (2014) in Figure 2.21 is not directly comparable to the other values plotted here and that the 1-σ upper limit for that study resides at a lower value.

In this chapter, we established a binary frequency of $5.5^{+5.2}_{-3.3}$% for the T5−Y0 population on the separation range 1.5−1000 AU. Based on the output of our statistical analysis, we inferred a corresponding overall binary frequency of 8 ± 6% for $\geqslant$ T5 ultracool dwarfs, placing the furthermost points along the spectral type sequence in Figure 2.21. Our results appear to be consistent with the idea of a decreasing substellar binary frequency with spectral type in the Galactic field. The trend seen in the stellar population is thus believed to continue across and throughout the brown dwarf mass regime and to persist all the way down to the lowest-mass and coolest late-T and Y brown dwarfs. The smooth continuity in binary rate points towards a common primary formation mechanism for these populations down to the very lowest masses (Whitworth et al. 2007).

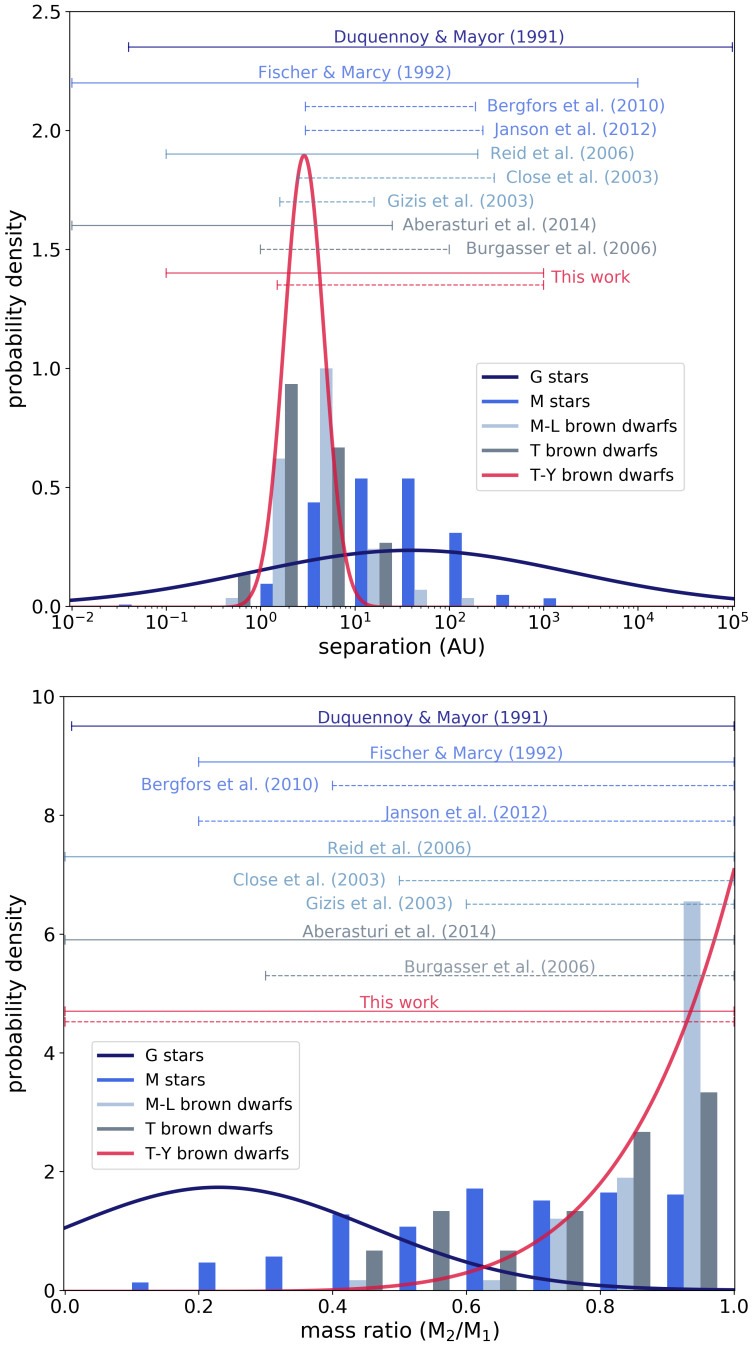

Figure 2.22. Separation (top) and mass ratio (bottom) distributions for companions to stellar and substellar objects, showing the clear shift towards smaller orbital separations and higher mass ratios around lower-mass primaries. The data used to compile the figure are described in the text. The distributions derived in this work for late-T and Y brown dwarfs are shown in red. The horizontal lines show the ranges considered for each of the binary frequencies plotted in Figure 2.21, where the solid lines represent surveys that estimated overall binary fractions.

2.7.3 Companion Separation and Mass Ratio Distributions

With only one binary in the extended sample of T8−Y0 objects, we were not able to place any new constraints on the separation or mass ratio distributions of companions to $\geqslant$ T8 field objects. The only detection (from Gelino et al. 2011) is inside the 100% completeness region of the combined survey (see Figure 2.11). As a result, we cannot distinguish between a truly low binary fraction and population distributions peaking outside the dynamic and resolution ranges covered by the survey. The same is true of the only mid-T binary present in the T5−T7.5 sample, located at a 83% detection probably level for that sample. Combining the two subsets, on the other hand, allowed us to improve the constraints obtained in the individual analyses. From our MCMC run performed for the full sample of 47 objects, we inferred a peak in separation at $\rho_0 = 2.9^{+0.8}_{-1.4}$ AU with a logarithmic width of $\sigma = 0.21^{+0.14}_{-0.08}$, and a power law index of $\gamma = 6.1^{+4.0}_{-2.7}$ for the mass ratio distribution. As discussed in Section 2.6.2.5, these results are perfectly consistent with the presence of the known tight binary, W0146+4234AB, unresolved in our data, and based on our detection limits, suggest that we are unlikely to be missing more than one other binary companion in total for the 47 targets.

The derived parameters for the underlying population distributions are in good agreement with results obtained in previous studies. Numerous surveys have observed changes in the shapes of companion distributions with primary spectral type, with a separation distribution peaking at closer separations and mass ratios shifting towards unity for lower-mass objects. Figure 2.22 shows the separation and mass ratio distributions of companions to Sun-like stars, low-mass stars and brown dwarfs, clearly showing the shift in companion distributions with primary mass. The data for the stars come from the distributions derived in Duquennoy & Mayor (1991) for G-stars and the binaries in Fischer & Marcy (1992), Bergfors et al. (2010) and Janson et al. (2012b) for M-stars. For late-M and L dwarfs, we considered all field systems from the Very Low Mass Binaries Archive[1] with primary masses < 0.1 $M_\odot$. The T-dwarf histogram used data from table 8 in Huélamo et al. (2015) for 15 confirmed T-binaries (see references therein). The T−Y distributions plotted in red correspond to the distributions derived in this work for T5−Y0 brown dwarfs. The horizontal lines show the ranges of

[1] `http://www.vlmbinaries.org`

separations and mass ratios over which the binary fractions in Figure 2.21 were estimated. Studies that estimated an "overall" binary fraction are represented with a solid line (corresponding to the filled symbols in Figure 2.21). As shown in Figure 2.22, the physical and dynamical ranges considered in these surveys cover a sufficiently large part of the $\rho - q$ space to provide what we consider a complete view of the underlying binary population, assuming that the plotted distributions are representative of the true companion populations.

We note that the data for G and M stars in Figure 2.22 contain a mix of semi-major axes and projected separations. Dupuy & Liu (2011) computed conversion factors (a/ρ) between projected separations (ρ) and semi-major axes (a) for Solar-type stars and very low-mass binaries for various cases of discovery biases. The majority of the stellar binaries considered here have separations larger than the inner working angle of the discovery observations. We can thus assume that we are likely in the "no discovery bias" case for these binaries, leading to corresponding conversion factors ranging from $\sim$0.8$-$2. Nevertheless, we argue that this is not a major concern since shifting the separation distributions in Figure 2.22 by such factors would not significantly affect the overall shapes of the distributions in logarithmic space and the results discussed above would still hold. The separation values for the histograms of brown dwarfs, on the other hand, correspond to projected separations only and are directly comparable to our results as we worked in observed projected separation space in the analysis carried in this chapter.

Duquennoy & Mayor (1991) found that companions to Sun-like stars show a broad peak centred around $\sim$30 AU and exhibit a continuous increase towards small secondary masses down to the hydrogen-burning limit (Figure 2.22). Fischer & Marcy (1992) observed a comparably broad distribution around M-stars, with a peak around 3$-$30 AU, at slightly closer separations than G-stars. That study revealed a roughly flat companion mass function (down to the substellar boundary), similar to the field mass function at low masses. In the brown dwarf regime, Reid et al. (2006) derived a lognormal distribution in semi-major axis with a peak at $\sim$6.3 AU and a standard deviation of 0.3 for late-M and L objects. This corresponds to a peak in projected separation (ρ_0) around $\sim$5$-$8 AU, using the conversion factors from Dupuy & Liu (2011) for visual very low-mass binaries. The inferred width of the logarithmic Gaussian represents a much narrower distribution than for stellar primaries, reinforcing the idea of a tighter

binary population in the substellar regime. Reid et al. (2006) report a strong preference for high mass ratios among M and L substellar binaries, with a best-fit of 3.6 ± 1 for the power law index. Studies by Allen (2007) and Burgasser et al. (2007) obtained similar results for M-L-T objects and confirmed the tighter separations and higher mass ratios of brown dwarf binary systems relative to the stellar field population.

In this chapter, we constrained the companion projected separations of T5−Y0 objects to follow a lognormal distribution peaking around 2.9 AU, with a logarithmic width of ∼0.21. The obtained distribution is in very good agreement with the observed projected separations of the known T binaries shown in Figure 2.22, which peak around ∼3 AU. Our results predict a slightly narrower distribution than the T-dwarf histogram in Figure 2.22 due to a couple of wider (> 10 AU) systems present in those data. The power law index derived here for the mass ratio distribution of companions to $\geqslant$ T5 objects is also consistent with the brown dwarf data collected for Figure 2.22. Our results thus confirm the idea of a steady shift towards tighter orbital configurations and more equal mass ratios with decreasing primary mass. The continuous trends in the demographics of binary populations among stars and brown dwarfs further support the hypothesis of a common dominant formation process between the stellar and substellar regimes, extending to the latest-type T and Y brown dwarfs.

2.7.4 Effects of Observational Biases and Incompleteness

We comment on the fact that the survey is biased by the limited sensitivity at the lowest separations and flux ratios. Our results are based on an analysis of the resolved binary population of brown dwarfs, which we extrapolated to the unseen part of the observed parameter space. The presence of a significant number of undetected binaries could therefore result in considerably different companion populations.

For the low primary masses of our observed targets the achieved mass ratio limits correspond to secondary masses of ∼5−10 M_{Jup} for adopted ages of 5 Gyr. Despite an apparent strong preference for near equal-mass configurations (Allen 2007; Burgasser et al. 2007), we cannot exclude the possibility of an undetected

population of very low mass companions, even if a bimodal mass ratio distribution seems unlikely in the current context of formation models. Similarly, the observed peak of the separation distribution for resolved field binaries (∼4 AU; Allen 2007; Burgasser et al. 2007) is close to the resolving limit of our survey, like for most direct imaging programs. It is possible that this observational feature is a direct consequence of the imaging resolution limit rather than a real peak and a significant fraction of very tight binaries could still remain undetected (see Burgasser et al. 2007).

For instance, the close T9+Y0 binary W0146+4234AB discovered by Dupuy et al. (2015) was part of our observed *HST* program but the tight 87.5±2.1 mas angular separation of the system did not allow us to resolve the two components in the obtained images. Our analysis was thus limited and biased by our resolution limits at small separations. While our results proved to be consistent with the presence of the unresolved W0146+4234 binary system in our data, they do not predict many more missing binaries and are not compatible with a significant number of very short-orbit binaries (down to ∼0.5 AU), if such a population exists. We believe that given the completeness level of the survey down to separations of ∼1 AU, the MCMC sampler would have converged towards such a population had it been compatible with our observed data. Despite allowing ρ_0 to take values down to 0.3 AU in our MCMC runs, we found a best-fit value of $2.9^{+0.8}_{-1.4}$ AU at the 68% confidence level, with a sharply-defined peak and no sign of bimodal distribution over the probed range. While these results do not rule out the possibility of a substantial, secondary population of tighter binaries below ∼0.5 AU, they do suggest that the data from our compiled sample of 47 objects is not highly compatible with a separation distribution peaking just outside the resolving limit of imaging programs. We discuss the unresolved binary fraction further in Section 2.7.5.

2.7.5 The Frequency of Unresolved Binaries

Burgasser et al. (2007) suggested that substellar binaries with separations < 3 AU may be as frequent or possibly even more prevalent than currently-known resolved systems. The true peak of the separation distribution for brown dwarf binary pairs could thus lie below the current resolving limit of imaging surveys. A

number of alternative detection methods are available to probe the shortest-orbit binaries, currently unreachable with high angular resolution imaging. Radial velocity measurements, monitoring of astrometric variability and the spectral binary technique are all sensitive to very close separation systems and may provide valuable and robust insights into the unresolved binary fraction.

Bardalez Gagliuffi et al. (2015) found evidence that spectral binary searches are starting to uncover a significant population of tight binaries. Out of a sample of 33 spectral binary candidates, the authors report 3 resolved binaries and 5 known binary systems that remain unresolved, suggesting a high ratio of unresolved-to-resolved binaries among this sample. An accurate measurement of the unresolved binary fraction must take into account the occurrence of successful spectral binary candidacy for the brown dwarf population. For example, Gagliuffi et al. (2014) investigated spectra of 738 objects from the SpeX Prism Library, from which only 35 were retained as spectral binary candidates based on visual or spectral index selection. From these, 14 were found to likely be binaries after spectral fitting. If all final candidates are confirmed, this would lead to a spectral binary rate of only $\sim$2% (14/738), although this method is mainly conceived to retrieve M/L+T binaries.

Likewise, Kellogg et al. (2017) identified 30 out of 420 M, L and T dwarfs as candidate spectral binaries based on spectral index criteria and via spectral fitting. This places an upper limit of $\sim$7% for the binary fraction of this sample. However, as that study is a spectroscopic survey of brown dwarfs with unusual colours, the sample is thus biased towards spectral binaries. The authors also note the possibility of contaminants from highly variable T-dwarfs that may resemble spectral binaries. For example, 2MASS J21392676+0220226 was originally classified as a L8.5+T3.5 binary (Burgasser 2007; Burgasser et al. 2010) but was later identified as a high-amplitude variable by Radigan et al. (2012). Further studies of unbiased samples are thus required to confirm the occurrence of unresolved spectral binaries relative to the resolved binary population.

Sahlmann et al. (2014) searched for astrometric signatures of giant planets around M8$-$L2 dwarfs. The authors derived a binary fraction of $\sim$10% within $\sim$1 AU and placed an upper limit of 9% on the occurrence of planets with masses > 5 M_{Jup} in the separation range 0.01$-$0.8 AU. Given the $\sim$15% resolved binary frequency

of late-M to early-L brown dwarfs (Close et al. 2003), the results from this work could reflect a population of very tight binaries comparable to that of resolved systems. Basri & Reiners (2006) conducted a radial velocity survey targeting mid-M to late-L field dwarfs. This study revealed a binary fraction of ∼11% at separations 0−6 AU, and after accounting for the overlap in separation range between their survey and the direct imaging programs, the authors concluded that their results are consistent with an estimated overall binary rate of ∼20%. For a resolved binary frequency of ∼15% (Close et al. 2003; Gizis et al. 2003) from separations of ∼2−3 AU, this suggests an unresolved binary fraction of ∼5% for M and L dwarfs. Blake et al. (2010) searched for substellar and giant planetary companions to field brown dwarfs and found a rate of $2.5^{+8.6}_{-1.6}$% for < 1 AU binaries among late-M and L objects. In young regions, Joergens (2008) found that the binary fraction of low-mass stars and brown dwarfs within 1 AU is < 10 % and that radial velocity programs do not reveal an excess of companions at closer separations. The authors concluded that direct imaging surveys do not miss a significant fraction of brown dwarf binaries and that the observed decrease in binary frequency with stellar mass is also confirmed at separations < 3 AU.

These results are consistent with those obtained by direct imaging programs in Allen (2007) and Burgasser et al. (2007) for M-L-T dwarfs that estimated binary fractions of 3−4% and 2−3% within 1 AU, respectively, by extrapolating results from the resolved binary population. Extending the outputs of our Bayesian MCMC analysis to the unresolved separation range, we inferred in this chapter a binary fraction at separations < 1.5 AU of ∼2±2% for the full T5−Y0 sample in good agreement with the values cited above. Overall, these results point towards an unresolved binary fraction of about ∼20−60% that of resolved systems, although large discrepancies remain between various surveys and methods. We may therefore regard the observed peak around ∼3−4 AU for substellar binaries as a real feature and conclude that the declining binary frequency with spectral type is not a result of the shrinking separation distribution and observational incompleteness. Further studies with a reliable sensitivity at these small orbital periods will however be required to confirm these results, which are strongly limited by the small statistics of the unresolved substellar binary population currently available.

2.7.6 The Dearth of Wide Binaries in the Field

We note that no wide (> 10 AU separation) binary was uncovered in our observed program or around the targets probed by Gelino et al. (2011) and Aberasturi et al. (2014). From the posterior distributions of our MCMC analysis on the full T5−Y0 sample, we estimated that < 1% of mid-T to Y brown dwarfs are found in binary systems with orbital separation > 10 AU. This is in good agreement with empirical estimates in the literature (e.g. Allen 2007; Burgasser et al. 2007), that agree on a wide binary fraction of ∼1% at separation > 15−20 AU for the M-L-T dwarf field population. While direct imaging provides weak constraints on closely-separated binaries (see Section 2.7.5), imaging surveys typically have very good completeness levels at separations > 10 AU out to hundreds of AU and the lack of wide substellar field binaries is a very robust result.

While probing separations < 10 AU is challenging for young objects due to the large distances to young regions and moving groups, wider separations are accessible for the young substellar population, which may be compared to the observed wide binary population of the field. A number of wide systems with primary masses comparable to our sample have been detected in young (< 15 Myr) regions at separations of 15−800 AU (Taurus, Luhman et al. 2009; Todorov et al. 2010; Ophiuchus, Close et al. 2007; Chamaeleon, Luhman 2004; TW Hydra, Chauvin et al. 2005) and Biller et al. (2011) confirmed the existence of a statistically significant population of very low mass (< 0.1 $M_{\odot}$), wide separation (> 10−100 AU) binaries in > 2 Myr star-forming regions (Upper Sco, Taurus, and Chamaeleon). This presents a conundrum, as this wide population is not found around older (∼few Gyr) field brown dwarfs. Young substellar binary systems show a much broader range of separations than their older, field analogues, with separations spanning 3−4 orders of magnitude and 25% of known companions having orbital separations larger than 20 AU (Burgasser et al. 2006b). Bouy et al. (2006) and Close et al. (2007) claim wide binary fractions of at least 5% in young regions, significantly larger than for field objects. Young binaries also show a flatter mass ratio distribution than observed in the Galactic field, with a statistically significant shortfall in $q > 0.8$ systems (Burgasser et al. 2006b).

Probing star-forming regions facilitates the search for very low-mass objects, which are significantly more luminous at young ages. Nevertheless, the majority of

these systems have secondary masses of $\sim$5$-$25 M_{Jup} that fall within our achieved detection limits ($\sim$2$-$5 M_{Jup} at 1 Gyr, $\sim$5$-$10 M_{Jup} at 5 Gyr and $\sim$8$-$15 M_{Jup} at 10 Gyr). We would therefore most certainly have detected such companions, had they been present around our probed targets. The lack of wide systems in the field agrees with predictions from formation scenarios that only allow very tight systems to survive to field ages (Reipurth & Clarke 2001; Padoan & Nordlund 2004; Goodwin & Whitworth 2007). If dynamical evolution processes are responsible for the depletion of such wide, low-mass binaries in the field population, systems such as those discovered by Liu et al. (2012) may simply be uncommon.

The possibility that most field brown dwarfs were born under different conditions than objects from known young star-forming regions, where wide binaries are prevented from forming (Close et al. 2007), must also be considered, as this may hinder a direct comparison between field and young binary populations. Regions of similar ages but different densities must be probed to determine the effect of natal environment on the subsequent binary rate. Biller et al. (2011) and Todorov et al. (2014) investigated binarity as a function of environment, probing brown dwarfs in Taurus, Chamaeleon and the denser Upper Scorpius association (Preibisch & Mamajek 2008), finding comparable binary fractions between Upper Scorpius and the more diffuse clusters. Similarly, King et al. (2012) investigated the multiplicity of low-mass (> 0.1 $M_{\odot}$) stars across the same clusters and found no obvious trend over a factor of nearly 20 in density, suggesting that, within the density range encompassed by these regions, natal environment does not significantly affect the formation of low-mass binaries. However, Lada & Lada (2003) argued that the field population is mainly dominated by stars that originated from even richer clusters and these results may therefore not be relevant in a direct comparison to field objects.

2.8 Summary

We searched for low-mass companions to 12 nearby brown dwarfs with spectral types of T8 or later using WFC3/IR observations from the *Hubble Space Telescope*. Our observed sample is one of the largest subsets of very late-type,

ultracool ($T_{\rm eff}$ < 800 K) and exclusively low-mass (< 40 $M_{\rm Jup}$) brown dwarfs studied as part of a multiplicity search. We found no evidence for wide binary companions in our survey despite reaching sensitivity limits of 5−10 $M_{\rm Jup}$ or $q \sim$ 0.2−0.4 for ages of 5 Gyr at separations > 0.″5 (3.5−10 AU). PSF subtraction did not reveal the presence of tighter binaries, down to projected separations of ∼0.″1 (0.7−2.5 AU).

From our newly-developed statistical tool based on an MCMC sampling method, we inferred an upper limit on the binary frequency of our observed sample of < 10.7% (1-σ) at separations > 2 AU. Our statistical analysis allows us to marginalise over a range of possible companion population distributions, poorly constrained at the bottom of the substellar mass regime, while taking into account the survey's detection limits to correct for observational biases and incompleteness. Combining our observed program with prior studies, we derived a binary fraction of $f_{\rm T8-Y0} = 5.2^{+7.9}_{-3.9}$% (1-$\sigma$) for the ⩾ T8 substellar population on the separation range 1.5−1000 AU, placing the first statistically robust constraints to date on the binary fraction of T8−Y0 ultracool brown dwarfs. We obtained comparable results for earlier-type T5−T7.5 objects ($f_{\rm T5-T7.5} = 5.2^{+8.7}_{-4.0}$%) and further constrained the binary frequency of T5−Y0 objects to $f_{\rm T5-Y0} = 5.5^{+5.2}_{-3.3}$% (1-$\sigma$) at separations > 1.5 AU.

We derived best-fit values of $\rho_0 = 2.9^{+0.8}_{-1.4}$ AU and $\sigma = 0.21^{+0.14}_{-0.08}$ for the peak and logarithmic width of the lognormal distribution in projected separation, and found a power law index of $\gamma = 6.1^{+4.0}_{-2.7}$ for the mass ratio distribution. These outputs support the idea of tighter and higher mass ratio binary systems for lower-mass primaries. From these results, we were able to estimate the overall (0.1−1000 AU) binary frequency of T5−Y0 brown dwarfs to $f_{\rm tot} = 8 \pm 6$%, with a 2 ± 2% binary rate within 1.5 AU and less than ∼1% beyond 10 AU. Our results are consistent with previous studies and suggest that the decline in binary fraction with decreasing primary mass seen in the field stellar population continues across the substellar boundary, down to the very coolest and lowest-mass known brown dwarfs. The smooth continuity in multiplicity properties and statistics between stars and brown dwarfs is indicative of a common formation channel between the stellar and substellar regimes.

Published in Fontanive et al. 2019, MNRAS, 485, 4967.

3

Massive Close-in Giant Planets and Brown Dwarfs in Binaries

Contents

3.1 Introduction

In the search for analogues to the planets in our own Solar System, exoplanet studies originally firmly excluded known binary systems, despite the fact that about half of Solar-type stars are found in multiple systems (Raghavan et al. 2010). Serendipitous discoveries and subsequent dedicated surveys later revealed that a significant fraction of exoplanets are actually found in binary-star systems (e.g. Patience et al. 2002; Desidera et al. 2004; Mugrauer et al. 2006; Mugrauer & Neuhäuser 2009), mostly with binary separations of at least a few hundred AU. These findings led to numerous studies investigating how stellar binarity affects planet formation and the characteristics and demographics of planetary populations (e.g. Desidera & Barbieri 2007; Eggenberger et al. 2007, 2011; Daemgen et al. 2009; Adams et al. 2012, 2013; Ginski et al. 2012). The dominant results that emerged from these surveys were a strong deficit of binary companions within $\sim$50$-$100 AU for planet hosts (Roell et al. 2012; Bergfors et al. 2013; Wang et al. 2014a,b; Kraus et al. 2016), and the idea that massive short-period planets appear to be preferentially found in multiple-star systems (Zucker & Mazeh 2002; Eggenberger et al. 2004).

These studies, however, focused primarily on systems in which the planet had a mass less than $\sim$4 M_{Jup}. Theoretical calculations (Kratter et al. 2010; Forgan & Rice 2011) and numerical simulations (Stamatellos & Whitworth 2008; Stamatellos 2013; Hall et al. 2017) both suggest that planets that form via disc fragmentation in gravitationally unstable discs (Boss 1997) typically have masses above $\sim$4 M_{Jup}. Therefore the planets in these existing studies probably formed via the standard core accretion scenario (CA; Pollack et al. 1996) – or the newer, more competitive pebble accretion theory (Lambrechts & Johansen 2012, 2014) – rather than via gravitational instability (GI).

When it comes to planets that formed via core accretion, binarity on close separations is generally considered to have a negative influence (see Thebault & Haghighipour 2015 for a review of planet formation in binaries and the issues introduced by the presence of a close binary companion). Theoretical studies have concluded that close stellar companions can hinder planet formation by stirring up protoplanetary discs (e.g. Mayer et al. 2005), tidally truncating the discs (e.g.

Pichardo et al. 2005; Kraus et al. 2012), or leading to the ejection of planets (Kaib et al. 2013; Zuckerman 2014). More compact, truncated discs generally have just enough mass left to form a low-mass Jovian planet (Jang-Condell et al. 2008), and planet formation is then further complicated by the very short lifetime ($\lesssim$1 Myr) of these truncated discs (Kraus et al. 2012).

On the other hand, Batygin et al. (2011) and Rafikov (2013) predict that stellar companions should have little influence on planetesimal growth. It has also been proposed that the presence of an outer companion could raise spiral arms in protoplanetary discs, creating regions of high gas and particle densities, favourable for planetesimal formation (Youdin & Goodman 2005) and pebble accretion (Johansen et al. 2007; Lambrechts & Johansen 2014). For example, the spiral arm structures observed in the disc around HD 100453 (Wagner et al. 2015) may be due to perturbations from the M-dwarf companion (Dong et al. 2016), located at 120 AU from the primary and originally reported by Chen et al. (2006). Similarly, the asymmetric disc of HD 141569 is attributed to the stellar companions in this triple system (Augereau & Papaloizou 2004). In the "Friends of hot Jupiters" series of papers, Knutson et al. (2014), Piskorz et al. (2015) and Ngo et al. (2015, 2016) found a binary fraction 3 times higher for hosts to hot Jupiters (mostly up to $\sim$4 M_{Jup}) than for field stars on separations of 50$-$2000 AU, and concluded that wide binary systems may either facilitate the formation of Jovian planets, or help the inward migration of planets formed at wider separations.

It has also been suggested that binary companions could induce the inward migration of planets through secular interactions such as the Kozai-Lidov mechanism (Kozai 1962; Lidov 1962). In this scenario, an outer companion with a large mutual inclination between the planetary and binary orbits can excite large periodic oscillations of the eccentricity and inclination of the planet. Tidal interactions between the planet and its host star can then drive the planet onto a final orbit with a very small orbital separation when compared to its initial location (e.g. Fabrycky & Tremaine 2007; Naoz et al. 2012; Petrovich 2015). In particular, the Kozai-Lidov migration process has been proposed to explain the high obliquities often observed in hot Jupiters, although recent studies indicate that this mechanism can only account for about 20$-$30% of the observed hot Jupiter population (Naoz et al. 2012; Ngo et al. 2016). Similarly, it has been suggested (Rice et al. 2015) that Kozai-Lidov oscillations could drive planetary-

mass bodies that form on wide orbits via GI onto short-period orbits. Since disc fragmentation preferentially forms massive planets or brown dwarfs (Stamatellos & Whitworth 2008; Kratter et al. 2010; Forgan & Rice 2011), such a process would tend to be associated with more massive planets or brown dwarfs.

Although the true influence of binarity on planet formation and evolution is still unclear, systems hosting planets with masses up to a few Jupiter masses have been extensively surveyed. In contrast, systems with more massive planets (> 4 M_{Jup}), and objects within the brown dwarf mass regime, have yet to be studied in detail in the context of stellar multiplicity. Zucker & Mazeh (2002) were the first to point out that massive (> 4 M_{Jup}) short-period planets tend to be predominantly found orbiting one component of a multiple-star system and possess distinctive characteristics compared to planets orbiting single stars (Eggenberger et al. 2004).

Such massive planetary and substellar companions are very challenging to form at small separations. Giant planet formation, whether by CA or GI, is thought to occur preferentially in the relatively cool outer regions of protoplanetary discs, from a few AU for CA (Pollack et al. 1996), to several tens of AU for GI (Rafikov 2005). Massive hot Jupiters are thus expected to have formed at wide orbital separations from their host stars, where the lower temperatures in the protoplanetary disc allow for planet formation to proceed (Bell et al. 1997), or to be born under very different conditions than currently encompassed by most planet formation models. Recently, Schlaufman (2018) found evidence for two distinct populations of close-in giant planets, with a suggestion of a transition between CA and GI companions occurring at around $\sim$4$-$10 M_{Jup}. This is consistent with both semi-analytic (Kratter et al. 2010; Forgan & Rice 2011) and numerical simulations (Stamatellos & Whitworth 2008; Stamatellos 2013; Hall et al. 2017) which suggest that objects that form via GI have masses above $\sim$3$-$5 M_{Jup}, and might indicate that these more massive close-in planets formed by GI rather than via CA.

In this chapter, we aim to constrain the multiplicity statistics of hosts to the most massive giant planets (> 7 M_{Jup}) and brown dwarfs found within $\sim$1 AU, in order to investigate the role of binarity in the formation or evolution of these systems. This will allow us to assess if a wide binary companion could be responsible for the observed orbital configurations of these objects, which are both scarce

and challenging to explain with current formation theories. Our investigation will provide an indication of whether the Kozai-Lidov mechanism could play a role in the origin of the most massive short-period gas giant planets and brown dwarfs. This study will also help us determine if these massive companions are an extension of the population of lower-mass, CA giant planets, or if they belong to a separate population formed through a distinct mechanism (i.e. GI on wide orbits, followed by inward migration; Nayakshin 2010; Rice et al. 2015). In particular, we will explore the binary properties of hosts to members of the "brown dwarf desert" (Marcy & Butler 2000), depicting the significant deficit of brown dwarf companions found within a few AU around Sun-like stars (e.g. Grether & Lineweaver 2006; Ma & Ge 2014).

In Section 3.2, we present our selected sample of targets. Section 3.3 describes the direct imaging observations acquired for this project and the data reduction. In Section 3.4, we detail our search for wide companions, using past imaging surveys found in the literature to complement our new direct imaging data, as well as the *Gaia* Data Release 2 (DR2; Gaia Collaboration et al. 2016, 2018b) catalogue. Section 3.6 describes our approach to the statistical analysis of our survey, and we present our results in Section 3.7. Finally, we discuss our interpretation of the obtained results in Section 3.8 and summarise the main results of our project in Section 3.9.

3.2 Sample Selection

The aim of this project is to search for wide, substellar or stellar companions to stars hosting a massive planet or brown dwarf on a very short orbit. Recent findings suggest that GI forms planets with masses larger than $\sim$4 M_{Jup} (Stamatellos 2013; Stamatellos & Herczeg 2015; Hall et al. 2017), and the transition between CA and GI companions is thought to occur around $\sim$4$-$10 M_{Jup} (Schlaufman 2018). Studies of core accretion populations found that CA rarely forms planets with masses larger than $\sim$5 M_{Jup} (Matsuo et al. 2007; Mordasini 2018), and shows a steep drop and a strong metallicity dependence in the formation of higher-mass planets (Mordasini et al. 2012; Jenkins et al. 2017). In order to investigate the higher-mass planetary population, which likely

formed by disc GI rather than through CA, we choose for this survey a lower limit on inner companion mass M_2 of 7 M_{Jup}, based on the studies mentioned above. This allows us to avoid the main region of overlap between CA and GI, while keeping a sufficiently large sample size for our study. We place an upper limit of 70 M_{Jup} (the hydrogen-burning limit) on the mass (or projected mass) of the inner companions, so as to limit our sample to likely substellar objects.

We place an upper limit of $P < 400$ days (about 1 AU around a Sun-like star) on the orbital period of the close-in companions. It is now well-accepted that if planet formation via GI does occur, it typically takes place in the outer regions (> 30 AU) of protostellar discs (Rafikov 2005; Clarke & Lodato 2009; Rice & Armitage 2009). This thus ensures that all selected companions have undergone significant migration between their expected GI formation location and their current observed configurations, or that they had to be formed under considerably different natal environments than for standard planet formation in order to be born *in-situ*. We set an upper limit of 500 pc on the distances of our targets in order to be sensitive to wide companions from 50−100 AU around most stars in our sample. We use the distance estimates from Bailer-Jones et al. (2018) to infer distances for our targets. These distances are derived from the highly-precise parallax measurements provided by the *Gaia* DR2 catalogue, correcting for the nonlinearity of the transformation between parallax and distance. Finally, we only consider stellar primaries and place a lower limit on the host's mass of $M_* > 0.1$ $M_\odot$.

Based on the arguments presented above, we selected all systems from the NASA Exoplanet Archive[1], the Exoplanet Data Explorer[2] and the Extrasolar Planets Encyclopaedia[3] with confirmed transiting or radial velocity companions with well-constrained orbits that satisfy the following criteria:

- inner companion mass M_2 (or $M_2 \sin i$) between 7−70 M_{Jup}.
- inner companion orbital period $P < 400$ days.
- distance within 500 pc based on *Gaia* DR2 parallax.
- primary mass $M_* > 0.1$ $M_\odot$.

[1] `https://exoplanetarchive.ipac.caltech.edu`
[2] `http://exoplanets.org`
[3] `www.exoplanet.eu`

Our final sample consists of 38 objects, and includes some very short period ($P < 10$ days) transiting systems, together with radial velocity objects extending to larger separations. Properties of the inner companions are presented in Table 3.1 and the host stars are listed in Table 3.2. We selected our sample without regard to the targets' multiplicity, known or unknown. However, radial velocity and transit surveys are typically biased against binaries, excluding known multiple systems in target selection processes. As these biases are difficult to quantify and account for, our obtained results may somewhat underestimate the multiplicity rate of the population probed here, but we consider that our study is in no way biased towards the presence of wide companions.

About three quarters of the selected systems were discovered and characterised via radial velocity measurements. Mass estimates for companions discovered through this method only allow for the determination of a lower limit on the companion mass due to the unknown inclination i of the system. Radial velocity systems are therefore expected to be more massive than the estimated $M_2 \sin i$ as a result of the projection factor. Selected systems discovered via this method are thus likely to be more massive than the minimum masses reported in Table 3.1. Given the projected masses of these companions and assuming a uniform distribution of inclinations between 0 and 90 degrees, we can easily show with a Monte-Carlo approach that an average of 72% of the radial velocity systems considered here are statistically likely to be above the deuterium burning limit at 13 M_{Jup}. Combining this with our transiting systems, this means that more than ∼60% of our targets are likely in the brown dwarf mass regime, and close to 80% of our sample is expected to have a true mass > 10 M_{Jup}. We therefore consider that our gathered sample of objects is representative of the population of the most massive planets found on tight orbits and provides a robust insight into short-period brown dwarf desert members.

We define in Table 3.1 a tidal circularisation timescale $\tau_{\rm circ}$ for each planet and brown dwarf companion in our sample, given in $\log_{10}$[yr]. We estimate this parameter using the formalism presented in Rice et al. (2012), which is based on that developed by Eggleton et al. (1998) (see also Mardling & Lin 2002 and Dobbs-Dixon et al. 2004). We assume that the star has a tidal quality factor of $Q'_* = 5{\times}10^6$ and the planet has a tidal quality factor of $Q'_p = 10^5$. We take the star mass, planet mass, orbital semi-major axis, and orbital eccentricity from Tables

Table 3.1. Orbital properties of the planets considered.

Planet ID	$N_{\rm p}$	P (days)	a (AU)	M_2 ($M_{\rm Jup}$)	$M_2 \sin i$ ($M_{\rm Jup}$)	e	$\tau_{\rm circ}$ ($\log_{10}$[yr])	Ref.
4 UMa b	1	269.30 ± 1.96	0.87 ± 0.04	...	7.1 ± 1.6	0.432 ± 0.024	16.4	Döllinger et al. (2007)
11 Com b	1	326.03 ± 0.32	1.29 ± 0.05	...	19.4 ± 1.5	0.231 ± 0.005	15.9	Liu et al. (2008)
30 Ari B b	1	335.1 ± 2.5	0.995 ± 0.012	...	9.88 ± 0.94	0.289 ± 0.092	16.7	Guenther et al. (2009)
59 Dra b	1	28.44 ± 0.01	0.2	...	25	0.20 ± 0.01	12.5	Galland et al. (2006)
70 Vir b	1	116.6884 ± 0.0044	0.484 ± 0.028	...	7.49 ± 0.61	0.4007 ± 0.0035	14.5	Butler et al. (2006)
τ Gem b	1	305.5 ± 0.1	1.17	...	20.6	0.031 ± 0.009	15.6	Mitchell et al. (2013)
υ And c	4	240.9402 ± 0.047	0.8259 ± 0.0043	$13.98^{+2.3}_{-5.3}$	1.96 ± 0.05	0.245 ± 0.006	15.9	McArthur et al. (2010)
AS 205A b	1	24.84 ± 0.03	0.162 ± 0.04	...	19.25 ± 1.96	0.34 ± 0.06	11.9	Almeida et al. (2017)
BD+24 4697 b	1	145.081 ± 0.016	0.50 ± 0.08	...	53 ± 3	0.50048 ± 0.00043	14.9	Wilson et al. (2016)
CI Tau b	1	8.9891 ± 0.0202	0.079	12.29 ± 2.13	8.08 ± 1.53	0.28 ± 0.16	10.2	Johns-Krull et al. (2016)
EPIC 219388192 b	1	5.292569 ± 0.000026	0.0593 ± 0.0029	36.84 ± 0.97	...	0.1929 ± 0.0019	9.4	Nowak et al. (2017)
HAT-P-2 b	1	5.6334729 ± 0.0000061	0.06878 ± 0.00068	9.09 ± 0.24	...	0.5171 ± 0.0033	8.5	Pál et al. (2010)
HAT-P-20 b	1	2.875317 ± 0.000004	0.0361 ± 0.0005	7.246 ± 0.187	...	0.015 ± 0.005	8.3	Bakos et al. (2011)
HD 5891 b	1	177.11 ± 0.32	0.76 ± 0.02	...	7.6 ± 0.4	0.066 ± 0.022	16.4	Johnson et al. (2011)
HD 33564 b	1	388 ± 3	1.1	...	9.1	0.34 ± 0.02	16.8	Galland et al. (2005)
HD 39392 b	1	$394.3^{+1.4}_{-1.2}$	1.08 ± 0.03	...	13.2 ± 0.8	0.394 ± 0.008	16.9	Wilson et al. (2016)
HD 41004 B b	1	1.328300 ± 0.000012	0.0177	...	18.37 ± 0.22	0.081 ± 0.012	8.0	Zucker et al. (2004)
HD 77065 b	1	119.1135 ± 0.0026	0.438 ± 0.013	...	41 ± 2	0.69397 ± 0.00036	13.3	Wilson et al. (2016)
HD 87646 A b	2	13.481 ± 0.001	0.117 ± 0.003	...	12.4 ± 0.7	0.05 ± 0.02	11.4	Ma et al. (2016)
HD 89744 b	1	256.78 ± 0.05	0.918 ± 0.010	...	8.44 ± 0.23	0.673 ± 0.007	14.7	Wittenmyer et al. (2009)
HD 104985 b	1	199.505 ± 0.085	0.95	...	8.3	0.090 ± 0.009	16.8	Sato et al. (2008)
HD 112410 b	1	124.6	0.565	...	9.18	0.23	16.1	Jones et al. (2013)
HD 114762 b	1	83.9151 ± 0.0030	0.353 ± 0.001	...	10.98 ± 0.09	0.3354 ± 0.0048	14.2	Kane et al. (2011a)
HD 134113 b	1	201.680 ± 0.004	0.638 ± 0.010	...	47^{+2}_{-3}	0.891 ± 0.002	11.2	Wilson et al. (2016)
HD 156279 b	1	131.05 ± 0.54	0.495 ± 0.017	...	9.71 ± 0.66	0.708 ± 0.018	12.9	Díaz et al. (2012)

Table 3.1. (Continued.)

Planet ID	$N_{\rm p}$	P (days)	a (AU)	M_2 ($M_{\rm Jup}$)	$M_2 \sin i$ ($M_{\rm Jup}$)	e	$\tau_{\rm circ}$ ($\log_{10}$[yr])	Ref.
HD 156846 b	1	359.5546 ± 0.0071	1.096 ± 0.021	...	10.57 ± 0.29	0.84785 ± 0.00050	13.1	Kane et al. (2011b)
HD 160508 b	1	178.9049 ± 0.0074	0.68 ± 0.02	...	48 ± 3	0.5967 ± 0.0009	14.5	Wilson et al. (2016)
HD 162020 b	1	8.428198 ± 0.000056	0.0751 ± 0.0043	...	14.4 ± 2.1	0.277 ± 0.002	10.2	Udry et al. (2002)
HD 168443 b	2	58.1112 ± 0.0009	0.290 ± 0.005	...	7.48 ± 0.27	0.530 ± 0.001	12.6	Udry et al. (2002)
HD 178911 B b	1	71.484 ± 0.002	0.339 ± 0.006	...	7.03 ± 0.28	0.114 ± 0.003	14.4	Wittenmyer et al. (2009)
HD 180314 b	1	396.03 ± 0.62	$1.34^{+0.02}_{-0.08}$	...	$20.3^{+0.6}_{-2.4}$	0.257 ± 0.010	15.8	Sato et al. (2010)
HD 203949 b	1	184.2 ± 0.5	0.81 ± 0.03	...	8.2 ± 0.2	0.02 ± 0.03	15.5	Jones et al. (2014)
KELT-1 b	1	1.217514 ± 0.000015	0.02466 ± 0.00016	$27.23^{+0.50}_{-0.48}$	...	$0.0099^{+0.0100}_{-0.0069}$	8.0	Siverd et al. (2012)
Kepler-13 A b	1	1.763588 ± 0.000001	0.03641 ± 0.00087	9.28 ± 0.16	...	0.00064 ± 0.00015	8.0	Esteves et al. (2015)
NLTT 41135 b	1	2.889475 ± 0.000025	0.024 ± 0.001	$33.7^{+2.8}_{-2.6}$	...	< 0.02	8.8	Irwin et al. (2010)
WASP-14 b	1	$2.24376524 \pm 0.00000044$	0.0371 ± 0.0011	7.76 ± 0.47	...	0.0830 ± 0.0030	8.1	Wong et al. (2015)
WASP-18 b	1	$0.94145299 \pm 0.00000087$	0.02026 ± 0.00068	10.30 ± 0.69	...	0.0092 ± 0.0028	8.0	Hellier et al. (2009)
XO-3 b	1	3.1915239 ± 0.0000068	0.04540 ± 0.00082	11.79 ± 0.59	...	0.260 ± 0.017	8.4	Winn et al. (2008)

Notes. $N_{\rm p}$ is the number of known planets in the system. Tidal circularisation timescales were calculated in this paper (see text). All other parameters come from the given references and references therein.

Table 3.2. Stellar properties for the selected systems.

Object ID	RA (J2000)	Dec. (J2000)	SpT	V (mag)	Distance (pc)	[Fe/H] (dex)	M_* ($M_\odot$)	Age (Gyr)	Ref.	Other name
4 UMa	08:40:12.82	+64:19:40.6	K1 III	4.787 ± 0.005	73.5 ± 1.2	-0.25 ± 0.04	1.234 ± 0.15	4.6 ± 2.0	(1)	HD 73108
11 Com b	12:20:43.03	+17:47:34.3	G8 III	4.74 ± 0.02	93.2 ± 1.9	-0.31 ± 0.02	2.02 ± 0.11	1.17 ± 0.28	(2)	HD 107383
30 Ari B	02:36:57.74	+24:38:53.0	F6 V	7.020 ± 0.011	44.7 ± 0.1	$+0.245 \pm 0.195$	1.16 ± 0.04	0.91 ± 0.83	(3)	HD 16232
59 Dra	19:09:09.88	+76:33:37.8	A9 V	5.107 ± 0.009	27.4 ± 0.1	$+0.016$	1.447 ± 0.015	0.436 ± 0.200	(4)	HD 180777
70 Vir	13:28:25.81	+13:46:43.6	G5 V	5.045 ± 0.009	17.9 ± 0.1	-0.012	1.07 ± 0.01	8.1 ± 0.4	(5,6)	HD 117176
τ Gem	07:11:08.37	+30:14:42.6	K2 III	4.42	112.5 ± 4.1	$+0.14 \pm 0.10$	2.3 ± 0.3	1.22 ± 0.76	(7)	HD 54719
υ And	01:36:47.84	+41:24:19.6	F8 V	4.10 ± 0.05	13.4 ± 0.1	$+0.131 \pm 0.067$	1.31 ± 0.02	3.12 ± 0.22	(8)	HD 9826
AS 205A	16:11:31.34	−18:38:26.0	K5 V	12.63 ± 0.21	127.5 ± 1.6	-0.043 ± 0.060	1.086 ± 0.100	0.001	(9)	V866 Sco
BD+24 4697	23:01:39.32	+25:47:16.5	K2 V	9.847 ± 0.022	44.7 ± 0.3	-0.16 ± 0.03	0.754 ± 0.016	5.207 ± 4.150	(2)	HIP 113698
CI Tau	04:33:52.01	+22:50:30.1	K7 V	13.80	158.0 ± 1.2	-0.727 ± 0.050	0.80 ± 0.02	0.002	(10)	
EPIC 219388192	19:17:34.03	−16:52:17.8	G V	12.535 ± 0.020	305.0 ± 4.6	$+0.03$	1.01 ± 0.04	$3.6^{+1.8}_{-1.5}$	(11)	
HAT-P-2	16:20:36.36	+41:02:53.1	F8 V	8.743 ± 0.013	127.8 ± 0.5	$+0.14 \pm 0.08$	1.36 ± 0.04	2.6 ± 0.5	(12)	HD 147506
HAT-P-20	07:27:39.95	+24:20:11.5	K3 V	11.346 ± 0.030	71.0 ± 0.2	$+0.35 \pm 0.08$	0.756 ± 0.028	$6.7^{+5.7}_{-3.8}$	(13)	
HD 5891	01:00:33.19	+20:17:33.0	G5 III	8.11 ± 0.01	283.5 ± 4.9	$+0.13 \pm 0.08$	1.242 ± 0.041	$1.0^{+0.8}_{-0.5}$	(14)	HIP 4715
HD 33564	05:22:33.53	+79:13:52.1	F6 V	5.140 ± 0.009	21.0 ± 0.1	-0.12	1.25 ± 0.04	$3.0^{+0.6}_{-0.3}$	(15)	HIP 25110
HD 39392	05:53:19.00	+22:04:19.7	F8 V	8.449 ± 0.013	102.5 ± 0.7	-0.54 ± 0.01	0.94 ± 0.04	9.06 ± 1.40	(2)	HIP 27828
HD 41004 B	05:59:49.65	−48:14:22.9	M2 V	12.63	41.6 ± 0.5	$+0.10$	0.4	1.6	(16)	HIP 28393
HD 77065	09:00:47.45	+21:27:13.4	G5 V	8.786 ± 0.021	32.7 ± 0.1	-0.42 ± 0.02	0.71 ± 0.01	7.59 ± 3.69	(2)	HIP 44259
HD 87646 A	10:06:40.77	+17:53:42.4	G1 IV	8.143 ± 0.013	137.1 ± 15.6	-0.17 ± 0.08	1.12 ± 0.09	4.75 ± 1.1	(17,18)	HIP 49522
HD 89744	10:22:10.56	+41:13:46.3	F7 V	5.782 ± 0.009	38.6 ± 0.1	$+0.26 \pm 0.03$	1.558 ± 0.048	2.50 ± 0.30	(6,19)	HIP 50786
HD 104985	12:05:15.12	+76:54:20.6	G8.5 III	5.785 ± 0.009	100.6 ± 0.7	-0.15	1.2 ± 0.1	4.9 ± 1.2	(6,20)	HIP 58952
HD 112410	12:57:31.96	−65:38:47.3	G8 III	6.86 ± 0.01	156.5 ± 0.7	-0.28 ± 0.05	1.21 ± 0.25	4.17 ± 2.34	(21)	HIP 63242
HD 114762	13:12:19.74	+17:31:01.6	F9 V	7.361 ± 0.013	40.2 ± 0.4	-0.774 ± 0.030	0.83 ± 0.01	12.4 ± 0.6	(6,22)	HIP 64426
HD 134113	15:07:46.50	+08:52:47.2	F9 V	8.339 ± 0.018	72.2 ± 0.4	-0.92 ± 0.02	0.85 ± 0.02	10.98 ± 0.66	(2)	HIP 74033
HD 156279	17:12:23.20	+63:21:07.5	K0 V	8.167 ± 0.013	36.2 ± 0.1	$+0.14 \pm 0.01$	0.93 ± 0.02	7.40 ± 2.20	(6,23)	HIP 84171

Table 3.2. (Continued.)

Object ID	RA (J2000)	Dec. (J2000)	SpT	V (mag)	Distance (pc)	[Fe/H] (dex)	M_* ($M_\odot$)	Age (Gyr)	Ref.	Other name
HD 156846	17:20:34.31	−19:20:01.5	G1 V	6.564 ± 0.010	47.7 ± 0.1	$+0.18 \pm 0.02$	1.38 ± 0.05	2.78 ± 0.37	(2,21)	HIP 84856
HD 160508	17:39:12.70	+26:45:27.1	F8 V	8.177 ± 0.012	111.6 ± 0.8	-0.16 ± 0.02	1.14 ± 0.04	5.55 ± 0.57	(2)	HIP 86394
HD 162020	17:50:38.36	−40:19:06.1	K3 V	9.227 ± 0.022	30.8 ± 0.1	$+0.01 \pm 0.11$	0.75 ± 0.01	3.10 ± 2.70	(6,24)	HIP 87330
HD 168443	18:20:03.93	−09:35:44.6	G6 V	7.000 ± 0.011	39.6 ± 0.1	$+0.06 \pm 0.05$	1.02 ± 0.01	10.00 ± 0.30	(6,25)	HIP 89844
HD 178911 B	19:09:04.39	+34:36:01.6	G5 V	7.494 ± 0.010	41.0 ± 0.1	$+0.34 \pm 0.03$	1.03 ± 0.02	4.80 ± 1.30	(6,19)	HIP 94075
HD 180314	19:14:50.21	+31:51:37.3	K0 III	6.721 ± 0.010	122.4 ± 0.5	$+0.24 \pm 0.07$	2.13 ± 0.13	1.14 ± 0.24	(2)	HIP 94576
HD 203949	21:26:22.87	−37:49:46.0	K2 III	5.620 ± 0.009	78.6 ± 0.8	$+0.28 \pm 0.06$	1.99 ± 0.10	1.23 ± 0.19	(21)	HIP 105854
KELT-1	00:01:26.92	+39:23:01.8	F5 V	10.701 ± 0.057	268.4 ± 3.0	-0.85	1.335 ± 0.063	1.75 ± 0.25	(26)	
Kepler-13 A	19:07:53.15	+46:52:05.9	A5 V	10.349 ± 0.037	473.3 ± 18.3	-0.50 ± 0.10	1.72 ± 0.10	1.12 ± 0.10	(27,28)	KOI-13
NLTT 41135	15:46:04.26	+04:41:30.0	M5.1 V	18	34.1 ± 0.1	-0.5	0.164 ± 0.020	5	(29)	
WASP-14	14:33:06.36	+21:53:41.0	F5 V	9.798 ± 0.026	162.0 ± 0.8	-0.13 ± 0.08	1.35 ± 0.12	$2.4^{+1.5}_{-1.0}$	(30,31)	
WASP-18	01:37:25.03	−45:40:40.4	F6 IV/V	9.357 ± 0.018	123.5 ± 0.4	$+0.00 \pm 0.09$	1.20 ± 0.01	0.90 ± 0.20	(6,32)	HD 10069
XO-3	04:21:52.71	+57:49:01.9	F5 V	9.904 ± 0.027	213.1 ± 2.7	-0.177 ± 0.080	1.213 ± 0.066	$2.82^{+0.58}_{-0.82}$	(33)	

Notes. Distances are based on the estimates from Bailer-Jones et al. (2018) derived from *Gaia* DR2 parallax measurements. All other parameters come from the given references and references therein.

References: (1) Döllinger et al. (2007); (2) Maldonado & Villaver (2017); (3) Guenther et al. (2009); (4) Jones et al. (2015); (5) Butler et al. (2006); (6) Bonfanti et al. (2016); (7) Mitchell et al. (2013); (8) McArthur et al. (2010); (9) Almeida et al. (2017); (10) Guilloteau et al. (2014); (11) Nowak et al. (2017); (12) Pál et al. (2010); (13) Bakos et al. (2011); (14) Johnson et al. (2011); (15) Galland et al. (2005); (16) Santos et al. (2002); (17) Aguilera-Gómez et al. (2018); (18) Ma et al. (2016); (19) Wittenmyer et al. (2009); (20) Sato et al. (2008); (21) Jofré et al. (2015); (22) Kane et al. (2011a); (23) Díaz et al. (2012); (24) Udry et al. (2002); (25) Wittenmyer et al. (2007); (26) Siverd et al. (2012); (27) Morton et al. (2016); (28) Shporer et al. (2014) (29) Irwin et al. (2010); (30) Southworth (2012); (31) Knutson et al. (2014); (32) Hellier et al. (2009); (33) Winn et al. (2008).

3.1 and 3.2. We assume that the star has a rotation period of 20 days and that the planet is rotating synchronously. We estimate the circularisation timescale by simply evolving each system for a short period of time and determining the resulting change in eccentricity (i.e., $\tau_{\rm circ} = e/\dot{e}$).

Petrovich (2015) found that planets migrating via the Kozai-Lidov mechanism (Kozai 1962; Lidov 1962), under the influence of a distant companion, spend most of their lifetimes undergoing eccentric oscillations at separations > 2 AU, or as hot Jupiters at < 0.1 AU. All the inner companions considered here have orbital separations smaller than 1 AU. If they migrated from wider separations to their current locations through the Kozai-Lidov scenario, they should be able to circularise onto hot Jupiter orbits fairly rapidly. Inner companions with circularisation timescales longer than the age of the Universe are thus unlikely to be driven by secular perturbations such as the Kozai-Lidov mechanism. On the other hand, objects with timescales smaller than the age of the Universe (i.e., less than $\sim$10.2 in $\log_{10}$[yr]) could have migrated inwards via the Kozai-Lidov scenario. A total of 12 targets have tidal circularisation timescales shorter than that and may thus be consistent with a Kozai-Lidov migration process. The subset of Kozai-consistent objects corresponds to all the inner companions in our sample with an orbital period shorter than 10 days. This is in good agreement with the idea that planets migrating via the Kozai-Lidov mechanism spend most of their lifetime around their initial, wide separations, or on hot Jupiter orbits, as discussed in Petrovich (2015).

3.3 New Observations

3.3.1 Observations and Data Reduction

We used direct imaging facilities at the Very Large Telescope (VLT), Gemini North and the WIYN Observatory to acquire data for six objects in the sample presented in Section 3.2, four of which did not have any previously reported direct imaging observations. Our new observations are summarised in Table 3.3.

Table 3.3. Summary of our new observations.

Target	Observation Date	Telescope / Instrument	Filter	Field of View	Pixel Scale	Previous Observations
WASP-18	September 4, 2017	VLT/NACO	L'	$28'' \times 28''$	$0''.027$	Ngo et al. (2015)
HD 162020	September 6, 2017	VLT/NACO	L'	$28'' \times 28''$	$0''.027$	Eggenberger et al. (2007)
BD+24 4697	September 6, 2017	Gemini North/NIRI	Ks	$22'' \times 22''$	$0''.022$	–
HD 77065	December 12, 2017	Gemini North/NIRI	Ks	$22'' \times 22''$	$0''.022$	–
HD 134113	June 22, 2018	WIYN/NESSI	562, 832	$4.6'' \times 4.6''$	$0''.040$	–
HD 160508	June 24, 2018	WIYN/NESSI	562, 832	$4.6'' \times 4.6''$	$0''.040$	–

3.3.1.1 VLT / NACO Observations

We obtained images in the L' filter (3.8 μm) using the AO-assisted imager NACO at VLT (Lenzen et al. 2003; Rousset et al. 2003) for HD 162020 and WASP-18 (programme 099.C-0728, PI Fontanive). These new data were acquired with the aim to confirm or refute a candidate reported in Eggenberger et al. (2007) around the former target, and to achieve deeper detection limits than in currently available imaging data of the latter object (Ngo et al. 2015; see Appendix 3.A). The observing setup included the L27 camera, and the data were taken in the pupil tracking mode, where the telescope pupil is held fixed, and the field rotates. Each target was observed using a three-point dither pattern, designed to avoid a bad quadrant of the NACO detector. We used short integration time (0.2 s) in order not to saturate the primaries, allowing photometric and astrometric calibrations.

Standard near-infrared data reduction techniques were applied using our custom IDL routines, including sky subtraction, flat-fielding and bad-pixel correction. Some of the frames were affected by the horizontal additive noise pattern, that sporadically appeared in the NACO data, and was variable in intensity and time. The pattern was removed following the procedure described in Hußmann et al. (2012). Individual frames were de-rotated according to the parallactic angle, and finally stacked together. We retrieved in our final images the unconfirmed candidate companion around HD 162020 reported by Eggenberger et al. (2007) and were able to refute the bound nature of this source based on our new data. The detailed analysis of the rejected candidate is presented in Section 3.3.3. No companion was detected around WASP-18 within the field of view of our images.

3.3.1.2 Gemini North / NIRI Observations

We acquired images in K_s band (1.95−2.30 μm) using the Gemini Near-Infrared Imager (NIRI; Hodapp et al. 2003) instrument at the Gemini North telescope for BD+24 4697 and HD 77065 (programme GN-2017B-Q-40, PI Fontanive). Targets were observed in the standard imaging mode, using the Gemini North adaptive optics (AO) system ALTAIR (Herriot et al. 2000) to obtain diffraction-limited images with the f/32 camera. Both our target were bright enough to be used

as natural guide stars. The observing strategy adopted was similar to the one described in Lafrenière et al. (2008) and Daemgen et al. (2015). Each target was observed at five dither positions to allow for sky subtraction and bad pixel correction. At each dither position we acquired one non-saturated short exposure (divided into many coadds) in high read noise mode, followed by a longer exposure in low read noise mode. This prevents our observations from being limited by the high read out noise, resulting in a high observing efficiency and a large dynamic range, providing sensitivity at both small and large separations. Our targets were not saturated, even in the deeper exposures.

We followed standard procedures for near-infrared data reduction, using the Gemini NIRI IRAF package and our dedicated IDL routines. A sky frame was constructed by taking the median of the dithered images, masking the regions dominated by the target's signal. The individual images were then sky-subtracted and divided by a normalised flat field, and bad pixels were replaced by a median calculated over their good neighbours. For all images, field distortion was corrected as described in Lafrenière et al. (2014). No candidate companion was identified around either target.

3.3.1.3 WIYN / NESSI Observations

We acquired observations of HD 160508 and HD 134113 with the WIYN 3.5-m telescope at Kitt Peak National Observatory (KPNO). We used the NASA-NSF Exoplanet Observational Research (NN-Explore) Exoplanet and Stellar Speckle Imager (NESSI) in diffraction-limited speckle imaging mode. NESSI is based on an upgraded design of the Differential Speckle Survey Instrument (DSSI; Horch et al. 2009, 2012). Each target was observed simultaneously in two cameras, with a filter centered on 562 nm (r-narrow) on the blue channel and a bandpass at 832 nm (z-narrow) on the red channel. The standard NESSI observing strategy was followed, with typical integration times of 40 ms (see Scott et al. 2018). Data were reduced by the KPNO speckle reduction pipeline that generates reconstructed images and contrast limit curves for each observation (Scott et al. 2018). We did not identify any candidate companion in the obtained data around these two targets.

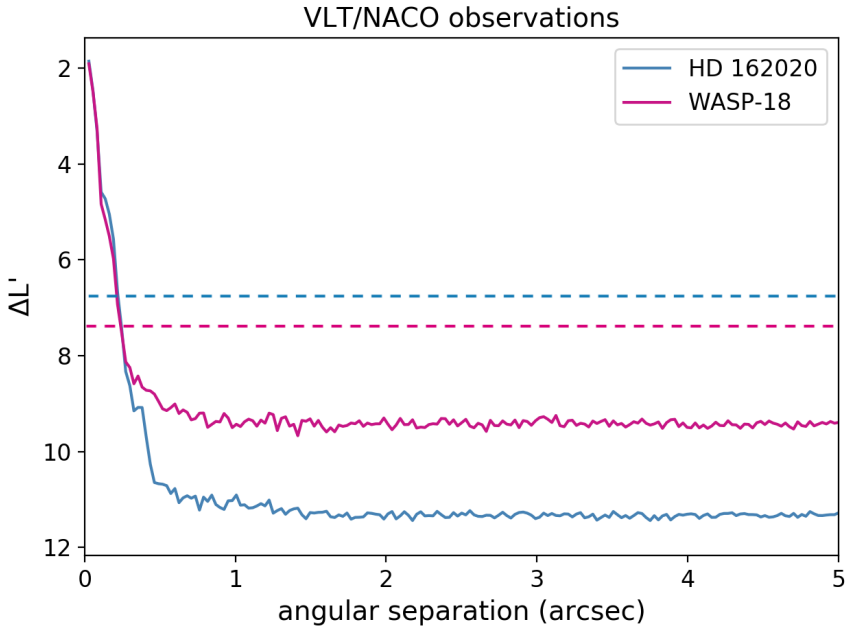

]

Figure 3.1. Achieved sensitivities showing the 5-σ magnitude differences in L' as a function of angular separation for our two targets observed with VLT/NACO. The dashed lines indicate the magnitude differences corresponding to the hydrogen-burning limit for each target.

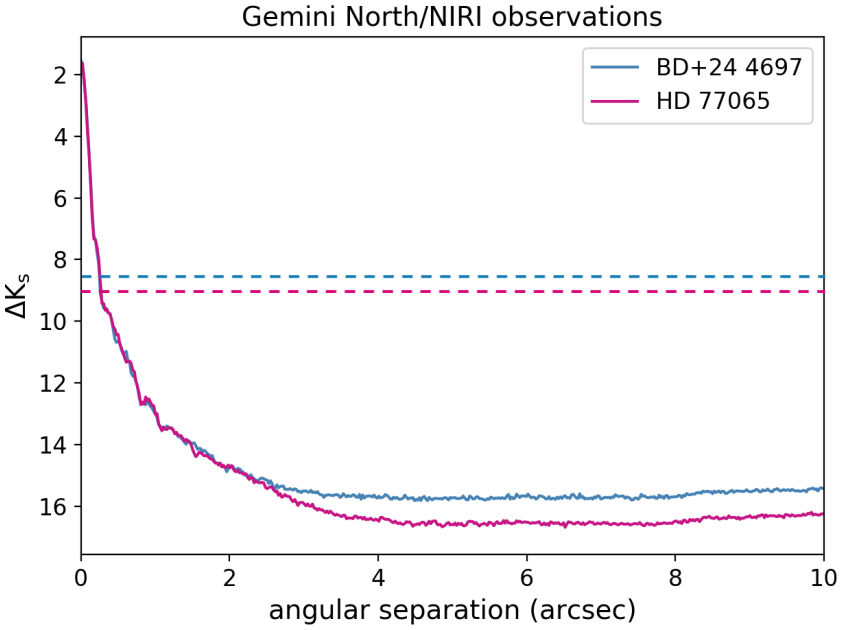

Figure 3.2. 5-σ magnitude differences achieved in K_s for our two targets observed with Gemini North/NIRI, showing the corresponding hydrogen-burning limits (dashed lines).

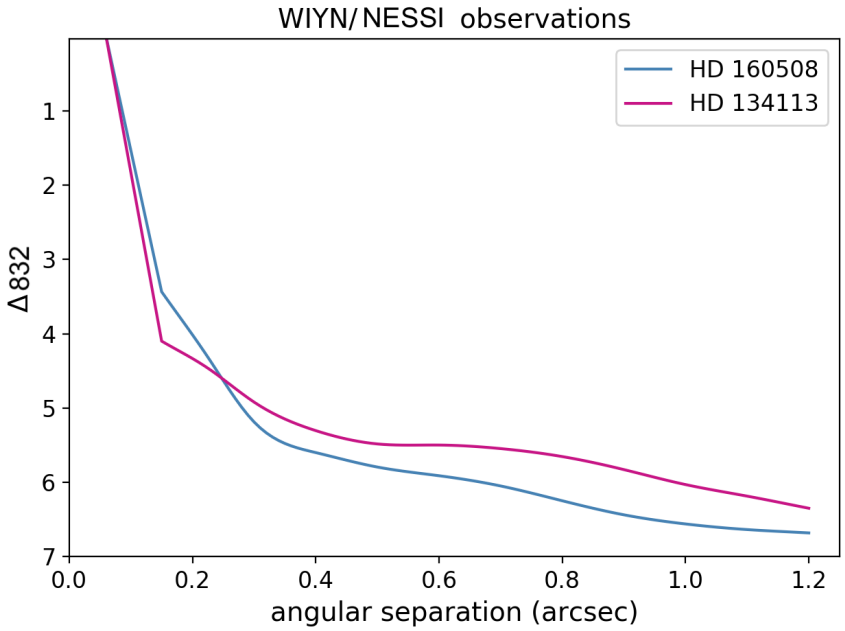

Figure 3.3. 5-σ magnitude differences achieved in the 832 nm filter for our two targets observed with WIYN/NESSI. These observations do not reach the hydrogen-burning limit.

3.3.2 Achieved Sensitivities

We estimated the limiting sensitivities reached around our observed targets in order to establish the full range of detectable companions covered by the obtained data. For the VLT/NACO and Gemini North/NIRI data, detection limits were determined from the final images described above. The 5-σ noise curves were calculated as a function of radius by computing the standard deviation in circular annuli with 1-pixel widths, centred on the primary targets. Noise levels were then converted into magnitude contrasts by dividing by the peak pixel values of the targets (which were not saturated), and converting the obtained flux ratios into magnitude differences in the considered filters. The contrast curves generated from the custom KPNO pipeline in the 832 nm filter were considered for the WIYN data, as the redder filter is better suited for the detection of warm, low-mass companions.

The achieved magnitude contrasts are presented in Figures 3.1, 3.2 and 3.3 for our NACO, NIRI and NESSI observations, respectively. The hydrogen-burning

limits are shown for the first two data sets, showing that we are sensitive to substellar companions around these stars. We did not reach the stellar/substellar boundary in the WIYN observations and are only able to detect low-mass stellar companions in these data.

3.3.3 Refuted Candidate around HD 162020

HD 162020 had previously been observed with NACO as part of the survey conducted in Eggenberger et al. (2007). Eggenberger et al. (2007) reported two point sources within $5''$ from the star, one of which was found by the authors to clearly be a background source. They found that the second candidate, at $4\farcs98 \pm 0\farcs03$, was more likely unbound than bound, although the low significance level of this result led them to report the companionship of this candidate as inconclusive based on their data alone. Both sources are retrieved in our new NACO images (Section 3.3). The positions of the detected sources were extracted using the StarFinder PSF-fitting algorithm (Diolaiti et al. 2000), employing an empirical PSF extracted from the primary.

To calibrate the pixel scale and the True North (TN) of the detector, we used the astrometric calibrator system θ_1 Orionis C, observed on October 6 2017. Using the same procedure as described in Chauvin et al. (2012), we obtain the pixel scale of 27.10 ± 0.05 mas, and the TN position of -0.45 ± 0.10 deg. However, as previously pointed out by Eggenberger et al. (2007) and Chauvin et al. (2012), additional systematic errors might be present in the determination of the TN of the NACO detector in a case where different sets of calibrator stars were used between the epochs. Since we do not know which calibrators were used to derive astrometry in the previous epochs by Eggenberger et al. (2007), we add 0.5 deg to the TN error budget (G. Chauvin, priv. comm.).

With a baseline larger than a decade between the observations used in Eggenberger et al. (2007) and ours, and given the proper motion of the primary from *Gaia* DR2, we were able to refute the bound nature of this companion. Figure 3.4 shows the relative positions of the primary and candidate at the various epochs available, together with the expected motion of a background object. The plot clearly demonstrates that the candidate does not share common

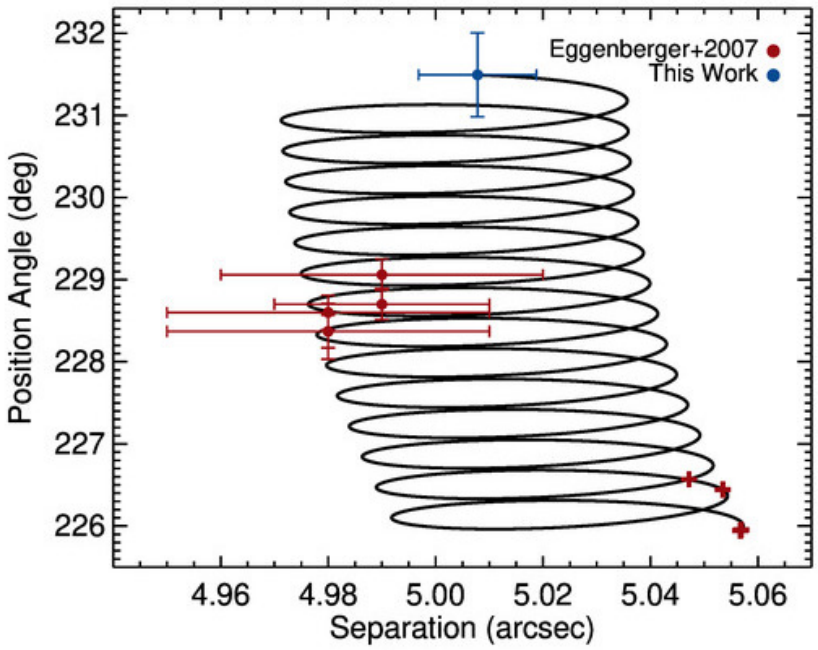

Figure 3.4. Common proper motion analysis of the faint candidate around HD 162020, originally identified by Eggenberger et al. (2007). The black solid line represents the motion of a background object relative to the primary, computed using the proper motion and parallax measurements of HD 162020 from *Gaia* DR2. The blue and red circles mark the relative positions of the components in our new NACO observations and in the data from Eggenberger et al. (2007), respectively. The red crosses indicate the expected positions of a background source at the dates of the observations used by Eggenberger et al. (2007). The relative motion of the candidate over the available epochs is not consistent with a comoving pair.

proper motion with the primary. The fact that the relative positions at the old epochs of observation are not consistent with the primary, nor with the expected background positions, suggests that the source has a non-negligible proper motion of its own.

3.4 Search for Wide Companions

We searched for wide companions to the 38 systems from our core sample using our new data and published direct imaging observations, as well as the *Gaia* DR2 catalogue. A total of 16 objects were found to have at least one wide stellar or substellar companion confirmed to be comoving, listed in Table 3.4. Another 7

Table 3.4. Confirmed common proper motion systems.

System	Separation		Comp.	SpT	Photometry	Mass	G	GDR2 ϖ	GDR2 $\mu_\alpha*$	GDR2 μ_δ	References
	($''$)	(AU)			(mag)	($M_\odot$)	(mag)	(mas)	(mas yr^{-1})	(mas yr^{-1})	
11 Com	9.1	850	**A**	G8 III	V=4.8	2.02	4.37	10.71 ± 0.22	-109.24 ± 0.32	88.17 ± 0.28	CCDM; WDS
			B	...	V=12.9	*0.7*	12.2	9.56 ± 0.05	-108.09 ± 0.08	89.64 ± 0.05	
30 Ari	0.536	22	**B**	F8 V	V=7.1,i=6.9	1.16	6.96	22.36 ± 0.05	141.41 ± 0.08	-10.68 ± 0.09	B-C: Riddle et al. (2015)
			C	M1 V	i=11.2	0.5	...	...	...	...	
	38.2	1520	A	F5 V	V=6.5	1.32	6.38	22.13 ± 0.07	136.86 ± 0.14	-15.19 ± 0.14	A-BC: Guenther et al. (2009)
τ Gem	1.9	187	**A**	K2 III	V=4.5	2.3	3.95	8.88 ± 0.32	-31.49 ± 0.49	-48.28 ± 0.43	CCDM; WDS; *this work*
			B	K0 V	V=11	0.8	9.42	...	...	...	
υ And	55	750	**A**	F8 V	J=3.2	1.31	3.90	74.57 ± 0.35	-172.25 ± 0.52	-382.90 ± 0.54	Lowrance et al. (2002)
			B	M4.5 V	J=9.4	0.2	12.51	74.21 ± 0.09	-172.08 ± 0.13	-383.90 ± 0.14	
AS 205	1.3	166	**A**	K5 V	J=8.1	1.086	12.37	7.82 ± 0.10	-7.45 ± 0.20	-26.89 ± 0.14	A-BC: Ghez et al. (1993)
			BC	K7+M0 V	J=9.2	0.22	13.40	6.38 ± 0.19	-9.48 ± 0.47	-23.17 ± 0.43	B-C: Eisner et al. (2005)
HAT-P-20	6.86	500	**A**	K3 V	J=9.3	0.756	10.99	14.05 ± 0.04	-4.99 ± 0.07	-96.23 ± 0.06	WDS; Bakos et al. (2011)
			B	M V	J=10.2	*0.57*	12.80	...	...	...	
HD 41004	0.54	23	**B**	M2 V	Hp=12.5	0.4	...	...	...	...	Zucker et al. (2003); Hip-Tyc
			A	K1 V	Hp=8.8	0.7	8.38	24.04 ± 0.26	-41.52 ± 0.48	59.65 ± 0.56	
HD 87646	0.26	20	**A**	G1 IV	Hp=8.3	1.12	7.93	7.40 ± 0.78	-82.88 ± 1.55	-27.08 ± 1.35	Ma et al. (2016); Hip-Tyc
			B	K V	Hp=11.0	0.6	...	...	...	...	
HD 89744	63	2460	**A**	F7 V	J=4.9	1.558	5.59	25.85 ± 0.07	-120.57 ± 0.11	-138.14 ± 0.13	Mugrauer et al. (2004)
			B	L0 V	J=14.9	0.08	19.66	25.96 ± 0.95	-119.93 ± 0.98	-140.08 ± 1.07	

Table 3.4. (Continued.)

System	Separation		Comp.	SpT	Photometry	Mass	G	ϖ	$\mu_\alpha*$	μ_δ	References
	($''$)	(AU)			(mag)	($M_\odot$)	(mag)	(mas)	(mas yr^{-1})	(mas yr^{-1})	
HD 114762	3.2	140	**A**	F9 V	J=6.2	0.83	7.14	24.86 ± 0.27	-586.29 ± 0.71	2.26 ± 0.24	Patience et al. (2002)
			B	M9 V	J=13.8	0.09	...	...	...	...	
HD 156846	5.1	250	**A**	G1 V	J=5.5	1.38	6.36	20.92 ± 0.05	-137.10 ± 0.10	-143.20 ± 0.07	Tamuz et al. (2008); WDS
			B	M4 V	J=9.4	0.59	12.19	21.43 ± 0.42	-129.62 ± 0.70	-132.84 ± 0.58	
HD 178911	16.1	790	**B**	G5 V	Hp=8.3	1.03	7.87	24.38 ± 0.03	57.18 ± 0.04	195.90 ± 0.05	AC-B: Hip-Tyc
			AC	G1+K1 V	Hp=6.8	1.9	6.57	20.23 ± 0.38	76.62 ± 0.69	207.13 ± 0.66	A-C: McAlister et al. (1987)
Kepler-13	1.15	610	**A**	A5 V	V=10.35	1.72	10.55	2.09 ± 0.08	-3.95 ± 0.18	-15.05 ± 0.26	A-BC: Szabó et al. (2011)
			BC	A+G V	V=10.48	1.68	10.37	1.91 ± 0.11	-4.40 ± 0.19	-15.78 ± 0.24	B-C: Santerne et al. (2012)
NLTT 41135	2.4	55	**B**	M5.1 V	z=13.1	0.164	14.94	29.27 ± 0.12	162.51 ± 0.18	-282.72 ± 0.18	Irwin et al. (2010)
			A	M4.2 V	z=12.4	0.21	13.97	29.11 ± 0.16	153.67 ± 0.24	-281.98 ± 0.24	
WASP-14	1.45	300	**A**	F5 V	J=8.9	1.35	9.65	6.14 ± 0.03	29.24 ± 0.06	-6.95 ± 0.06	A-B: Ngo et al. (2015)
			B	...	J=14.1	0.33	...	...	...	...	
	11.5	1900	C	*K5 V*	...	*0.280*	17.32	6.08 ± 0.10	27.97 ± 0.20	-6.15 ± 0.18	AB-C: *This work.*
WASP-18	26.7	3300	**A**	F6 IV/V	V=9.3	1.20	9.17	8.07 ± 0.02	25.24 ± 0.03	20.60 ± 0.03	*This work*
			B	*M7.5 V*	...	*0.092*	20.92	9.43 ± 1.52	23.65 ± 1.98	18.38 ± 2.40	

Notes. The top component of each system (marked in bold) is the planet host considered in the sample studied here. Spectral types and masses in italic were derived in this work. G-magnitudes, parallaxes and proper motions come from the *Gaia* DR2 catalogue.
CCDM: Catalog of Components of Double and Multiple stars, Dommanget & Nys (2000).
GDR2: *Gaia* Data Release 2, Gaia Collaboration et al. (2018b).
Hip-Tyc: The *Hipparcos* and Tycho Catalogues, ESA (1997).
WDS: the Washington Double Star Catalog, Mason et al. (2001).

Table 3.5. Candidate binary companions.

System	Comp.	SpT	Photometry	Mass	Separation		Prob.	Companionship	References
			(mag)	($M_\odot$)	($''$)	(AU)	(%)		
70 Vir	**A**	G5 V	$I = 3.98, J = 3.80$	1.07	–	–	–	–	
	B	> M5 V	$\Delta I = 11.4 \pm 1.2$	*0.08*	2.86	52	99.67	likely bound	Roberts et al. (2011)
	C	L V	$J = 15.84 \pm 0.16$	*0.07*	42.7	848	76.91	inconclusive	Pinfield et al. (2006)
EPIC 219388192	**A**	G V	$H = 10.734, K = 10.666$	1.01	–	–	–	–	
	B	M V	$\Delta K = 2.24$	0.52	0.082	24	99.99	likely bound	Curtis et al. (priv. com.)
	C	> M8 V	$\Delta H = 7.087 \pm 0.032$	< 0.1	5.988	1769	14.33	likely background	Nowak et al. (2017)
	D	> M8 V	$\Delta H = 7.663 \pm 0.057$	< 0.1	7.538	2224	4.65	likely background	Nowak et al. (2017)
HD 89744	**A**	F7 V	$I = 5.2$	1.558	–	–	–	–	
	C	...	$\Delta I = 13 \pm 2$	*0.08*	5.62	219	99.17	likely bound	Roberts et al. (2011)
KELT-1	**A**	F5 V	$H = 9.534 \pm 0.030, K = 9.437 \pm 0.019$	1.335	–	–	–	–	
	B	M4-5 V	$\Delta H = 5.90 \pm 0.10, \Delta K = 5.59 \pm 0.12$	*0.2*	0.588	154	99.95	likely bound	Siverd et al. (2012)

Notes. The top component of each system (marked in bold) is the planet host considered here.

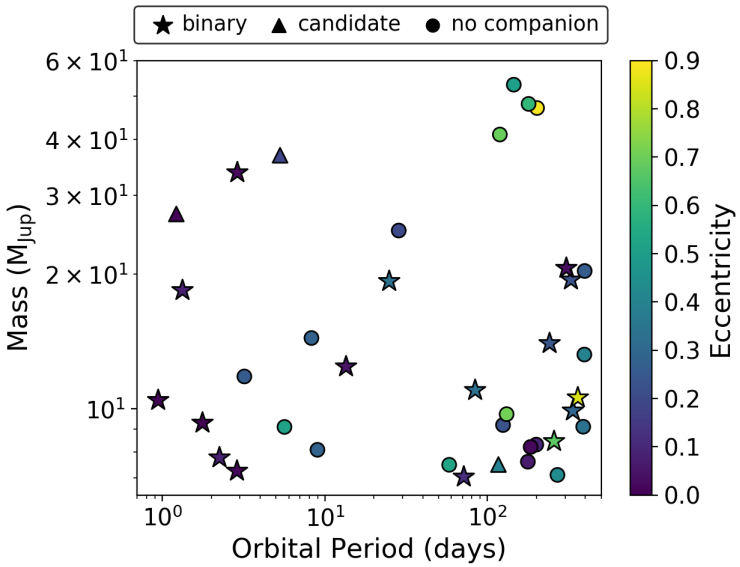

Figure 3.5. Orbital properties of the inner companions in our sample showing the systems that are known to be binaries or higher-order multiples (stars), those with a candidate companion (triangles) and stars that are apparently single (circles).

candidate companions are reported in the literature around 4 of our targets and are presented in Table 3.5. One of the targets with a reported candidate is already a confirmed wide binary (HD 89744). Figure 3.5 displays the properties of the inner planets and brown dwarfs, showing the positions in the planet period-mass space of confirmed binaries (star symbols), targets with a candidate companion (triangles) and apparently single objects (circles). In Figure 3.6 we present the architecture of each identified hierarchical system, plotting the semi-major axes of the inner companions in blue and the projected separations of detected wide binary components in red, with symbol sizes proportional to the planetary masses and binary mass ratios, respectively.

3.4.1 Literature Search and Imaging Surveys

We conducted an extensive literature search to compile available observations of all objects in our sample and gather existing knowledge about the multiplicity of our targets. We present our findings for each individual target in Appendix 3.A, providing detailed information about every companion, candidate or confirmed, reported around our targets in imaging surveys or catalogues, as well as null

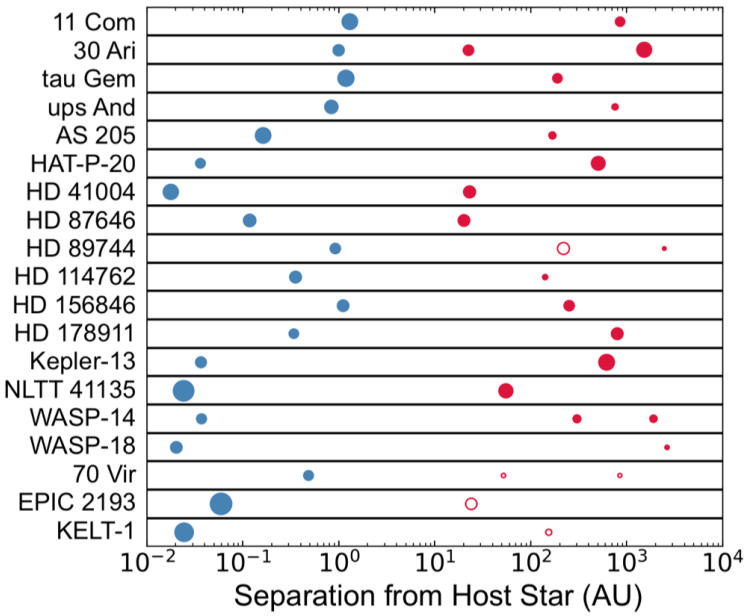

Figure 3.6. Architecture of all binary or higher-order multiple systems found in our sample, following the order of the targets shown in Tables 3.4 and 3.5. The blue circles represent the inner brown dwarfs and planets, with symbol sizes proportional to their masses. Red circles show the positions of all known confirmed (filled symbols) and candidate (open symbols) wide companions, with radii proportional to the mass ratios of these outer companions to the planet hosts. Separations of inner companions correspond to semi-major axes, while observed projected separations are displayed for the wide binary companions.

detections. A total of 30 targets are mentioned in the literature in the context of a search for wide companions (with or without detections), to which we add 4 of our 6 observed targets that had no previously reported observations (Table 3.3).

Of these 34 objects, we found 21 targets with reported detections in the literature. Among those, 15 are confirmed bound systems (11 Com AB, 30 Ari ABC, τ Gem AB, υ And AB, AS 205 ABC, HAT-P-20 AB, HD 41004 AB, HD 87646 AB, HD 89744 AB, HD 114762 AB, HD 156846 AB, HD 178911 ABC, Kepler-13 AB, NLTT 41135 AB and WASP-14 AB), which we detail in Appendix 3.A.1. 14 of these binaries or higher-order multiple were demonstrated to form physical pairs in the literature and we confirm the true companionship of the τ Gem AB system in this work (see Figure 3.20 in Appendix 3.A.1). We list all confirmed multiples in Table 3.4. Three of these systems, HD 87646, HD 41004 and HD 178911, were

identified as binaries in the Tycho-*Hipparcos* catalogues, and our planet-host stars correspond to the fainter component of the binary for the latter two systems.

The remaining 6 targets are mentioned to have unconfirmed candidate companions and are discussed in Appendices 3.A.2 and 3.A.3. We discarded the 3 point sources reported by Moutou et al. (2017) around HD 168443, which are highly likely to be background contaminants given the crowded galactic latitude of the target (Moutou et al. 2017; see discussion of HD 168443 in Appendix 3.A.3). In Section 3.3.3, we showed that the faint candidate reported around HD 162020 by Eggenberger et al. (2007) does not share common proper motion with the primary and thus rejected this candidate. We were also able to refute the candidate companion reported around XO-3 by Bergfors et al. (2013) and Wöllert & Brandner (2015) based on the inconsistent parallax and proper motion of this source and XO-3 in *Gaia* DR2. This leaves 3 targets with unconfirmed candidates, namely, 70 Vir (two candidates), EPIC 219388192 (three candidates) and KELT-1 (one candidate). A candidate companion is also reported by Roberts et al. (2011) around HD 89744, already known to be a confirmed wide binary (Mugrauer et al. 2004). These final 7 candidate companions retained for this study are presented in Table 3.5.

We are not able to make any clear statement on the physical association of these candidates based on the available data. We can however make a statistical argument on the chance of finding an unrelated background source at close angular separation from the primaries. For each source, we used the Trilegal galaxy models (Vanhollebeke et al. 2009) to calculate a probability of the observed candidates being true companions. This was done by estimating the surface density ρ of background sources expected to be found within $30'$ from the primary targets, given the galactic latitude and longitude of the objects and the depth and wavelength of the obtained observations. From Brandner et al. (2000), the probability $P(\Theta, m)$ of detecting one or more background stars within an angular separation Θ (in arcsec) and down to a limiting magnitude m is then given by:

$$P(\Theta, m) = 1 - e^{-\pi\Theta^2 \rho(m)}. \tag{3.1}$$

The probability of an observed candidate being physically associated to the primary is then given by the complement of the chance of alignment, that is,

$1-P(\Theta, m)$. The resulting probabilities are listed in Table 3.5 for each candidate. The two faint candidates identified beyond $7''$ from EPIC 219388192 by Nowak et al. (2017) were found to likely be background sources, with probabilities $< 15\%$ of being physically associated. With the exception of the wider candidate around 70 Vir, most other candidates were found to have very high probabilities of being bonafide companions: the close candidates around 70 Vir, EPIC 219388192, HD 89744 and KELT-1 have $> 99\%$ probabilities of being bound. While additional observations will be required to confirm their true companionship through common proper motion analyses, these objects are therefore highly likely to be true companions.

Finally, a total of 9 targets from our core sample are mentioned as single objects in the literature and have reported null detections from direct imaging surveys (CI Tau, HAT-P-2, HD 5891, HD 33564, HD 104985, HD 156279, HD 180314, HD 203949 and WASP-18; see Appendix 3.A.4). We add to these objects 4 of our observed targets that had no previous observations (BD+24 4697, HD 77065, HD 134113 and HD 160508) and around which we did not find any companion. No published data were found in the literature for the targets 4 UMa, 59 Dra, HD 39392 and HD 112410, which we were not able to observe either.

3.4.2 Companions in Gaia DR2

Raghavan et al. (2010) found that the period distribution of binary companions to nearby FGK stars is approximately a Gaussian in the logarithm of the period, with a broad peak around 300 yrs ($\sim$50 AU), and a 1-σ Gaussian interval spanning from 2 to 1500 AU, in reasonable agreement with previous studies by Duquennoy & Mayor (1991). Most of the imaging data considered here only allow for the detection of companions out to several hundred AU. Hence a significant number of wider companions could remain outside the field of view of these observations and be missed by direct imaging surveys. At these wide separations, outer companions are expected to be massive (i.e. a stellar binary) in order to be able to affect the formation or evolution of close-in planets or brown dwarfs. Such wide stellar companions are expected to be found in the *Gaia* Data Release 2 (DR2; Gaia Collaboration et al. 2016, 2018b), which may thus be used to search for widely-separated comoving components to the objects in our sample. We therefore

searched for *Gaia* DR2 sources with parallaxes and proper motions consistent with those of our targets, to complement our direct imaging search for wide companions in Section 3.4.1.

The recent release of the *Gaia* DR2 catalogue provides unprecedentedly-precise astrometric measurements on the parallaxes and proper motions of stars. However, these highly precise measurements must be considered and handled with caution in the context of a search for common proper motion systems. Shaya & Olling (2011) accurately pointed out that astrometric missions spanning a few years only (e.g. *Hipparcos*, 3.5-yr baseline) capture the reflex motions of multiple systems in their kinematics measurements. Indeed, the components of a binary wobble around the centre of mass of the system and a short-term proper motion measurement is highly likely to reflect this orbital motion. Longer time spans are required to ensure that the observed proper motions correspond to the true barycentric motion (e.g. the Tycho-2 catalogue which uses data from over a century timescale). The apparent changes in proper motions between short and long-term measurements can be as large as several tens of mas yr^{-1}, based on the components masses, binary separation, orbital phase and parallax of the system (Shaya & Olling 2011). These changes in proper motion may even be exploited as a way to search for hidden companions, as was done by Makarov & Kaplan (2005) with the *Hipparcos* and Tycho-2 catalogues (see Chapter 4). Despite the excellent precision of *Gaia* DR2, the catalogue is based entirely on data collected between July 2014 and May 2016, spanning a period of only 22 months, and the same problem as for *Hipparcos* is encountered.

While these effects are reduced at very wide separations, further complications can also arise from the presence of an unresolved binary. Shaya & Olling (2011) estimated that a tight system separated by a few AU could induce proper motion fluctuations of several mas yr^{-1} on the primary, orders of magnitude larger than the errors on *Gaia* DR2 measurements. Close binaries not resolved in *Gaia* are treated as single objects in the second Data Release, which can lead to specious astrometric solutions (Arenou et al. 2018). A third component at a wide separation around an unresolved binary is therefore likely to show somewhat different astrometric parameters (proper motion and parallax) compared to its comoving, unresolved primary.

As a result, we adopted rather loose selection criteria to search for comoving companions to the objects in our sample using the *Gaia* DR2 catalogue. We considered the relative differences in parallax ϖ, i.e. $\Delta\varpi/\varpi_0 \equiv |(\varpi_0 - \varpi_i)/\varpi_0|$, where the subscript 0 corresponds to our science target and i to other *Gaia* sources. We then defined similar relative differences for the proper motion components, $\mu_{\alpha*}$ and μ_δ. To account for the uncertainties in the *Gaia* measurements, we generated, for each pair of objects, 10^5 parallaxes and proper motions drawn from Gaussian distributions centred on the measured values, with a standard deviation set to the *Gaia* uncertainties. We then calculated 10^5 corresponding fractional differences in ϖ, $\mu_{\alpha*}$ and μ_δ and set the final relative differences and associated uncertainties to the mean and standard deviation of the output distributions.

We selected sources that were consistent with relative differences of less than 20% in parallax and in at least one of the two proper motion components (including the correct direction), with a maximum relative discrepancy of 50% in the other proper motion component. We searched for such companions in the *Gaia* DR2 catalogue for all targets in our sample, out to angular separations corresponding to projected separations of 10^4 AU. We found a total of 11 systems fulfilling the above selection criteria, 9 of which were previously known systems. These systems are listed in Table 3.4, in which we give the *Gaia* DR2 parallaxes and proper motions for each binary component. The characterisation of the two newly-identified *Gaia* systems, WASP-14 AB-C and WASP-18 A-B, is detailed in Sections 3.4.2.1 and 3.4.2.2 below.

In Figure 3.7 we plot the relative differences in parallax and proper motion (R.A. and Decl. directions) between the components of all identified *Gaia* binaries. The shaded area represents our arbitrary cut at 20% in the relative differences in parallax and proper motion. The 9 previously known systems are marked in blue and the two new systems discovered here are shown in red. The obtained values and their associated uncertainties are given in Table 3.6 and are all consistent with our chosen constraints at the 1-σ level.

In Appendix 3.B we examined those systems more carefully, as well as other known binaries in our sample, in order to assess our selection criteria. We found that our selection method successfully identified all known binaries that were

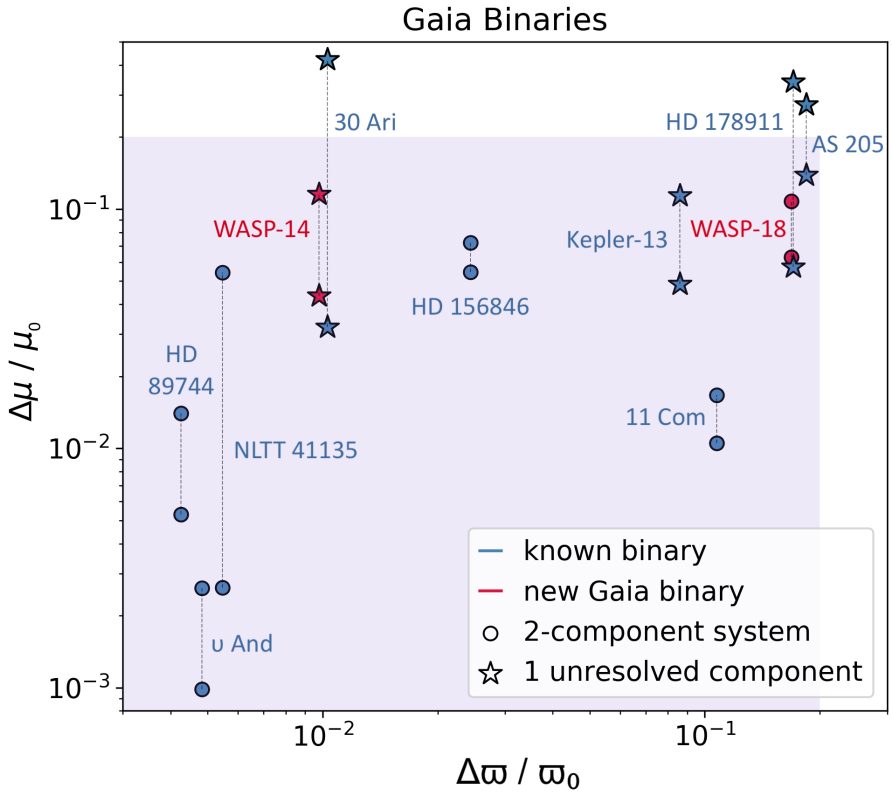

Figure 3.7. Binaries identified in *Gaia* DR2, showing the relative difference in parallax (x-axis) against the relative differences in proper motion (y-axis, both RA and Dec components) between the science target and the selected companion. Our selection criteria correspond to the shaded area (see text). Systems marked with stars rather than circles indicate binaries that have a component known to be unresolved in *Gaia*. The two new binaries identified in this work are marked in red. We do not plot error-bars for clarity of the figure but show them in Table 3.6 instead.

recoverable given the sensitivity and completeness of *Gaia* DR2, and consider that we unlikely missed additional binaries present in the *Gaia* DR2 catalogue. Based on the location of systems with a known unresolved component in Figure 3.7 (marked with stars), we conclude that most binaries should have relative discrepancies of $< 10\%$ in all astrometric parameters (ϖ, $\mu_{\alpha*}$ and μ_δ), while systems agreeing to within 20% in parallax and in one of the proper motion coordinates are likely to be hierarchical systems with an unresolved component (see Appendix 3.B for details).

Table 3.6. Relative differences in parallax and proper motion, with their associated errors, between the components of all *Gaia* binaries. Fractional differences are calculated relative to the first component listed for each system (single or binary), and our science targets always correspond to the first component given. The two new binaries identified in this work are marked in bold.

System	$\Delta\varpi/\varpi_0$ (%)	$\Delta\mu_{\alpha*}/\mu_{\alpha*,0}$ (%)	$\Delta\mu_\delta/\mu_{\delta,0}$ (%)
11 Com ..... A-B	10.74 ± 1.92	1.05 ± 0.30	1.67 ± 0.33
30 Ari ..... BC-A	1.03 ± 0.39	3.21 ± 0.11	42.23 ± 1.81
υ And ..... A-B	0.48 ± 0.38	0.10 ± 0.19	0.26 ± 0.14
AS 205 ..... A-BC	18.41 ± 1.55	27.25 ± 7.14	13.83 ± 1.66
HD 89744 ..... A-B	0.43 ± 2.24	0.53 ± 0.58	1.40 ± 0.75
HD 156846 ..... A-B	2.44 ± 1.70	5.46 ± 0.51	7.23 ± 0.41
HD 178911 ....B-AC	17.02 ± 1.58	33.40 ± 1.20	5.73 ± 0.34
Kepler-13 ..... A-BC	8.61 ± 5.46	11.39 ± 6.55	4.85 ± 2.38
NLTT 41135 ... B-A	0.55 ± 0.51	5.44 ± 0.18	0.26 ± 0.11
WASP-14 .. AB-C	0.98 ± 1.17	4.34 ± 0.71	11.51 ± 2.69
WASP-18 .... A-B	16.85 ± 14.60	6.30 ± 5.94	10.78 ± 9.03

3.4.2.1 WASP-14

WASP-14 A is already known to have a 0.33 $M_\odot$ bound companion at 300 AU (Ngo et al. 2015; Wöllert & Brandner 2015) as discussed in Appendix 3.A.1 (see Table 3.4). This companion is not detected in *Gaia* due to the small angular separation (1.″45) and large magnitude difference (ΔJ=5.2 mag) of the WASP-14 A-B system (see discussion in Appendix 3.B). We report a new companion to this system, WASP-14 C (*Gaia* DR2 1242084166679297920), at a separation of 11.″5397 ± 0.″0001 and a position angle of 4.5827 ± 0.0003 deg. The measured angular separation corresponds to a wide projected separation of 1900 AU at the distance of WASP-14 (see Table 3.4). WASP-14 AB and C have measured *Gaia* DR2 parallaxes in excellent agreement, with a relative difference $< 1\%$. The relative discrepancies in proper motion are slightly larger but still in very good agreement: 4.34% in $\mu_{\alpha*}$ and 11.51% in μ_δ. Given the consistent parallax and small offsets in proper motion, we conclude that the two objects are comoving and form a physical pair. Comparing the placement of WASP-14 in Figure 3.7 to the other *Gaia* binaries in our sample also reinforces the idea that WASP-14 is a true

binary and confirms our intuition that systems with an unresolved component tend to show larger disparities in their observed short-term proper motions.

WASP-14 C has a *Gaia* G-band magnitude of 17.32 mag, for a magnitude difference of ΔG=7.67 mag with the unresolved WASP-14 AB primary. Photometry in the blue ($G_{\rm BP}$) and red ($G_{\rm RP}$) filters of *Gaia* indicate fairly red colours for this object, with $G_{\rm BP} - G_{\rm RP} = 2.67$ mag. This suggests a mid-K to early-M main sequence star according to the *Gaia* DR2 HR diagram analysis in Gaia Collaboration et al. (2018b). The new companion to WASP-14 is also found in the 2MASS catalogue, with magnitudes of $J = 14.297 \pm 0.054$, $H = 13.801 \pm 0.049$ and $K_s = 13.592 \pm 0.058$. According to Schmidt-Kaler (1982), the 2MASS colours correspond to a K5 V spectral type. This implies a bolometric correction of BC_K of $\sim$2.3 $\pm$ 0.1 mag (Masana et al. 2006). From these values, we calculated a bolometric luminosity and used the BT-Settl models (Allard et al. 2012) to infer a mass for WASP-14 C. Adopting a distance based on the *Gaia* DR2 parallax of the target and the age of the system given in Table 3.2, we derived a mass 0.280 ± 0.016 $\mathrm{M}_\odot$ for the newly-discovered stellar component of the triple system WASP-14, making this companion the lowest-mass component of the system.

With its low mass and extremely wide separation, WASP-14 C is unlikely to have played a role in the formation or evolution of the 7.8 $\mathrm{M}_{\rm Jup}$ planet on a 2.2-day orbit around WASP-14 A, as the closer and more massive WASP-14 B component would have had a much stronger influence (if any) on the inner substellar companion. In Figure 3.8, we show the relative positions of WASP-14 AB and C from the 2MASS and *Gaia* DR2 catalogues, confirming over a $\sim$20-yr baseline that the companion is indeed comoving. The WASP-14 A-B pair is unresolved in both 2MASS and *Gaia*.

3.4.2.2 WASP-18

WASP-18 was not previously known to have any companions. We report here the detection of a faint comoving companion at $26\farcs728 \pm 0\farcs001$ ($\sim$3300 AU projected separation) and a position angle of 200.520 ± 0.001 deg, found in the *Gaia* DR2 catalogue (*Gaia* DR2 4931352153572401152), outside the field of view of our VLT/NACO data (see Section 3.3). The source has a *Gaia* magnitude $G = 20.92$

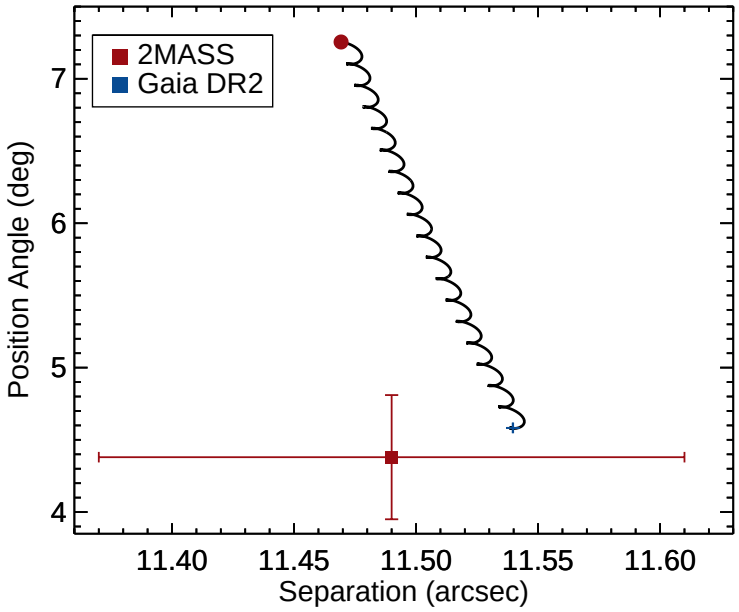

Figure 3.8. Common proper motion analysis of the WASP-14 AB-C system. The black solid line represents the motion of a background object relative to the primary, WASP-14 AB, computed using the proper motion and parallax measurements of our science target the *Gaia* DR2 catalogue. The blue cross and red square mark the measured position of the components in *Gaia* DR2 and in 2MASS, respectively. The red circle indicates the expected position of a background source at the date of the 2MASS observations (June 1997). The *Gaia* DR2 epoch is 2015.5, providing an 18-yr baseline between the two epochs available. As expected from the *Gaia* astrometry of the system, the relative motion of the companion between the two epochs is consistent with a comoving pair.

mag, and a $G-G_{\rm RP}$ colour of 1.79 mag. We do not consider the $G_{\rm BP}$ photometry of this source because of the known poor quality of fluxes in this bandpass for red sources with $G \sim 20-21$ mag (Gaia Collaboration et al. 2018b). At the distance of WASP-18, this places the companion on the M/L-dwarf sequence in the HR diagram for *Gaia* DR2 sources presented in Gaia Collaboration et al. (2018b).

We searched for the same object in the 2MASS catalogue and retrieved a source at the same relative position ($26\farcs71 \pm 0\farcs15$ and 200.36 ± 0.08 deg), in excellent agreement with the consistent proper motions of the two sources in *Gaia* DR2. Figure 3.9 shows the relative positions of WASP-18 A and B at the time of the 2MASS and *Gaia* DR2 observations, together with the expected motion of a

background source between the two epochs. The two objects are clearly found to be comoving based on this analysis, confirming our findings from the *Gaia* DR2 catalogue. The 2MASS photometry of WASP-18 B is $J = 16.289 \pm 0.096$, $H = 15.513 \pm 0.083$ and $K_s = 15.146 \pm 0.121$. Using the relation between spectral type and M_J from Filippazzo et al. (2015), we infer a spectral type of M7.5 for the companion, in agreement with our rough estimate from the *Gaia* HR diagram. We used this spectral type to estimate a bolometric correction BC_J from the relations in Filippazzo et al. (2015) for field objects, and derived a corresponding bolometric luminosity. We finally interpolated the obtained luminosity into the BT-Settl evolutionary models (Allard et al. 2012) at an age of 0.90 ± 0.20 Gyr (Bonfanti et al. 2016), to obtain a mass of 0.092 ± 0.003 $M_\odot$ for WASP-18 B.

WASP-18 B is our *Gaia* source with the largest uncertainties in its parallax and proper motion measurements, with significant errors of 1.52 mas in ϖ, 1.98 mas in $\mu_{\alpha*}$ and 2.40 mas μ_δ. This is due to the fact that this source only has 169 observations in the Along-Scan direction and none in the Across-Scan direction. In comparison, WASP-14 A has 412 observations in both the Along-scan and Across-scan directions, allowing a much higher precision on its astrometric measurements (0.02−0.03 mas). Propagating the measurement errors we found fractional differences in parallax and proper motion between WASP-18 A and B of 16.85 ± 14.60 %, 6.30 ± 5.94 % and 10.78 ± 9.03 %, respectively. While these errors are all very large and comparable to the obtained value for $\Delta\varpi$, $\Delta\mu_{\alpha*}$ and $\Delta\mu_\delta$, they are still consistent with our selection criteria at the 1-σ level. In particular, the 1-σ intervals in the fractional difference of both proper motion components remain within 20%, which strongly indicates that both objects are travelling in the same direction. With the close angular proximity of the two sources (26″) and parallax measurements consistent with each other, we conclude that WASP-18 A and B form a physically-associated pair.

This is further supported by the red colours of the companion, its placement on the *Gaia* HR diagram, and the consistent relative positions of the two components over 16 years between 2MASS and *Gaia* DR2 (Figure 3.9). The possible offset in the *Gaia* DR2 parallaxes could indicate that one of the components is an unresolved binary, as we found in our analysis that systems with an unresolved component tend to show higher inconsistencies in the short-term astrometric measurements available in *Gaia* DR2 (e.g. AS 205 A-BC and HD 178911 AC-B

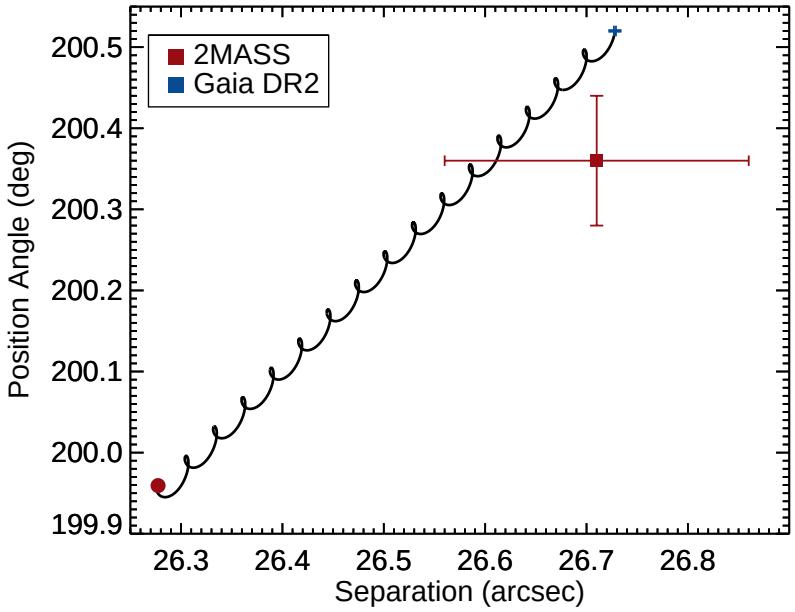

Figure 3.9. Same as Figure 3.8 for the WASP-18 A-B system. The *Gaia* DR2 epoch is again 2015.5 and the 2MASS observations date from August 1999, providing a 16-yr time span, clearly demonstrating that the two objects share common proper motion.

have relative differences in parallax close to 20%). Alternatively, this discrepancy could also reflect a much wider binary separation, along the line of sight, with one component located at a slightly larger distance. Further observations will be required to reduce the uncertainties in the parallax of WASP-18 B, which will be available in future data releases of the *Gaia* mission. Despite these large uncertainties, we are nevertheless able to confirm that WASP-18 A and B form of a common proper motion pair, in which the fainter component is a low-mass M dwarf close to the stellar/substellar boundary.

3.5 Detection Limits

In order to take into account observational biases and survey sensitivities in our analysis, we gathered and generated detection limits for each target in our sample. We searched for existing contrast curves from the literature for the targets with

previous observations (Section 3.5.1) and derived *Gaia* detection limits for all targets in our sample (Section 3.5.2). Combining those with our own sensitivity limits for our six observed targets (see Section 3.3.2), we are able to define a detection probability map which is presented and described in Section 3.5.3.

3.5.1 Imaging Contrast Curves

The data used to derive detection limits for all targets with existing imaging data (new or from the literature) are summarised in Table 3.7. Sensitivity limits were found to be available for a total of 29 objects, including our 6 observed targets. When multiple sets of observations were found, we chose the best limits available. For a few targets, the deepest contrast curves found only covered a limited range of separations. In those cases, we also consider the shallower detection limits and keep the best value available at any given projected separation.

We used the contrast curves presented in Section 3.3.2 for the 6 targets observed as part of this survey. Most targets with archival observations have contrast curves provided in the literature that are specific to the best set of observations for each target. We flag those with a 0 in the "Curve flag" column in Table 3.7. A number of surveys only provide average detection limits for the observed sample (Ginski et al. 2012; Bergfors et al. 2013; Ngo et al. 2015), which we flag as 1. Finally, we considered the typical sensitivities achieved by specific facilities and instruments when no detection limits were available. These curves are flagged with a 2 in Table 3.7, and are detailed below.

Three of our targets have past observations with the AEOS telescope presented in the survey by Roberts et al. (2011). As the authors do not provide detection limits for their observations, we used the typical performance curves for the AEOS telescope given in Turner et al. (2006) for the same observation set up as that described in Roberts et al. (2011), and consider that they are representative of those data. Similarly, Siverd et al. (2012) acquired NIRC2 images of KELT-1 with Keck but do not present their achieved sensitivities. We therefore assumed a similar performance to that achieved in Ngo et al. (2015) for comparable NIRC2 observations and used the average detection limits from that work for this target.

Table 3.7. Detection limits used.

Object ID	Facilities / Instrument	Filter	Phot. (mag)	Limits units	Curve flag	Data Set
30 Ari B	Keck / NIRC2	J	6.080 ± 0.02	Δmag	0	Kane et al. (2015)
70 Vir	AEOS	I	3.98	mag	2	Roberts et al. (2011)[a]
	2MASS	J	3.80	mag	2	Pinfield et al. (2006)
υ And	AEOS	I	3.35	mag	2	Roberts et al. (2011)[a]
	Lick / LIRC II	K'	2.86	Δmag	0	Patience et al. (2002)
BD+24 4697	Gemini North / NIRI	Ks	7.474 ± 0.023	Δmag	0	This paper
CI Tau	Subaru / HiCIAO	H	8.43 ± 0.04	Δmag	0	Uyama et al. (2017)
EPIC 219388192	Keck / NIRC2	K	10.666 ± 0.0216	Δmag	0	Curtis et al. (priv. com.)
	Subaru / IRCS	H	10.734 ± 0.021	flux ratio	0	Nowak et al. (2017)
HAT-P-2	Calar Alto / AstraLux	z'	9.506 ± 0.001	Δmag	1	Bergfors et al. (2013)
HAT-P-20	Keck / NIRC2	K	8.601 ± 0.019	Δmag	1	Ngo et al. (2015)
HD 5891	Calar Alto / AstraLux	i'	7.47 ± 0.01	Δmag	0	Ginski et al. (2016)
HD 33564	Calar Alto / AstraLux	i'	4.6	Δmag	1	Ginski et al. (2012)
HD 41004 B	Hipparcos	Hp	$8.785 \pm 0.014^{*}$	Δmag	2	Hipparcos and Tycho Catalogues
HD 77065	Gemini North / NIRI	Ks	6.638 ± 0.020	Δmag	0	This paper
HD 87646 A	Hipparcos	Hp	8.203 ± 0.002	Δmag	2	Hipparcos and Tycho Catalogues
HD 89744	AEOS	I	5.2	mag	2	Roberts et al. (2011)[a]
	UKIRT / UFTI	H	4.53	mag	0	Mugrauer et al. (2004)
HD 104985	Calar Alto / AstraLux	i'	8.302 ± 0.145	Δmag	1	Ginski et al. (2012)
HD 114762	Keck / NIRC2	K	5.888 ± 0.017	Δmag	0	Patience et al. (2002)
HD 134113	WIYN / NESSI	z'	7.6	Δmag	0	This paper
HD 156279	Calar Alto /AstraLux	i'	7.65 ± 0.03	Δmag	0	Ginski et al. (2016)

Table 3.7. (Continued.)

Object ID	Facilities / Instrument	Filter	Phot. (mag)	Limits units	Curve flag	Data Set
HD 160508	WIYN / NESSI	z'	7.4	Δmag	0	This paper
HD 162020	VLT / NACO	L'	6.539 ± 0.024	Δmag	0	This paper
HD 168443	VLT / SPHERE	H	5.325 ± 0.016	Δmag	0	Moutou et al. (2017)
	VLT / SPHERE	Ks	5.211 ± 0.015	Δmag	0	Moutou et al. (2017)
HD 178911 B	Hipparcos	Hp	$6.835 \pm 0.013^*$	Δmag	2	Hipparcos and Tycho Catalogues
HD 180314	Calar Alto /AstraLux	i'	6.14 ± 0.05	Δmag	0	Ginski et al. (2016)
HD 203949	VLT / SPHERE	H	3.107 ± 0.200	Δmag	0	Moutou et al. (2017)
	VLT / SPHERE	Ks	2.994 ± 0.232	Δmag	0	Moutou et al. (2017)
KELT-1	Keck / NIRC2	K'	9.437 ± 0.019	Δmag	2	Siverd et al. (2012)[b]
Kepler-13 A	Palomar HALE / PHARO	K'	9.958	Δmag	0	Adams et al. (2012)
WASP-14	Keck / NIRC2	K	8.621 ± 0.019	Δmag	1	Ngo et al. (2015)
WASP-18	VLT / NACO	L'	8.131 ± 0.027	Δmag	0	This paper
XO-3	Calar Alto / AstraLux	z'	9.798	Δmag	0	Bergfors et al. (2013)

Notes. Curve flags: 0 is contrast curve specific to the observations of the target; 1 is average limits of observed sample (or subset); 2 is typical sensitivity of instrument for the observational set up used (see text for more detail).

[a] we used the typical performance curves given in Turner et al. (2006) for the same observational set up.

[b] as no limits are provided in Siverd et al. (2012), we assumed a similar performance as in Ngo et al. (2015) which used a comparable observing strategy on the same instrument, and used the average detection level from that paper.

[*] magnitude of the primary (see text).

Pinfield et al. (2006) searched for companions to 70 Vir out to 30″ using 2MASS. As no detection limits are available in that paper, we generated a 2MASS contrast curve based on the typical resolving and completeness limits of the 2MASS survey. According to the 2MASS documentation (Skrutskie et al. 2006), close doubles with separations $< 5''$ are not reliably resolved by 2MASS and stellar PSFs can contaminate neighbour sources up to 10″. The J-band completeness limit is given at 16.0 mag. We therefore start our 2MASS contrast curve at 5″ with $\Delta J = 0$ (equal mass binary at the resolving limit). We then use the completeness limit $J = 16.0$ from 10″ out to 300″, the radial search limit from Pinfield et al. (2006), with a linear increase in ΔJ between $5''-10''$.

Finally, three targets in our sample were found to be *Hipparcos*-Tycho binaries, namely, HD 41004 B, HD 87646 A and HD 178911 B. For those three targets, we used the typical sensitivity to binaries in the *Hipparcos* catalogue based on the plot of separation against ΔH_p of all *Hipparcos* binaries found in the ESA documentation (ESA 1997). We extend the separation range out to 30″, the given widest separation of identified *Hipparcos*-Tycho binaries. For two of these systems, our sample targets correspond to the fainter, lower-mass component of the binary system, which were detected as companions to the brighter primaries. We thus considered the magnitude of the primary of these systems to derive detection limits around the primary binary component.

Most of the obtained detection limits are in units of magnitude difference, Δmag, while a few are provided in magnitudes and one in flux ratio. These are indicated in the "Limits units" column of Table 3.7. All sensitivity limits are given as a function of angular separation. For all limits that were not in units of magnitudes we started by converting the contrast curves into apparent magnitudes using the photometry of our targets in the considered filters and given in Table 3.7. Using the distances from Table 3.2, we then converted all magnitude limits into absolute magnitudes and the angular separations into physical projected separations, in AU. Adopting the ages from Table 3.2 for our targets, the obtained absolute magnitude curves were then interpolated into the BT-Settl evolutionary models by Allard et al. (2012) to derive corresponding minimum detectable companion masses. The BT-Settl models provide isochrones for numerous photometric systems. We were therefore able to use models corresponding to the specific facilities and filters considered and infer mass limits for each target. Finally, we

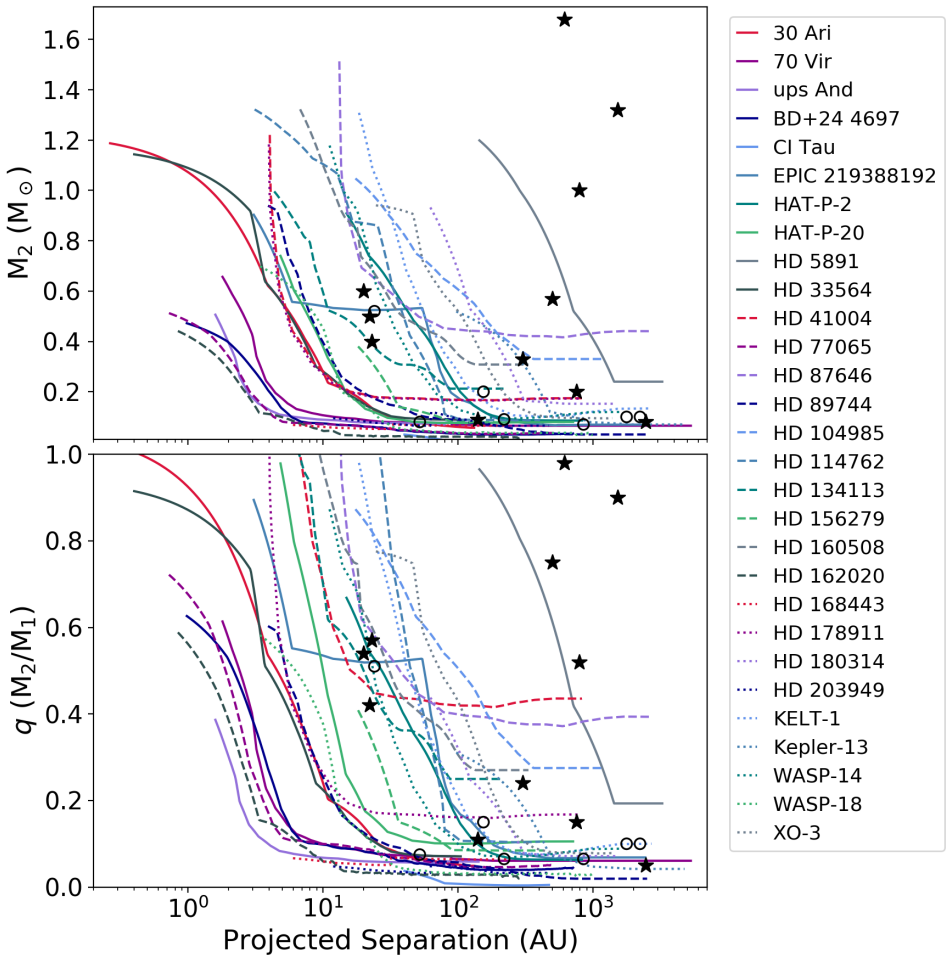

Figure 3.10. Detection limits for all targets in our sample with published or new direct imaging observations in terms of secondary mass (top) and system mass ratio (bottom). Limits were derived using the data listed in Table 3.7 and following the approach described in the text. The black stars indicate the positions of confirmed companions to the stars with imaging limits and the open circles correspond to direct imaging candidate companions.

used the stellar masses listed in Table 3.2 for our sample to convert the obtained mass limits into mass ratios q (using the masses of the binary primaries for the two *Hipparcos* systems mentioned above). For the few targets with multiple entries in Table 3.7, we considered the lowest mass ratio value in the overlapping regions of separations in order to define a unique sensitivity curve for each object. The final mass and mass ratio curves for each target with direct imaging data are shown in Figure 3.10, together with the positions of all confirmed (black stars) and candidate (open circles) companions around these objects.

3.5.2 Gaia Detection Limits

Since all objects in our sample are found in the *Gaia* DR2 catalogue, we are able to derive *Gaia* detection limits for each of our targets. *Gaia* DR2 is found to be complete between $G = 12$ mag and $G = 17$ mag, with a limiting magnitude of $G \sim 21$ mag and a bright limit of $G \sim 3$ mag (Gaia Collaboration et al. 2018b). Ziegler et al. (2018) investigated the recoverability of close binaries in *Gaia* DR2 looking for known binaries from the Robo-AO Kepler survey (Law et al. 2014; Baranec et al. 2016; Ziegler et al. 2017) in the *Gaia* DR2 catalogue. They found that near equal-brightness binaries ($\Delta G < 1$ mag) were consistently retrieved from separations of $1''$ and that binaries down to $\Delta G = 6$ mag were recovered at separations of $\sim 3''$. Based on their results, we define our *Gaia* DR2 sensitivity limits to start at $1''$and $\Delta G = 1$ mag, with a linear decrease to $\Delta G = 6$ mag from $1''-3''$. We then adopt a linear decrease out to $5''$ from $\Delta G = 6$ mag to $G = 21$ mag, the *Gaia* faint limit, and use that limiting magnitude at wider separations, out to projected separations corresponding to 10^4 AU.

Figure 3.11 shows the obtained sensitivity limits in terms of apparent G magnitude and mass ratio for all objects in our sample. The derived limits are consistent with the *Gaia* detection limits derived by Brandeker & Cataldi (2019). We plot on the left panels the limits for the targets without a known companion and on the right panels the limits for all confirmed multiple systems, with the positions the known companions. Magnitude limits were converted into corresponding mass ratio curves adopting the properties of our targets listed in Table 3.2 and following the approach described in the previous section with BT-Settl isochrones specific to the *Gaia* filter system.

While *Gaia* is essentially complete in the range $G \sim 12-17$ mag, the catalogue has an ill-defined faint magnitude limit which depends on celestial position (Gaia Collaboration et al. 2018b). In addition, the number of sources with a full 5-parameter astrometric solution (position, parallax and proper motion) decreases towards the faint end, where a larger fraction of sources only have positional measurements available, as discussed in the assessment of the *Gaia* DR2 astrometric performance by Lindegren et al. (2018). We must take into account the catalogue completeness in our detection limits to account for companions that are missed by *Gaia*, but also for those like τ Gem B and HAT-P-20 B

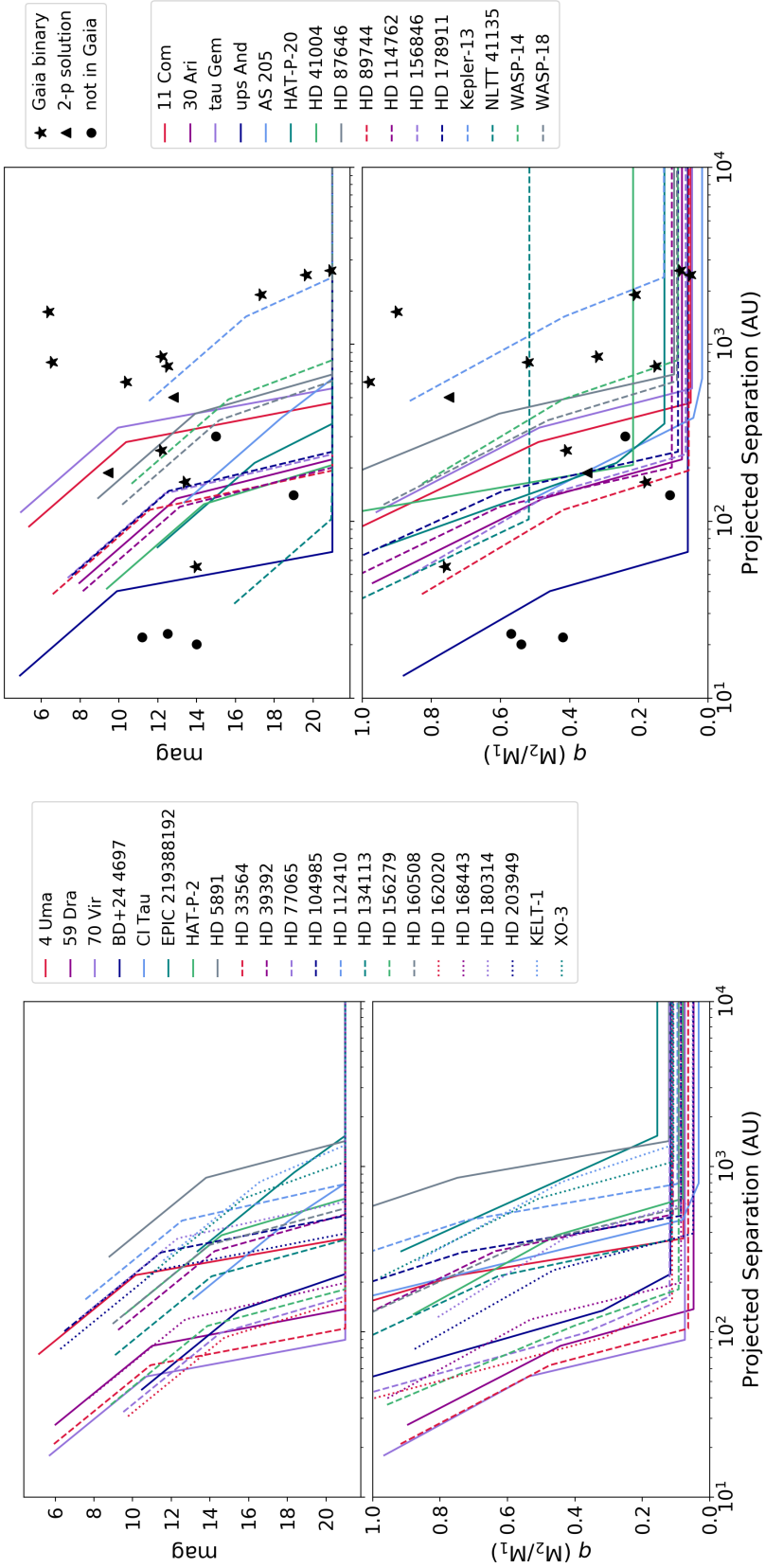

Figure 3.11. *Gaia* detection limits for all targets without a known companion (left panels) and those that are confirmed binaries or higher order multiples (right panels). The top panels show the *Gaia* G-band detection limits as defined in the text. Bottoms panels correspond to the same magnitude sensitivities converted into mass ratios using the BT-Settl models (Allard et al. 2012) and the stellar properties from Table 3.2. On the right panels, we also show the positions of the confirmed companions to our targets. Companions detected in *Gaia* are marked with stars. The two companions present in *Gaia* DR2 but with a 2-parameter astrometric solution only are shown by triangles. Binary companions not retrieved in *Gaia* are indicated with filled circles.

that only have a 2-parameter solution and which we were not able to identify as *Gaia* companions in our analysis in Section 3.4.2. Arenou et al. (2018) report the completeness of the *Gaia* DR2 catalogue as a function of G-band magnitude in their catalogue validation work. The provided completeness level for sources with full astrometric solutions decreases from ∼99% at $G < 17$ mag to ∼80% at $G = 20$ mag, before sharply dropping to 0% as G approaches 21 mag (see figure A.1. in the appendix of Arenou et al. 2018). We thus use the completeness levels provided in that paper to account for these effects.

In Figure 3.12 we show an example of *Gaia* sensitivity curves for a primary of $G = 8$ mag with a parallax of 20 mas, corresponding to a mass of 1 $M_\odot$ at 3 Gyr, representative of the targets in our sample. In the top panel, we show the detection limits for such an object in terms of apparent magnitude, defined as described above. The horizontal dashed lines indicate the G magnitudes associated with various completeness levels using the information from Arenou et al. (2018), down to the faint magnitude limit of *Gaia* DR2 at $G = 21$ mag (grey line). The bottom panel shows the same contrast curve, converted into mass ratios using the BT-Settl models and adopting an age of 3 Gyr. Since we assumed a primary mass of 1 $M_\odot$, the plot in the bottom panel is also representative of the corresponding mass limits in units of Solar masses.

Figure 3.12 clearly demonstrates that when working in mass ratio space, the range over which *Gaia* DR2 is not complete for sources with 5-parameter solutions ($< 99\%$ completeness, below the red dashed lines) is significantly reduced relative to the span of the same incompleteness levels in magnitude space, going from $G = 17{-}21$ mag to $q = 0.16{-}0.09$ $M_\odot$. This implies that in addition to the targets too faint for *Gaia* ($G > 21$ mag) only the lowest-mass companions have a high chance of being missed due to survey incompleteness. We note however that the two known companions from our sample that only have a 2-parameter astrometric solution in *Gaia* DR2 (τ Gem B and HAT-P-20 B) have relatively bright G-band magnitudes of 9.42 mag and 12.80 mag, respectively. Their apparent magnitudes fall into a $> 99\%$ completeness level of sources with full astrometric solutions according to Arenou et al. (2018). We conclude that it was statistically unlikely to have two bright companions in our sample present in the DR2 catalogue but lacking a 5-parameter solution, and that these two sources are not representative of the completeness of *Gaia* DR2.

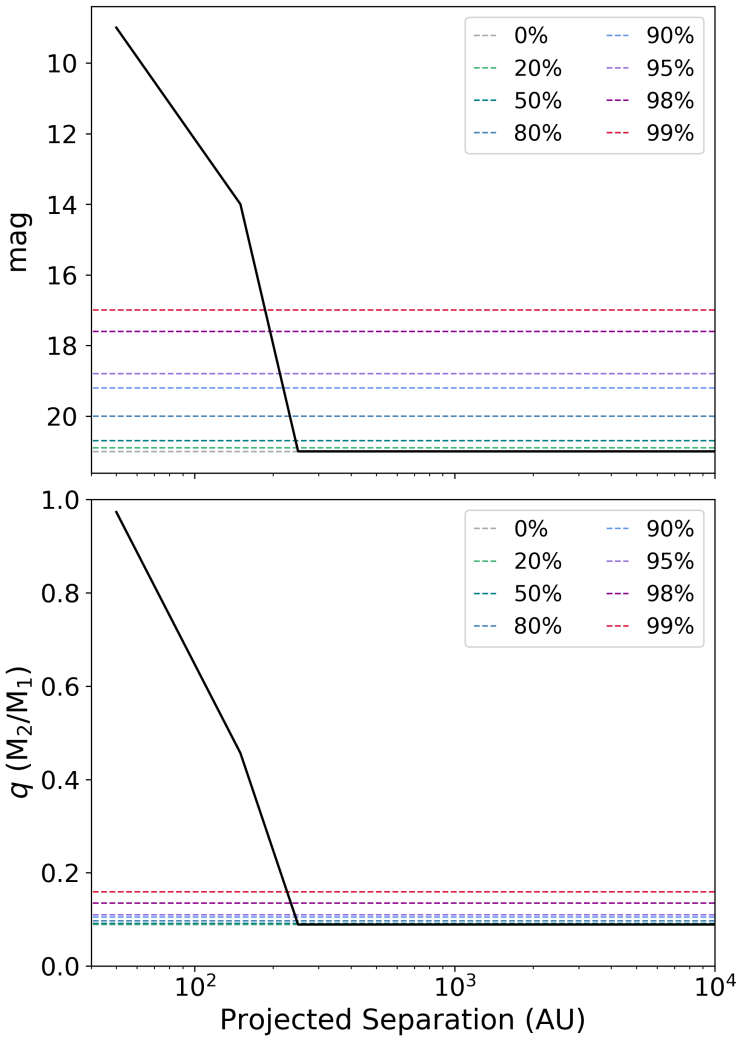

Figure 3.12. Completeness of *Gaia* DR2 compared to the *Gaia* detection limits for a representative target of 1 $M_\odot$ at 3 Gyr, with a parallax of 20 mas and a G-band magnitude of 8 mag. The top panel shows the contrast curve in terms of apparent magnitude of the secondary and the bottom panel displays the corresponding sensitivity in terms of mass ratio, computed in the same way as the *Gaia* detection limits for our targets in Figure 3.12. The coloured dashed lines represent the completeness levels of *Gaia* DR2 taken from Arenou et al. (2018) for sources with a 5-parameter solution.

For all targets in our sample, we converted the completeness curve obtained from Arenou et al. (2018) into mass ratios as we did for our example target in the bottom panel of Figure 3.12. We are thus able to assign a completeness factor to each mass ratio value for every detection limit presented in Figure 3.11. Instead of traditional sensitivities, where anything above the mass ratio curves is considered as detectable and anything below is not retrievable, we now associate every point in the separation-mass ratio space to a detection probability, given by the completeness level at any given mass ratio value. The part of the parameter space below the final limits remains at the zero detection probability level regardless of the associated completeness value. We will use these probabilities in the next section to define a 2-dimensional detection probability map for our sample.

3.5.3 Detection Probability Map

We combined all sensitivity curves obtained in Section 3.5.1 from imaging data and in Section 3.5.2 from *Gaia* DR2 to define a single detection probability map for our survey, as was done in Chapter 2. For targets with both *Gaia* and imaging limits, we started by combining the two sets of contrast curves. Following the approach described in Section 3.5.1, we considered the best value available (lowest q value) in the separation ranges where the *Gaia* and imaging limits overlapped, keeping track of the ranges over which the final curves corresponded to the *Gaia* limits. This allowed us to define a unique sensitivity curve for each object.

The mass ratio limits for each target in the sample were then placed on a grid of separations and mass ratios with a resolution of 0.002 in q and steps of 0.01 in $\log(\rho)$. For every cell in the grid, we then identified the number of targets around which a companion of given separation and mass ratio would have been retrieved given the data gathered for this survey. When the considered separation corresponded to the *Gaia* limit of a given target, we then scaled this detection by the *Gaia* completeness level at the associated mass ratio, which we previously computed in Section 3.5.2. The number obtained for each cell of the grid was then divided by the total number of objects in our sample, providing a value between 0 and 1 representing the average probability that a companion of projected separation ρ and mass ratio q would have been detected around our 38 targets given the data considered in this work.

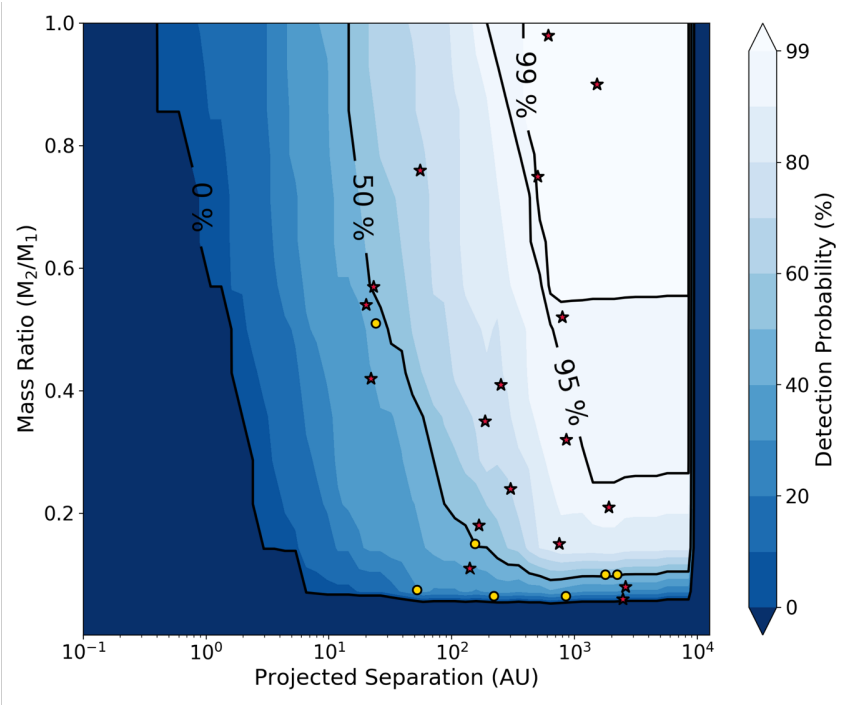

Figure 3.13. Detection probability map for our sample using the mass ratio sensitivities for our targets from Sections 3.5.1 and 3.5.2, including the completeness of *Gaia* DR2 (see Section 3.5.2). Black contours denote the 0%, 50% and 95% and 99% completeness regions for the full survey. Red stars show the positions of all confirmed companions and yellow circles indicate the positions of candidate companions (see Tables 3.4 and 3.5).

Figure 3.13 shows the resulting detection probability map for our full sample of 38 objects. Companions inside the 99% completeness region are essentially detectable around all targets in the sample. We are complete to companions with $q > 0.2$ at separations > 1000 AU around 90% of our sample, and down to $q \sim 0.1$ from separations of $\sim$100 AU around half of our targets (50% detection probability contour). Confirmed comoving companions were found to be relatively evenly distributed throughout the parameter space (both in separation and mass ratio). In contrast, most candidate companions are concentrated around $q \sim 0.1$, which we attribute to the fact that these fainter companions are not detected by *Gaia* and are more likely to lack a second direct imaging epoch, necessary to be astrometrically confirmed. Interestingly, no companion was found at projected separations < 20 AU, despite reaching a completeness level up to 50%, while a number of companions (confirmed and candidates) were retrieved at the same detection probability level at wider separations and low mass ratios.

3.6 Statistical Analysis

We used the statistical tool described in Chapter 2 to constrain the multiplicity properties of our sample. Examining the binary statistics of these objects will allow us to investigate the possible role of binarity in the formation or evolution of massive, close-in brown dwarfs and planets. The code is based on a Markov Chain Monte Carlo (MCMC) sampling method, using the EMCEE Python package (Foreman-Mackey et al. 2013), and allows us to place robust Bayesian statistical constraints on the binary frequency and companion population distributions for the sample gathered in this study. We add a new capability to the tool in order to account for unconfirmed candidates, which we describe below.

The statistical approach uses the detection limits of the survey, in the form of a detection probability map (see Section 3.5.3, Figure 3.13), and the properties of detected companions (total number of detections, separations and mass ratios of identified systems) to derive posterior distributions of model parameters (binary fraction and parameters describing the shapes of companion distributions) most compatible with the gathered data. Based on previous studies of stellar multiplicity in the field (Duquennoy & Mayor 1991; Raghavan et al. 2010), we adopt a lognormal distribution in companion separation ρ (Equation 3.2) and a power law in mass ratio q (Equation 3.3):

$$P(\rho \mid \mu, \sigma) \propto \exp\left[-\left(\log_{10}(\rho) - \mu\right)^2 \;/\; 2\sigma^2\right] \tag{3.2}$$

where μ and σ are the mean and standard deviation of the underlying normal distribution in $\log(\rho)$. The mass ratio distribution ranges from 0 to 1 and is defined by the power law index γ:

$$P(q \mid \gamma) \propto \begin{cases} q^{\gamma} & \text{for } \gamma \geqslant 0 \\ (1-q)^{-\gamma} & \text{for } \gamma < 0 \end{cases} \tag{3.3}$$

so that negative and positive indices produce symmetric distributions about $q = 0.5$ for the same absolute value of γ.

As was done in Chapter 2, we truncated the model distributions at $\rho = 20{-}10{,}000$ AU and $q = 0.05{-}1$, in order to constrain the binary frequency on those separation

and mass ratio ranges. We adopted flat priors for each model parameter, set to unity over the following ranges and to zero elsewhere: 0.5−4 for μ, 0.1−3 for σ, -3−3 for γ and 0−1 for the binary fraction f.

In order to also take into account the candidate companions identified around the targets in our sample, we used the probabilities of the candidates being physically bound derived in Section 3.4.1 and listed in Table 3.5. At each step in the MCMC chain, we drew for each target with a candidate companion a number between 0 and 1, and counted the candidate as a bonafide companion if the drawn value was below the companionship probability. This ensures that each candidate companion is selected in a fraction of MCMC steps that is representative of its probability of being physically associated to the primary target. For hierarchical systems (e.g. 30 Ari, WASP-14), we considered the properties of all detected components in the part of the code that constrains the shape of the separation and mass ratio distributions, accounting for candidate companions only when they were selected (e.g. 70 Vir, EPIC 219388192, HD 89744). For systems in which the binary companion is itself a tight binary (AS 205, HD 178911, Kepler-13), we used the combined mass of the binary component, since this total mass would be responsible for any dynamical effect on the close-in planet or brown dwarf. For the section of the tool constraining the binary fraction, we considered the number of multiple systems rather than the total number of companions in order to constrain the multiplicity rate of our sample.

3.7 Results

3.7.1 MCMC Analysis for the Full Sample

We ran the MCMC sampler with 2000 walkers taking 5000 steps each on our full sample of 38 objects. We found that walkers were expanding from their initial positions to a reasonable sampling of the parameter space in less than 100 steps, and removed the first 100 steps of this "burn-in" phase. We found a mean fraction of steps accepted for each walker of 0.44, in good agreement with the rule of thumb acceptance fraction suggested by Foreman-Mackey et al. (2013) between 0.2 and 0.5, and trust the obtained value to be a reliable indication of convergence.

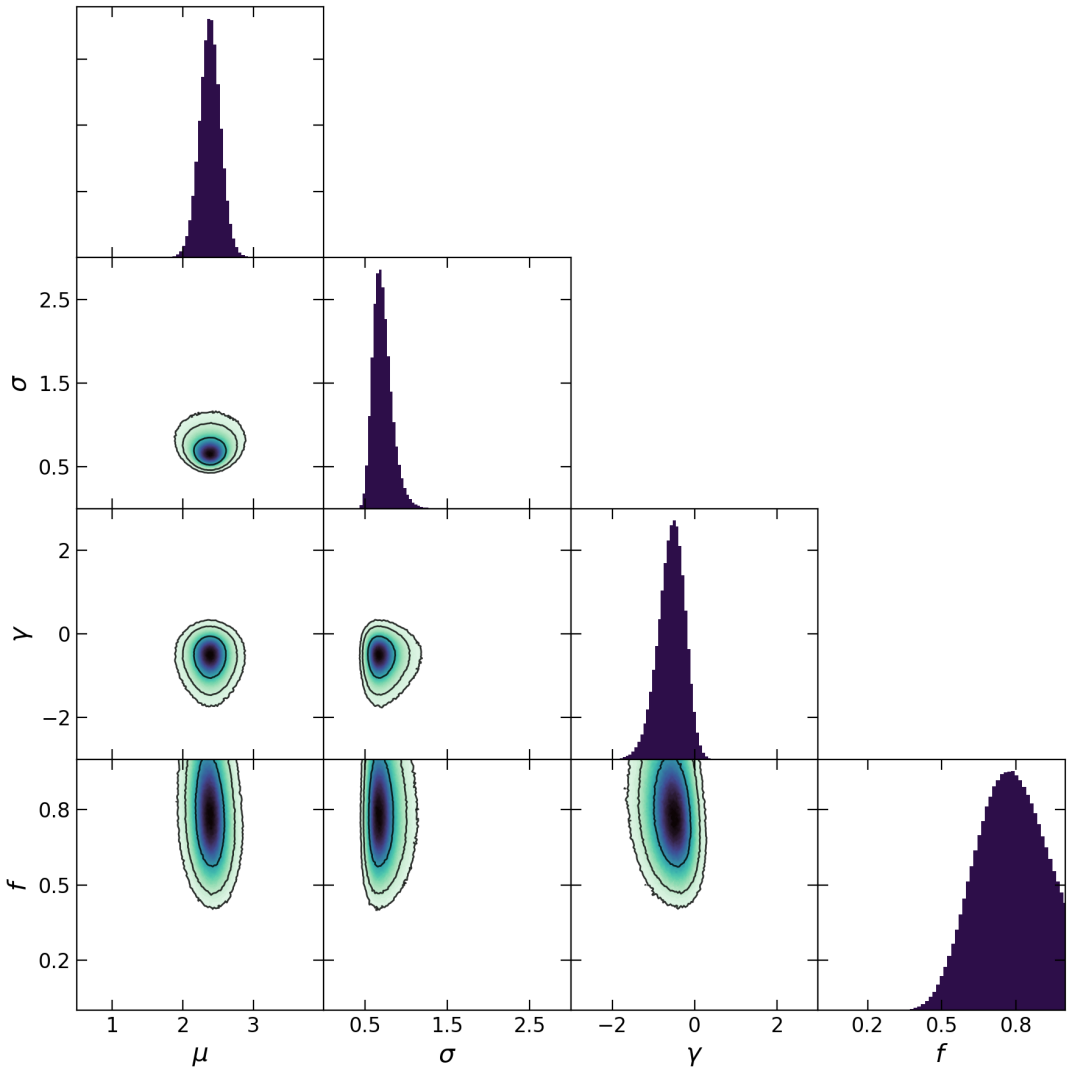

Figure 3.14. Posterior probability distributions of all model parameters (diagonal) from our MCMC analysis performed on the full sample of 38 objects and correlation among all pairs of parameters (triangle plot). Normalised histograms at the ends of rows are marginalised over all other parameters. Black contour lines in the correlation plots correspond to regions containing 68%, 95% and 99% of the posterior.

The full output from our MCMC analysis is presented in Figure 3.14. The best-fit values for the binary parameters of our core sample on separations in the range 20−10,000 AU are summarised in Table 3.8. Errors correspond to 68% confidence intervals, estimated using a highest posterior density approach to determine the boundaries of Bayesian credible intervals (see Chapter 2). The highest density region method provides a set of the most probable values of a given parameter. All 4 model parameters were found to be well constrained, converging to sharply-defined peaks in the posterior distributions, with the binary fraction f showing the broadest posterior distribution.

The obtained posterior distribution for the binary frequency of our sample, $f = 79.0^{+13.2}_{-14.7}\%$, was found to be much higher than the overall multiplicity rate of FGK stars in the field, generally observed to be around 40−50% (Duquennoy & Mayor 1991; Raghavan et al. 2010). The peak of the lognormal in separation corresponds to a value of ∼250 AU, also much wider than for the field population (Raghavan et al. 2010). We discuss these features further in Section 3.8 where we provide a detailed assessment of the possible sources and implications of these results.

3.7.2 Sample Division at 10 Days in Inner Companion Period

We divided our sample into two subsets, with a cut at 10 days in the period of the inner planets and brown dwarfs, the commonly-accepted threshold for hot Jupiters (Wang et al. 2015; Dawson & Johnson 2018). This allows us to investigate possible differences in the binary properties of the stars with companions on orbits comparable to hot Jupiters, and those with planets or brown dwarfs at slightly wider separations. The hot Jupiter-like subset includes 12 targets, 6 of which are confirmed binaries, with 2 additional targets having at least one high-probability candidate companion. The sample of wider inner companions contains 26 objects, including 10 confirmed multiples and 1 candidate binary.

Following the approach described above, we created detection probability maps for each subset, considering the available imaging and *Gaia* DR2 detection limits for all targets from each subsample. We then performed the same statistical analysis as that presented above to constrain the multiplicity rates and binary

properties of our samples of objects with periods shorter and longer than 10 days, so as to assess whether statistically significant discrepancies are observed between the two underlying populations. Figures 3.15 and 3.16 show the output of the MCMC sampler for the shorter and longer-period samples, respectively. As expected from the smaller sample sizes of the two subsets relative to the full sample, the walkers are slightly more widely spread throughout the parameter space than in Figure 3.14, and this effect is amplified for the smaller sample of $<$ 10-day companions. Nevertheless, all 4 model parameters are still well constrained within the explored parameter space in both subsamples. The best-fit values and corresponding 1-σ intervals are given in Table 3.8 for each subset.

The model parameters describing the companion separation distribution (μ and σ) peak at very similar values for the two subsets, indicating that no significant difference is observed between the binary separations of these two sub-populations. The power law index γ describing the mass ratio distribution appears to shift to slightly lower values for the sample of longer-period inner companions, which reflects the generally lower mass ratios of multiple systems found in that subset.

The binary fraction f, on the other hand, shows a larger discrepancy in the output posterior distributions between the two subsets of targets. The obtained probability density function for the sample with inner companions on very short orbits (Figure 3.15) was found to peak at $92.0^{+8.0}_{-19.0}$% (68% confidence), consistent with a binary rate of 100% at the 1-σ level. In contrast, the subset of wider inner companions (Figure 3.16) has a binary frequency of $74.0^{+14.4}_{-15.9}$%. We plot these two distributions in Figure 3.17, together with the obtained posterior distribution for f for the full sample. The red line shows the corresponding multiplicity rate of field stars based on results from Raghavan et al. (2010), scaled to our probed separation range of 20$-$10,000 AU (see Section 3.8 for details). While all 3 distributions are consistent with one another, a clear shift is observed in the peak of the posteriors. In particular, the peak of the binary fraction distribution for the $<$ 10-day sample is located outside or at the edge of the 68% confidence interval of the other two posterior distributions. The resulting binary fractions are all much higher than the corresponding value expected for the overall field star population.

Table 3.8. Summary of multiplicity properties from our study, with a comparison to field stars and hosts to lower-mass planets.

Sample	N	M_2 (M_{Jup})	μ	σ	γ	f (%)	Binary sep. (AU)	Binary q	Reference
Full sample	38	7−70	$2.39^{+0.14}_{-0.15}$	$0.68^{+0.12}_{-0.10}$	$-0.52^{+0.31}_{-0.32}$	$79.0^{+13.2}_{-14.7}$	20−10,000	0.05−1	This work
						70 ± 10	50−2000	0.05−1	This work
< 10 day subset	12	7−70	$2.36^{+0.28}_{-0.31}$	$0.76^{+0.29}_{-0.16}$	$0.03^{+0.38}_{-0.40}$	$92.0^{+8.0}_{-19.0}$	20−10,000	0.05−1	This work
> 10 day subset	26	7−70	$2.40^{+0.18}_{-0.17}$	$0.63^{+0.15}_{-0.12}$	$-0.89^{+0.55}_{-0.64}$	$74.0^{+14.4}_{-15.9}$	20−10,000	0.05−1	This work
FGK field stars	454	–	1.70	1.68	$\sim$0	44 ± 2	overall	overall	Raghavan et al. (2010)
						36 ± 2	20−10,000	overall	Scaled in this work
						16 ± 1	50−2000	overall	Scaled in Ngo et al. (2016)
Friends of HJs	77	< 4*	...	...	...	47 ± 7	50−2000	0.05−1	Ngo et al. (2016)

*5 objects from the Friends of hot Jupiters survey have masses between 7−12 M_{Jup}, all of which are part of our studied sample (see text).

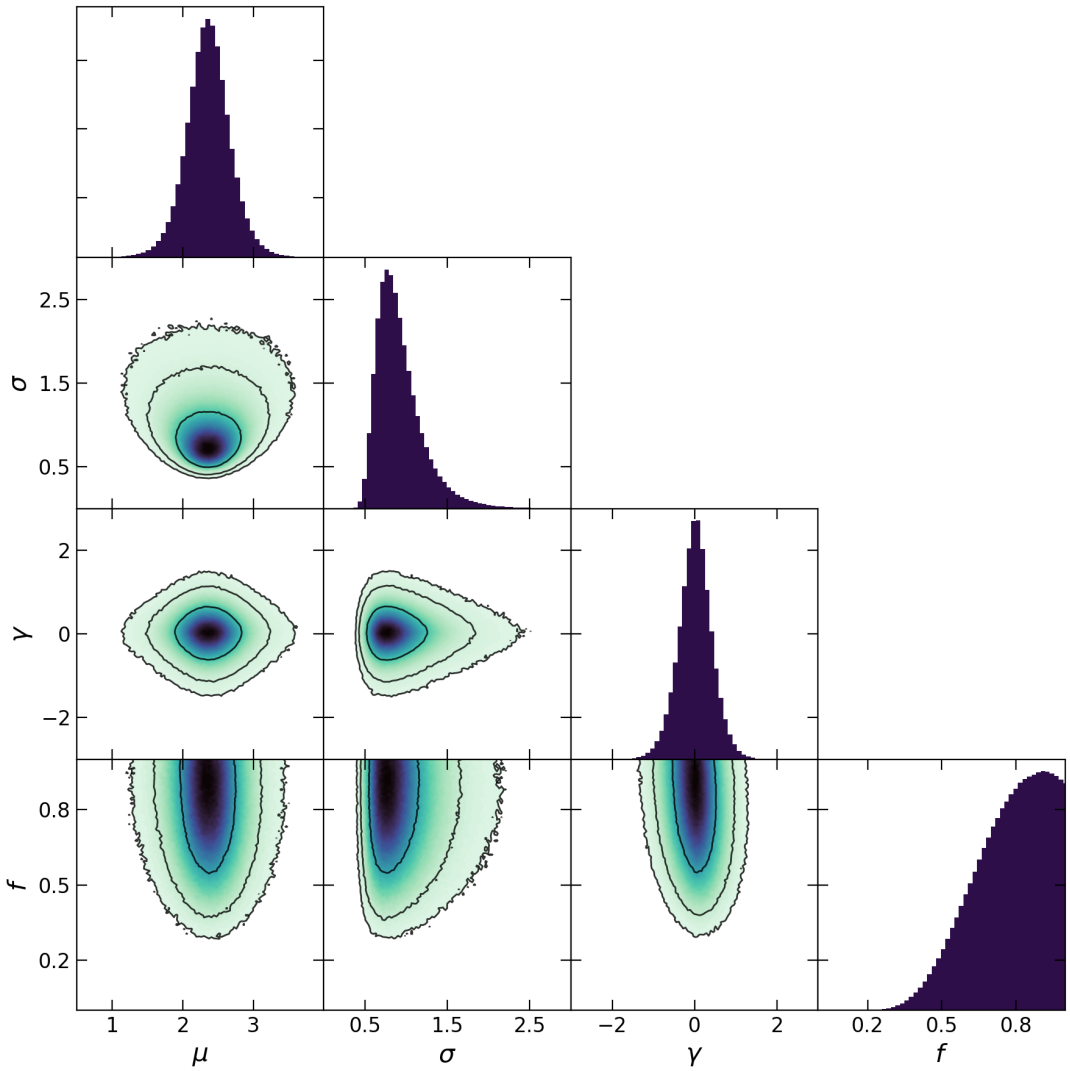

Figure 3.15. Same as Figure 3.14 for the subset of objects with an inner planet or brown dwarf on an orbit shorter than 10 days.

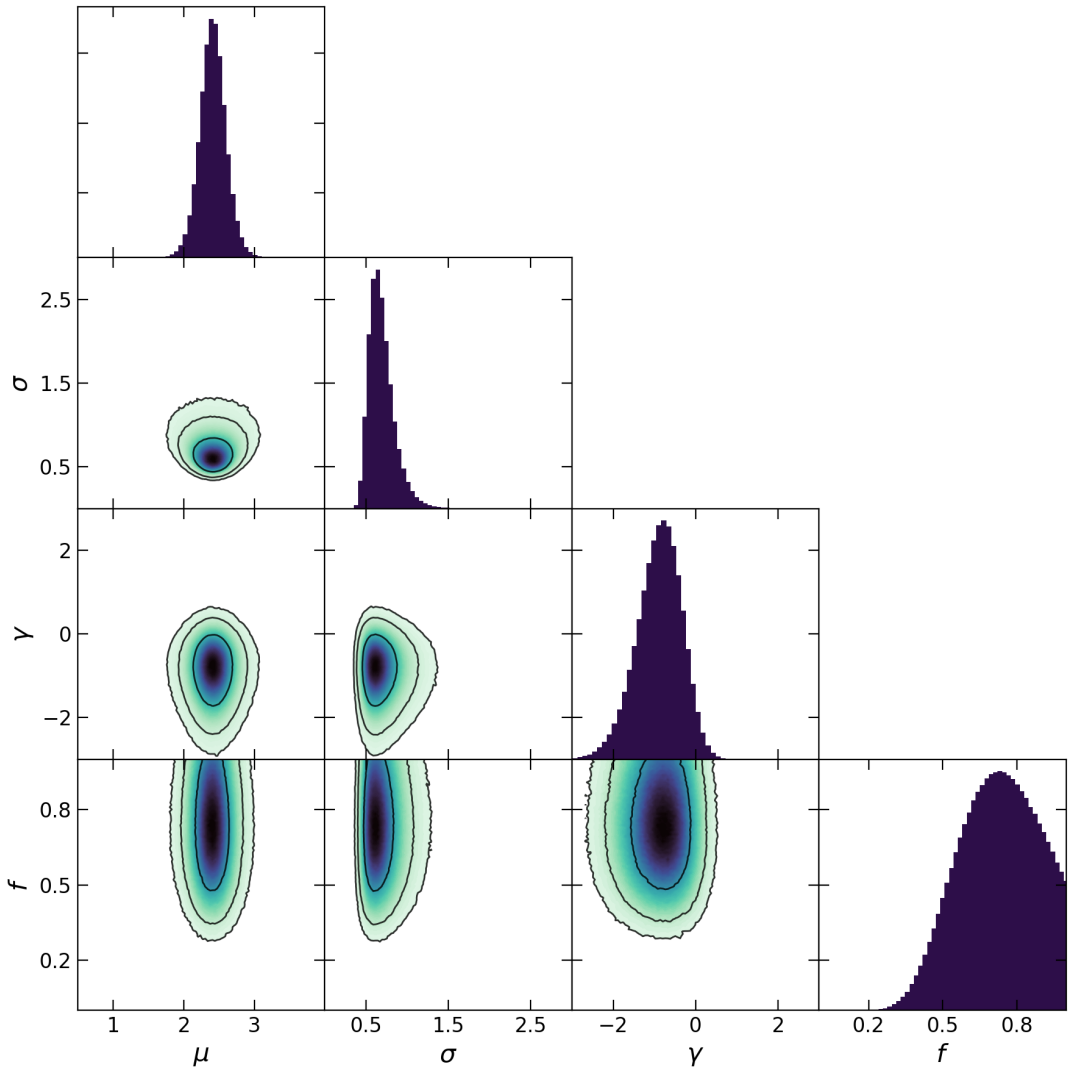

Figure 3.16. Same as Figure 3.14 for the subsample of targets with an inner companion with a period larger than 10 days.

3.8 Analysis and Discussion

3.8.1 Comparison with Field Stars

3.8.1.1 Multiplicity Fraction

Raghavan et al. (2010) provided a comprehensive assessment of the multiplicity properties of Solar-type stars, searching for companions to 454 F6−K3 primaries in the field. Taking into account the completeness limits of their survey, the authors found that about $56 \pm 2\%$ of stars are single, for an overall multiplicity fraction of $44 \pm 2\%$, in good agreement with previous results from Duquennoy & Mayor (1991). Our binary fractions derived in Section 3.7 were limited to separations in the range 20−10,000 AU. We must therefore restrict the overall binary rate from Raghavan et al. (2010) to this separation range in order to compare our findings to the general field population. Taking into account the shape of the distributions obtained by Raghavan et al. (2010) and excluding all companions from that study with separations outside our considered range, the fraction of stars found in binaries or higher-order multiples becomes $36 \pm 2\%$. This is more than twice as low as the binary rate obtained for our full sample of 38 objects, with a 3-σ significance ($f = 79.0^{+13.2}_{-14.7}\%$; see Table 3.8). We also find the value for field stars to be lower than the binary rates derived for our two separate subsets, although these results have a lower significance ($\sim$2.5-σ level) as a result of the smaller number statistics of the individual subsamples. In Figure 3.17 we compare the expected fraction of multiples on this separation range to the posterior distributions obtained for the full sample studied in this work and to the two subsets defined in Section 3.7.2. The plot clearly shows that our derived binary rates are statistically larger than the binary fraction from the overall FGK stellar population.

Zucker & Mazeh (2002) noted a substantial paucity of high-mass planets with short-period orbits around single stars. In contrast, this feature is not observed around binary star systems, which exhibit a prevalence of short-orbit massive planets (Zucker & Mazeh 2002; Eggenberger et al. 2004; Desidera & Barbieri 2007; Mugrauer et al. 2007). Our results are highly consistent with these observations,

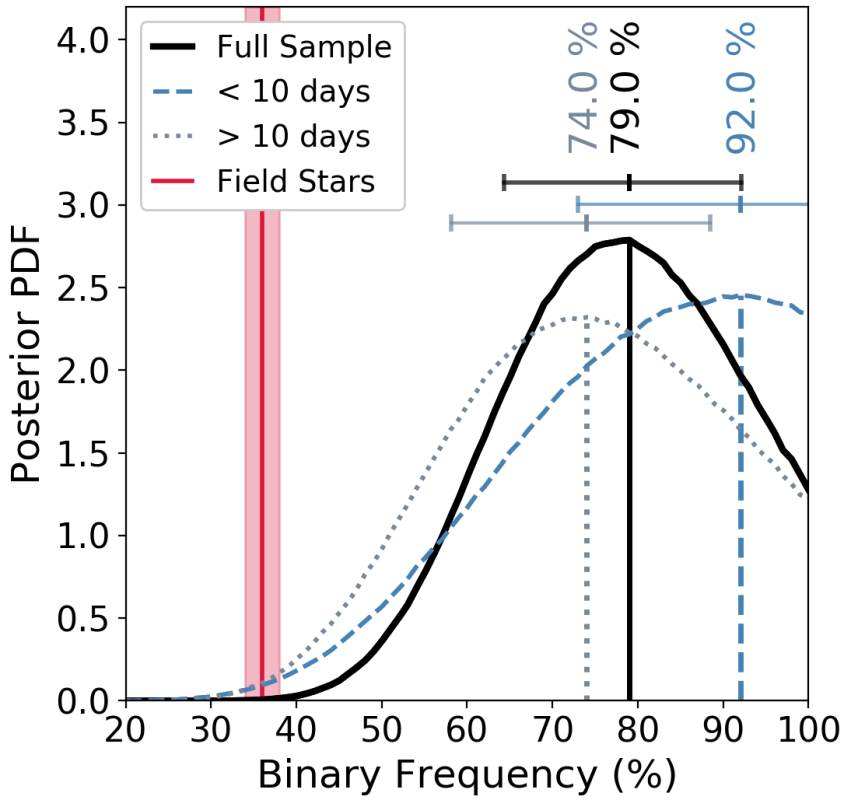

Figure 3.17. Posterior probability distributions obtained from our MCMC analysis for the binary frequency of our full sample of 38 objects (solid black line), the subset of 12 objects with inner companions on orbits shorter than 10 days (dashed blue line) and the subsample of 26 systems with a wider inner companion (dotted grey line). Binary frequencies are constrained over the separation range 20−10,000 AU. The vertical lines show the positions of the most likely value for each distribution and the corresponding values are indicated above. The ranges of the horizontal lines correspond to the 68% intervals of highest probability. The red line and shaded region show the multiplicity fraction of field stars from Raghavan et al. (2010) which we scaled to the same separation range.

suggesting that almost all stars with a > 7 M_{Jup} companion within $\sim$1 AU are part of multiple stellar systems. The statistically higher binary occurrence of hosts to massive planets relative to the general field population indicates that stellar companions may play an important role in the existence of the most massive giant planets and brown dwarfs observed on tight orbits, and that a binary companion may be required to explain their presence. The much higher binary fractions we find for our sample compared to field stars, despite the known biases from transit and radial velocity surveys against close binaries, reinforces the idea of a significant correlation between stellar binarity and the existence of the massive inner companions studied here. While the nature and magnitude of this role are not clear and cannot be established based on this study alone, a number of possibilities have been formulated and explored in the literature to explain the possible influence of binary companions on giant planet formation and evolution. We discuss these theories in Section 3.8.3.

A caveat of this analysis is that Raghavan et al. (2010) studied stars in a volume limited to 25 pc in distance. In order to compare our results to the overall field population, we extrapolated the measurements from Raghavan et al. (2010) out to distances of 500 pc. While the distributions found by Raghavan et al. (2010) are valid for 0.5$-$1.5 $M_{\odot}$ stars, our sample contains two targets from young star-forming regions (one confirmed binary and one not known to have any companion), as well as a number of giants and subgiants. These populations may have different binary statistics than the main sequence stars probed by Raghavan et al. (2010) and the assumptions made in our analysis may not be entirely valid. The field study by Raghavan et al. (2010) was also heavily biased towards G stars, while our sample contains a number of more massive A and F stars, which are expected to have a higher binary fraction, as well as some M-dwarfs, expected to have a lower binary frequency. The mass dependence of stellar binarity could therefore be another factor affecting our results. The field stars sample may also be contaminated with planet hosts, and it must be pointed out that the results presented above are not a comparison between planet-free stars and planetary hosts, but rather an assessment of planet hosts multiplicity properties relative to the general stellar population. That being said, the extremely high binary fraction derived for our studied sample is still a robust and significant result by itself, even if the comparison to field stars may not be fully reliable.

3.8.1.2 Mass Ratio Distribution

Raghavan et al. (2010) found a roughly flat mass ratio distribution for binaries separated by more than 100 days. The value obtained for the power law index in our full sample indicates a slight preference for lower-mass companions, but is fairly consistent with a flat distribution (i.e. $\gamma = 0$, see Table 3.8). Our subset of > 10 day inner companions indicates a moderately larger preference towards low mass ratio companions for these systems, and the subsample of short-period planets was found to exhibit a uniform distribution in wide companion mass ratio. Our probed samples are thus in reasonable agreement with the mass ratios observed around multiple stars in the field, and we find no evidence for distinct populations between our studied targets and the general field population.

3.8.1.3 Separation Distribution

In contrast, we found larger and more significant disparities in binary companion separation between the distributions obtained in Section 3.7 and the expected distribution from FGK field stars, as shown in Table 3.8. Raghavan et al. (2010) reported a lognormal distribution in companion separation peaking at 1.70 in $\log_{10}(a)$, with a Gaussian width of 1.68, corresponding to a broad peak around 50 AU. This is significantly smaller than our derived value of $\mu = 2.39^{+0.14}_{-0.15}$ for our full sample, with a mean located at $\sim$250 AU. We also found a much narrower separation distribution, with a Gaussian width of $\sigma = 0.68^{+0.12}_{-0.10}$. The results obtained for our two subsets are in good agreement with each other and with the full sample (Table 3.8). Figure 3.18 shows the constraints obtained from our statistical analysis on the separation distribution of the multiple systems in our core sample and defined subsets. The red distribution represents the results obtained by Raghavan et al. (2010) for solar-type stars in the field, clearly demonstrating the preference for wider binaries among our targets and the strong deficit of closely-separated systems in our studied sample.

While we restricted ourselves to a 20−10,000 AU separation range to constrain the binary frequency f, the parameters describing the separation distribution (μ and σ) were explored over a broad parameter space. The MCMC walkers would have been able to converge to a distribution peaking near or even inside

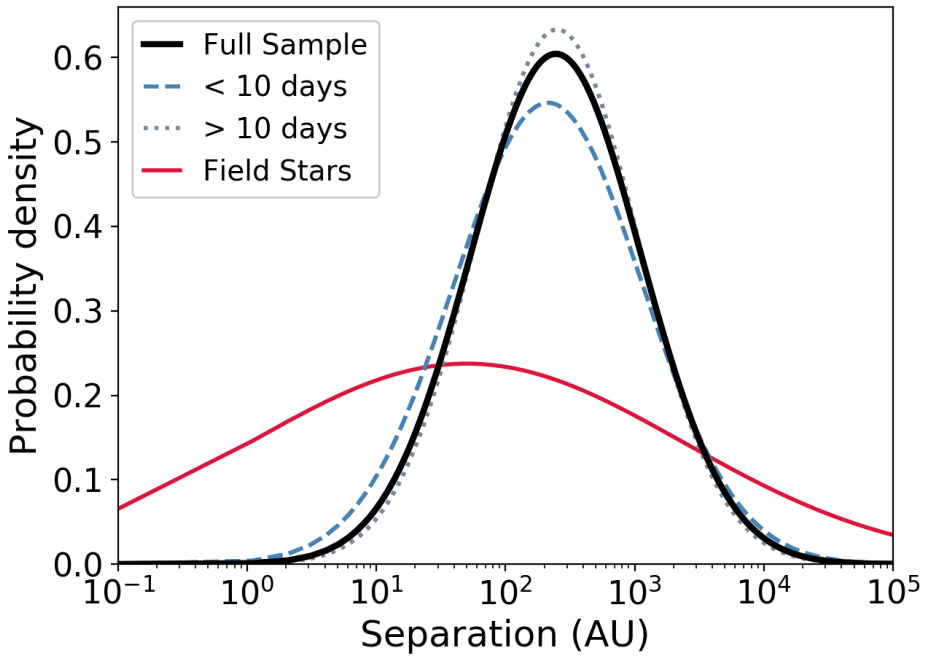

Figure 3.18. Separation distributions of wide binary or hierarchical companions, comparing the output from our MCMC analysis on the full sample of 38 objects (solid black line) and two subsets (dashed blue line and grey dotted line), to the field population from Raghavan et al. (2010) in red. Our obtained density functions show narrower distributions, peaking at larger separations than for field stars.

20 AU had it been compatible with the observed data. As we noted in Section 3.5.3, the lack of tight binaries is unlikely to be the sole result of observational biases and limiting sensitivities. Indeed, we are sensitive to binary companions with separations of 5−20 AU around 20−60% of our targets depending on the system mass ratio, and a number of companions (confirmed and candidates) are retrieved at the same detection probability level at larger separations and low-mass ratios (see Figure 3.13). If the true underlying separation distribution in our sample was comparable to that of field stars, with a broad peak near 50 AU, we would have expected to detect numerous close binaries given the number of wide multiple systems already present in the sample. We thus consider that this observed feature is real and not due to observational limitations.

This deficiency of tight binaries could however be due to selection effects in exoplanet surveys, which are often biased against close binary systems. In

addition, it may be harder to detect planets via the radial velocity method in the presence of a close, massive stellar companion. The spurious assumption that a planet host is single when it is in fact an unresolved binary will also lead to erroneous measurements of the planet's physical properties. A population of massive planets and brown dwarfs in closely-separated binaries could hence exist and be underrepresented or misreported among detected exoplanets. If this is the case, the true multiplicity rate of systems hosting massive, close-in planets or brown dwarfs should then be even higher than what we found here.

Nevertheless, our observations are consistent with previous studies. The shortfall of close binaries among planet hosts has indeed been vastly reported in the literature (Roell et al. 2012; Bergfors et al. 2013; Wang et al. 2014a,b; Kraus et al. 2016) and is generally attributed to a hindrance of planet formation in very tight binaries. While observational constraints remain sparse, the current census is that binarity on scales comparable to the Solar system ($\lesssim 50-100$ AU) has the potential to affect planet formation and evolution. However, different conclusions have been reached on the theoretical side, and it is not clear whether these processes are altered, inhibited or facilitated by the presence of a binary companion and on what separations these effects may take place. This is further discussed in Section 3.8.3.

Another possible explanation for the depletion with tight binary systems among our sample is that the inner planetary and brown dwarf companions to our targets may have formed at much wider separations than their current locations, at radii overlapping with the missing population of binary companions. Such massive planets are indeed expected to form outside at least a few AU for formation by CA (Mordasini et al. 2012), and more likely several tens of AU for GI, in regions of the circumstellar discs that are massive and cool enough to form massive giant planets (Rafikov 2005). If inner companions did form at such wide orbital separations, additional, massive binary companions should not exist within a few tens to hundreds of AU around these systems, which would be reconcilable with our observations. However, as this trend is also observed around systems hosting low-mass planets, for which a formation at very large distances is not required, this may not be the primary phenomenon responsible for the shortfall of tight binaries in our gathered sample.

3.8.2 Binarity as a Function of Planet Properties

3.8.2.1 Binary Frequency Versus Inner Companion Period

In Section 3.7.2, we divided our sample into two subsets in order to investigate possible differences in the demographics of stars hosting planetary or brown dwarf companions within and beyond orbital periods of 10 days. While we found no evidence for distinct binary mass ratio or separation distributions between these two populations, our statistical analysis revealed a possibly larger binary frequency for the subset of shorter-period companions, with a peak at 92%, compared to 74% for the subsample of more widely-separated systems. These results are marginal due to the less stringent constraints we were able to place on the individual subsets, as shown by the broader posterior distributions in Figure 3.17 relative the one obtained for the full sample. Larger sample sizes will be required to confirm this tendency.

This theory is nonetheless supported by the similar trend seen for hosts to lower-mass planets. Surveys searching for wide companions to radial velocity planets from sub-Jupiter masses up to a few M_{Jup} and out to 5 AU found that less than $\sim$25% of these systems were part of binaries or multiple systems (e.g. Raghavan et al. 2006; Ginski et al. 2012), although these surveys may be biased or incomplete. In contrast, studies of slightly shorter-period transiting planets (typically < 100 days) observed rather higher binary fractions, generally around $\sim$50%, for planets of comparable masses (Adams et al. 2012, 2013; Ngo et al. 2016). Furthermore, Tokovinin et al. (2006) found that 96% of spectroscopic binaries with periods < 3 days have a third component, compared to only 34% of systems with periods longer than 12 days, albeit some selection biases may affect these results to a limited extent.

The marginal difference in binary occurrence observed in this work between very short-period transiting planets and brown dwarfs, and the somewhat wider population of radial velocity companions, thus indicates that this trend, if real, may also hold for the very massive inner companions studied here. This trend could suggest that binarity greatly helps the formation or migration of massive giant planets and brown dwarfs observed within $\sim$1 AU, and essentially becomes necessary for these companions to reach orbital periods shorter than 10 days.

3.8.2.2 Binary Frequency Versus Inner Companion Mass

In the final paper of the Friends of hot Jupiters campaign (Knutson et al. 2014; Ngo et al. 2015; Piskorz et al. 2015), Ngo et al. (2016) found that $47 \pm 7\%$ of hot Jupiter systems have a stellar companion between 50 and 2000 AU, a binary rate 3 times higher that for field stars in this separation range. The authors concluded that binary companions on these separations facilitate planet formation or help the inward migration of giant planets. Our study probed higher-mass planets than those considered in that survey, allowing us to examine trends in stellar multiplicity as a function of planet mass, including inside the brown dwarf regime. The Friends of hot Jupiters survey looked at systems with planet masses mostly limited to 4 M_{Jup}. Only five objects with more massive companions were studied in that work, with masses between 7 and 12 M_{Jup}, all of which are part of our selected targets (3 are confirmed multiples: HAT-P-20, WASP-14 and WASP-18; 2 are apparently single: HAT-P-2 and XO-3). The binary fraction derived here for more massive objects was estimated for separations between 20 and 10,000 AU. The corresponding binary rate restricted to the 50−2000 AU separation range becomes $70 \pm 10\%$ for our core sample, 1.5 times larger than the value from Ngo et al. (2016) at the 2.3-σ level. This fraction is 4 times larger for field stars on these separations (see Ngo et al. 2016), with a 5-σ significance. These results are summarised in Table 3.8.

Our results for the shorter-period subset are less significant due to the looser constraints we were able to place on the smaller-sized subsample. We thus only compare previous studies with the binary fraction estimated for the full sample, and keep in mind that hosts to shorter-period planets may have an enhanced binary rate, as discussed previously. Our findings suggest that the trends characterised by Ngo et al. (2016) for hosts to hot Jupiters are also observed and even strengthened for the highest-mass close-in planets and brown dwarfs. These results are in excellent agreement with early observations by Zucker & Mazeh (2002) and Eggenberger et al. (2004), who determined that the most massive planets on orbits of a few days are consistently found in binary systems, suggesting that this planetary population does not exist around single stars.

We note that four targets in our sample have notably high mass estimates (40−60 M_{Jup}) relative to the rest of our sample, namely BD+24 4697, HD 77065, HD

134114 and HD 160508. These objects appear somewhat isolated in the period-mass parameter space in Figure 3.5. Given that their mass measurements are lower limits derived from RV information, their true masses are most certainly even higher. Assuming random orientations of orbits in space (i.e. a uniform distribution in $\sin i$), we may calculate the minimum value for the projected mass that corresponds to a true substellar mass $M_2 < 70$ M_{Jup} at a given confidence level. This translates to $M_2 \sin i < 47$ M_{Jup} for a 68% confidence of a true mass M_2 below the hydrogen-burning limit. These four targets thus have a non-negligible chance of being stellar, in which case they would likely have formed as tight stellar binary systems, rather than brown dwarf companions forming in a circumstellar disc around the host star. None of these systems were found to have a wide binary companion. Excluding these systems from our survey to focus on a confidently-substellar sample would hence have resulted in a higher binary fraction for the remaining sample. This further reinforces the idea that the most massive planets and brown dwarfs forming in discs and detected within $\sim$1 AU require a wide stellar companion to form or evolve to their observed orbital configurations.

3.8.3 Implications for Formation and Evolution Processes

Our results demonstrate a very robust correlation between binary occurrence rate and the sporadic population of close-in massive giant planets and brown dwarf desert inhabitants. Whatever the underlying processes, this concurrence implies that wide binaries must have an influence on the observed population of short-period planetary and brown dwarf companions, which could occur at the stage of formation or during later evolution.

Zucker & Mazeh (2002) were the first to raise the possibility that planets in binaries may have a different mass-period distribution, a trend subsequently confirmed by Eggenberger et al. (2004), Desidera & Barbieri (2007), Mugrauer et al. (2007) and others. Our results are in very good agreement with these studies, suggesting that the most massive planets observed within $\sim$1 AU are almost exclusively found in binary systems, and that this feature is amplified as planets or brown dwarfs reach shorter periods. Desidera & Barbieri (2007) concluded that the presence of a stellar companion on separations < 300 AU may be able to modify the formation or evolution of giant planets. Eggenberger et al.

(2004) also found that massive planets in binary systems with periods shorter than 40 days have very low eccentricities, suggesting that these planets likely underwent some form of migration, possibly induced or driven by outer binary companions, to evolve to their current orbits. Duchêne (2010) investigated these observational trends and concluded that binarity does not affect the formation and growth of planetesimals (see also Batygin et al. 2011 and Rafikov 2013). Duchêne (2010) proposed that planet formation in binaries tighter than $\sim$100 AU occurs at a similar rate but through different mechanisms than around wider binaries and single stars, possibly explaining the observed preponderance of very massive, close-in planets found in binaries but rarely seen around isolated stars.

Simulations by Kley (2001) showed that perturbations from a secondary star may alter the formation and evolution of a planet, in particular by enhancing the mass accretion and orbital migration rates. This could explain why the most massive short-period planets are found in multiple systems, the presence of stellar companions enabling massive planets to achieve smaller orbital separations than the corresponding limit for planets orbiting single stars (Eggenberger et al. 2004). Jensen & Akeson (2003) found that the distribution of disc mass in $>$ 200 AU binary systems among T Tauri stars is not always determined by the stellar masses and may be more asymmetric, with the primary retaining a more substantial disc and the secondary being left with a very low-mass disc. Massive discs around primaries in wide binaries could thus provide larger reservoirs of material for planet formation, which is thought to be favourable to the formation of higher-mass planets, as discussed in Mordasini et al. (2012). The shorter lifetime of circumstellar discs in tight binaries (e.g. Kraus et al. 2012) argues for a formation via gravitational collapse of the circumstellar disc (thousand year timescale) rather than through core accretion, which requires $1-10$ million years. A favoured formation by gravitational disc instability is further supported by the very high masses of the giant planets or brown dwarfs considered here. Furthermore, theoretical work by Boss (2006) suggested that a close stellar companion could rapidly induce gravitational perturbations and trigger the instabilities needed for gravitational fragmentation to proceed, even if the disc is not initially unstable to its own gravity. However, simulations by Forgan & Rice (2009) indicate that, rather than promoting fragmentation, perturbations from an outer companion are more likely to make the disc more stable.

The brown dwarf desert is thought to be a natural feature arising from formation around single stars, where massive objects with brown dwarf masses can only form at wide separations and can be challenging to bring inwards through disc migration alone. By modifying the circumstellar disc environment, allowing for different conditions facilitating *in-situ* formation, and/or by triggering migration processes, the presence of a binary companion could help populate the low-mass end of the brown dwarf desert and explain the puzzling existence of the scarce population of very close-in brown dwarf desert inhabitants.

It is worth noting that over half of detected binary companions in our study have projected separations larger than 200 AU. We therefore argue that wider binaries must also be able to impact, almost to the same degree, the formation and/or evolution of these systems. The processes described above must therefore also be possible from wider separations in order to account for the existence of the planets and brown dwarfs probed in this work. An easy way to facilitate this is to form the inner companions at significantly larger orbital distances (tens of AU), increasing the initial gravitational influence of the outer companion. As mentioned previously, this theory could tentatively explain the shortfall of binaries with separations $< 50-100$ AU, which would then not be expected around such systems.

3.8.4 Scattering and Migration via the Kozai-Lidov Mechanism

One way binary companions could assist the migration of these systems is through the Kozai-Lidov mechanism (Kozai 1962; Lidov 1962). In this alternative scenario to produce hot Jupiters, an outer binary companion on an inclined orbit relative to the orbital plane of the planet triggers periodic oscillations of the planet's eccentricity and inclination (Fabrycky & Tremaine 2007; Wu et al. 2007; Dong et al. 2014; Petrovich 2015). Combined with the effects of tidal dissipation, these secular interactions can result in a very short orbit for the inner companion (Rice et al. 2015), possibly with a high spin-orbit misalignment with its host star. The amplitude of these interactions mostly depends on the initial mutual inclination

between the inner and outer companions (Fabrycky & Tremaine 2007), allowing Kozai-Lidov cycles to be induced by very distant perturbers.

As noted in Section 3.2, the subset of targets with a planet or brown dwarf within a 10-day orbit corresponds to the systems in our sample with a tidal circularisation timescale shorter than ∼15 Gyr, which we consider to be fully consistent with the Kozai-Lidov migration scenario. In Section 3.7.2, we showed that this subsample may have a marginally higher binary fraction than the already very high multiplicity rate observed for our full sample. This is thus compatible with the idea that the inner companions from this subsets could have been driven to their current orbital configurations through Kozai-Lidov oscillations under the effect of wide companions. We also note that 4 of our 5 targets also studied in the Friends of hot Jupiters campaign have high obliquities (placed in the "misaligned" sample in Knutson et al. 2014), a feature often associated with the Kozai-Lidov mechanism.

Unfortunately, full orbital parametrisation, including inclination measurements, is not possible for wide, directly-imaged binaries. Nevertheless, we can determine if the observed wide companions could be responsible for a Kozai-Lidov scattering of the inner planets and brown dwarfs based on their masses and orbital distances. This is done by estimating the minimum companion mass required to excite Kozai-Lidov oscillations on a timescale shorter than the pericentre precession, as was done in Ngo et al. (2016). We adopted a primary stellar mass of 1 $M_{\odot}$ and a mass of 15 $M_{\rm Jup}$ for the inner companion, close to the median of our Kozai-consistent sample. Equating equations (1) and (23) from Fabrycky & Tremaine (2007) for the Kozai-Lidov oscillation timescale and pericentre precession due to general relativity, respectively, we computed in Figure 3.19 the minimum masses and separations necessary to migrate a 15 $M_{\rm Jup}$ companion with initial orbital separations of 1 AU, 5 AU, 10 AU and 20 AU through this scenario. We assumed initially circular orbits for the inner companions and eccentricities of 0.5 for the outer companions, based on the roughly uniform eccentricity distribution between 0 and 1 found by Raghavan et al. (2010) for wide field binaries. We found that almost all detected binary companions could explain the presence of the inner companions in this subset via the Kozai-Lidov mechanism, assuming they formed at separations larger than at least 1−10 AU.

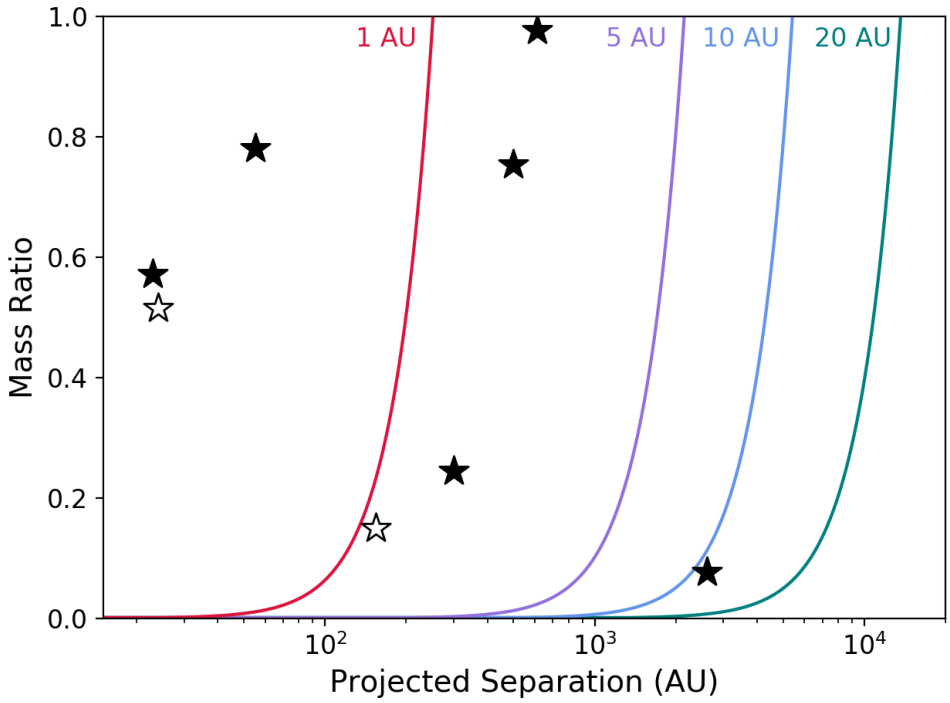

Figure 3.19. Minimum companion mass ratios necessary to excite Kozai-Lidov oscillations for a 15 M_{Jup} planet with an initial semi-major axis of 1 AU, 5 AU, 10 AU and 20 AU around a 1 $M_{\odot}$ star, as a function of wide companion separation. Companions lying to the left of each line are close and massive enough to induce Kozai-Lidov oscillations and overcome the pericenter precession of inner planets at 1, 5, 10 and 20 AU (see text). We overplot the positions of the confirmed (black symbols) and candidate (white symbols) binaries in our Kozai-consistent subsample.

These hierarchical systems are hence compatible with a migration of the inner companions through the Kozai-Lidov scenario based on this simple analysis. However, the subset of objects inconsistent the Kozai-Lidov mechanism, based on our tidal circularisation timescale argument (see Section 3.2), was also found to have a particularly large binary frequency. This suggests that these systems do not primarily migrate via Kozai-Lidov oscillations. This is in good agreement with the theoretical study by Naoz et al. (2012) and observational constraints placed by Ngo et al. (2016), which concurred that only 20−30% of all hot Jupiters can be explained by the Kozai-Lidov migration process. Kozai-Lidov oscillations are therefore unlikely to be the dominant mechanism driving close-in massive planets to their current locations.

3.9 Summary and Conclusions

We have gathered a compilation of 38 planets or brown dwarfs with masses of at least 7 M_{Jup} and orbiting within $\sim$1 AU from their host stars, with the aim of examining the multiplicity statistics of these systems. We searched for wide binary companions to these objects using new direct imaging data, observations reported in the literature and the *Gaia* DR2 catalogue. A total of 16 confirmed multiple systems were found, and another 3 targets have at least one high-probability candidate companion. We report here the discovery of two new comoving companions found in the *Gaia* DR2 catalogue, a wide M7.5 binary companion to WASP-18 and a low-mass mid-K tertiary component to the WASP-14 binary system. We used a robust MCMC statistical approach to constrain the binary properties of our sample, correcting for observational biases and incompleteness. Our main results are summarised below.

1. *A very high binary fraction.* Our analysis revealed a very large binary frequency of $f = 79.0^{+13.2}_{-14.7}\%$ for these outer companions on separations between 20 and 10,000 AU, which is more than twice as high as for field stars on the same separation range, with a 3-σ significance. These results demonstrate that wide binary companions greatly influence the formation or evolution of these close-in massive planets and brown dwarfs. The presence of a binary companion could allow for different natal environments in circumstellar discs, enabling *in-situ* formation at locations where giant planet formation is not normally possible. Stellar companions could also facilitate disc migration beyond the extent normally seen around single stars, or could trigger alternative migration processes through induced secular interactions.

2. *A deficit of close binaries.* The output of our statistical analysis also showed a strong preference for wide binaries, with a peak around 250 AU, compared to $\sim$50 AU for the overall field population. The apparent shortfall of $< 50-100$ AU binaries is consistent with previous studies. It is not clear whether this deficiency indicates that planet formation is inhibited in tight binaries, that our probed planets formed near these separations, or if it is the result of selection biases in exoplanet surveys. Based on these observations, we argue that the mechanisms assisting planet formation or evolution in multiple star systems must

be associated with widely-separated binaries, on distances larger than several hundreds of AU. However, we did find that the Kozai-Lidov mechanism is unlikely to be the dominant underlying process.

3. *A higher binary rate for higher-mass planets.* A comparison with the population of lower-mass planets suggests that binary occurrence increases with planet mass for these close-in objects. This is in good agreement with prior studies that found the most massive planets to be almost exclusively observed in binary systems, and indicates that the role played by binary companions in the existence of these systems becomes more critical for higher-mass planets and members of the brown dwarf desert.

4. *A higher binary rate for shorter-period planets.* Dividing our sample into two subsets, we found that stars hosting planets or brown dwarfs with orbital periods < 10 days have a marginally larger binary rate than systems with longer-period inner companions, consistent with a 100% multiplicity fraction at the 1-σ level. If confirmed, this trend could suggest that the influence of binarity on the formation/evolution of the most massive planetary companions is enhanced for shorter-period planets, and may even become a requirement for the very closest planets and brown dwarfs.

We conclude that wide binary companions have a crucial influence on planet formation and/or evolution and may be responsible for the sporadic population of high-mass planets and brown dwarf desert members observed on very tight orbital configurations, which seem to rarely exist around isolated stars.

3.A Notes on Individual Targets

3.A.1 Bound Systems

11 Com (HD 107383, HIP 60202) is a common proper motion binary found in the Catalog of Components of Double and Multiple Stars (CCDM; Dommanget & Nys 2000). The system has a magnitude difference $\Delta V = 8.0$ mag and an angular separation of $9\farcs1$, corresponding to a projected separation of 850 AU at the distance of 11 Com. From the reported magnitude difference, we infer a mass of 0.7 $M_\odot$ for the secondary using the BT-Settl models (Allard et al. 2012) and stellar parameters given in Table 3.2 for the primary.

30 Ari B (HD 16232, HIP 12184) is part of a hierarchical system. Along with 30 Ari A (HD 16246, HIP 12189), it forms a physical pair with a projected separation of $38\farcs2$ or 1520 AU (Shatsky 2001). Both components of the F5V+F8V 30 Ari system are in turn close binaries. In addition to the 9.88 $M_{\rm Jup}$ planet orbiting 30 Ari B with a period of 335.1 ± 2.5 days (Guenther et al. 2009), Riddle et al. (2015) found that 30 Ari B is also orbited by another companion, 30 Ari C, with a separation of 22 AU ($0\farcs536$). Roberts et al. (2015) subsequently demonstrated that the B-C pair is indeed comoving and inferred a mass of 0.5 $M_\odot$ for the C component, classified as an M1V dwarf (see also Kane et al. 2015). Moreover, the primary component 30 Ari A is itself a spectroscopic binary with a 1.1 day period (Morbey & Brosterhus 1974) and a total mass of 1.32 $M_\odot$ (Guenther et al. 2009).

τ Gem (HD 54719, HIP 34693) is reported in the CCDM and Washington Double Star (WDS; Mason et al. 2001) catalogues to have a candidate companion at a separation of $1\farcs9$ and a magnitude $V = 11$ mag. The system was determined to be most likely bound in (Mitchell et al. 2013), who estimated the companion to be a K0 dwarf with a mass of 0.8 $M_\odot$ separated by 187 AU, if real. Roberts & Mason (2018) recently provided astrometry for this candidate using data obtained in 2004. They found a separation of $1\farcs76$ at a position angle of 162.5 deg. This source is also found in *Gaia* DR2, although it only has a 2-parameter astrometric solution (position only) and therefore does not have parallax and proper motion measurements. From the relative positions of the primary target and candidate

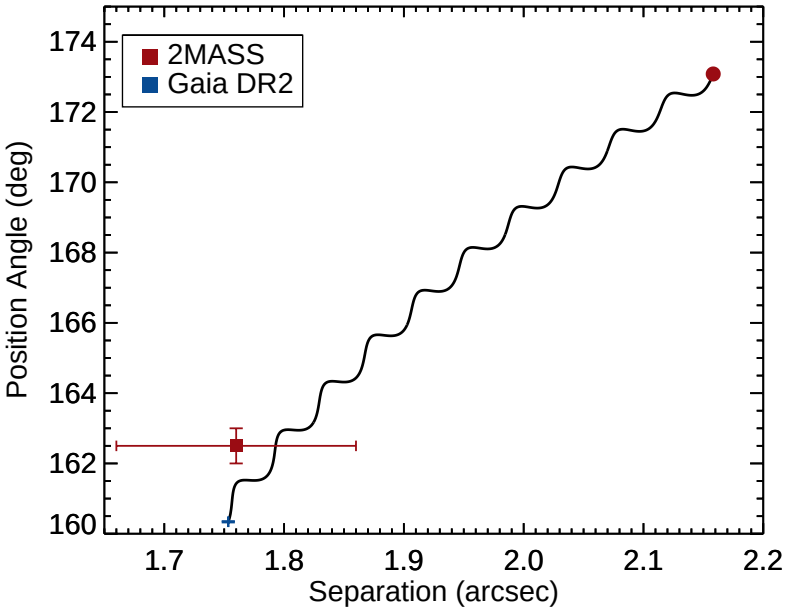

Figure 3.20. Common proper motion analysis of τ Gem and its companion over the ∼10 year baseline between *Gaia* DR2 (red cross) and the astrometry from 2004 data provided by Roberts & Mason (2018) (red square). The black line shows the motion of a background object relative to τ Gem based on the *Gaia* DR2 parallax and proper motion of the primary, and the red dot indicates the expected position of a background object at the epoch of the 2MASS observations. The close companion is clearly found to be comoving with our target.

in *Gaia* we are able to confirm the bound nature of this system based on the 10 year baseline between the 2004 observations and *Gaia* measurements. Figure 3.20 shows the relative positions of of τ Gem and its companion at the two epochs, clearly demonstrating that the two objects share common proper motion and thus confirming that they form a physical pair. The CCDM also reports another candidate to τ Gem at 59″. However this latter source is found in the Naval Observatory Merged Astrometric Dataset (Nomad-I; Zacharias et al. 2004) to have a proper motion inconsistent with that of the primary (see Roell et al. 2012) and we therefore discard this candidate in our survey.

υ **And** (HD 9826, HIP 7513) was found by Lowrance et al. (2002) to be a wide common proper motion pair on a 55″ separation (750 AU). The secondary stellar component υ And B has a J-band magnitude of 9.39±0.03 mag and was estimated by Lowrance et al. (2002) to have an M4.5 V spectral type and a mass of 0.2 $M_{\odot}$.

The primary is the host to 4 close-in planets and substellar companions (Butler et al. 1997, 1999; McArthur et al. 2010; Curiel et al. 2011). This binary system is also mentioned as a physical pair in Raghavan et al. (2006, 2010). Patience et al. (2002) and Roberts et al. (2011) also observed the target but did not have a sufficiently wide field of view in their images to detect the distant companion υ And B. Neither studies report any additional, more closely-separated candidates around υ And A.

AS 205 (V866 Sco, EPIC 205249328) is an extremely young ($\sim$0.5 Gyr) T Tauri star part of a hierarchical system in Upper sco (Reboussin et al. 2015). The K5 dwarf, and brightest component of the system, was found by Ghez et al. (1993) to form a common proper motion system separated by 1$''$.3 (corresponding to 166 AU at the distance of the system) with a low-mass spectroscopic binary (K7+M0; Eisner et al. 2005). Prato et al. (2003) estimated a mass of a mass ratio of $q \sim 0.2$ between the A and BC components, suggesting a mass of $\sim$0.22 $M_\odot$ for the binary secondary.

HAT-P-20 has a red M-dwarf companion at a separation of 6$''$.86 (500 AU) fainter by $\sim$2 mag (WDS catalogue), which was confirmed by Bakos et al. (2011) to form a common proper motion pair using Palomar sky survey archival data. The companion was successfully imaged in the Lucky Imaging survey by Wöllert & Brandner (2015) but was missed in observations from Ngo et al. (2015) due to the restricted field of view of their data. From the reported photometry of the secondary and adopting the stellar parameters in Table 3.2, we derive a mass of 0.57 $M_\odot$ for this companion using the BT-Settl models at the age and distance of the system.

HD 41004 B (HIP 28393) was identified in Santos et al. (2002) and Zucker et al. (2003) as the lowest-mass component of a K1V+M2V visual binary with a 0$''$.54 separation, corresponding to 23 AU. The system has a V-magnitude difference of 3.7 mag and is catalogued as a physical pair in the WDS, CCDM and Tycho-*Hipparcos* catalogues (see Roell et al. 2012). Both components are hosts to close-in substellar companions: the 0.7 $M_\odot$ primary, HD 41004 A, is orbited by a giant planet at 1.33 AU with a projected mass of 2.54 ± 0.74 $M_{\rm Jup}$ (Zucker et al. 2004), while HD 41004 B (0.4 $M_\odot$) hosts a brown dwarf companion at 0.017 AU with a minimum mass of 18.37 ± 0.22 $M_{\rm Jup}$ (Zucker et al. 2003).

HD 87646 A (HIP 49522) is flagged as a binary in the Tycho and *Hipparcos* catalogues with a magnitude difference in the *Hipparcos* V-band of 2.66 ± 0.97 mag. Ma et al. (2016) acquired high-resolution images of the system and found a separation $0\farcs26$ ($\sim$20 AU) between the G-dwarf primary and K-dwarf secondary. The authors derive a mass of 1.12 ± 0.09 $M_\odot$ for the A component and estimate a mass ratio of $q \sim 0.5$ for the system. In addition to the 12.4 M_{Jup} giant planet found at 0.117 AU around HD 87646 A, Ma et al. (2016) also report a 57 M_{Jup} brown dwarf candidate companion on an eccentric 1.6 AU orbit around the primary star.

HD 89744 (HIP 50786) is a wide binary on a $63''$ separation first identified spectroscopically by Wilson et al. (2001) and subsequently confirmed astrometrically to form a common proper motion pair by Mugrauer et al. (2004). The large angular separation of the binary corresponds to a projected separation of $\sim$2460 AU for the distance of the primary. Mugrauer et al. (2004) estimated a mass of 0.08 $M_\odot$ for the secondary, near the hydrogen-burning limit. Raghavan et al. (2006) estimated an L0 V spectral type for the companion. HD 89744 was also observed by Roberts et al. (2011) with Adaptive Optics on the AEOS telescope, who found a faint candidate companion at $5\farcs62$ with a magnitude difference of $\Delta I = 13 \pm 2$ mag that is yet to be confirmed. Other sets of observations with PUEO-KIR at CFHT by Chauvin et al. (2006) or the UFTI data obtained by Mugrauer et al. (2004) do not go deep enough at that separation to retrieve this candidate. Given the observed magnitude difference, we infer a mass of 0.08 $M_\odot$ for this candidate from the BT-Settl isochrones.

HD 114762 (HIP 64426) is a $3\farcs2$ (140 AU) binary pair confirmed to be comoving by Patience et al. (2002) using data from Keck/NIRC and Shane/IRCAL. The binary is also found in the WDS catalogue (Mason et al. 2001). Bowler et al. (2009) further characterised the system, estimating an M9 spectral type and inferring a mass of 0.09 $M_\odot$ for the secondary companion. The companion is also reported in the Adaptive Optics survey by Roberts et al. (2011).

HD 156846 (HIP 84856) is reported as a wide, bound binary in the WDS catalogue, with a separation of $5\farcs1$ ($\sim$250 AU). Tamuz et al. (2008) characterised the companion to the G0 planet host HD 156846 A as an M4 dwarf of mass of 0.59 $M_\odot$.

HD 178911 B (HIP 94075) is the fainter component of a 16.″1 (790 AU) physical pair found in the Tycho-*Hipparcos* catalogue. The primary component HD 178911 AC is itself a 4.9 AU spectroscopic binary discovered by McAlister et al. (1987). The triple system was established to be comoving by Tokovinin et al. (2000) and subsequently confirmed by Raghavan et al. (2006). Tokovinin et al. (2000) estimated a combined mass of 1.9 $M_\odot$ for the AC component, consistent with the value reported in Mugrauer et al. (2007), while the planet host HD 178911 B has a mass of 1 $M_\odot$ (Mugrauer et al. 2007; Bonfanti et al. 2016).

Kepler-13 A (KOI-13) has been extensively targeted with direct imaging (Adams et al. 2012; Law et al. 2014; Shporer et al. 2014; Wöllert & Brandner 2015; Kraus et al. 2016). Szabó et al. (2011) reported and confirmed Kepler-13 as a common proper motion system composed of two massive A stars, also found in the CCDM catalogue. Santerne et al. (2012) found the secondary component to be a spectroscopic binary. Johnson et al. (2014) later constrained the mass of Kepler-13 C to be between 0.4−0.75 $M_\odot$, for a total mass of 1.68 ± 0.10 $M_\odot$ for the BC component, and 1.72±0.10 $M_\odot$ for Kepler-13 A, respectively (Shporer et al. 2014). The A-BC system has a projected angular separation of 1.″15, corresponding to a physical projected separation of 610 AU (Szabó et al. 2011; Adams et al. 2012; Law et al. 2014).

NLTT 41135 was identified by Irwin et al. (2010) as a physically associated companion to NLTT 41136 at 2.″4 separation (55 AU given the parallax of the target). From their characterisation of the system, the authors inferred masses of 0.16 $M_\odot$ for the M5.1 NLTT 41135 secondary, and 0.21 $M_\odot$ for the M4.2 NLTT 41136 primary, respectively.

WASP-14 was found in Wöllert et al. (2015) to have a candidate companion at 1.″4, 5.4 magnitudes fainter than the primary in AstraLux Norte observations at the Calar Alto 2.2 m telescope. Ngo et al. (2015) independently identified the same candidate and were able to confirm the source to be a common proper motion companion to WASP-14 with a mass of 0.33 ± 0.04 $M_\odot$. We also found in this work a distant companion to the system at 1900 AU, identified in the *Gaia* DR2 catalogue. We characterise WASP-14 C as an 0.28 $M_\odot$ K5 dwarf (see Section 3.4.2.1).

3.A.2 Unconfirmed Candidate Companions

70 Vir (HD 117176, HIP 65721) was observed by Roberts et al. (2011) using the Advance Electro-Optical System (AEOS) telescope. The authors report a candidate companion at a separation of 2.″86 (52 AU) around 70 Vir, which they classify as an M5 dwarf or later. With a magnitude difference of $\Delta I = 11.4 \pm 1.2$ mag, we estimate a mass of 0.08 $M_\odot$ for this candidate using the BT-Settl models. Pinfield et al. (2006) reported an L-dwarf another candidate at 43″ (848 AU) from 70 Vir, based on data from the 2MASS All Sky Catalogue. Common proper motion with the primary has yet to be determined for both candidates. We did not find the latter candidate as a *Gaia* DR2 source, most likely too faint for *Gaia*. 70 Vir had also previously been observed by Patience et al. (2002). Observations from this survey are not deep enough to retrieve the faint candidate found by Roberts et al. (2011), and do not have a sufficiently large field of view to detect the wide source detected by Patience et al. (2002). Given the faint infrared 2MASS magnitude of this wide candidate ($J = 15.84 \pm 0.16$ mag), we estimate a mass of 0.07 $M_\odot$ for the candidate companion adopting the age of the primary and the BT-Settl isochrones.

EPIC 219388192 is solar twin in the old Ruprecht 147 star cluster (Curtis et al. 2013; Nowak et al. 2017) which was found was Nowak et al. (2017) to host an eccentric transiting brown dwarf companion. The team acquired Subaru/IRCS+AO188 images of the target to search for nearby companions and found two point sources at 6″ and 7.″5 with contrasts of $\Delta H = 7.1$ mag $\Delta H = 7.7$ mag, respectively. Nowak et al. (2017) estimated that the candidates, if found to be bound, would be late-type M dwarfs with masses less than $\sim$0.1 $M_\odot$. Both sources are found in the *Gaia* DR2 catalogue with separations and position angles consistent with those reported by Nowak et al. (2017). However, given the relatively small proper motion of the target and the short time baseline between *Gaia* DR2 and the direct imaging data ($\sim$1 year), we are not able to confirm or refute either of those candidates. A longer temporal baseline will be required to esetablish the true nature of these candidates. Curtis et al. independently studied the same object and found 4 km s^{-1} offset between the centre-of-mass radial velocity of the star and Ruprecht 147's bulk velocity (announced at the

Cool Stars 19 workshop [1]). As the star's proper motion supports its cluster membership, Curtis et al. also obtained aperture-masking interferometry with Keck II and uncovered a 0.52 $M_\odot$ companion at 82 mas (24 AU) with a magnitude contrast $\Delta K = 2.24$ mag, explaining the observed offset (Curtis et al. private communication).

KELT-1 was found by Siverd et al. (2012) to have a faint candidate companion at 588±1 mas (154±8 AU) based on Keck/NIRC2 AO data. The relative brightness of the candidate was found to be $\Delta H = 5.90 \pm 0.10$ mag and $\Delta K' = 5.59 \pm 0.12$ mag. The reported photometry suggests a mass of 0.2 $M_\odot$ based on the BT-Settl models. Siverd et al. (2012) estimated an M4−5 spectral type and concluded that the companion is physically associated to the primary, with a ∼0.05% probability of being an unrelated background star based on Galatic models, in excellent agreement with our estimates (see Table 3.5). This target was more recently observed by Coker et al. (2018) with the WIYN 3.5 m telescope and by Wöllert & Brandner (2015) with the Calar Alto 2.2 m telescope, although neither of these sets of observations were deep enough the retrieve the candidate identified in Siverd et al. (2012).

3.A.3 Rejected Candidates

HD 162020 (HIP 87330) had previously been observed with NACO by Eggenberger et al. (2007), who found two point sources within 5″ from the star. The first, closer candidate was found by Eggenberger et al. (2007) to be background, while the nature of the second source was inconclusive. With new NACO data for this target, we were able to refute the bound nature of this companion based on the *Gaia* DR2 astrometry of the primary and a decade-long baseline between the archival and new observations (see Figure 3.4). Our proper motion analysis of HD 162020 and this rejected candidate is presented in Section 3.3.3.

HD 168443 (HIP 89844) was observed with SPHERE at VLT in the survey conducted in Moutou et al. (2017). Three point sources are reported within 2.″5 of the primary in that paper. Moutou et al. (2017) found that given the galactic

[1] `https://doi.org/10.5281/zenodo.58758`

latitude of the target and the crowded field of view at wider separations around this object, the three identified sources are likely background contaminants due to the local environment of HD 168443. Using the Trilegal galactic models (Vanhollebeke et al. 2009) and following the approach described in Section 3.4.1, we infer probabilities $< 1\%$ for any of these three sources to be physical associated to the primary and do not consider them as bonafide candidates for the purpose of our study.

XO-3 has a faint candidate companion ($i = 18.43$ mag) first reported in Bergfors et al. (2013). The widely-separated candidate ($6''$ or 1500 AU projected separation) was found by Bergfors et al. (2013) to likely be a physically unrelated background object if it is a main-sequence star based on a colour analysis, although the authors mention the possibility of a coeval white dwarf. This target was observed with Keck/NIRC2 in Ngo et al. (2015) but was not retrieved in the field of view of the images acquired for that survey. Wöllert & Brandner (2015) also imaged XO-3 in a search for wide companions and detected the same source in AstraLux Norte data. A faint source is found in *Gaia* DR2 ($G = 18.45$ mag) at the same angular separation and position angle as the detected candidate. Given the comparable photometry and the short timespan between the *Gaia* DR2 epoch (2015.5) and the observations from Wöllert & Brandner (2015) (March 2015), we conclude that this is indeed the same source. The *Gaia* DR2 source (GDR2 4706504576983112 96) has a full 5-parameter astrometic solution and has parallax and proper motion measurements highly inconsistent with those of XO-3 in *Gaia* DR2. We thus conclude that it is an unrelated background object and rule out this candidate.

3.A.4 Null Detections

BD+24 4697 (HIP 113698) was observed with Gemini North/NIRI as part of this survey. Our data did not reveal the presence of any candidate companion within the field of view and detection limits of our observations.

CI Tau (EPIC 247584113) is a $\sim$2 Myr T Tauri star located in the Taurus star-forming region with an infrared excess in its spectral energy distribution, in addition to a circumstellar disc resolved by Andrews & Williams (2007). It

was observed by Uyama et al. (2017) with the Subaru Telescope, using the NIR camera HiCIAO together with the AO188 adaptive optics system. The authors did not find any candidate companion within the 20″×20″field of view of their observations. This targets is also reported to be single in Kraus et al. (2012) based on analyses of 2MASS images, as well as in the *HST* young binary survey conducted by White & Ghez (2001).

HAT-P-2 (HD 147506, HIP 80076) was found by Lewis et al. (2013) to have a long-term radial velocity trend, suggesting the presence of an outer companion in addition to its known 9 M_{Jup} planet on an eccentric 5-day orbit. Bonomo et al. (2017) subsequently placed lower limits on the period and mass of this possible outer companion of $\geqslant$ 49.2 yrs ($\sim$13 AU) and $\geqslant$ 39.5 M_{Jup} based on radial velocity data. This is consistent with results from Knutson et al. (2014), who constrained the companion properties to $M_2 \sin i = 8{-}200$ M_{Jup} and $a = 4{-}31$ AU. Observations with NIRC2 on Keck II (Lewis et al. 2013; Ngo et al. 2015) and with AstraLux Norte (Bergfors et al. 2013) did not reveal any companion but only excluded the presence of a roughly equal-mass binary from $\sim$10 AU and companions near the hydrogen-burning limit from $\sim$50−100 AU. A companion responsible for the observed RV trend could therefore still remain undetected.

HD 5891 (HIP 4715) was observed by Ginski et al. (2016) with the Lucky Imaging instrument AstraLux at the Calar Alto 2.2 m telescope and did not find any companion, achieving contrasts of 4 mag at 1″ and magnitude differences of 9.5 mag at 5″.

HD 33564 (HIP 25220) is listed in the CCDM as a 25″ binary although the 2 components display inconsistent proper motions and do not form a physical pair (Roell et al. 2012). Ginski et al. (2012) acquired observations of HD 33564 and excluded the presence of companions down to the substellar limit on separations of 20−100 AU. This star is also reported as a single object in Eggleton & Tokovinin (2008).

HD 77065 (HIP 44259) is one of the two targets we observed with NIRI on Gemini North. We did not find any candidates around this target in our obtained images, ruling out the presence of companions at the hydrogen-burning limit from separations of 5 AU, and substellar companions with masses $>$ 40 M_{Jup} from separations of 70 AU.

HD 104985 (HIP 58952) was observed with the lucky imaging camera AstraLux on the Calar Alto 2.2-m telescope by Ginski et al. (2012). The team did not find any candidate around this target.

HD 134113 (HIP 74033) is part of the Arcturus moving group. We observed this target with the WIYN telescope and did not find any companions within our detection limits. HD 134113 has no previous direct imaging observations reported in the literature.

HD 156279 (HIP 84171) was observed by Ginski et al. (2016) with the AstraLux instrument on the Calar Alto 2.2-m telescope. No companion was detected in the obtained lucky imaging data.

HD 160508 (HIP 86394) was observed as part in this work using the WIYN imaging facilities. We did not detect any companions around this object within the field of view of our images.

HD 180314 (HIP 94576) was targeted by Ginski et al. (2016) with lucky imaging at Calar Alto. No source was uncovered in the obtained data within 12″, down to low-mass stellar companions.

HD 203949 (HIP 105854) was observed with VLT/SPHERE in Moutou et al. (2017). That survey does not report the detection of any candidates around this target.

WASP-18 (HD 10069, HIP 7562) was part of our observed sample and no source was detected in the field of view of our images. This object had already been observed with Keck II/NIRC2 as part of the study conducted by Ngo et al. (2015). No candidate was reported around WASP-18 in that survey. We achieved a better contrast than that reported in Ngo et al. (2015), both at diffraction and background-limited separations, and our observations allowed us to rule out the presence of lower-mass companions around WASP-18. A comoving object was however found in this work in GDR2 at a very large projected separation of 3300 AU, outside the field of view of the direct imaging data (26.″7). We estimated a spectral type of M7.5 for the secondary, and a mass of 0.092 $M_{\odot}$ (see Section 3.4.2.2 for our detailed analysis of the new companion).

3.B Gaia DR2 Analysis

In Section 3.4.2 we searched for sources in the *Gaia* DR2 catalogue with fractional differences of less than 20% in parallax and at least one proper motion component relative to the *Gaia* astrometry of our targets. Using these selection constraints, we identified a total of 11 binaries in *Gaia* DR2 among the targets in our sample, 9 of which were previously known. We now examine those systems more carefully as well as the remaining systems from Table 3.4 in order to evaluate and refine our selection criteria, if needed.

3.B.1 Binary Completeness

For completeness, we first searched for other known binaries in our sample that may have been missed by our chosen constraints. A total of 7 known, comoving systems are missing from our identified *Gaia* binaries, corresponding to the companions with no parallax or proper motion listed in Table 3.4. From those, 30 Ari BC, HD 41004 AB and HD 87646 AB have angular separations $< 1''$, the resolving limit of *Gaia* DR2, and were therefore missed because of angular resolution limitations.

While near-equal brightness binaries ($\Delta G < 1$ mag) are typically resolved with *Gaia* from separations of $\sim 1''$ (e.g. Kepler-13, $1''.15$ separation, Δmag = 0.2 mag; AS 205 AB, $1''.3$, $\Delta G = 1$ mag), larger separations are required to resolve lower mass ratio binaries. Ziegler et al. (2018) estimated that companions with ΔG down to $\sim$6 mag are consistently recovered at separations of $3''-5''$, with a roughly linear decrease in the recoverable magnitude difference between $1''-3''$. Based on these results, it is not surprising that systems such as WASP-14 AB ($1''.45$, $\Delta J = 5.2$ mag) and HD 114762 AB ($3''.2$, $\Delta J = 7.6$ mag) are not retrieved in *Gaia* DR2. We thus conclude that these companions are missing from our *Gaia* binary sample because they are fainter than the completeness level of *Gaia* DR2.

Finally, the last missing binaries are τ Gem AB and HAT-P-20 AB. In both cases, the two binary components were found to be *Gaia* DR2 sources, but the fainter component only had a two-parameter astrometric solution (position only) rather

than the full 5-parameter solution (position, parallax and proper motion). With no parallax and proper motion measurements, we were not able to select these systems in our analysis and we attribute the fact that we missed them to the remaining incompleteness of *Gaia* DR2 and not to our selection criteria. We thus conclude that our selection method successfully identified all known binaries that were recoverable.

3.B.2 Binaries with Excessive Astrometric Disparities

Table 3.6 reports the relative differences in parallax and proper motion, together with their associated uncertainties, obtained for all identified *Gaia* binaries (see also Figure 3.7). While the majority of the errors are comparable in size to the calculated values themselves, all systems remain fully within our arbitrary cuts at 20% at the 1-σ level (with the exception of the newly discovered WASP-18 AB system which is discussed in Section 3.4.2.2).

A number of binaries in Table 3.4 are part of hierarchical systems and we find that 4 of the 9 previously known *Gaia* systems have an unresolved component in *Gaia* DR2 (30 Ari BC, AS 205 BC, HD 178911 AC and Kepler-13 BC), which correspond to the blue stars in Figure 3.7. Looking at the positions of these specific systems in the parameter-space from Figure 3.7, we find that they have the largest relative offsets in parallax and/or proper motion, and are the only systems for which the relative difference in proper motion was larger than our 20% threshold in one of the coordinates (outside the shaded area in Figure 3.7).

This is consistent with the idea that unresolved components can have a significant effect on the measured astrometry of binary pairs, reinforcing the argument for loose constraints in order to ensure that such hierarchical systems are not missed. With the exception of AS 205 and HD 178911, all known binaries detectable by *Gaia* would also have made a more stringent cut at $\sim$10% in the relative difference in parallax and in one of the proper motion components. Furthermore, the 5 known binaries that are not known to have an unresolved component (blue circles in Figure 3.7) also make that 10% cut in both proper motion components. We thus conclude that most binaries should have relative discrepancies of $< 10\%$ in all astrometric parameters (ϖ, $\mu_{\alpha*}$ and μ_δ), while systems agreeing to within

20% in parallax and in one of the proper motion coordinates are likely to be hierarchical systems with an unresolved component.

We note that such wide companions are not necessarily presently bound systems. Formerly physically associated components of a binary system may continue to travel along a nearly identical trajectory. However, we are seeking in this study companions that may have affected the formation or early evolution of inner companions and therefore also consider as bonafide any pair that previously constituted a bound system. We also point out that such a configuration would likely result in small discrepancies in the observed astrometric parameters of the individual components, an additional argument for the loose constraints considered above. In conclusion we trust that systems passing the selection criteria described above have consistent astrometric parameters and kinematics, and may be treated as binaries for the purpose of this work.

4

Finding and Characterising the Orbit of Directly-Imaged Companions with the New COPAINS Tool

Contents

4.1 Introduction

The majority of known exoplanets and brown dwarf companions to stars were discovered using indirect detection techniques, such as the radial velocity (RV) and transit methods (Charbonneau et al. 2007; Marcy et al. 2008; Mayor & Udry 2008). These approaches require observations covering multiple full orbital periods to confirm candidates, and are thus not suitable to identify wide-orbit companions, on orbital separations larger than a few AU. Direct imaging, on the other hand, is sensitive to companions > 1 M_{Jup}, at separations of tens to thousands of AU (see Bowler 2016 for a review).

Only a small number of directly-imaged substellar or planetary-mass companions are known, as a result of the low occurrence rates of wide brown dwarfs and giant planets, combined with the current limitations of high-contrast imaging instruments (Biller et al. 2007; Lafrenière et al. 2007; Metchev & Hillenbrand 2009; Nielsen & Close 2010; Vigan et al. 2012; Biller et al. 2013a; Rameau et al. 2013; Galicher et al. 2016; Vigan et al. 2017). With little information available about the demographics of these populations, target selection is a challenging process. Direct imaging surveys typically target young stars (< 100 Myr) to assure that the sought planets are still bright and increase the chances of detection, but selected stars generally have no a priori evidence for companions. Formation theories can provide indications of stellar properties that might be correlated or more favourable to planet formation (e.g. stellar mass, metallicity; see Alibert et al. 2011; Mordasini et al. 2012) and samples can be gathered based on such stellar characteristics.

Alternatively, a more robust approach would consist in identifying independent, physical signs of the presence of a hidden companion to select promising targets in direct imaging campaigns. For example, in the TRENDS survey Crepp et al. (2012b) searched for direct imaging companions to stars exhibiting long-term radial velocity accelerations (see also e.g. Kasper et al. 2007; Janson et al. 2009; Rodigas et al. 2016). However, as RV is unsuitable for young, active stars, these campaigns focused on older stars and the companions imaged are mostly in the stellar and substellar regimes. Precision astrometry can also be used to investigate nonlinear changes in stellar positions induced by an unseen

companion. A significant discrepancy in proper motion measurements between different catalogues is a good indication of the presence of a perturbing body, and may be used to select potential binaries (e.g. Makarov & Kaplan 2005; Tokovinin et al. 2013). So far, this method has mostly been restricted to stellar binaries due to the limited precision of astrometric measurements.

While the RV and transit detection methods allow for prompt characterisations of orbits, direct imaging only provides measurements of a companion's relative position and luminosity. Only a small fraction of the full orbit is observed for long-period, directly-imaged companions to stars, and the small orbital coverage available is generally insufficient to place strong constraints on the orbit based on imaging data alone. As a result, masses for these objects are typically estimated from evolutionary models, which carry very high uncertainties especially at young ages (Bowler 2016). The estimated masses then rely entirely on the knowledge of stellar ages, which are not always available, especially for field stars (Jeffries 2014; Soderblom et al. 2014). The resulting masses for directly-imaged exoplanets and brown dwarfs are therefore heavily model-dependent and highly uncertain.

Alternative determinations of masses are thus crucial to circumvent the large uncertainties introduced by models and refine the theories. The combination of relative astrometry with RV data can provide robust orbital constraints and the measurement of dynamical masses (e.g. Crepp et al. 2016; Bowler et al. 2018), although this approach is limited by the small overlap between the distinct age and separation domains probed by the RV and direct imaging methods. Alternately, absolute astrometric measurements may be used to complement the information derived from direct imaging (and RV) data to obtain model-independent mass constraints for substellar companions. If relative astrometry can provide the total mass of a system, the addition of absolute astrometric measurements to the analysis enables the key determination of mass ratios. Individual masses have been achieved this way for visual, tight brown dwarf binaries via careful, long-term orbital monitoring (Liu et al. 2008; Dupuy et al. 2009, 2015; Dupuy & Liu 2017; Konopacky et al. 2010). More recently, proper motion measurements were used to refine the constraints on the orbits and dynamical masses of substellar companions to stars, in conjunction with direct imaging data and RV measurements (Brandt et al. 2018; Calissendorff & Janson 2018; Dupuy et al. 2019).

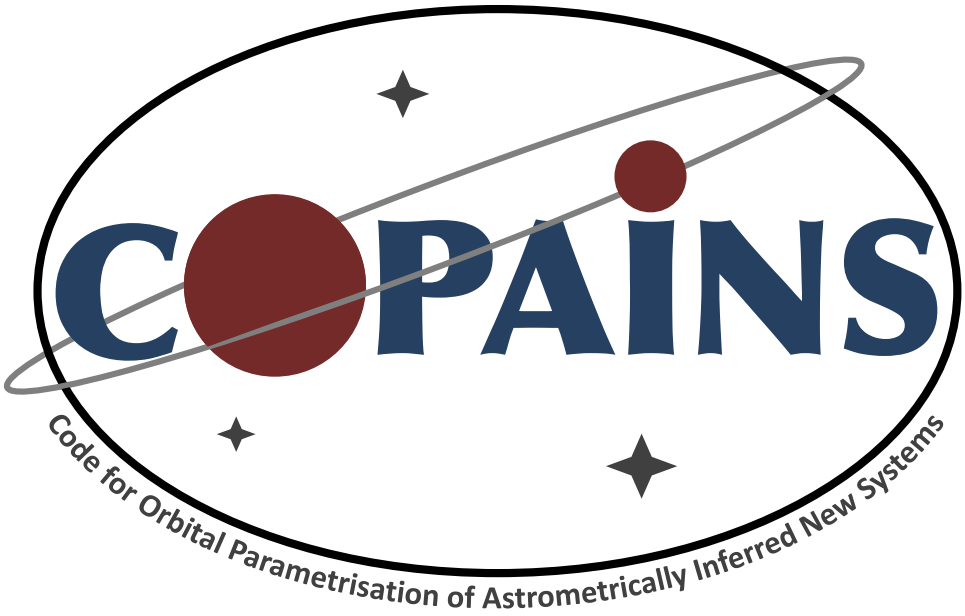

Figure 4.1. Logo of the COPAINS tool: Code for Orbital Parametrisation of Astrometrically Inferred New Systems.

In this work, we present a new tool developed to address the target selection and mass estimates problems encountered in direct imaging studies: COPAINS (Code for Orbital Parametrisation of Astrometrically Inferred New Systems; logo in Figure 4.1). By exploiting the synergy between direct imaging and astrometry, our innovative approach provides a robust, informed selection method for promising systems in direct imaging searches, as well as enabling the orbital characterisation and the measurement of dynamical masses for identified companions. We present the selection functionality of the code in Section 4.2. We provide a detailed assessment of the efficiency of the selection method, together with examples of application of our approach to known targets. In Section 4.3, we introduce the part of the code designed to constrain the orbital elements and masses of directly-imaged companions, tested and validated using well-constrained systems. Our results on the performance of both aspects of the tool are summarised in Section 4.4.

4.2 Selecting Direct Imaging Targets with COPAINS

4.2.1 $\Delta\mu$ Astrometric Binaries

The wobble of a star in its orbit induced by the gravitational pull of a companion is one of the most efficient way to detect the presence of that companion. When this wobble is (partly) along the line of sight, it can be observed through a periodic Doppler effect in the radial velocity of the host star. Hundreds of radial velocity planets have been identified via this technique, mostly on short orbital separations, where the method is most successful (Charbonneau et al. 2007). When the movement of the host star is in the plane of the sky, it can be visible as a change in the star's apparent position. This effect is illustrated in Figure 4.2, which shows the astrometric displacement of the two components of a binary around the center of mass of the system. A nonlinear apparent motion for a star may thus serve as evidence for the existence of a gravitationally bound, unseen companion.

The long orbital periods of most directly-imaged companions, together with the large jitter induced by the strong activity of young stars, make high precision radial velocity measurements extremely challenging for these targets. In contrast, the detectability of astrometric signatures increases with separation, while youth and stellar activity are not an issue for positional measurements. This makes astrometry highly compatible with direct imaging in terms of the optimal parameter space probed. Changes in stellar positions have successfully been used to identify stellar binaries (Makarov & Kaplan 2005; Tokovinin et al. 2012), although up to now, astrometric determinations have been too inaccurate to detect lower-mass companions inside the substellar regime.

The difference $\Delta\mu$ between the instantaneous velocity (tangential vector to any point on the blue curve in Figure 4.2) of a star of mass M_1 and the true barycentric motion (dashed black line) is given by Equation 4.1 (Makarov & Kaplan 2005):

$$\Delta\mu \leq \frac{2\pi\,\varpi\,\mathcal{R}_0 M_2}{\sqrt{a\,M_{tot}}}, \tag{4.1}$$

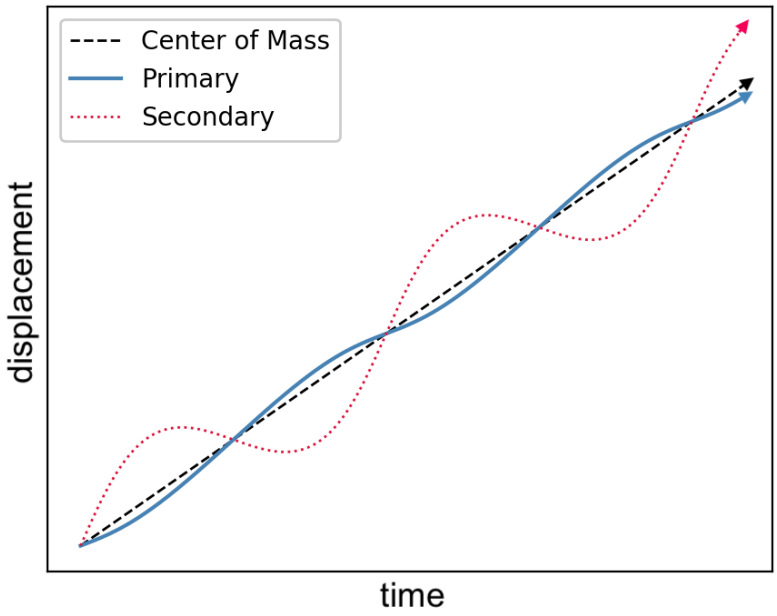

Figure 4.2. Example of the astrometric wobble of binary components around the centre of mass of the system. Measurements of the displacement of the primary star (solid blue line) relative to the center of mass (dashed black line) can be used to infer the existence of the hidden secondary companion (dotted red line).

where ϖ is the parallax of the system (in mas), M_2 the mass of the secondary (in $M_\odot$), $M_{tot} = M_1 + M_2$ the total mass of the system (in $M_\odot$), and a the total semi-major axis of the binary (in AU), providing a $\Delta\mu$ in mas yr^{-1}. $\mathcal{R}_0$ is the time-dependent orbital phase factor, given by the eccentricity e and the eccentric anomaly E:

$$\mathcal{R}_0 = \left(\frac{1 + e\cos E}{1 - e\cos E} \right)^{1/2} . \tag{4.2}$$

The inequality in Equation 4.1 arises from projection effects in cases of inclined orbits relative to the plane of the sky. More massive components are required to produce the same projected astrometric deviations (Makarov & Kaplan 2005). As a result, Equation 4.1 provides an upper limit on the observable offset in apparent velocity, which varies between zero and this maximum value for inclined orbits. For face-on orbits, the inequality becomes an exact equation.

Short-term proper motion measurements such as those provided by the *Hipparcos* mission (∼3.3-yr baseline; ESA 1997) and the *Gaia* DR2 catalogue (∼1.8-yr time-span; Gaia Collaboration et al. 2018b) can capture this reflex orbital motion

caused by a companion on a sufficiently long period. On the other hand, long-term astrometric measurements like those from the Tycho-2 catalogue (almost a century timescale; Høg et al. 2000) and the Tycho-*Gaia* Astrometric Solution (TGAS; Michalik et al. 2015) subset of the *Gaia* DR1 catalogue (∼25-yr baseline; Gaia Collaboration et al. 2016) can provide values which are closer to the true centre-of-mass motion of the system. In this case, the difference in proper motion between a short and a long-term astrometric catalogue will be well approximated by the $\Delta\mu$ variable given in Equation 4.1. A significant discrepancy in proper motion between measurements acquired over very different time baselines can therefore probe the acceleration of a star in its inertial frame of reference. This can in turn be used to highlight the presence of a hidden companion and be connected to the orbital properties of the system via Equation 4.1. We refer to stars exhibiting significant proper motion offsets between various astrometric catalogues as $\Delta\mu$ stars.

Several of such $\Delta\mu$ binaries have been identified by comparing the *Hipparcos* and Tycho-2 catalogues (e.g. Makarov & Kaplan 2005). Targeted searches have subsequently led to the imaging of the unseen companions, mostly stellar, compatible with the measured astrometric trends (see e.g. Tokovinin et al. 2012, 2013). Thanks to the excellent precision of the new ESA *Gaia* satellite, the accuracy of astrometric measurements is finally sufficient to exploit stellar displacements due to the influence of lower-mass companions. This method can now be used to unveil much smaller trends, pointing towards the presence of companions in the brown dwarf and planetary mass regimes, well within the reach of current direct imaging technologies.

4.2.2 Selection Success Rate

In this section, we quantify the success rate of a selection procedure based on this $\Delta\mu$ approach via two separate analyses. In Section 4.2.2.1, we investigate the binary fraction of $\Delta\mu$ stars relative to the overall stellar population, based on existing catalogues of stellar multiplicity and *Gaia* DR2. In Section 4.2.2.2, we check whether our selection method would have selected targets with known directly-imaged substellar and planetary companions.

4.2.2.1 Binary Fraction of $\Delta\mu$ Stars

In order to estimate the multiplicity of $\Delta\mu$ stars compared to stars showing no significant changes in proper motion between long and short-term astrometric catalogues, we consider the Tycho-2 and *Gaia* DR2 catalogues. The former catalogue is one of the largest archival data sets providing proper motion measurements acquired over timescales close to a century (Høg et al. 2000), while the highly precise astrometric data from *Gaia* DR2 are based on only 22 months of observations (Lindegren et al. 2018). The combination of these two catalogues thus provides the best estimates of instantaneous and barycentre motions. $\Delta\mu$ measurements obtained from these catalogues are expected to be well approximated by Equation 4.1 for systems with a wide range of orbital periods. We note however that any proper motion discrepancies over time would highlight the presence of a perturbing object, even if the observed changes in proper motion do not correspond to the $\Delta\mu$ in Equation 4.1. As a result, any combination of astrometric catalogues can be used to identify stars with invisible companions. In particular, with the extremely high precision of *Gaia* relative to previous astrometric missions, using the first two *Gaia* data releases might provide the best chance at picking up on very small trends induced by very low-mass planetary companions, as discussed in Section 4.2.2.2 below.

We obtained the entire cross-match of the Tycho-2 and *Gaia* DR2 catalogues, and selected all targets with *Gaia* DR2 parallaxes larger than 20 mas, so as to construct a volume-limited sample within 50 pc. We then removed all targets that lacked proper motion measurements in either catalogue, and excluded sources with excessive astrometric noise in *Gaia*, adopting a 10% relative precision criterion in parallax and proper motion as was done in Gaia Collaboration et al. (2018a). This provided us with a sample of 8738 objects.

For each star in this sample, we then checked its multiplicity flag in the *Hipparcos* main catalogue (ESA 1997), and its presence in the Catalog of Components of Double & Multiple stars (CCDM; Dommanget & Nys 2000) and Ninth Catalogue of Spectroscopic Binary Orbits (SB9; Pourbaix et al. 2009). We also queried the position of the star in the *Gaia* DR2 catalogue and searched for comoving sources within a angular radius corresponding to a projected separation of 10^4 AU given the parallax of the star. We define comoving objects in *Gaia* as sources

with a fractional difference of $< 20\%$ in parallax and at least one of the proper motion coordinates, following the approach from Chapter 3 to search for wide binary companions in *Gaia* DR2. This ensures that binary components showing significant disparities in their kinematics due to their gravitational influence on one another (i.e. the $\Delta\mu$ stars of interest here) do get selected as binaries in this analysis. In a statistical search for wide binaries in TGAS based on parallaxes and proper motions, Andrews et al. (2017) found a contamination rate from random chance of alignment of $\lesssim 5\%$ for binaries with projected separations smaller than 4×10^4 AU. We therefore trust our binary selection criteria in *Gaia* DR2 to select bonafide systems and consider that our resulting sample of *Gaia* binaries is unlikely to be polluted by unassociated random alignments.

We then calculated the total change in proper motion between Tycho-2 and *Gaia* DR2 for each star, given by:

$$\Delta\mu = \sqrt{\left(\mu_{\alpha*,\mathrm{T}} - \mu_{\alpha*,\mathrm{G}}\right)^2 + \left(\mu_{\delta,\mathrm{T}} - \mu_{\delta,\mathrm{G}}\right)^2}\,, \tag{4.3}$$

where the subscripts T and G correspond to Tycho-2 and *Gaia* DR2, respectively. The corresponding uncertainty $\sigma_{\Delta\mu}$ can then be calculated from the quadrature sum of the component uncertainties, following standard error propagation rules.

The fraction of multiple systems in the initial list of 8738 objects was found to be 33.9 ± 0.6 %. We found that 2407 stars had a $\Delta\mu$ with a significance larger than 3σ (i.e. $\Delta\mu/\sigma_{\Delta\mu} > 3$). The subset of objects with significant $\Delta\mu$ trends had a multiplicity rate of 54.2 ± 1.5 %, while the stars with no observed changes in proper motion only had a binary frequency of 26.2 ± 0.6 %. With a final binary fraction more than twice as large for $\Delta\mu$ stars relative to the rest of the sample, these robust results demonstrate the high efficiency of our $\Delta\mu$ approach to select targets for companion searches.

4.2.2.2 Known Targets with Direct Imaging Companions

The binary search performed in Section 4.2.2.1 was mostly sensitive to stellar companions due to limitations in sensitivity of the catalogues considered. In order to establish whether the $\Delta\mu$ method for target selection is also valid for low-mass companions, inside the substellar regime, we compiled a list of host

stars with directly-imaged brown dwarf and planetary companions, and checked if our approach would have selected these systems.

We gathered all objects from the Extrasolar Planet Encyclopaedia[1] with a confirmed substellar or planetary companion discovered via direct imaging. We then queried the *Gaia* DR2, TGAS and Tycho-2 proper motions and their associated errors for each target, and removed targets that lacked kinematic data in at least two of the three catalogues, providing a sample of 38 objects. We then checked if the stars in the remaining sample were flagged as binaries when performing the same analysis as in Section 4.2.2.1. We eliminated systems with an additional, tertiary component, as the gravitational influence from a more massive stellar companion would likely dominate the observed $\Delta\mu$ of the brown dwarf or planet host. This left us with a sample of 29 targets with no apparent higher-order companion, for which there was at least one, and up to three, $\Delta\mu$ measurements between the *Gaia* DR2, TGAS and Tycho-2 catalogues.

Most of the direct imaging programs in which these substellar companions were identified did not consider excursions in stellar astrometry in the target selection processes. We therefore consider that our sample is not biased towards or against the presence of detectable astrometric signatures. This means that the fraction of $\Delta\mu$ stars in this sample should be representative of the fraction of hosts to substellar companions that our approach detect, given the precision of currently-available data.

Using Equation 4.3 to compute proper motion disparities, we found that 9 stars in the final sample had at least one $\Delta\mu$ value significant to more than 3σ. Thus, about a third of the gathered sample would have been selected with this strategy. The most precise changes in proper motion came from the combination of the *Gaia* DR2 and TGAS catalogues, as a result of the high accuracy achieved by *Gaia* (typically < 0.1 mas yr^{-1}) compared to previous missions. In particular, 16 targets in the sample had a *Gaia* DR2-TGAS $\Delta\mu$ measurement, 7 of which had a significance $> 3\sigma$, which represents the large majority of the significant proper motion offsets obtained in the full sample. In contrast, only 4 out of 45 changes in proper motion computed from Tycho-2 data were found to be above the 3-σ threshold. This is shown in Figure 4.3, which displays the significance of the

[1] `http://exoplanet.eu`

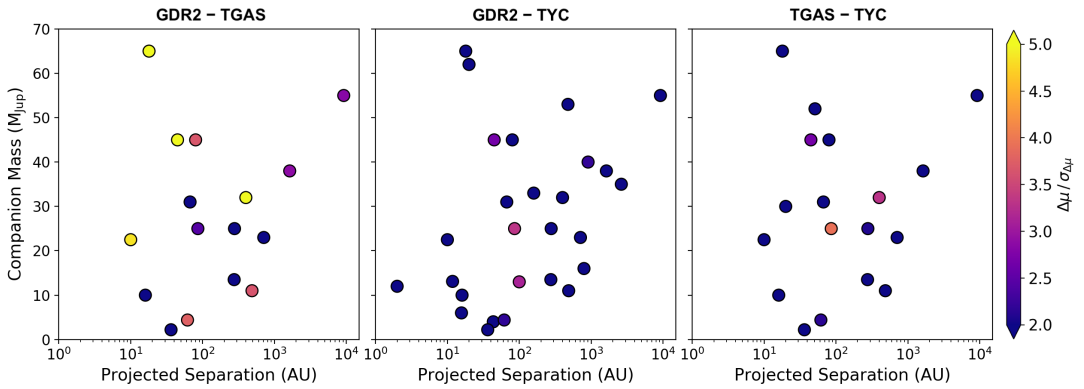

Figure 4.3. Measured changes in proper motion for 29 stars with directly-imaged brown dwarf or planetary companions, based on *Gaia* DR2, TGAS and Tycho-2, showing the significance of measured $\Delta\mu$ values in the colour bar. About half of the available proper motion offsets between *Gaia* DR2 and TGAS (left panel) are significant to more than 3σ (from pink to yellow). In contrast, most $\Delta\mu$ values involving data from the Tycho-2 catalogue have a < 2-σ significance, highlighted by the excess of blue symbols in the middle and right panels.

proper motion measurements ($\Delta\mu/\sigma_{\Delta\mu}$) for each target with existing astrometric data in the two catalogues considered in each panel. We note that no obvious trend of detectability as a function of companion mass or separation is seen in Figure 4.3, although the inhomogeneity of the sample in stellar mass and distance means that the observed parameter space is not directly comparable between the various targets.

While these results are limited by the small size of the sample considered here, they suggest that the fraction of hosts to substellar companions that can be identified with a $\Delta\mu$ analysis increases significantly when using *Gaia* data only. Given the small astrometric offsets induced on primaries by such low-mass companions (typically of only a few mas yr^{-1} at most), it is not surprising that these signals are only rarely recovered when considering data like those provided by Tycho-2, with typical proper motion uncertainties of $\sim$1$-$2 mas yr^{-1}. The high precision of *Gaia* DR1 and DR2 data, on the other hand, allows for the detection of much smaller trends, and can highlight the existence of substellar companions for $\sim$50% of currently-known direct imaging systems. This is extremely promising in anticipation of future *Gaia* Data Releases, which will certainly improve these numbers and allow for robust detections of many more brown dwarf and planetary companions to be observed with direct imaging facilities.

4.2.3 Methodology of the COPAINS Tool

Based on Equation 4.1, we can constrain the region of the parameter space in which a hidden companion responsible for an observed proper motion trend may be. For a given $\Delta\mu$ measurement, our COPAINS tool allows us to evaluate the possible companion mass and separation pairs compatible with the astrometric data, as a function of eccentricity.

We first investigate the behaviour of Equation 4.1 with eccentricity. For any fixed eccentricity value e, the orbital phase $\mathcal{R}_0$ (Equation 4.2) varies between a minimum and maximum value determined by the eccentric anomaly E. E is itself a function of the time-dependent mean anomaly $\mathcal{M}$:

$$\mathcal{M} = 2\pi \frac{(t - T_0)}{P} = E - e \sin E. \tag{4.4}$$

where T_0 is the periastron epoch and P the orbital period of the system. $\mathcal{M}$ thus varies between 0 and 2π, and we can solve for E over all possible $\mathcal{M}$ values and estimate the corresponding orbital phase factor $\mathcal{R}_0$ from Equation 4.2. The left panel of Figure 4.4 shows $\mathcal{R}_0$ as a function of the orbital phase $(t - T_0)/P$ for various eccentricity values, from which we can get the minimum and maximum values allowed for $\mathcal{R}_0$.

Assuming a face-on orbit and treating Equation 4.1 as an equality, we can then find the mass-separation pairs of secondary companions that could produce the observed $\Delta\mu$ for these $\mathcal{R}_0$ upper and lower limits. This provides the boundaries of the region in the $M_2 - a$ space where the unseen companion inducing the observed change in proper motion could be, for a fixed eccentricity e for the system. In the right panel of Figure 4.4, we present the output of the code for an example target of mass $M_1 = 1$ $M_\odot$ with a parallax $\varpi = 50$ mas (distance of 20 pc) and a supposed change in proper motion of $\Delta\mu = 5 \pm 1$ mas yr^{-1}, for the same eccentricity values as in the left panel. For each eccentricity, the pairs of mass and semi-major axis of companions compatible with the $\Delta\mu$ value correspond to the parameter space enclosed within the shaded areas for that e value. The compatible range of $M_2 - a$ pairs steadily broadens as the eccentricity increases and more $\mathcal{R}_0$ values are allowed, as a result of the wider ranges of possible $\mathcal{R}_0$ values in the left panel. Assuming a circular orbit results in a single line of possible

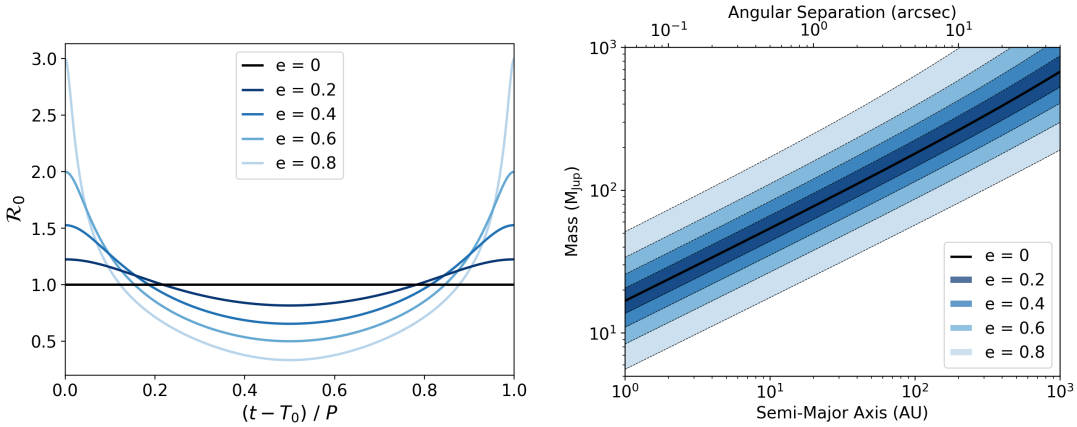

Figure 4.4. Left: Orbital phase factor $\mathcal{R}_0$ as a function of the orbital phase $(t - T_0)/P$, for various fixed eccentricity values, calculated using Equation 4.2. **Right:** Pairs of masses and semi-major axes for secondary companions compatible with the $\Delta\mu$ of an example star of mass $M_1 = 1$ M$_\odot$ and parallax $\varpi = 50$ mas, with a proper motion offset of $\Delta\mu = 5 \pm 1$ mas yr^{-1}. For each eccentricity, we plot the edges of the range of possible solutions, found by considering the minimum and maximum values allowed for $\mathcal{R}_0$ in the left panel, and using Equation 4.1 at those boundary $\mathcal{R}_0$ values.

solutions (black solid line), as $\mathcal{R}_0$ is constant for $e = 0$. For inclined orbits, the derived lines of solutions provide lower mass limits at each separation.

Assuming a plausible distribution of eccentricities, we can now apply the same approach to obtain a single distribution of mass-separation pairs for the companion causing the proper motion offset observed on the primary. To take into account the uncertainty in the astrometric data, we generate 10^5 $\Delta\mu$ values drawn from a Gaussian distribution centred on the measured value, with a standard deviation set to the error on the measurement. For each $\Delta\mu$ value, we then draw an eccentricity e from the adopted distribution. In order to marginalise over all possible orbital phases, we randomly draw a value between 0 and 2π for the mean anomaly $\mathcal{M}$ (equivalent to picking a random fraction of the orbital period from a uniform distribution), and compute the corresponding $\mathcal{R}_0$ for the considered e value. Finally, we can find the pairs of masses and semi-major axes that produce the drawn $\Delta\mu$ for the resulting orbital phase factor $\mathcal{R}_0$.

This provides us with a collection of 10^5 sets of solutions, from which we can obtain a 2-dimensional map of the resulting distribution in the mass-separation space. Figure 4.5 shows the output of the code for the model target considered

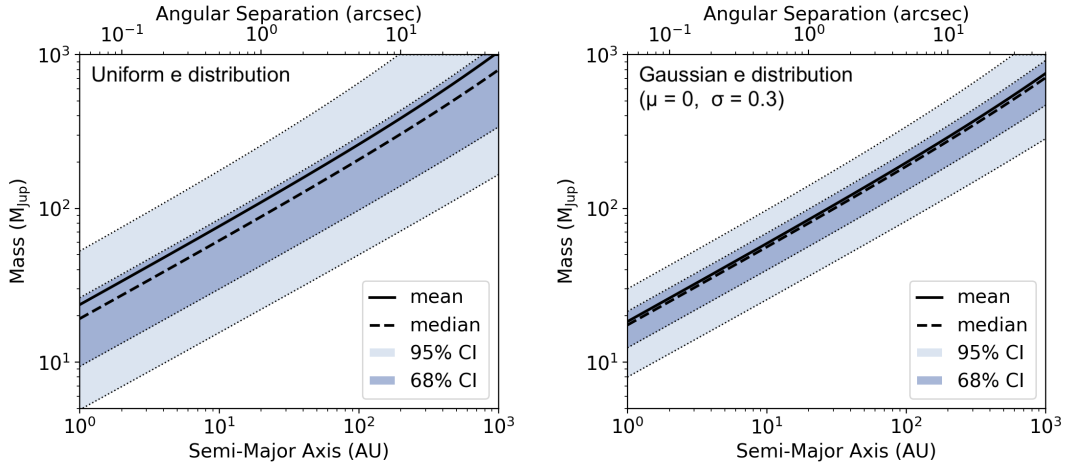

Figure 4.5. Output of our COPAINS tool showing the 2-dimensional $M_2 - a$ distribution for our example target of mass $M_1 = 1$ $M_\odot$ and parallax $\varpi = 50$ mas, with an observed change in proper motion of $\Delta\mu = 5 \pm 1$ mas yr^{-1}. In the left panel, we adopted a uniform distribution in eccentricity, while a Gaussian distribution of mean 0 and width 0.3 was used in the right panel. The dark and light shaded areas correspond to the regions enclosing 68% and 95% of the sets of solutions, respectively.

above, adopting a uniform distribution in e between 0 and 1 in the left panel (Raghavan et al. 2010), and a Gaussian distribution of mean $e = 0$ and width 0.3, truncated to the range $e = 0-1$, in the right panel (Bonavita et al. 2013). The thick lines indicate the positions of the mean (solid line) and median (dashed line) mass at each separation value. The shaded areas mark the limits of the 68% (dark purple) and 95% (light purple) confidence intervals. We adopt a highest probability density approach to compute the confidence levels, which provides the shortest interval enclosing a fraction α of the output distribution (see Chapters 2 and 3).

As expected from Figure 4.4, assuming a uniform distribution in eccentricity results in a much broader output (left panel of Figure 4.5) than for a distribution concentrated around low eccentricity values (right panel). We note that in both cases the median (dashed black line) is very close to the $e = 0$ line of solutions in Figure 4.4. As a wider range of eccentricities is allowed, the mean of the resulting solutions shifts to higher masses at the same separations, as a result of the highly asymmetric intervals around the $e = 0$ for high eccentricities (see Figure 4.4; note that the plots are all shown on logarithmic scales). The uniform

eccentricity distribution is likely to be more accurate for companions in the stellar mass range, consistent with the roughly flat e-distribution observed by Raghavan et al. (2010) for binaries with mass ratios larger than $q \sim 0.1$. On the other hand, the truncated Gaussian distribution considered here is thought to be more representative of the substellar and planetary population (see Bonavita et al. 2013 and references therein). This normal distribution, restricted to the range $e = 0-1$, is also very close to the Beta distribution derived by Kipping (2013) for the exoplanet eccentricity distribution, and is thus in good agreement with the observed properties of known exoplanets, at least on short orbital separations.

4.2.4 Promising Candidates for Direct Imaging Searches

Based on stellar proper motions from various astrometric catalogues, we can select stars showing significant discrepancies (e.g. $> 3\sigma$) between short-term proper motions (i.e. *Gaia* DR2, *Hipparcos*) and measurements acquired over longer time baselines (e.g. TGAS, Tycho-2). Using the output from the previous section to evaluate the characteristics of possible hidden companions, our new COPAINS tool can be used to assess whether a selected $\Delta\mu$ star might be a promising target in a direct imaging search for low-mass companions. The obtained results may not be fully accurate depending on the periods of the systems and the proper motion measurements considered (see Section 4.A). Nevertheless, the output of the code provides a fairly robust idea of the region of the parameter space where the hidden companion might be located, given the assumptions made. Comparing the resulting 2-dimensional distribution of masses and separations to typical performances of direct imaging facilities, we can rule out targets for which the achieved sensitivities do not probe the part of the parameter-space corresponding to substellar or planetary companions. We can also use detection limits from direct imaging data with null detections to rule out a range of solutions and further constrain the region of the parameter space in which the unseen companion may be located.

For example, Figure 4.6 shows the results obtained with COPAINS on our example target from Section 4.2.3, in which we overplotted typical sensitivities from various instruments. The VLT/NACO and VLT/SPHERE detection limits were taken from the median performances achieved in Rameau et al. (2013)

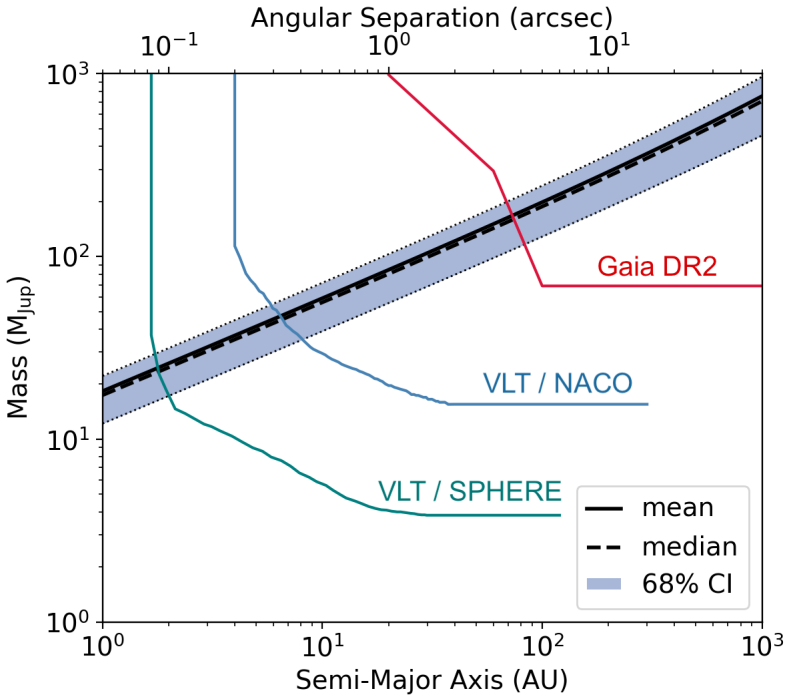

Figure 4.6. Output of COPAINS for our example target, assuming a Gaussian distribution in eccentricity (see right panel of Figure 4.5), showing the typical sensitivity limits to secondary companions from *Gaia* DR2 (red), VLT/NACO (blue) and VLT/SPHERE (green). Detection limits were converted to masses using the AMES-Cond evolutionary models (Baraffe et al. 2003) and adopting an age of 100 Myr for our model target.

and Maire et al. (2017), respectively. The *Gaia* limit corresponds to the *Gaia* DR2 99% binary completeness limit described in Chapter 3. Magnitudes were converted into masses using the AMES-Cond evolutionary models (Baraffe et al. 2003) in the corresponding filter systems, adopting an age of 100 Myr for our 1 $M_{\odot}$ target located at 20 pc. These values are representative of stars observed in direct imaging surveys, which typically target young and nearby objects to increase the detectability of low-mass, faint companions (Vigan et al. 2017).

The absence of comoving sources around this star in the *Gaia* DR2 catalogue would allow us to rule out the part of the parameter space above the *Gaia* limit (red line), eliminating low-mass stellar companions from ∼100 AU. The positions of the detection limits from the two VLT instruments then suggest that an intermediate-mass brown dwarf would be detectable with NACO (blue line), down to separations of around 10 AU. On the other hand, observations with

SPHERE (green line) would be required to retrieve a hidden companion at the low-mass end of the substellar regime on separations of a few AU. We note that the angular separation axis in which the detection limits are plotted corresponds to the semi-major axis of the system rather than the projected separation, which would be expected to be slightly offset due to orbital eccentricity effects.

Finally, we can also use the plot in Figure 4.6 to conclude that a combination of VLT/SPHERE data with a binary search in *Gaia* DR2 should allow for the retrieval of the unseen companion given that its separation is larger than ∼2 AU. A null detection in both data sets would place robust constraints on the mass and separation upper limits of the companion triggering the observed astrometric trend. A complementary detection method such as radial velocity could then be used to detect this companion, given that the orbital inclination of the system is not face-on.

We provide a detailed assessment of the validity and limitations of our approach in Appendix 4.A. The accuracy of the results obtained with this method strongly depends on how close the long-term proper motion measurement is to the true motion of the system's barycentre, and how close the short-term proper motion is to the instantaneous velocity due to the reflex orbital motion of the primary. If the period of the binary is too short, the short-term proper motion will cover a relatively large fraction of the orbit and be highly inconsistent with the tangential instantaneous velocity at the mean epoch of the proper motion observations. Similarly, in binary systems with sufficiently-long periods, long-term proper motions may still capture some of the orbital motion of the primary and differ significantly from the true barycentric motion.

We analysed these effects in Appendix 4.A.1 and quantified the uncertainties introduced by using catalogues of various duration. We found that in general, intermediate-separation systems with semi-major axes from ∼few AU up to several tens of AU have the lowest relative offsets in both short and long-term measurements (see Figure 4.14). For the same companion masses and separations, relative offsets were found to decrease with increasing distance (Figure 4.15) and increasing system proper motion (Figure 4.16), as a result of the weaker observable trends induce on the host stars. The region of optimal coverage corresponds to the part of the parameter space in which most direct imaging companions are located.

These results thus suggest that the $\Delta\mu$ from Equation 4.1 will be reasonably well approximated by e.g. *Gaia* DR2 and Tycho-2 proper motions, for the part of Figure 4.6 probed by the SPHERE or NACO sensitivity limits.

Another source of uncertainty present in our procedure comes from the orbital inclination of binary systems. Equation 4.1 is treated as an equality to produce the plots in Figures 4.5 and 4.6. The code therefore assumes face-on orbits and our method does not account for orbital inclination. As noted previously, in cases of inclined orbits a projected $\Delta\mu$ is observed, which can take values between 0 and a maximum value corresponding to the face-on configuration. By assuming that the observed $\Delta\mu$ corresponds to the maximum value, the true maximum given by Equation 4.1 may be underestimated. The solutions obtained thus provide lower bounds on the region of the parameter space where the hidden companions might be (i.e. above and to the left of the resulting curves). In Appendix 4.A.2, we showed that the uncertainty introduced by the assumption of face-on orbits typically leads to the $\Delta\mu$ values used in the code being underestimated by $<$ 10−15%, with larger disparities observed with higher inclination values. With negligible offsets of $< 5\%$ for half of all cases, this additional source of uncertainty will generally be significantly smaller than the error on the measured $\Delta\mu$.

Finally, the method also implicitly assumes that the astrometric data always correspond to observations of the primary component of a binary system. In reality, for unresolved binaries the measurements reflect the space motion of the photocentre rather than the primary star itself. As the astrometric displacement of the photocentre is smaller than the excursion of the primary, the observed $\Delta\mu$ may thus be further underestimated (Makarov & Kaplan 2005).

4.2.5 Application of COPAINS to known Systems

We considered the five targets studied by Brandt et al. (2018) in order to validate the methodology of our tool (HD 4747, GJ 86, HD 68017 and GJ 758, HR 7672). The companions in all these systems have well-constrained orbits and dynamical mass estimates from combinations of radial velocity, direct imaging and astrometric data (Brandt et al. 2018), allowing us to robustly test the performance of COPAINS to select such systems.

Table 4.1. Properties and astrometry of the systems from Brandt et al. (2018).

Property	HD 4747	GJ 86	HD 68017	GJ 758	HR 7672
Primary mass M_1 ($M_\odot$)	$0.82^{+0.07}_{-0.08}$	1.36 ± 0.23	0.98 ± 0.07	$0.76^{+0.13}_{-0.27}$	$0.96^{+0.04}_{-0.05}$
Secondary mass M_2 (M_{Jup})	$66.2^{+2.5}_{-3.0}$	623 ± 11	154 ± 3	$38.1^{+1.7}_{-1.5}$	72.8 ± 0.8
Semi-major axis a (AU)	$10.1^{+0.4}_{-0.5}$	$21.7^{+0.5}_{-0.7}$	$16.0^{+1.0}_{-1.2}$	30^{+5}_{-8}	$19.6^{+0.8}_{-1.0}$
Orbital period P (yr)	$34^{+0.8}_{-1.0}$	72^{+7}_{-8}	60^{+6}_{-8}	180^{+60}_{-90}	86^{+7}_{-8}
Eccentricity e	$0.7353^{+0.0027}_{-0.0029}$	$0.53^{+0.04}_{-0.03}$	$0.325^{+0.017}_{-0.024}$	0.40 ± 0.09	0.542 ± 0.018
Inclination i (deg)	$49.4^{+2.3}_{-2.4}$	$125.5^{+0.8}_{-0.9}$	170.3 ± 0.4	41 ± 6	97.4 ± 0.4
Parallax ϖ (mas)	53.18 ± 0.13	92.70 ± 0.05	46.33 ± 0.06	64.06 ± 0.02	56.43 ± 0.07
GDR2-TYC $\Delta\mu$ (mas/yr)	$0.95 \pm 1.45^*$	43.36 ± 2.44	19.93 ± 0.81	$3.21 \pm 1.20^*$	12.91 ± 1.02
HIP-TYC $\Delta\mu$ (mas/yr)	5.57 ± 1.60	60.48 ± 2.54	5.01 ± 1.37	$2.79 \pm 1.32^*$	$1.96 \pm 1.24^*$
GDR2-TGAS $\Delta\mu$ (mas/yr)	3.29 ± 0.35	18.37 ± 0.08	...	0.93 ± 0.04	8.45 ± 0.09
HIP-TGAS $\Delta\mu$ (mas/yr)	6.08 ± 0.74	18.74 ± 0.52	...	1.75 ± 0.52	6.32 ± 0.64

Notes. Orbital elements come from Brandt et al. (2018). Astrometric offsets were computed in this work based on proper motions taken directly from the *Gaia* DR2 (Lindegren et al. 2018), TGAS (Michalik et al. 2015), *Hipparcos* (van Leeuwen 2007) and Tycho-2 (Høg et al. 2000) catalogues, when available. Proper motion changes marked with a * have a significance $< 3\sigma$. Parallax measurements correspond to *Gaia* DR2 parallaxes.

From Equation 4.3, we estimated $\Delta\mu$ values for each target using the TGAS and Tycho-2 catalogues as long-term proper motion measurements, and adopting the *Gaia* DR2 and *Hipparcos* data as instantaneous velocities. For *Hipparcos*, we consider the new reduction of the raw data by van Leeuwen (2007) as those data were used in the TGAS solutions. All systems have at least one significant measurement of a change in proper motion based on these catalogues. Table 4.1 summarises the physical properties and astrometric information for each system. This sample provides a range of secondary companions, with masses extending from the substellar regime to low-mass stars, in addition to the white dwarf companion to GJ 86. With orbital periods varying between 30 and 180 yr for these systems, both *Gaia* DR2 and *Hipparcos* are expected to provide good approximations to the instantaneous velocities of the primaries. TGAS and Tycho-2 proper motions, on the other hand, are likely to be somewhat discrepant from the proper motions of the systems' barycentres given the long orbital periods of some of these targets (see Appendix 4.A).

Using the information from Table 4.1, we ran our COPAINS tool on each system and for each observed $\Delta\mu$ measurement. We adopted uniform distributions in eccentricity based on the spread of eccentricity values observed among the five targets. The output of the code for each combination of long and short-term astrometric data is presented in Figure 4.7 for all systems. The solid lines show the median set of solutions and the shaded areas correspond to 68% confidence levels. The red stars indicate the positions of the companions based on the results from Brandt et al. (2018), allowing us to compare the predictions from COPAINS to reliable semi-major axes and dynamical mass estimates for each system.

Most trends were found to be consistent with the positions of the secondary companions at the 2-σ level, with about half agreeing within 1σ (shaded areas in the plots). This suggests that the uncertainties introduced by the time baselines of the proper motions used are in most cases not highly significant, in agreement with our analysis in Appendix 4.A.1. Tycho-2 was typically found to provide a better estimate of the centre-of-mass motions, as a result of its longer temporal coverage (about a century) compared to the $\sim$25-yr baseline of TGAS. As the magnitude of the $\Delta\mu$ varies with orbital phase, the observed offsets between the usage of *Gaia* DR2 and *Hipparcos* as short-term measurements could (partly) reflect different phases at each individual epoch.

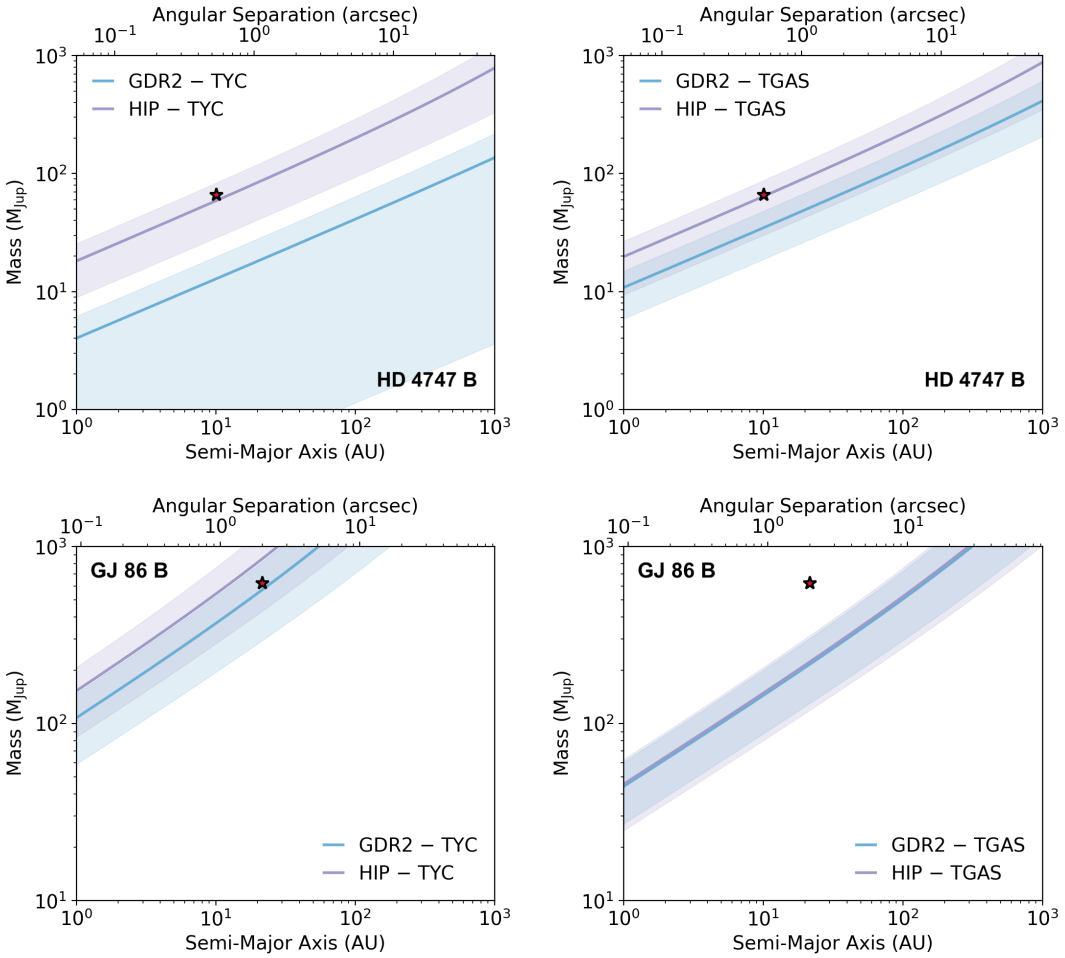

Figure 4.7. Output of COPAINS for the five targets studied in Brandt et al. (2018), using *Gaia* DR2 (blue) and *Hipparcos* (purple) as short-term proper motion measurements, and Tycho-2 (left panels) and TGAS (right panels) for long-term proper motions. The solid lines and shaded areas correspond to the median and 1-σ intervals, assuming a flat distribution in eccentricity. In general, the obtained results were found to be in good agreement with the positions of the secondary companions responsible for the observed astrometric trends (red stars).

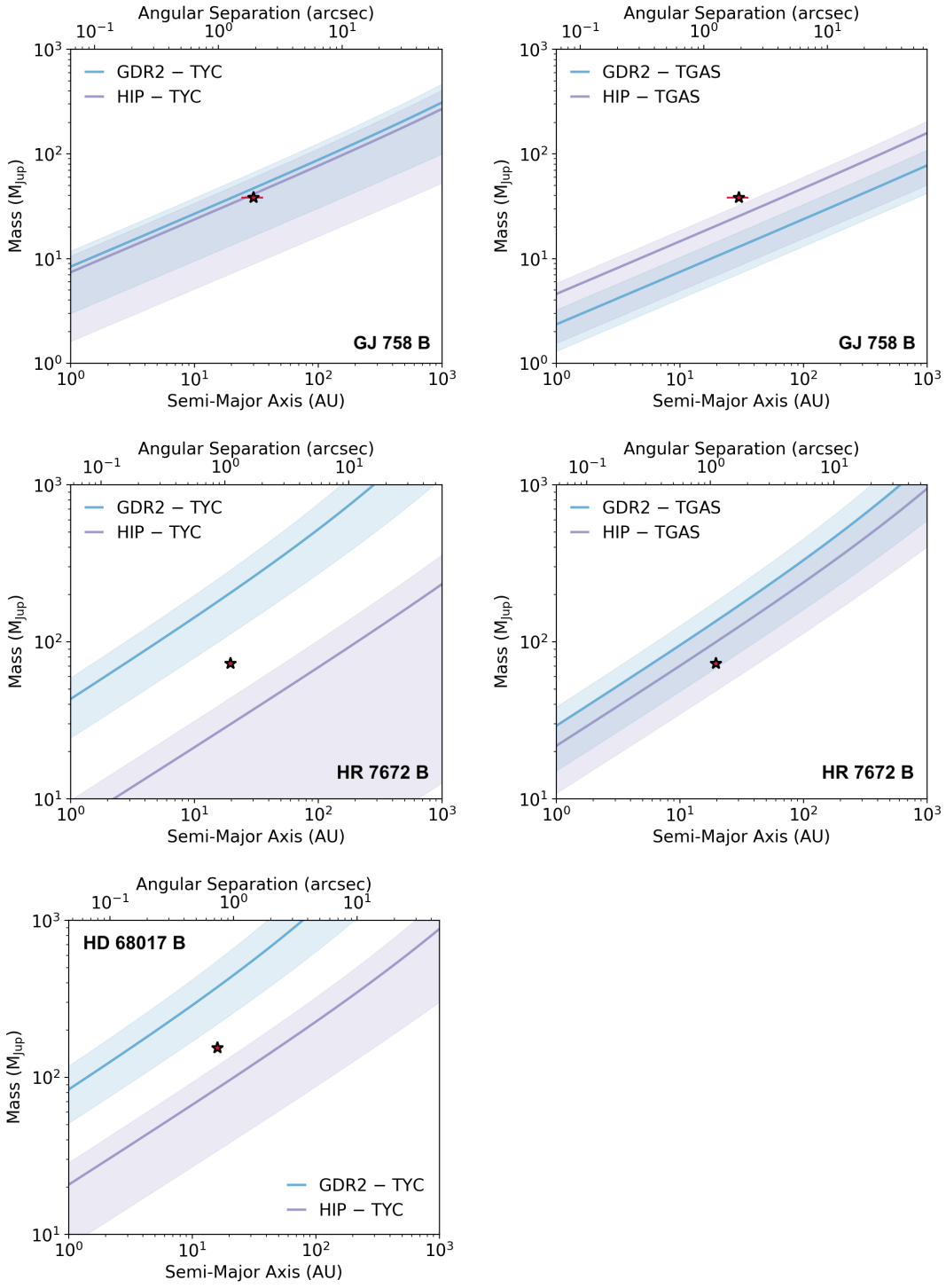

Figure 4.7. (Continued.)

As expected, larger uncertainties in the observed $\Delta\mu$ resulted in wider distributions for a given confidence interval. Low-significance $\Delta\mu$ values (marked with an asterisk in Table 4.1) produced a broad lower tail (e.g. GDR2-TYC for HD 4747, HIP-TYC for HR 7672). The various combinations of catalogues considered were also generally found to be consistent with each other for most systems, with the exception of these low-significance trends. These likely arise from the odd cases where the short-term and long-term proper motion vectors are close to alignment. While we considered these values here for the completeness of our analysis, such low-significance measurements would not normally be selected for an inspection with COPAINS. Only the narrower trends, providing strong constraints on the region of the parameter space in which the secondary companions may be located, would be used for a direct imaging target selection. No additional offset was found for the targets with the largest orbital inclinations (e.g. GJ 86, HR 7672) relative to very low-inclination systems (e.g. HD 68017), confirming that inclination will statistically rarely have a large impact on the results from our code, as we showed in Appendix 4.A.2. Similarly, comparable results were achieved over the range of eccentricities encompassed by the sample.

We conclude that our method allows for an efficient estimate of the probable location of a hidden companion based on astrometric displacements of its host star. Our tool was found to yield a good indication of the region of the parameter space of interest, despite the uncertainties introduced by assumptions made in our approach, and the disparities originating from the use of different astrometric catalogues. Comparing the output of the code to the typical sensitivity limits of various high-contrast imaging facilities, COPAINS thus provides a robust selection method for promising targets to be observed in direct imaging programs.

4.3 Orbital Parametrisation with COPAINS

For systems identified via the approach described in Section 4.2, we can then attempt to constrain the orbit of detected companions. This section focuses on a second functionality of our COPAINS tool, aimed at retrieving the orbital parameters and masses of newly-discovered companions. Such systems will typically have two direct imaging epochs of observations separated by $\sim$1 yr,

from the initial discovery and a subsequent follow-up epoch to confirm common proper motion with the primary. Relative astrometry from imaging data can then be combined with proper motion measurements from the *Hipparcos* and *Gaia* missions. As the temporal coverage of absolute astrometry data must be known rather precisely to fit orbits, proper motions like those provided by Tycho-2, with unknown original epochs, cannot be used. We constructed a binary system simulator, presented in Section 4.3.1, in order to model observed systems and compare measured absolute and relative astrometry to the expected values. Based on this simulator, we introduce our orbital fitting tool in Section 4.3.2, and test it in Section 4.3.3 on the five targets from Section 4.2.5.

4.3.1 Binary Simulator

We characterise a binary system with the 2 component masses, 6 Keplerian orbital elements, and 3 kinematics parameters. This provides us with an 11-parameter model based on the following elements:

- M_1: the mass of the primary star (in $M_\odot$).
- M_2: the mass of the secondary companion (in $M_\odot$).
- a: the total semi-major axis of the system (in AU).
- e: the eccentricity of the system.
- i: the orbital inclination (in deg).
- ω_2: the argument of periastron of the companion (in deg).
- Ω: the longitude of ascending node (in deg).
- T_0: the time of perisatron passage (UT date).
- ϖ: the absolute parallax of the system (in mas).
- $\mu_{\alpha*}$: the R.A. component of the centre-of-mass proper motion (in mas yr^{-1}).
- μ_δ: the Decl. component of the centre-of-mass proper motion (in mas yr^{-1}).

Indices 1 and 2 always refer to the primary star and secondary companion, respectively. The orbital period P (in yr) of the system can be inferred from

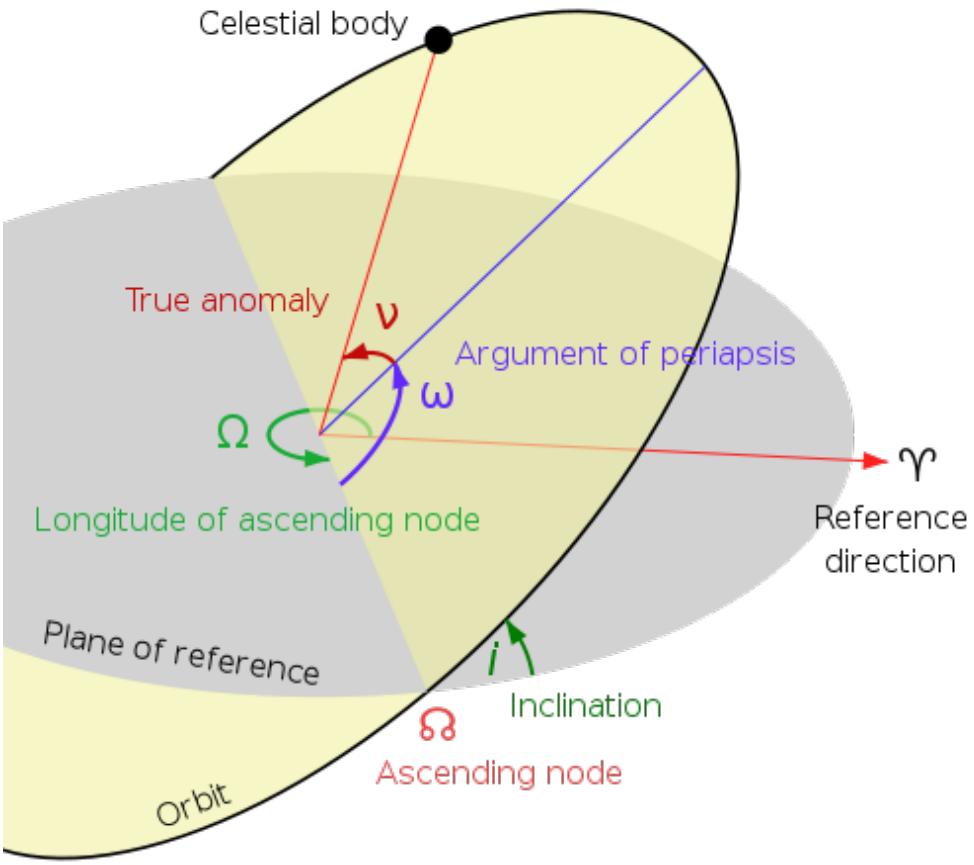

Figure 4.8. True and projected orbits of a component from a visual binary, and its geometrical elements. In this diagram, the orbital plane (yellow) intersects the plane of projection (gray), which corresponds to the plane of the sky. The intersection represents the line of nodes and connects the centre of mass (at the origin) with the ascending and descending nodes. The ascending node is marked, together with the longitude of ascending node Ω, defined from a reference direction (usually taken to be North). The argument of periastron ω is the angle in the true orbital plane from the ascending node to the periastron, for the considered binary component. The inclination i is the angle between the plane of projection and that of the true orbit.

the component masses and the system's semi-major axis:

$$P = \left[\frac{a^3}{M_1 + M_2} \right]^{1/2} . \tag{4.5}$$

The individual semi-major axes a_1 and a_2 of the components' orbits around the barycentre of the system are related by $a = a_1 + a_2$ and $a_1 M_1 = a_2 M_2$. The argument of periastron of the primary, ω_1 is offset by 180 deg from that of the secondary. Figure 4.8 presents a diagram of the geometrical elements of the orbit of a visual binary.

Our approach is based on the standard formalism involving the Thiele-Innes parameters (Thiele 1883). The computation of the Thiele-Innes elements for the orbit calculation is most advantageous to calculate rectangular coordinates (Heintz 1978). For the binary component n (where $n = 1$ for the primary star, and $n = 2$ for the secondary companion), the angular semi-major axis a''_n (in mas) is obtained from the physical semi-major axis a_n of that component and the parallax ϖ of the system: $a''_n = a_n \, \varpi$. The Thiele-Innes parameters are then given by:

$$\begin{aligned} A &= a''_n \, (\cos\omega_n \, \cos\Omega \, - \, \sin\omega_n \, \sin\Omega \, \cos i) \, , \\ B &= a''_n \, (\cos\omega_n \, \sin\Omega \, + \, \sin\omega_n \, \cos\Omega \, \cos i) \, , \\ F &= a''_n \, (-\sin\omega_n \, \cos\Omega \, - \, \cos\omega_n \, \sin\Omega \, \cos i) \, , \\ G &= a''_n \, (-\sin\omega_n \, \sin\Omega \, + \, \cos\omega_n \, \cos\Omega \, \cos i) \, . \end{aligned} \tag{4.6}$$

At any time t, the elliptical rectangular coordinates X and Y can be defined from the time-dependent eccentric anomaly E (Equation 4.4) and the eccentricity e of the system:

$$\begin{aligned} X &= \cos E \, - \, e \, , \\ Y &= \sqrt{1 - e^2} \, \sin E \, . \end{aligned} \tag{4.7}$$

The displacement of component n at time t, relative to the centre of mass of the system, is found by combining the Thiele-Innes elements (Equation 4.6) and the auxiliary parameters X and Y (Equation 4.7):

$$\begin{aligned} x &= AX + FY \, , \\ y &= BX + GY \, . \end{aligned} \tag{4.8}$$

This provides the on-sky astrometric displacement (in mas) of that component from the barycentre in the R.A. and Decl. directions, respectively. Given the parallax ϖ and proper motion components $\mu_{\alpha*}$ and μ_δ of the centre of mass, the total absolute motion of the binary component n at time t, relative to a reference epoch $t_{\rm ref}$, can be computed as:

$$\begin{aligned} \Delta\alpha &= x \,+\, \mu_{\alpha*}\,(t - t_{\rm ref}) \,+\, \varpi\,\Pi_{\alpha*}\,, \\ \Delta\delta &= y \,+\, \mu_\delta\,(t - t_{\rm ref}) \,+\, \varpi\,\Pi_\delta\,. \end{aligned} \tag{4.9}$$

The $\Delta\alpha$ term in the R.A. direction is in the appropriate rectilinear coordinates (i.e. taking into account the $\cos\delta$ term using the nominal declination value). The parallax factors of the system in R.A. and Decl., $\Pi_{\alpha*}$ and Π_δ, refer to the astrometric displacements due to parallax effects in each direction. These can be calculated for the sky coordinates of the system by getting the barycentric position of the Earth at time t from numerically integrated Solar system ephemerides (see Seidelmann 1992).

Our binary model thus allows us to compute the absolute position on the sky for either component of the modelled binary system, and at any point in time, relative to a reference epoch position. From this, we can also predict the relative astrometric displacement (projected separation and position angle) between the two binary companions at any given time, by taking the difference between the output of Equation 4.8 for the primary and secondary.

4.3.2 MCMC Fitting Tool

We can use the binary simulator described above to fit the orbit of observed systems using their measured proper motions and relative astrometry. In Section 4.2.5, we showed that the $\Delta\mu$ approach provides a reasonable estimate of the region of the parameter space where a hidden companion may be located. These estimates were obtained by considering that long-term proper motions are representative of centre-of-mass motions, and that short-term catalogues provide measurements of instantaneous velocities. We also assumed face-on orbits to estimate and constrain the relevant regions of the parameter space. As detailed in Appendix 4.A.1, such assumptions result in offsets that become non-negligible

when seeking accurate constraints on the orbits of systems. We must therefore drop these approximations when fitting orbits, and will instead consider the actual velocity vectors along the trajectory of the components to fit the complete set of orbital elements.

We use a Markov Chain Monte Carlo (MCMC) approach to perform a full orbital fit from combined relative and absolute astrometry, implemented with the affine-invariant sampler EMCEE Python package (Foreman-Mackey et al. 2013). Our MCMC model includes 10 parameters, corresponding to all elements listed in Section 4.3.1 with the exception of the primary mass M_1, which we do not attempt to fit at this stage. We consider reliable literature values for stellar masses instead, in order to reduce the large number of parameters to fit. For each set of model parameters, we can integrate the orbit of a model binary system using our binary simulator. The likelihood is then calculated in two steps, to fit the absolute astrometry from catalogue proper motions, and the relative astrometry from direct imaging data, respectively.

For the absolute astrometry, we estimate the proper motion that would be measured for the primary component over the observation timeframe of a specific astrometric mission. We consider the absolute positions of the primary at the beginning and end observation dates of that catalogue, relative to a reference position arbitrarily chosen to be at epoch 2000. We assume positions to be measured at the same time in the R.A. and Decl. directions. We can then estimate the linear velocity vector between these two points, given by their relative separation, scaled by the duration of the considered catalogue. This provides a model proper motion $[\mu'_{\alpha*}, \mu'_{\delta}]$ (we use apostrophes to denote model parameters) that can be compared to the measured values at the mean epoch of the catalogue ($[\mu_{\alpha*}, \mu_{\delta}]$), in both the R.A. and Decl. directions. Our approach differs from that used in Brandt et al. (2018) in that we treat all proper motion measurements separately and solve for the true motion of the system's barycentre, rather than fitting differences between instantaneous and mean proper motions. Our procedure thus allows us to retrieve and constrain the absolute motion in space of studied systems.

We remove the parallax term in Equation 4.9 when computing the total motion of the binary component to estimate the underlying proper motion. As the

catalogue proper motions considered are obtained from solutions fitting parallaxes and proper motions to individual observed positions (Lindegren et al. 2018), the parallax factors in the astrometric displacements are already subtracted and must therefore be excluded.

The total contribution to the likelihood from proper motion data of the primary, $\chi^2_{\rm PM}$, is then given by:

$$\chi^2_{\rm PM} = -0.5 \sum_{k=1}^{N_{\rm PM}} \sum_{j \in \{\alpha*,\delta\}} \frac{\left(\mu'_{j,k} - \mu_{j,k}\right)^2}{\sigma^2[\mu_{j,k}]}\,, \tag{4.10}$$

where $N_{\rm PM}$ is the total number of proper motion measurements available, j represents the R.A. or Decl. direction, and $\sigma[\mu]$ the uncertainties on the observed proper motions μ. In the event that the secondary companion is also detected in these catalogues and has measured proper motions of its own, a similar term can be computed for the secondary and added to the likelihood.

Similarly, relative astrometry from direct imaging data is compared to the expected values from the model. Using Equation 4.8, we can obtain the displacements, relative to the centre of mass of the system, for both binary components, at the exact dates of the imaging observations. This provides model values for the projected separations ρ' and position angles θ' at the various observation epochs, that can be compared in the same way to the measured values ρ and θ. The contribution to the likelihood from the imaging data, $\chi^2_{\rm DI}$, is:

$$\chi^2_{\rm DI} = -0.5 \sum_{k=1}^{N_{\rm DI}} \frac{\left(\rho'_k - \rho_k\right)^2}{\sigma^2[\rho_k]} + \frac{\left(\theta'_k - \theta_k\right)^2}{\sigma^2[\theta_k]}\,, \tag{4.11}$$

where $N_{\rm DI}$ is the number of direct imaging observations available, ρ and θ represent the two observables, and $\sigma[\rho, \theta]$ the uncertainties on the measured values. For the position angle term, we consider the smallest difference between $\Delta = |\theta' - \theta|$ and $|\Delta - 360\,\mathrm{deg}|$, in order to account for the periodic boundary condition in θ going from 360 deg to 0 deg.

Our goal with this tool is ultimately to provide dynamical constraints on the orbits of systems with only a couple of direct imaging points and proper motion measurements. We therefore adopt rather uninformative priors on all model

parameters, even if prior knowledge exists on the orbital elements of our test targets in Section 4.3.3. We use log-flat priors on the companion mass M_2 and total semi-major axis a over plausible ranges (see Section 4.3.3), as these parameters span multiple orders of magnitude. We assume a uniform prior in $\sin i$ and uniform priors in all other orbital elements, as was done in Brandt et al. (2018).

For the kinematic parameters, we consider *Gaia* DR2 parallax measurements to set a Gaussian prior on the parallax ϖ. We inflate the *Gaia* DR2 uncertainties by a generous factor of 5 in order to account for the fact that binarity was not worked into the *Gaia* DR2 astrometric solutions and that additional biases are expected for binary systems (Lindegren et al. 2018; Schönrich et al. 2019). For the barycentric proper motion, we use the mean $[\bar{\mu}_{\alpha*}, \bar{\mu}_{\delta}]$ of all existing proper motion measurements (including e.g. Tycho-2 proper motions that are not used in the orbital fit), with an uncertainty arbitrarily set to 5 times the standard deviation of these measurements, to place a Gaussian prior on the centre-of-mass proper motion. The mean of a number of measurements acquired over various, widely-spaced points along the orbit are statistically expected to be a good approximation of the barycentric space motion. This prior on the true centre-of-mass proper motion is important so as to take into account the most long-term proper motions available, even if these data cannot be included in the orbit fit, due to the unknown original epochs used in Tycho-2 data. This ensures that the solutions found by the MCMC routine are compatible with these key long-term measurements as well, which extend well beyond the orbital coverage provided by the rest of the considere data.

Accounting for these priors, the final log-likelihood $\mathcal{L}$ is calculated as:

$$\mathcal{L} = \chi^2_{\rm PM} + \chi^2_{\rm DI} + \chi^2_{\varpi} + \chi^2_{\mu} - \ln(M_2') - \ln(a') + \ln(\sin i')\,, \tag{4.12}$$

where

$$\chi^2_{\varpi} = -0.5\,\frac{\left(\,\varpi' - \varpi_{\rm GDR2}\,\right)^2}{25\,\sigma^2[\varpi_{\rm GDR2}]}\,, \tag{4.13}$$

and

$$\chi^2_{\mu} = -0.5\sum_{j\in\{\alpha*,\delta\}}\frac{\left(\,\mu_j' - \bar{\mu}_j\,\right)^2}{\sigma^2[\bar{\mu}_j]}\,. \tag{4.14}$$

4.3.3 Method Validation and First Results

We tested our orbital fitting tool on the five $\Delta\mu$ targets from Brandt et al. (2018) studied in Section 4.3.3 and presented in Table 4.1. Even though a large amount of relative astrometry data is available for most of these well-monitored targets, we only use two direct imaging points in our orbit fits. This allows our obtained results to be representative of cases of newly-confirmed companions, for which only one initial and one follow-up epoch will generally be available. For each target, we selected two imaging data points separated by $\sim$1 year among the values listed in Brandt et al. (2018), to be consistent with the typical orbital coverage that would be available for new discoveries. We preferably picked, when possible, data acquired with the same instruments, in order to avoid introducing additional uncertainties from the calibration of separate facilities (Bowler et al. 2018). The data considered are summarised in Table 4.2.

It is important to note that this is not an attempt to obtain the best possible orbital and dynamical constraints given the available data for these targets. This analysis is rather a test of the performance of our approach to infer the orbital elements and model-independent masses based on only a couple of direct imaging observations and data from a few astrometric catalogues (i.e. recently-discovered young targets for which RV observations are not feasible). As a result, we do not consider existing radial velocity measurements as was done in Brandt et al. (2018) or Dupuy et al. (2019). We also choose not to use existing constraints on the orbital elements as prior information for our model parameters, as was done in Calissendorff & Janson (2018).

In Section 4.2, we used proper motion measurements from various missions as given in the corresponding catalogues for the target selection procedure. Given the number of imprecise assumptions made in our $\Delta\mu$ approach for target selection, we did not consider the additional uncertainties introduced by using these measurements at face value. When fitting binary orbits, all proper motions used need to be placed in the same reference frame, defined at the same epoch. We therefore use in this section the *Hipparcos-Gaia* Catalog of Accelerations (HGCA) defined by Brandt (2018). This catalogue provides *Hipparcos* and *Gaia* DR2 proper motions, as well a *Gaia* DR2-*Hipparcos* scaled positional differences (very close to the TGAS proper motions), placing all proper motions at epoch

Table 4.2. Absolute and relative astrometry used in the orbital fits.

Obs. Date	ρ (mas)	θ (deg)	Cat.	$\mu_{\alpha*}$ (mas yr^{-1})	μ_δ (mas yr^{-1})
HD 4747					
2016.95	594.4 ± 5.1	187.2 ± 0.3	HIP	516.619 ± 0.736	120.446 ± 0.588
2017.74	581.2 ± 5.8	190.6 ± 0.5	HG	515.305 ± 0.024	125.564 ± 0.025
			GDR2	518.372 ± 0.552	123.849 ± 0.587
GJ 86					
2004.73	1941 ± 17	105.3 ± 0.6	HIP	2091.883 ± 0.428	654.345 ± 0.462
2005.57	1969 ± 15	102.7 ± 0.5	HG	2106.955 ± 0.016	641.619 ± 0.017
			GDR2	2124.853 ± 0.133	638.092 ± 0.113
HD 68017					
2011.15	594.5 ± 1.5	248.20 ± 0.17	HIP	-461.602 ± 0.924	-644.467 ± 0.524
2012.02	574.6 ± 1.5	240.30 ± 0.17	HG	-471.298 ± 0.026	-639.023 ± 0.019
			GDR2	-484.315 ± 0.157	-642.974 ± 0.097
GJ 758					
2016.49	1626 ± 5	210.3 ± 0.4	HIP	82.805 ± 0.475	162.757 ± 0.447
2017.77	1588 ± 5	213.5 ± 0.3	HG	82.189 ± 0.017	161.325 ± 0.016
			GDR2	81.803 ± 0.058	160.392 ± 0.069
HR 7672					
2001.64	786 ± 6	157.9 ± 0.5	HIP	-394.580 ± 0.492	-407.286 ± 0.516
2002.54	788 ± 6	156.6 ± 0.9	HG	-392.151 ± 0.018	-412.462 ± 0.016
			GDR2	-387.590 ± 0.143	-419.542 ± 0.143

Notes. Relative astrometry data taken from Brandt et al. (2018) and references therein. Proper motions come from the HGCA catalogue (Brandt 2018): HIP: *Hipparcos* proper motions; HG: *Hipparcos-Gaia* scaled positions; GDR2: *Gaia* DR2 proper motions.

2015.5, with recalibrated uncertainties. The three HGCA proper motions for each of the five targets are listed in Table 4.2.

Using the data from Table 4.2 as the observational input, we applied the COPAINS MCMC orbital fitting tool described above to constrain the orbit of our five test targets. The MCMC walkers were initialised at random positions uniformly distributed throughout the parameter space over the following ranges: $M_{2,\mathrm{min}} < M_2/\mathrm{M_{Jup}} < M_{2,\mathrm{max}}$, $1 < a/\mathrm{AU} < 100$, $0 < e < 1$, $0 < i/\mathrm{deg} < 180$, $0 < \omega_2/\mathrm{deg} < 360$, $0 < \Omega/\mathrm{deg} < 180$, $1950 < T_0 < 2100$, $0.8 \times \varpi_{\mathrm{GDR2}} < \varpi < 1.2 \times \varpi_{\mathrm{GDR2}}$, $0.8 \times \bar{\mu}_{\alpha*} < \mu_{\alpha*} < 1.2 \times \bar{\mu}_{\alpha*}$ and $0.8 \times \bar{\mu}_\delta < \mu_\delta < 1.2 \times \bar{\mu}_\delta$. The boundaries for the companion mass M_2 are different for each target and the chosen limits are listed below in the dedicated subsection for each individual

system. The $\varpi_{\rm GDR2}$ term is the *Gaia* DR2 parallax of the studied target, and the $\bar{\mu}$ terms are the mean of all available proper motion measurements in each direction for that target, as defined in Section 4.3.2. The priors described in Section 4.3.2 were restricted to these same ranges for all model parameters, so as to limit the region of the parameter space to be explored.

The longitude of the ascending node Ω and the argument of periastron ω_2 both range from 0 deg to 360 deg. However, astrometric data cannot distinguish the ascending node from the descending one (Beust et al. 2014; Ranalli et al. 2018). As a result, the same projected orbital motion is observed by adding 180 deg to both Ω and ω_2. In order to break this degeneracy, we restrict the allowed range of Ω to the 0−180 deg interval to obtain a single solution for the (Ω, ω_2) pair (Perryman et al. 2014). If the ascending node lies between 180−360 deg, the resulting solution for Ω will thus correspond to the descending node.

We used 500 walkers in our MCMC runs to sample our 10-parameter model over 2×10^5 steps. We found that the walkers stabilised in less than $\sim 1\times10^5$ steps and discarded the first half of the chains as the burn-in phase. Finally, we removed the 450 warmest chains (with lower likelihood values), retaining only the 10% coldest, best converged parts of the obtained samples. Results are presented below for each individual system. We report the peak values and 68% intervals of highest probability for each model parameter in Tables 4.3 to 4.7, and compare the obtained results to those from Brandt et al. (2018) and any other existing orbital and dynamical constraints found in the literature for each system. In Figures 4.9 to 4.13 we show the posterior distributions for the companion mass M_2, semi-major axis a, eccentricity e and inclination i, highlighting the positions of the most likely values, together with the boundaries of the 1 and 2-σ confidence intervals. All confidence intervals were computed adopting a highest density region approach, to infer the shortest ranges containing 68% and 95% of the posteriors for each parameter. The full MCMC outputs are presented in Appendix 4.B for each target (Figures 4.18 to 4.22).

From the obtained M_2 and a posterior distributions, we can compute a probability distribution for the orbital period P, using Equation 4.5 and the primary masses from Table 4.1. We report the peak and 1-σ interval for the orbital period of each target with our results in the tables below. The time of periastrion passage T_0

has one solution for every orbital period, and is therefore degenerate with modulo P. We did not restrict the allowed range of this parameter to a specific orbital period range in our MCMC runs because we assumed the periods of our targets to be unknown. We thus collapse the final posteriors for T_0 to the solutions closest to epoch 2000 using the nominal orbital period P at each MCMC step.

4.3.3.1 HD 4747

HD 4747 B was discovered by Crepp et al. (2016) as part of the TRENDS survey (Crepp et al. 2012b), at $\sim$0.″6 around a G9 V star with a radial velocity trend. Crepp et al. (2018) subsequently determined the companion to have a T1$\pm$2 spectral type. Radial velocity data acquired over 20 years indicate a lower mass limit of $M_2 \sin i = 55.3 \pm 1.9$ M_{Jup} for the companion, while evolutionary models suggest a mass of 72^{+3}_{-13} M_{Jup} based on a gyrochronology age of $3.3^{+2.3}_{-1.9}$ Gyr for the primary (Crepp et al. 2016). Based on the model-dependent mass estimate for HD 4747 B, we chose to constrain the companion mass M_2 between $M_{2,min} = 0.01$ $M_\odot$ and $M_{2,max} = 0.2$ $M_\odot$ in our MCMC analysis.

The orbit and dynamical mass of HD 4747 B was previously constrained by Crepp et al. (2016, 2018) and Peretti et al. (2018) using RV data and imaging astrometry. Brandt et al. (2018) further constrained this system by adding differences between *Gaia* and *Hipparcos* proper motions to the RV and imaging information, inferring a companion mass of $66.2^{+2.5}_{-3.0}$ M_{Jup}. The results from these studies are presented in Table 4.3, along with the output from our MCMC analysis.

All model parameters were found to converge very well (see Figure 4.18 in Appendix 4.B for the full MCMC corner plot). Our results were found to generally be in very good agreement with previous results, as shown in Table 4.3. The obtained posteriors were found to be consistent at the 1-σ level with the orbital constraints from Brandt et al. (2018) for all parameters, with the exception of the orbital inclination i and the longitude of ascending node Ω which were more discrepant. Our dynamical mass of $63.5^{+9.8}_{-9.3}$ M_{Jup} was at the lower end of previous estimates, but consistent within less than 1σ. For most model parameters, we obtained broader probability distributions than studies which considered larger and more complete data sets, including a 15% relative error in the companion

Table 4.3. HD 4747 results and comparison to other orbital constraints.

Parameter	This work	Brandt et al. 2018	Crepp et al. 2018	Peretti et al. 2018
M_2 (M_{Jup})	$63.5^{+9.8}_{-9.3}$	$66.2^{+2.5}_{-3.0}$	$65.3^{+4.4}_{-3.3}$	70.2 ± 1.6
a (AU)	$11.4^{+0.7}_{-0.8}$	$10.1^{+0.4}_{-0.5}$	12.3 ± 1.5	10.01 ± 0.21
e	$0.735^{+0.060}_{-0.073}$	$0.7353^{+0.0027}_{-0.0029}$	0.740 ± 0.002	0.7320 ± 0.0023
i (deg)	$65.0^{+2.9}_{-2.7}$	$49.4^{+2.3}_{-2.4}$	$58.5^{+4.0}_{-5.2}$	46.3 ± 1.1
ω_2 (deg)	$268.2^{+10.3}_{-9.7}$	267.0 ± 0.5	269.3 ± 0.6	-93.10 ± 0.47
Ω (deg)	$139.6^{+11.2}_{-10.2}$	$91.5^{+1.7}_{-1.8}$	$186.2^{+2.3}_{-1.7}$	89.8 ± 1.4
T_0 (UT)	$1999.7^{+2.8}_{-2.6}$	1997.06 ± 0.01	1997.04 ± 0.02	1997.07 ± 0.01
P (yr)	$42.8^{+4.3}_{-4.0}$	$34.0^{+0.8}_{-1.0}$	$37.85^{+0.87}_{-0.78}$	33.08 ± 0.70
ϖ (mas)	$53.37^{+0.57}_{-0.60}$	53.18 ± 0.13	...	...
$\mu_{\alpha*}$ (mas yr^{-1})	$516.73^{+0.28}_{-0.29}$	...	...	...
μ_δ (mas yr^{-1})	$123.67^{+0.34}_{-0.37}$	...	...	...

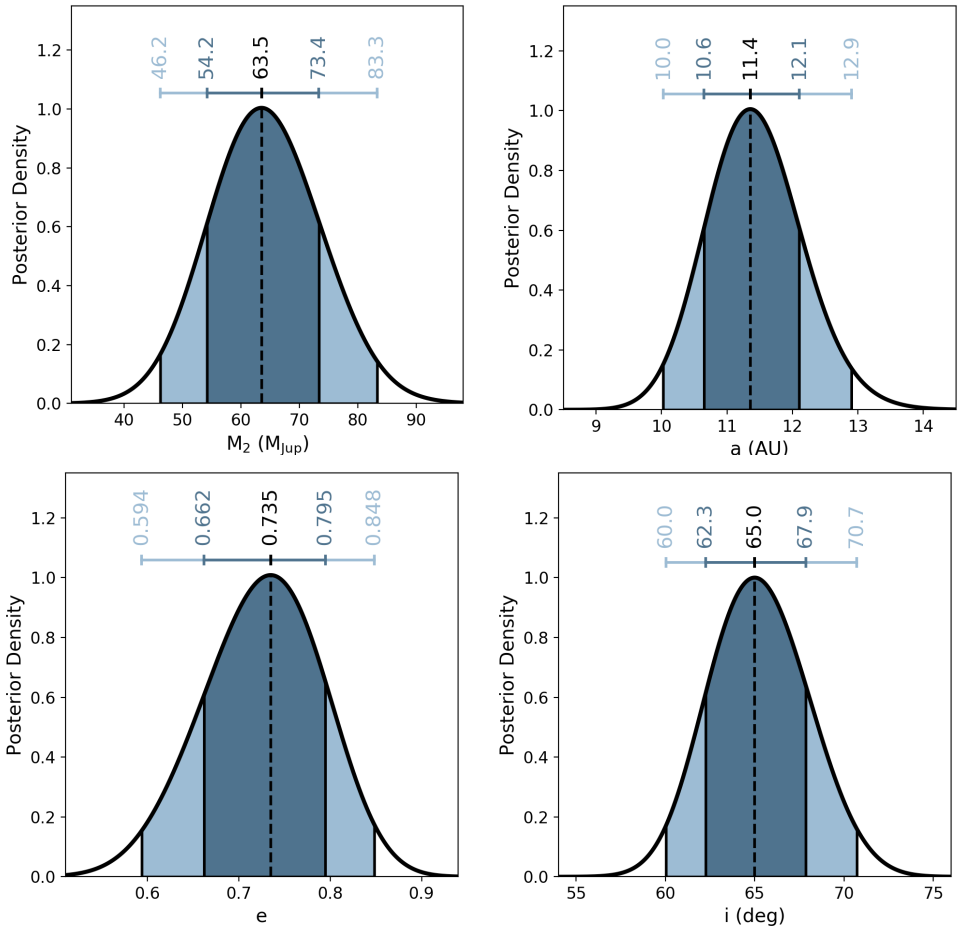

Figure 4.9. Marginalised posterior distributions for HD 4747.

mass M_2 (compared to 2−6% for these other studies). While the obtained value for ω_2 was in excellent agreement with previous works, Ω was found to be the most discrepant parameter ($\sim 10\sigma$) from the comparison values in Table 4.3. The reasons for this offset are not clear.

The remaining Keplerian elements for HD 4747 were nonetheless well constrained, despite using only two closely-separated relative astrometry data points. The inclusion of proper motion data from the *Hipparcos* and *Gaia* missions provides a substantial temporal coverage of ∼25 yr, significantly extending the typical orbital coverage available from RV surveys and direct imaging programs.

4.3.3.2 GJ 86

The K0 V star GJ 86 A was found by Els et al. (2001) to have a faint companion at ∼20 AU, initially thought to be a brown dwarf. Mugrauer & Neuhäuser (2005) later established GJ 86 B to be a white dwarf based on the large radial velocity drift of the primary and the photometry of the companion, which are not reconcilable with a low-mass star or brown dwarf. Farihi et al. (2013) estimated a mass of 0.59 ± 0.01 $M_\odot$ for the white dwarf from a photometric and spectroscopy analysis, suggesting an age of 2.5 Gyr for the system. However, Fuhrmann et al. (2014) determined an age of 10 Gyr for GJ 86 A given the chemistry and kinematics of the primary, which would imply a mass of 0.49 ± 0.02 $M_\odot$ for the white dwarf companion. Based on these results, we defined the allowed range for M_2 between 0.2−0.8 $M_\odot$ in our MCMC runs.

Lagrange et al. (2006) placed the first dynamical constraints on the orbit of GJ 86. Using direct imaging and RV data, they found a secondary mass between 0.48−0.62 $M_\odot$ and an eccentric, moderately-inclined orbit (see Table 4.4). Farihi et al. (2013) used relative astrometry measurements from *HST* data to constrain the orbital elements of the binary but were unable to place constraints on the mass of the white dwarf. More recently, Brandt et al. (2018) found a mass of 0.595 ± 0.010 $M_\odot$ for the companion, with orbital parameters roughly consistent with those obtained by Lagrange et al. (2006) and Farihi et al. (2013).

The results obtained here are presented in Table 4.4 (see Appendix 4.B, Figure 4.19 for the full MCMC output). From our MCMC analysis, we inferred a mass of

Table 4.4. GJ 86 results and comparison to other orbital constraints.

Parameter	This work	Brandt et al. 2018	Farihi et al. 2013	Lagrange et al. 2006
M_2 (M_{Jup})	$561.1^{+7.4}_{-8.8}$	623 ± 11	...	$500 - 650$
a (AU)	19.0 ± 0.4	$21.7^{+0.5}_{-0.7}$	$27.8 - 69.8$	$\gtrsim 20$
e	$0.615^{+0.023}_{-0.026}$	$0.53^{+0.04}_{-0.03}$	$0.00 - 0.61$	> 0.4
i (deg)	133.5 ± 0.5	$125.5^{+0.8}_{-0.9}$	$114.7 - 122.6$	$120 - 150$
ω_2 (deg)	$93.5^{+3.9}_{-4.0}$	$312.5^{+2.8}_{-3.5}$	$0 - 358$	...
Ω (deg)	$10.9^{+2.9}_{-3.3}$	$232.4^{+1.7}_{-1.5}$	$63.7 - 76.1$	...
T_0 (UT)	$1979.4^{+2.2}_{-2.3}$	1978.53 ± 1.9	$1933 - 2067$	$\sim 1986 - 2001$
P (yr)	$63.4^{+4.9}_{-4.8}$	72^{+7}_{-8}	$120 - 481$	$\gtrsim 200$
ϖ (mas)	$92.92^{+0.45}_{-0.54}$	92.70 ± 0.05	...	...
$\mu_{\alpha*}$ (mas yr^{-1})	$2119.35^{+0.88}_{-1.73}$	...	...	...
μ_δ (mas yr^{-1})	$663.28^{+1.17}_{-1.15}$	...	...	...

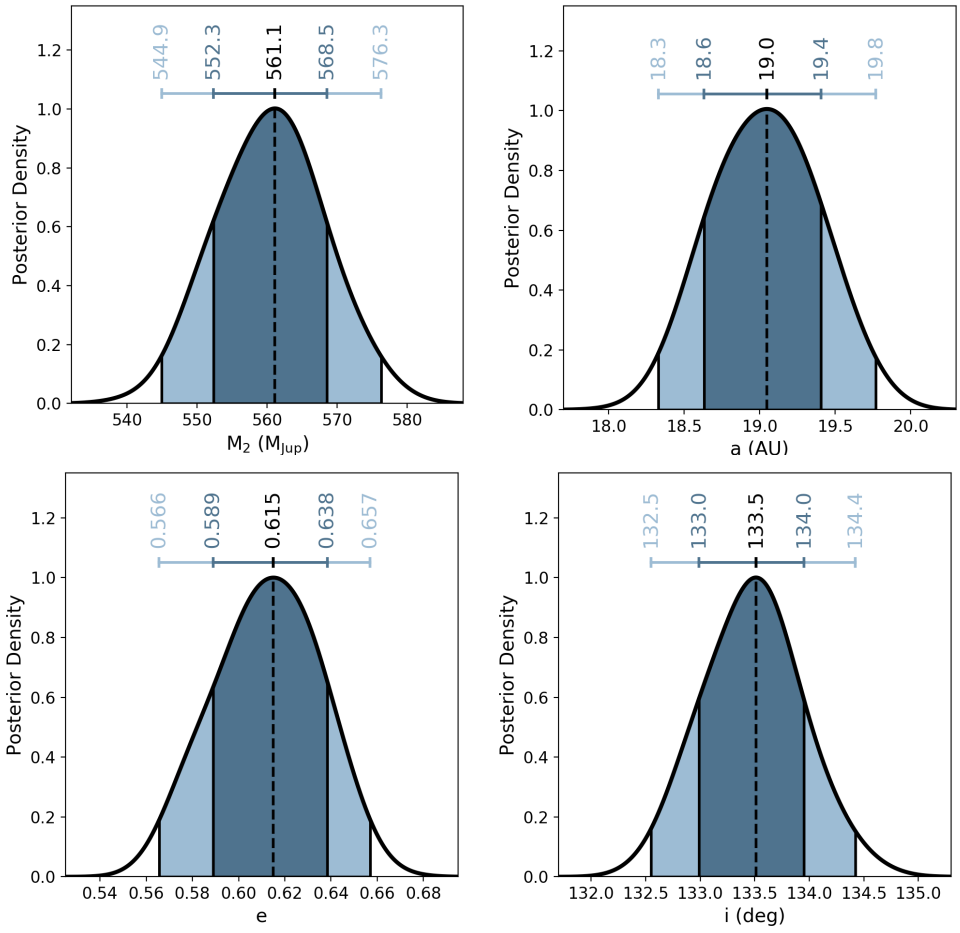

Figure 4.10. Marginalised posterior distributions for GJ 86.

$0.535^{+0.007}_{-0.008}$ $M_\odot$ for GJ 86 B, slightly lower than that found by Brandt et al. (2018). With the exception of the time of periastron passage T_0, all derived Keplerian orbital elements were somewhat discrepant from the Brandt et al. (2018) results, although a comparable precision was achieved in most parameters.

The small uncertainties obtained here are likely due to the very large significance of the substantial proper motion changes for GJ 86 A, allowing for few possible solutions at a high probability level. The observed disparities can be explained by the fact that the chosen imaging data points lie on either side of the best fit solution found by Brandt et al. (2018) in both projected separation and position angle. With only two points used in our fit, it is not surprising that a slightly different solution was obtained. In particular, the MCMC samples converged to solutions with very different ω_2 and Ω values (7 and 11σ for the Brandt et al. 2018 results, respectively). We note that both of these elements are offset by $\sim$220 deg from the values obtained by Brandt et al. (2018), although the reason for this joint offset is not clear.

Nonetheless, the obtained results in the remaining orbital parameters (a, e and i) and the companion mass M_2 are reasonably close to the expected values given the size of the explored parameter space and the very limited amount of data considered. These results thus illustrate that, by considering *Hipparcos* and *Gaia* proper motion measurements, our approach can provide viable orbital and dynamical constraints in most orbital elements for such systems, with no prior information and extremely limited observational data.

4.3.3.3 HD 68017

HD 68017 A is a G3 V Sun-like star exhibiting a significant RV acceleration. The M-dwarf companion responsible for this non-linear trend was imaged by Crepp et al. (2012b) as part of the TRENDS survey. Theoretical isochrones yield a mass of 0.16 ± 0.02 $M_\odot$ for HD 68017 B from its photometry (Crepp et al. 2012b). Based on the model-dependent mass of the secondary, we restricted our explored parameter space to companion masses in the range $0.05-0.5$ $M_\odot$.

Crepp et al. (2012b) estimated a lower mass limit of $M_2 > 0.08$ $M_\odot$ for the companion based on the observed RV amplitude, but did not place any constraints

Table 4.5. HD 68017 results and comparison to other orbital constraints.

Parameter	This work	Brandt et al. 2018
M_2 (M_{Jup})	$186.8^{+9.3}_{-10.8}$	154 ± 3
a (AU)	$17.9^{+0.8}_{-0.5}$	$16.0^{+1.0}_{-1.2}$
e	$0.375^{+0.014}_{-0.012}$	$0.325^{+0.017}_{-0.024}$
i (deg)	$159.0^{+2.8}_{-2.6}$	170.3 ± 0.4
ω_2 (deg)	$343.0^{+7.3}_{-5.1}$	280 ± 10
Ω (deg)	$160.9^{+4.3}_{-4.0}$	98.0 ± 0.9
T_0 (UT)	2018.0 ± 0.7	$1957.2^{+9.0}_{-6.6}$ (2017.2 ± 10)
P (yr)	$63.5^{+4.2}_{-3.6}$	60^{+6}_{-8}
ϖ (mas)	$46.56^{+0.43}_{-0.51}$	46.33 ± 0.06
$\mu_{\alpha*}$ (mas yr^{-1})	$-469.70^{+0.31}_{-0.28}$	...
μ_δ (mas yr^{-1})	$-648.22^{+0.52}_{-0.47}$	...

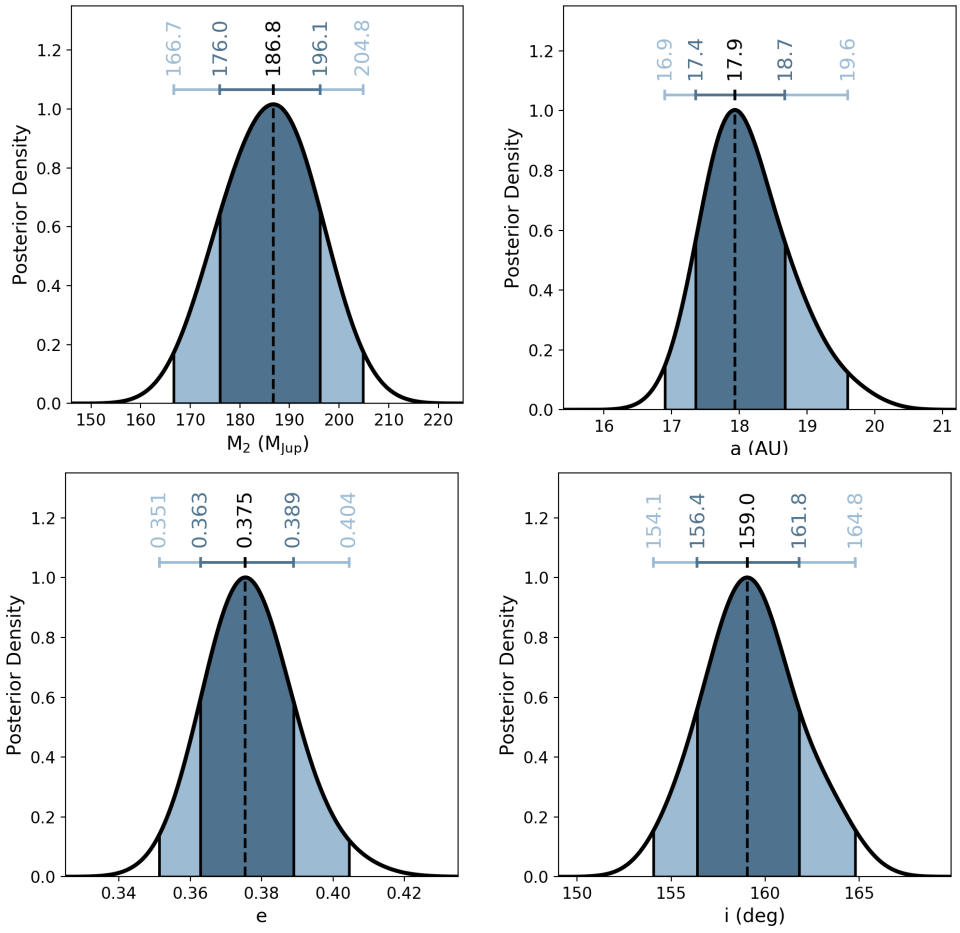

Figure 4.11. Marginalised posterior distributions for HD 68017.

on its orbit. The analysis performed by Brandt et al. (2018) represents the only orbital constraints to date for HD 68017. They inferred a mass of 0.147 ± 0.008 $M_\odot$ for the M-dwarf, on a 16 AU, almost face-on, low-eccentric orbit.

Our results are presented in Table 4.5 along with those from Brandt et al. (2018). The full output of our MCMC analysis is shown in Appendix 4.B (Figure 4.20). Our dynamical of $M_2 = 0.178^{+0.009}_{-0.010}$ $M_\odot$ is 2.4σ higher than that obtained by Brandt et al. (2018). We also found a somewhat larger semi-major axis (1.7σ) and higher eccentricity (2.5σ), and an inclination offset of $\sim$10 deg. The angular elements ω_2 and Ω were again the most discrepant parameters (5 and 15σ, respectively), both exhibiting an offset of $\sim$63 deg from the values found by Brandt et al. (2018). The time of periastron passage T_0 was found to be consistent with that obtained by Brandt et al. (2018), modulo one orbital period of $\sim$60 yr.

Despite some disparities, our derived orbital parameters are nonetheless fairly consistent with the more precise constraints from Brandt et al. (2018) for most orbital elements. These results thus demonstrate the power of our approach to recover good estimates of the mass, semi-major axis, eccentricity and inclination of an imaged companion, with minimal orbital coverage from direct imaging observations and high signal-to-noise proper motion measurements from *Gaia* and *Hipparcos*.

4.3.3.4 GJ 758

The brown dwarf GJ 758 B was discovered by Thalmann et al. (2009) to orbit a solar-type G9 V star. With an effective temperature $T_{\rm eff} = 600 \pm 100$ K, the cool companion has an estimated T8 spectral type (Vigan et al. 2016). Based on substellar evolutionary models, the brown dwarf has a mass of $\sim$20$-$40 $M_{\rm Jup}$ depending on the debated age of the system (Thalmann et al. 2009; Currie et al. 2010; Janson et al. 2011; Vigan et al. 2016). As a result, we allowed the M_2 MCMC model parameter to vary between 0.001 and 0.2 $M_\odot$.

Vigan et al. (2016) placed loose constraints on the orbit of the system using relative astrometry measurements from direct imaging observations, but did not constrain the dynamical mass of the companion. Bowler et al. (2018) combined RV and imaging data to derive more robust orbital constraints, inferring a mass

Table 4.6. GJ 758 results and comparison to other orbital constraints.

Parameter	This work	Brandt et al. 2018	Bowler et al. 2018	Vigan et al. 2016
M_2 (M_{Jup})	$35.6^{+1.7}_{-2.1}$	$38.1^{+1.7}_{-1.5}$	42^{+19}_{-7}	...
a (AU)	$34.1^{+1.5}_{-1.4}$	30^{+5}_{-8}	$21.1^{+2.7}_{-1.3}$	$33.36^{+50.34}_{-13.9}$
e	0.441 ± 0.012	0.40 ± 0.09	$0.58^{+0.07}_{-0.11}$	$0.505^{+0.488}_{-0.300}$
i (deg)	$41.0^{+2.4}_{-1.9}$	41 ± 6	28^{+12}_{-8}	$56.53^{+13.67}_{-13.03}$
ω_2 (deg)	$274.4^{+6.4}_{-6.6}$	150 ± 30	184^{+8}_{-9}	$[-37.15; 142.85]$
Ω (deg)	$21.8^{+2.3}_{-2.5}$	175^{+14}_{-16}	175 ± 5	$[-155.47; 24.53]$
T_0 (UT)	2038.7 ± 1.3	2046.9 ± 3.3	$2039.03^{+5.48}_{-2.19}$	$2039.3^{+12.1}_{-23.9}$
P (yr)	$224.7^{+16.5}_{-12.0}$	180^{+60}_{-90}	96^{+21}_{-9}	$128.3^{+373.7}_{-70.7}$
ϖ (mas)	64.09 ± 0.23	64.061 ± 0.022	...	...
$\mu_{\alpha*}$ (mas yr^{-1})	$80.74^{+0.12}_{-0.09}$	...	...	...
μ_δ (mas yr^{-1})	$162.57^{+0.15}_{-0.16}$	...	...	...

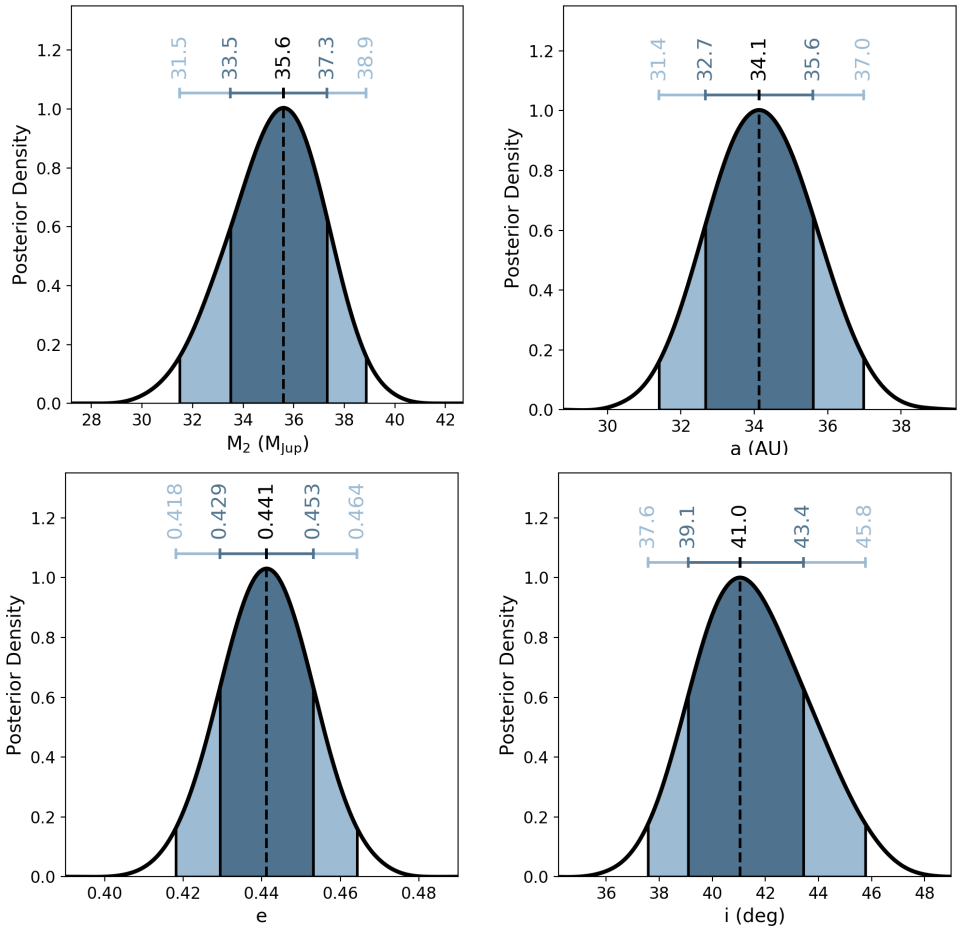

Figure 4.12. Marginalised posterior distributions for GJ 758.

of 42^{+19}_{-7} M_{Jup} for GJ 758 B (see Table 4.6). Calissendorff & Janson (2018) then refined this mass estimate to $42.4^{+5.6}_{-5.0}$ M_{Jup}, using the posteriors from Bowler et al. (2018) together with the difference in proper motion for the primary between the *Hipparcos* and *Gaia* DR2 catalogues. Combining RV, imaging and proper motion differences, Brandt et al. (2018) inferred a slightly lower mass for the brown dwarf ($38.1^{+1.7}_{-1.5}$ M_{Jup}) and somewhat different orbital elements, as shown in Table 4.6.

The results from our MCMC analysis are listed in Table 4.6 and presented fully in Appendix 4.B (Figure 4.21). We obtained a lower companion mass and larger semi-major axis than in previous studies ($M_2 = 35.6^{+1.7}_{-2.1}$ M_{Jup} and $a = 34.1^{+1.5}_{-1.4}$ AU), although consistent with the results from Brandt et al. (2018) at the 1-σ level. In particular, the eccentricity e and orbital inclination i were found to be highly consistent with the values obtained by Brandt et al. (2018). While our posteriors for ω_2 and Ω were again rather discordant from other work for reasons that remain unclear, the retrieved value for the time of periastron passage T_0 was in excellent agreement with that obtained in Bowler et al. (2018), and within 2σ from that inferred in Brandt et al. (2018). As for GJ 86, the imaging data points considered for our analysis are marginal outliers to the best fit solution from Brandt et al. (2018), which could explain the observed discrepancies.

We conclude that our approach was successful at recovering most orbital elements and the dynamical mass of GJ 758 B. This system has the longest orbital period of all targets studied here ($P \gtrsim 100-200$ yr). Even with an orbital coverage of only $\sim$1 yr from direct imaging observations, the proper motion measurements from *Gaia* and *Hipparcos* increase the fractional coverage of the orbit to $\sim$10$-$20% of the period. The combination of absolute and relative astrometry then allows for rather robust and accurate constraints on the primary elements defining the orbit of the system, without the need for radial velocity data.

4.3.3.5 HR 7672

Liu et al. (2002) discovered HR 7672 B as a companion to a G0 V star with a strong RV linear trend. The L4.5$\pm$1.5 companion has a model-derived mass of 55$-$78 M_{Jup} assuming a 1$-$3 Gyr age for the system (Liu et al. 2002). With an estimated mass near the hydrogen-burning limit, HR 7672 B could be a low-mass

Table 4.7. HR 7672 results and comparison to other orbital constraints.

Parameter	This work	Brandt et al. 2018	Crepp et al. 2012a
M_2 (M_{Jup})	$81.5^{+7.9}_{-8.5}$	72.7 ± 0.8	$68.7^{+2.4}_{-3.1}$
a (AU)	$14.9^{+2.7}_{-2.3}$	$19.6^{+0.8}_{-1.0}$	$18.3^{+0.4}_{-0.5}$
e	$0.403^{+0.066}_{-0.072}$	0.542 ± 0.018	0.50 ± 0.01
i (deg)	$97.4^{+5.5}_{-5.7}$	97.4 ± 0.4	$97.3^{+0.4}_{-0.5}$
ω_2 (deg)	$93.9^{+20.7}_{-18.5}$	$256.3^{+2.8}_{-2.7}$	259 ± 2
Ω (deg)	$152.7^{+2.2}_{-2.1}$	$330.95^{+0.32}_{-0.30}$	$61.0^{+0.3}_{-0.4}$
T_0 (UT)	$2014.9^{+1.1}_{-1.2}$	1929.0 ± 7.5	$2014.5 - 2014.7$
P (yr)	$59.3^{+13.9}_{-11.8}$	86^{+7}_{-8}	$73.3^{+2.2}_{-2.9}$
ϖ (mas)	$56.62^{+0.54}_{-0.60}$	56.43 ± 0.07	...
$\mu_{\alpha*}$ (mas yr^{-1})	$-392.08^{+0.41}_{-0.42}$	...	...
μ_δ (mas yr^{-1})	$-410.53^{+0.56}_{-0.54}$	...	...

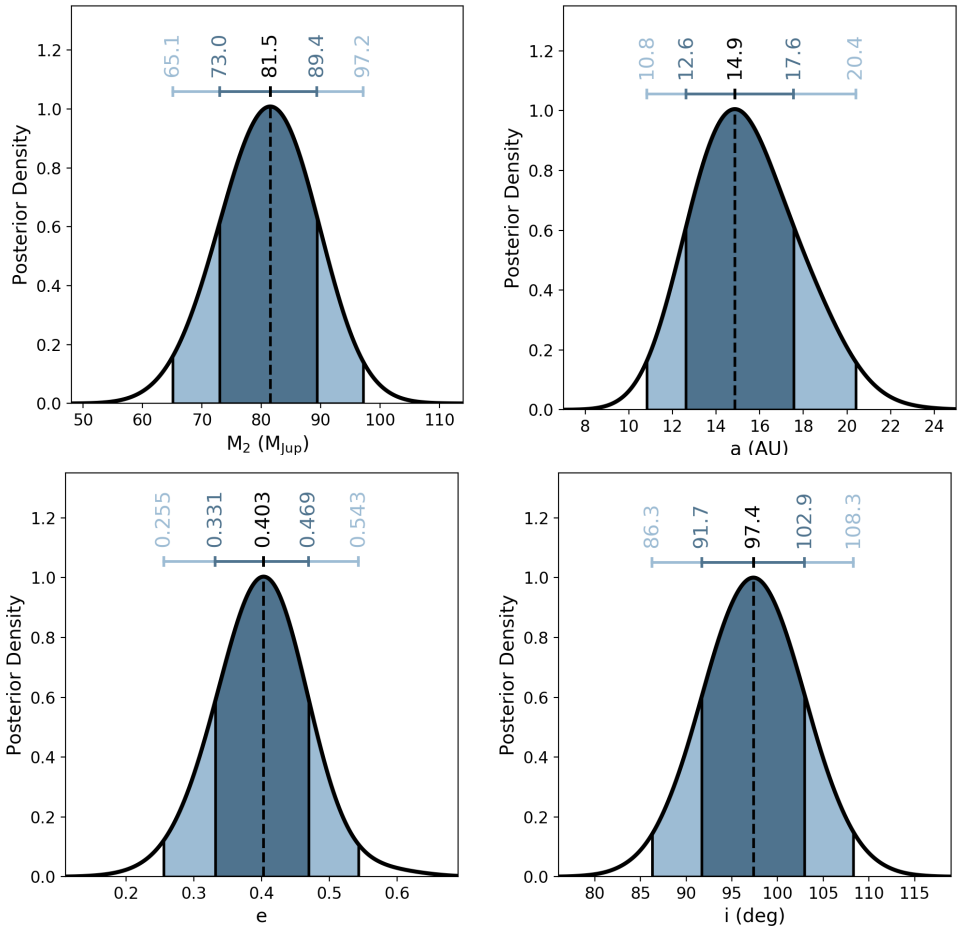

Figure 4.13. Marginalised posterior distributions for HR 7672.

star or a massive brown dwarf. Based on these results, we restricted the explored parameter space in our MCMC runs to $M_2 = 0.01{-}0.2$ $M_\odot$ for this target.

Using RV data in combination with relative astrometry, Crepp et al. (2012a) constrained the orbit of HR 7672, finding a dynamical mass of $68.7^{+2.4}_{-3.1}$ M_{Jup} for the companion. Adding absolute astrometry to the analysis, Brandt et al. (2018) obtained a higher secondary mass of 72.7 ± 0.8 M_{Jup}. We report these results in Table 4.7, along with our own orbital and dynamical constraints for the HR 7672 system (see Figure 4.22 in Appendix 4.B for the full corner plot of the MCMC output).

Our inferred posterior distribution for the companion mass peaked at a somewhat larger value than previous estimates ($81.4^{+7.9}_{-8.5}$ M_{Jup}), although still consistent at the $\sim 1\sigma$ level. The slightly smaller semi-major axis and eccentricity values obtained here were also consistent with past studies at the 2-σ level. The inclination and time of periastron passage were found to be in excellent agreement with these previous works. The angular terms ω_2 and Ω were offset by $\sim$180 deg from the Brandt et al. (2018) results, suggesting that our solution for Ω represents the longitude of descending node rather than the ascending one.

These results show once again that we are able to place strong constraints on the orbit of long-period companions with only two epochs of direct imaging observations, by taking advantage of long orbital coverage provided by precise *Gaia* and *Hipparcos* proper motions.

4.3.4 Summary of Results and Discussion

The results obtained in Section 4.3.3 for our five test targets demonstrate that our COPAINS tool for orbital parametrisation can successfully recover the dynamical masses and main Keplerian elements for directly-imaged companions to $\Delta\mu$ stars. The combination of relative astrometry from imaging observations with absolute astrometry from proper motion measurements allows for robust constraints on the orbital properties of a star and its companion using minimal observational data. We have showed that our method works for a large range of secondary masses, from low-mass brown dwarfs to massive white dwarf companions, with

semi-major axes between $\sim$10$-$30 AU. The long baseline of $\sim$25 years between the *Hipparcos* and *Gaia* astrometric missions makes our approach sensitive to systems with periods as long as centuries.

The dynamical masses inferred for secondary companions were consistent at the 1-σ level with the values from Brandt et al. (2018) for the substellar companions (HD 4747 B, GJ 758 B, HR 7672 B), and slightly more discrepant for more massive companions (GJ 86 B, HD 68017 B). Trusting that the results from Brandt et al. (2018) are close to the true masses for these systems, our approach consistently achieved a relative discrepancy smaller than $\sim$10% between our estimated masses and the true values. This is a considerable improvement from the typical uncertainties in model-dependent masses, which can vary by $\sim$30$-$50%, depending on the theoretical isochrones used and the uncertain system ages considered. The ability to obtain model-independent masses is critical for astronomical objects like brown dwarfs and white dwarfs which show a mass-age degeneracy and generally have poorly-constrained ages. The measurement of dynamical masses for such systems thus offers a rare opportunity to bypass the uncertainties introduced by unknown ages or unreliable models, and will provide unique chances to calibrate evolutionary tracks.

Our obtained semi-major axes were in good agreement with the results from Brandt et al. (2018) and other previous studies, consistent within 2σ for all targets except GJ 86, for which we obtained a 3.3-σ disparity. In terms of relative differences, we achieved typical divergences of $\sim$10$-$15% between the peak semi-major axis values obtained here and the most likely values reported in Brandt et al. (2018). This is a good achievement given the large range explored in our MCMC runs for this parameter (a = 1$-$100 AU), and the wider disparities seen in the literature for some of the studied targets. System eccentricities were generally well estimated by our tool, with differences in the obtained peak values < 0.1 for most targets, relative to the values in Brandt et al. (2018) or other orbital constraints. Similarly, our results for the orbital inclination of the five systems investigated were usually within $\sim$10$-$15 deg from the values determined by Brandt et al. (2018). In particular, the prograde ($i < 90$ deg) or retrograde ($i > 90$ deg) motion in the orbital plane was successfully recovered for each system. Given the span of allowed values ($0 < i/\mathrm{deg} < 180$ deg) and the

inconsistencies between various studies, we consider that our approach was rather successful at constraining the inclination of the examined targets.

The argument of periastron ω_2 and the longitude of ascending node Ω were the only orbital elements for which our tool failed to consistently recover previous results. Both parameters were retrieved with a 180 deg offset from the expected values for HR 7672, corresponding to the second, degenerate solution for the projected orbit. With the exception of the ω_2 value obtained for HD 4747, the results achieved in these two parameters for the remaining targets were found to be rather inconsistent with the Brandt et al. (2018) values. Significant discrepancies are observed between the constraints placed on these angular parameters across various studies (see Tables 4.3 to 4.7), including a recurrent 90 deg offset in Ω for the same ω_2 values (e.g. HD 4747, HR 7672). The true values for these Keplerian elements thus remain ambiguous for most systems. It is worth noting that for two targets (GJ 86 and HD 68017), both orbital elements seem to be offset by the same amount relative to expected orbital solutions. The reason for the apparent shared disparity between the two parameters is unclear. Despite the peculiar and questionable solutions obtained in our MCMC analyses for ω_2 and Ω, the time of periastron passage T_0 was consistently well retrieved, typically within $\sim$1 year from previous estimates. Our approach was thus highly successful at constraining the temporal orbital element, especially given the very long orbital periods of several decades to centuries of the studied systems.

These well-calibrated targets have allowed us to robustly test the performance of our MCMC approach and validate our method. We conclude that our orbit fitting tool with COPAINS enables us to place strong and reasonably accurate constraints on the orbit and dynamical mass of directly-imaged companions, with only two epochs of imaging observations combined with *Gaia* and *Hipparcos* proper motions. In addition, our orbital fitting strategy provides constraints on the parallax of studied systems without relying on *Gaia* DR2 measurements as heavily as in the method used by Brandt et al. (2018). Given that the *Gaia* DR2 parallaxes assume that sources are single when deriving astrometric solutions (Lindegren et al. 2018), the resulting values are expected to be somewhat spurious for the binary primaries investigated here. It is thus crucial to loosen the observational constraints on system parallaxes from the small *Gaia* uncertainties. We achieved typical uncertainties of $\sim$0.5 mas in the obtained parallaxes. We

were also able to place unique constraints on the proper motion of the centre of mass of probed systems. We achieved excellent precision levels in the resulting barycentric proper motions, varying from about 0.1 mas yr^{-1} for our target with the smallest proper motion changes (GJ 758), up to $\sim$1 mas yr^{-1} for the system exhibiting the largest proper motion disparities (GJ 86).

The main caveat of our approach is that the formalism followed in our binary simulator is only applicable to two-body systems. Our approach is thus not valid for higher-order multiples in which a third component will also have a non-negligible effect on the observed astrometry of the primary star. We have also assumed previously-established primary masses throughout this work, and did not attempt to constrain the masses of the host stars. Our results are thus somewhat dependent on the knowledge of stellar masses for studied systems. Further tests will be required to assess the effect of adding an extra model parameter on the obtained results, and determine whether our approach can also infer model-independent masses for the primaries.

The use of proper motions to constrain the orbits of binary systems has only recently started to be exploited (e.g Brandt et al. 2018; Calissendorff & Janson 2018; Dupuy et al. 2019). Most of these studies considered differences in proper motions as additional information, to complement large sets of imaging and RV data (generally with observations spanning decades), and refine the constraints obtained with these data only. We have demonstrated in this work that absolute astrometry from precise proper motion measurements can be used as primary observational input, and that a couple of additional imaging data points are sufficient to fully parametrise the orbital elements and secondary mass of a $\Delta\mu$ star and its companion. This means that orbital constraints and model-independent masses can be obtained for new direct imaging systems, without the need to wait for decades of imaging or RV data. Of course, larger data sets providing a more complete orbital coverage (from direct imaging or RV observations) will be needed to confirm and refine these initial results.

All the systems studied here are several Gyr old and are therefore easy to observe with radial velocity. In contrast, the young stars typically targeted in direct imaging surveys are too active for precise Doppler spectroscopy. While robust orbital constraints and dynamical masses can be achieved for old systems with

imaging observations, by including years of RV monitoring data in the orbit fits (e.g. Bowler et al. 2018; Crepp et al. 2018), this is not feasible for extremely young targets. The lowest-mass substellar companions, in particular companions in the planetary mass regime, are only detectable at the earliest stages of their evolution. The need for a method allowing orbital parametrisation without requiring RV measurements is thus crucial. The results obtained here with our new COPAINS tool represent very encouraging prospects towards determining the orbits of young, widely-separated companions, and obtaining model-independent masses for benchmark brown dwarfs and giant exoplanets.

4.4 Conclusions

We presented in this chapter a new code aimed at identifying new directly-imaged companions and constraining the orbit of these systems. Our COPAINS tool (Code for Orbital Parametrisation of Astrometrically Inferred New systems) exploits the synergy between direct imaging and astrometry to select promising targets for imaging campaigns searching for low-mass companions. Our approach is based on changes in stellar proper motions between long and short-term proper motion measurements induced by a hidden companion. From measurement astrometric offsets, our tool provides a good indication of where the unseen companion may be located in the mass-separation space. Using the typical sensitivity of imaging facilities or existing sets of observations, COPAINS offers a robust, informed selection method for ideal targets to observe in direct imaging programs.

Our COPAINS tool then allows us to constrain the orbit of discovered systems, using only two epochs of imaging observations separated by $\sim$1 yr. The use of *Hipparcos* and *Gaia* proper motions in our MCMC orbit fits significantly increases the orbital coverage of the observational data, making our approach sensitive to systems with orbital periods of several decades up to centuries. Testing our orbital fitting procedure on well-calibrated targets, we achieved relative precisions to the expected values $\lesssim 10-15\%$ in the dynamical masses, semi-major axes, eccentricities and inclinations of the wide-orbit companions. The method did a

poorer job at constraining the remaining orbital elements describing the angular orientation of orbits.

These results are extremely encouraging regarding the discovery and orbital parametrisation of new directly-imaged companions. This new selection method for direct imaging campaigns promises to reduce to null detection rates from current programs, and will significantly improve the current census of directly-imaged exoplanets and low-mass companions. The measurement of orbital elements and model-independent masses for new benchmark objects, without the need for extensive radial velocity observations or decades of direct imaging monitoring, will be crucial to calibrate and refine theoretical models in the substellar regimes.

4.A Quantitative Assessment of the Limitations of the Method

4.A.1 Effect of Duration of Catalogues

In order to test the effect of the offsets introduced by using catalogues of various baselines, we estimated the difference between the proper motion that would be observed over different time baselines, and the true instantaneous or center-of-mass displacements for a range binary of companions around an example target of mass $M_1 = 1$ M$_\odot$. We used a parallax of $\varpi = 50$ mas and assumed a proper motion of $\mu_{\alpha*} = 100$ mas yr^{-1} and $\mu_\delta = 100$ mas yr^{-1} for the barycentre of the system. We considered the *Gaia* DR2 and *Hipparcos* catalogues for short-term proper motions, and the TGAS and Tycho-2 catalogues for long-term measurements.

We first constructed a grid of semi-major axes a and companion masses M_2, with 100 log-spaced a values between 0.1−1000 AU, and 100 log-spaced M_2 in the range 0.001−1 M$_\odot$. For each cell in the grid, we generated 1000 random orbits by drawing from uniform distributions an eccentricity e, inclination i, argument of periastron ω, longitude of ascending node Ω and time of periastron passage T_0. Using the binary simulator tool described in Section 4.3.1, we then derived measured proper motions by considering the position of the primary at the start and end observation dates of the catalogues, and estimating the velocity vector between these two points given the length of the considered catalogues. For *Gaia* DR2, proper motions were calculated between 2014.6 and 2016.4, and were compared to instantaneous velocities at epoch 2015.5 (Gaia Collaboration et al. 2018b). For *Hipparcos*, we considered observing dates between 1989.8 to 1993.2 (Perryman et al. 1997), with a mean epoch of 1991.5 for the tangential velocity, a bit later than the catalogue epoch (1991.25; ESA 1997). Proper motions were estimated between 1900 and 2000 for Tycho-2, as the original epochs used to derive Tycho-2 proper motions from 144 ground-based photographic programs vary by a few decades (Høg et al. 2000) around this initial epoch. Finally, we used observing dates between 1991.25 and 2015.0 for TGAS, the epochs of the positional measurements in Tycho-2 and *Gaia* DR1 (Michalik et al. 2015).

For short-term proper motions, we computed the instantaneous velocity of the primary at the mean epoch of the short-term catalogue. For long-term catalogues, the obtained proper motion measurement was compared to the adopted true motion of the system given above. For each simulated orbit, we then computed the modulus of the vector difference between a short or long term-proper motion measurement and the true underlying tangential velocity or centre-of-mass motion. Finally, we calculated the upper limit of the 1-σ interval of the 1000 resulting differences to obtain a single value for each cell in the original grid. The 1-σ confidence level was found adopting a highest probability density approach, which provides the set of most probable values (see Section 4.2.3). We considered the upper boundary of the 68% credible interval rather than the mean or median of the samples in each cell of the grid in order to take into account the spread of the obtained distributions, which may vary throughout the parameter space. The final values thus provide uniformly-defined upper limits on the expected disparities, and only a small fraction of systems in the remaining low-probability upper tails are expected to be above these thresholds.

The top panels of Figure 4.14 shows the resulting 1-σ upper limits on the offsets on short-term proper motion measurements from the tangential velocities in the $a-M_2$ parameter space for *Gaia* DR2 (left) and *Hipparcos* (right) data. The solid lines show the regions where measured short-term proper motions are discrepant by 0.1%, 1% and 10% from the instantaneous velocities we assume they represent. As expected, high discrepancies arise in binaries of small separations, for which the short-term catalogues cover a significant fraction of the orbit (and up to multiple orbital periods). Large uncertainties will thus be introduced when using *Gaia* DR2 or *Hipparcos* as short-term proper motion measurements for systems with periods shorter than or comparable to the duration of the catalogues (red dotted lines). Longer orbital periods are required for the offsets to become insignificant, typically of at least several to tens of AU, for systems similar to our example target.

In the bottom panels of Figure 4.14, we present the disparities between long-term proper motion estimates and the true system proper motion using Tycho-2 (left) and TGAS (right). As for the top panels, the colour scale corresponds to the upper boundaries of the 68% confidence intervals of the obtained distribution in each 1-dimensional column. In this case, short-period binaries are preferred for the

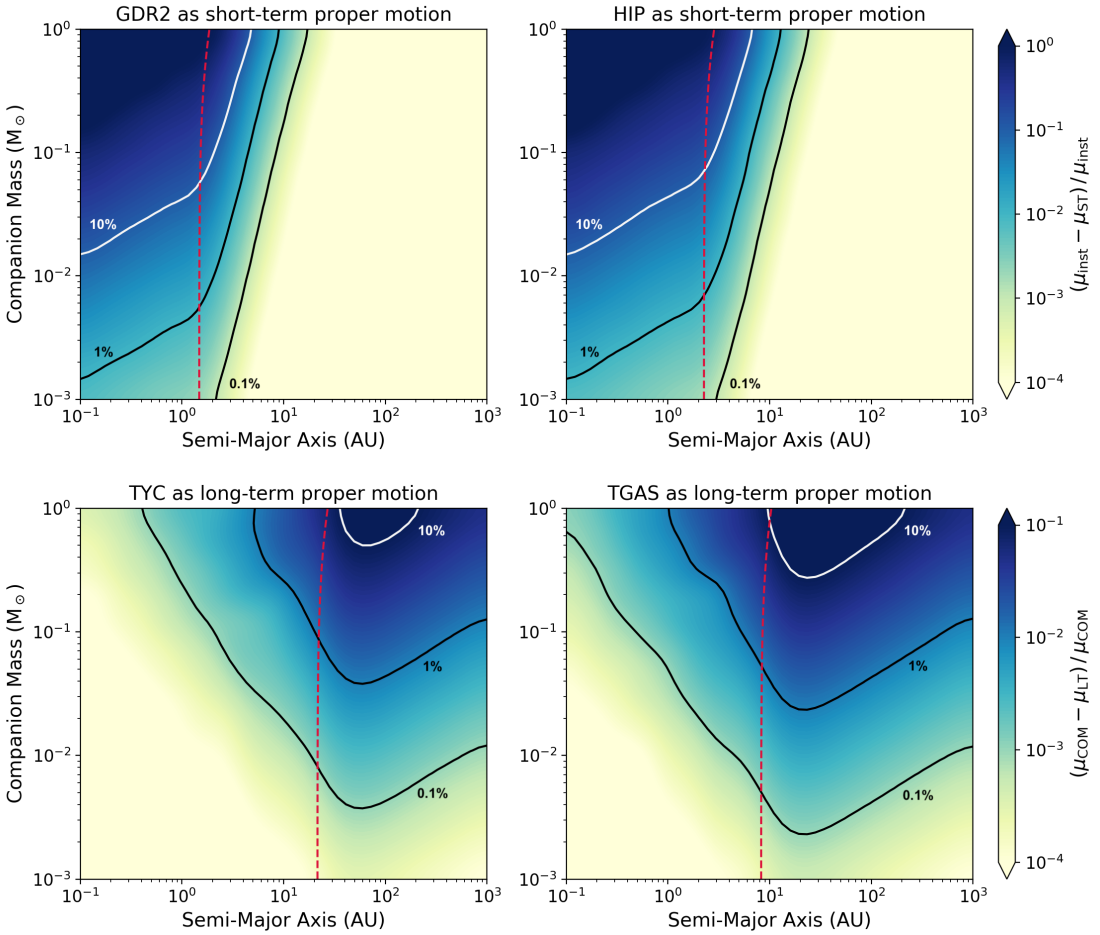

Figure 4.14. Top: 1-σ upper boundary of the relative offset between the true instantaneous velocity of the primary and *Gaia* DR2 (left) or *Hipparcos* (right) proper motion measurements. The results are marginalised over all possible orbital elements for each pair of semi-major axis and companion mass around our 1 $M_\odot$ example target at 20 pc ($\varpi = 50$ mas). We adopted a proper motion of $\mu_{\alpha*} = 100$ mas yr^{-1} and $\mu_{\alpha*} = 100$ mas yr^{-1} for the model target. Values correspond to the upper limit of the 68% interval of highest probability computed for 1000 randomly-selected orbital configurations for each mass-separation pair in the grid (see text). The red dotted lines indicate the mass-separation pairs for which the orbital periods of the systems are equal to the length of the catalogue (1.8 yr and 3.4 yr for *Gaia* DR2 and *Hipparcos*, respectively). **Bottom:** 1-σ upper boundary of the relative difference between the barycentric motion of the system and long-term proper motion measurements of the primary from Tycho-2 (left) and TGAS (right). The red dotted lines show the position on the parameter space where systems have orbital periods equal to the duration of the long-term proper motion baselines (100 yr and 23.75 yr for *Gaia* DR2 and *Hipparcos*, respectively).

approximations to be reliable, where the proper motion measurements encompass multiple orbital periods. The offsets get larger as the orbital periods approach the length of the catalogues (red dotted lines). The turn-over at wider semi-major axes can be explained by the fact that for the same companion mass, the wobble induced on the primary becomes smaller with larger separations (Equation 4.1). As a result, the proper motion of the primary generally remains closer to the barycentric motion, and the typical offset relative to the same true system motion decreases, even if the baseline of the catalogue only covers part of the orbital period. For our example star, the discrepancies are negligible for most substellar companions within $\sim$10 AU for Tycho-2 and a few AU when using TGAS.

We note that as the obtained values represent upper limits at the 1-σ level, our approach is rather conservative and these results are likely to be underestimating the good regions of the parameter space, in which the relative offsets are very small. In addition, proper motions are in reality acquired from many more positional measurements than the two data points at the beginning and end of the mission time spans. While *Gaia* sources were treated as single sources for astrometric solutions in the first two Data Releases (Michalik et al. 2015; Lindegren et al. 2018), some catalogues also account for the nonlinearity of stellar motions when deriving parallaxes and proper motions, as was done for Tycho-2 (Høg et al. 2000) and *Hipparcos* data (Perryman et al. 1997; van Leeuwen 2007). Measured proper motions might therefore be closer to the true values than in our estimates, which assume a straight vector for proper motion measurements based on only two points. The uncertainties obtained here are thus likely to be overestimated for these reasons.

That being said, some of the data used might also carry further sources of uncertainties. For example, Tycho-2 astrometry may contain systematic errors from the archival data used to derive proper motions (Michalik et al. 2015). Astrometric 5-parameter solutions for *Gaia* parallaxes and proper motions also assume that all stars are single (Lindegren et al. 2018). Since the $\Delta\mu$ targets of interest in this work are by definition not single, there may be some additional offset on the parallaxes and proper motions due to this effect, as a result of an erroneous disentanglement between parallax and proper motion on very short time spans (Schönrich et al. 2019).

We also investigated the dependence on distance in the results presented in Figure 4.14. We found that at larger distances (smaller parallaxes), the relative disparities become smaller in every point of the parameter space, for both the short and long-term proper motion measurements. This is due to the fact that the observable excursion of the primary decreases with increasing distance for the same companion mass and semi-major axis. As a result, the obtained fractional offsets are smaller and the achieved relative accuracies are improved. The changes with decreasing parallax can be thought of as sliding the values in Figure 4.14 upwards at every semi-major axis, resulting in lower relative differences at any given mass between the measured proper motions and the underlying tangential or centre-of-mass velocities. Figure 4.15 shows the same plots as in Figure 4.14, placing our example target of 1 $M_\odot$ at a distance of 100 pc ($\varpi = 10$ mas) instead of 20 pc (50 mas), illustrating the upward shift in the obtained values relative to Figure 4.14.

Similarly, we examined the effect of proper motion magnitude on the results obtained above. We set the proper motion of our example target to $\mu_{\alpha*} = 250$ mas yr^{-1} and $\mu_\delta = 250$ mas yr^{-1}, for a parallax of $\varpi = 50$ mas (closer to the proper motions of the targets studied in Section 4.2.5). The same outcome was observed compared to decreasing the assigned parallax, as shown in Figure 4.16. Smaller relative offsets were obtained throughout the parameter space for larger system motions, in both the estimates of tangential velocities (top panels) and barycentric motions (bottom panel). Again, this is attributed to the fact that the same observable astrometric displacement of the primary due to the presence of a secondary companion will be subdued by the larger space motion of the system. As expected, the combination of larger parallax and higher proper motion results in a joint outcome of the two individual effects noted here. In this case, a further upwards shift of the obtained values in Figures 4.14 to 4.16 is observed, decreasing the resulting uncertainties in every point in the parameter space.

4.A.2 Effect of Orbital Inclination

We inspected the consequence of the assumption of face-on orbits in our approach, introduced by treating Equation 4.1 as an equality. We considered the same example target as above (1 $M_\odot$, $\varpi = 50$ mas, $\mu_{alpha*} = \mu_\delta = 100$ mas yr^{-1}).

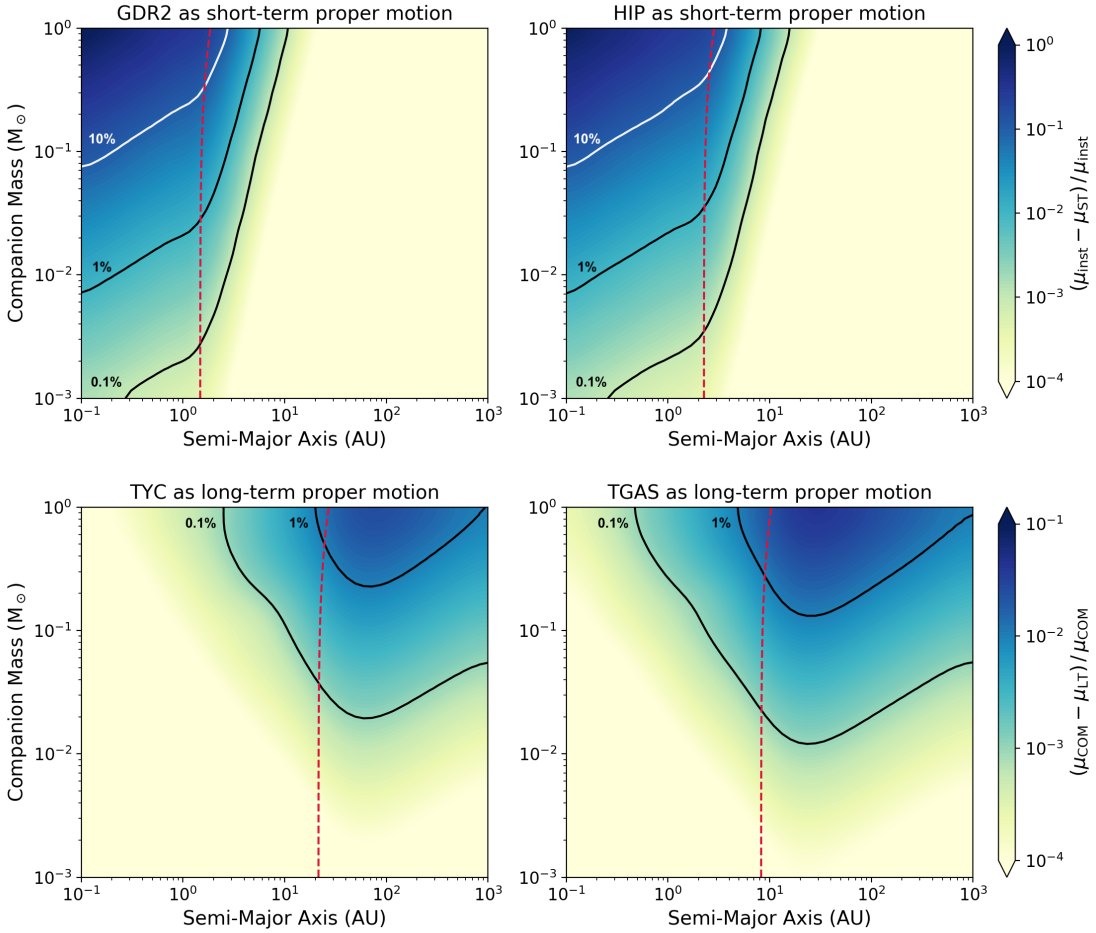

Figure 4.15. Same as Figure 4.14, placing our example target of mass 1 $M_\odot$ at 100 pc ($\varpi = 50$ mas), with a proper motion of $\mu_{\alpha*} = 100$ mas yr^{-1} and $\mu_\delta = 100$ mas yr^{-1}. The decrease in parallax leads to smaller fractional offsets for both the short-term proper motions (top panels) and long-term proper motions (bottom panels) relative to the instantaneous velocities and centre-of-mass motions we take them to represent, respectively.

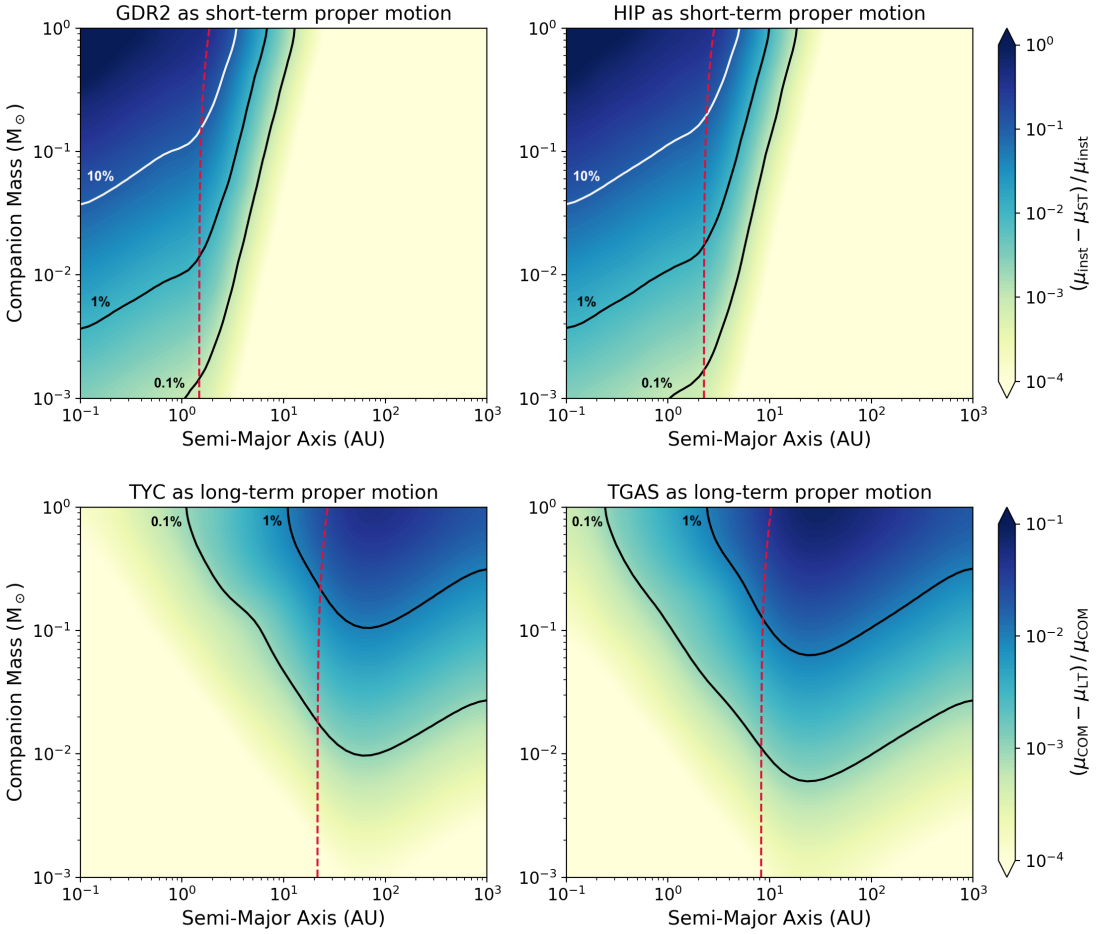

Figure 4.16. Same as Figure 4.14, assigning a proper motion of $\mu_{\alpha*} = 250$ mas yr^{-1} and $\mu_\delta = 250$ mas yr^{-1} to our example target of mass 1 M$_\odot$ located at 20 pc ($\varpi = 50$ mas). The increase in proper motion magnitude results in smaller fractional offsets in both short (top panels) and long-term (bottom panels) proper motion measurements.

We used a similar logarithmic $a - M_2$ grid, with 100 semi-major axes from 0.1 to 1000 AU, and 100 companion masses ranging from 0.001 to 1 $M_\odot$. For each mass-separation pair, we generated 1000 random orbits (see previous Section) and computed the projected proper motion offset $\Delta\mu_{\rm proj}$, given by the difference between the instantaneous velocity of the primary at epoch 2000 and the adopted centre-of-mass motion of the system ($\mu_{\alpha*}$ = 100 mas yr^{-1}, μ_δ = 100 mas yr^{-1}). For each simulated orbit, we considered in parallel the same orbital elements with an inclination of i = 0 deg, and calculated the proper motion discrepancy of the same system and at the same epoch, assuming a face-on orbit. Finally, we estimated the relative difference between the obtained projected and maximum $\Delta\mu$ values: $(\Delta\mu_{\rm max} - \Delta\mu_{\rm proj})$ / $\Delta\mu_{\rm max}$. The obtained differences were normalised to $\Delta\mu_{\rm max}$ in order to be able to compare the output throughout the parameter space, as the induced changes in proper motion vary with companion mass and separation.

Figure 4.17 shows the distribution of relative disparities between the projected and face-on changes in proper motion for all 1000 simulated orbits in each cell in the mass-separation grid (black line). The results are also divided into three inclination bins, shown in the filled, coloured distributions. We found that in most configurations, the resulting offset is typically very small, with a clear peak near 0, and a median of only 6%. The relative differences were found to be smaller than 17% at the 1-σ level (68% confidence interval) for the overall distribution. As expected, larger disparities were observed with higher inclination values. The normalised offsets between $\Delta\mu_{\rm proj}$ and $\Delta\mu_{\rm max}$ appeared to be distributed homogeneously throughout the parameter space.

We conclude that the assumption of a face-on orbit in our approach will typically lead to the $\Delta\mu$ values used in the code being underestimated by $< 10-15$%, and this offset will be negligible (less than $\sim$5% disparity) in about half of all cases. Based on this analysis, less than a quarter of systems are expected of be offset by more than 20% when assuming an orbit in the plane of the sky. Given that most selected $\Delta\mu$ targets have a proper motion trend just above the 3-σ selection threshold, this new source of uncertainty will generally be significantly smaller than the measurement uncertainty on the observed $\Delta\mu$.

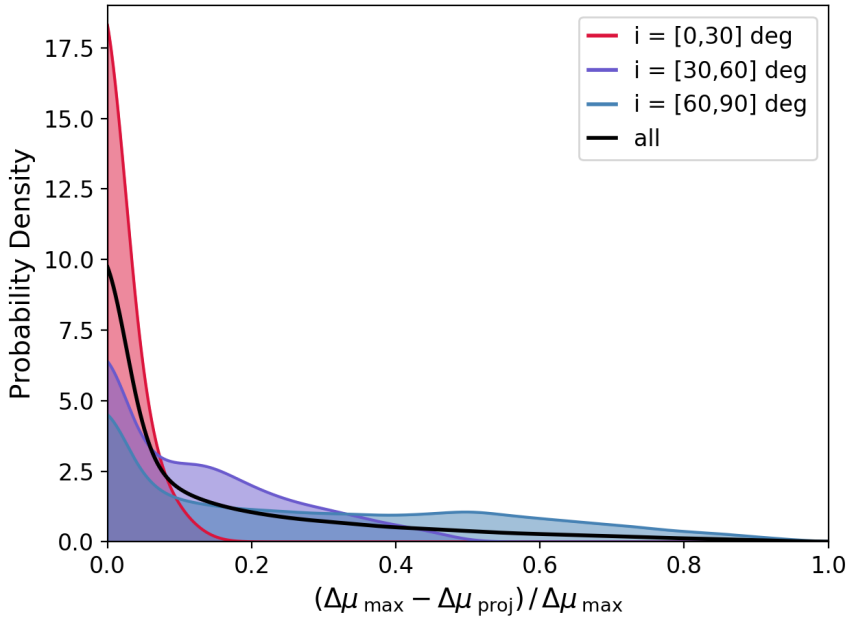

Figure 4.17. Distribution of relative offsets between projected $\Delta\mu$ measurements and the corresponding $\Delta\mu$ that would be observed if the same systems were in the plane of the sky (inclination $i = 0$ deg). The resulting disparities represent the error introduced in our approach by considering observed proper motion changes to correspond to face-on orbits (i.e. treating Equation 4.1 as an equality). The discrepancies were computed for 1000 randomly-selected orbits for each pair of semi-major axis and companion mass in a log-spaced grid of size 100 by 100 ranging from 0.1−1000 AU and 0.001−1 $M_\odot$. The solid black line represents the overall distribution, and the coloured segments correspond to various inclination bins.

4.B Full MCMC Results

The full output of our MCMC analyses in Section 4.3.3 are represented in Figures 4.18 to 4.22 for the five targets studied in this work. In each plot, the marginalised posterior probability distributions of all model parameters are showed along the diagonal. The correlation among all pairs of parameters are shown in the triangle plots. The contour lines in the correlation subplots correspond to regions containing 68% (dark blue), 95% (medium blue) and 99% (light blue) of the posterior. In general, the majority the fitted parameters were found to converge rather well, yielding sharply-defined unimodal distributions.

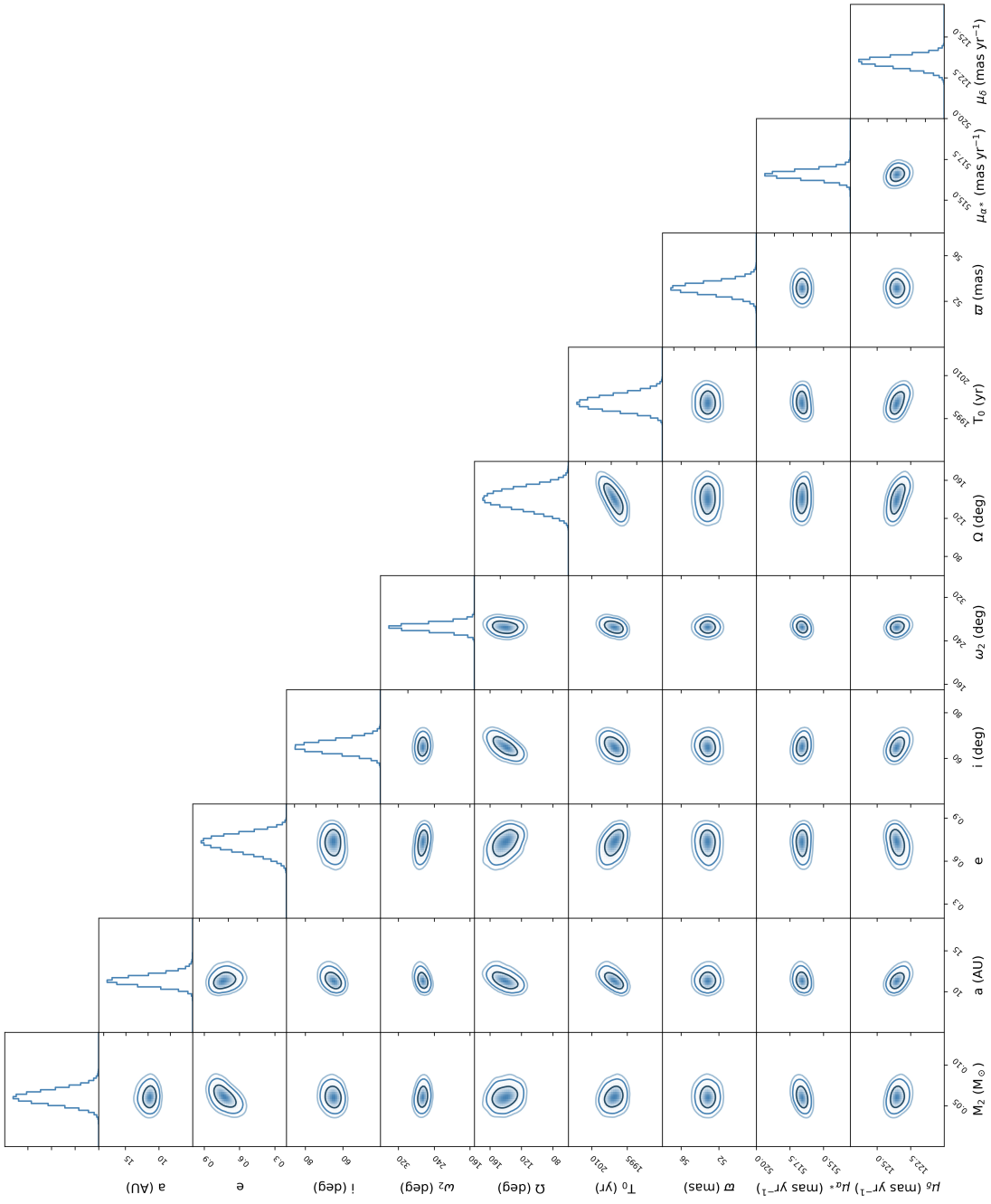

Figure 4.18. MCMC output for HD 4747.

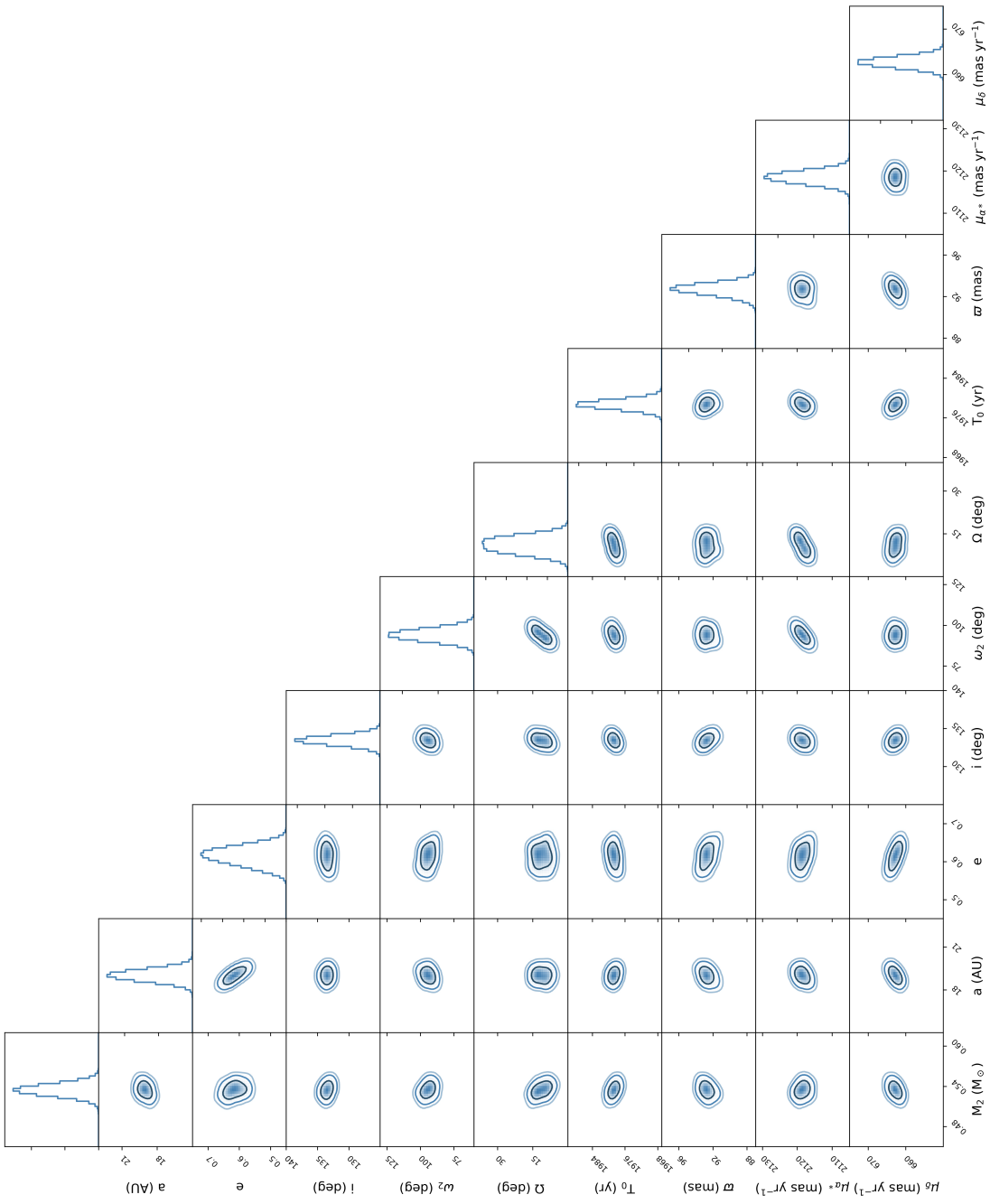

Figure 4.19. MCMC output for GJ 86.

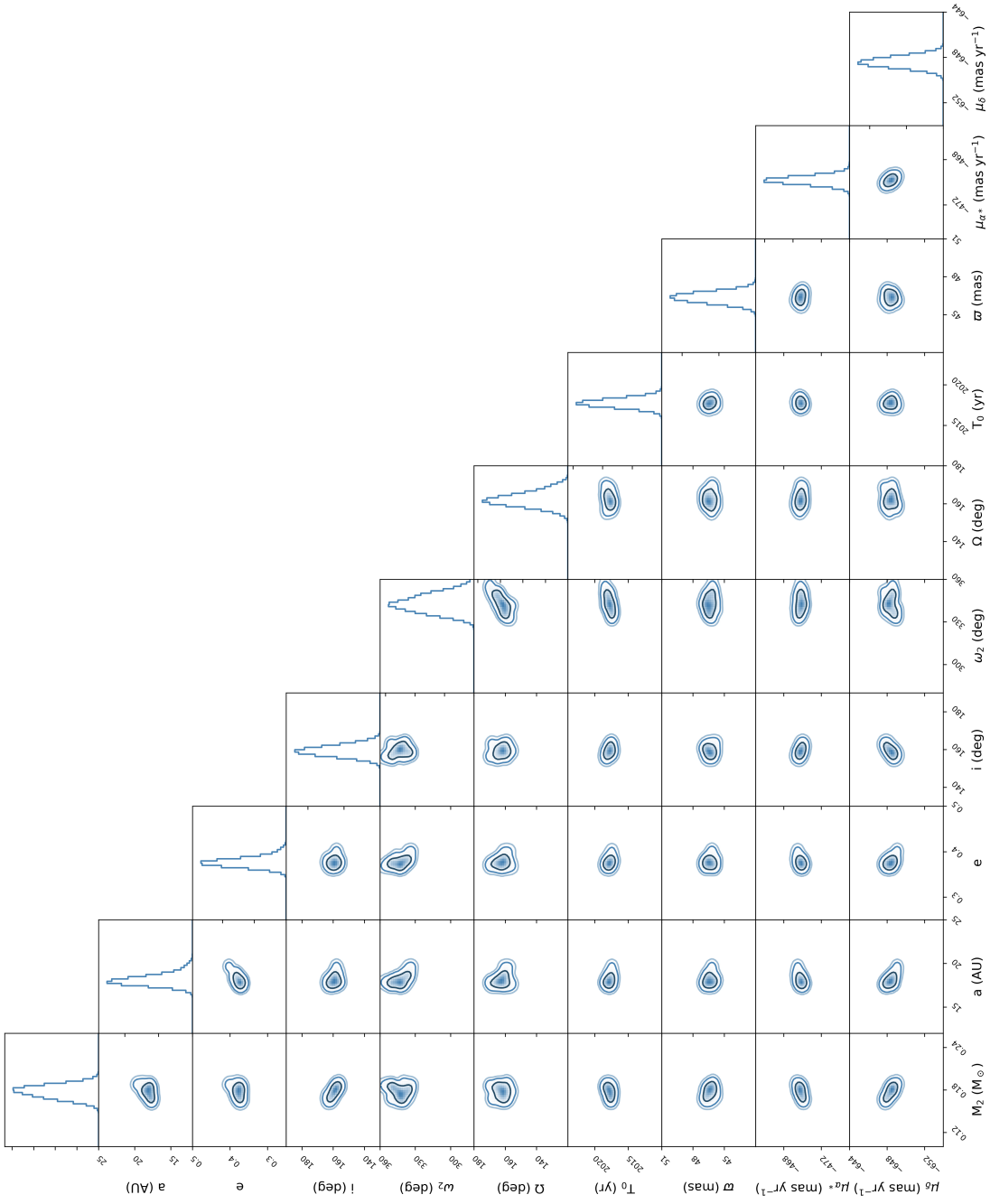

Figure 4.20. MCMC output for HD 68017.

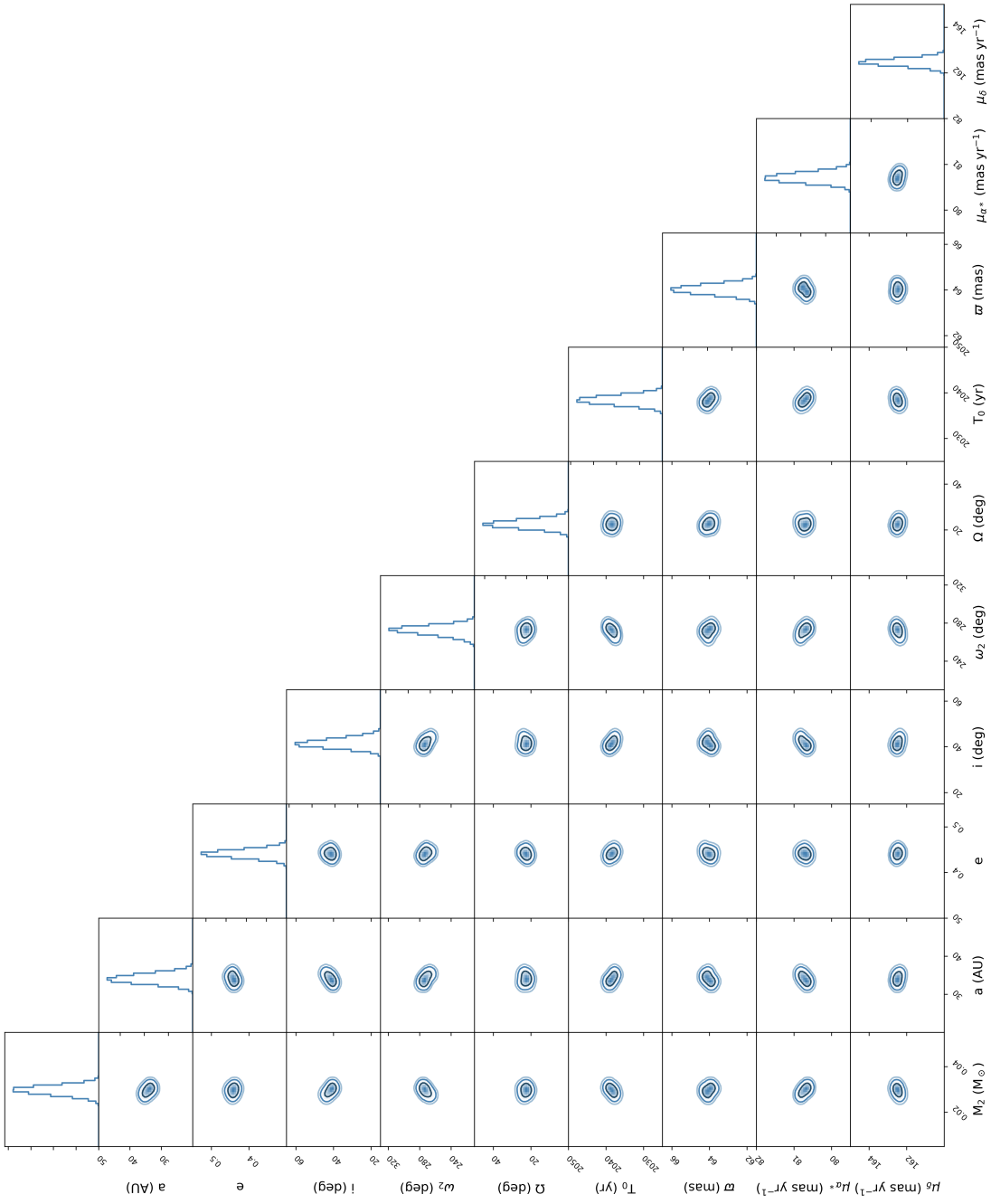

Figure 4.21. MCMC output for GJ 758.

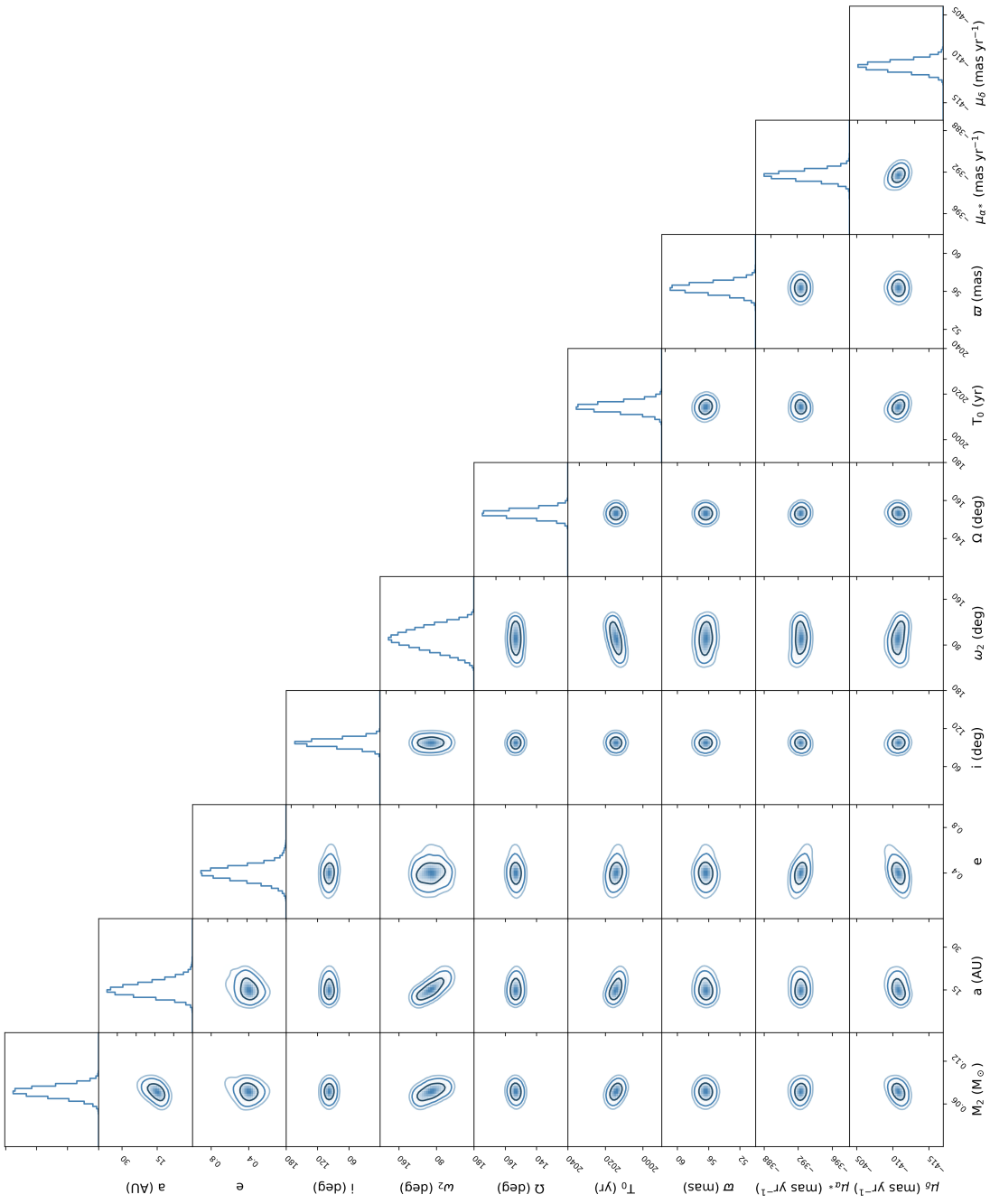

Figure 4.22. MCMC output for HR 7672.

Have no fear of perfection; you'll never reach it.

– Marie Curie

5 Conclusions

Contents

5.1 Thesis Summary

This thesis has explored the population statistics and demographics of substellar objects, with a focus on obtaining new observational constraints for theoretical models. The statistical studies presented in this thesis have provided new information for formation theories of brown dwarfs and giant exoplanets, enabling key probes of fundamental properties and empirical trends. With innovative

methods designed to increase sample sizes for benchmark objects and constrain physical and orbital characteristics, this work will considerably contribute to our understanding of the brown dwarf and extra-solar planet populations.

5.1.1 Chapter 2

In Chapter 2, I presented results from an extensive search for substellar companions to a sample of ultracool late-T and Y field brown dwarfs, using the *Hubble Space Telescope*. Combining this survey with prior searches, I placed the first statistically robust constraints to date on the multiplicity properties of the coolest, lowest-mass brown dwarfs in the field. Accounting for observational biases and incompleteness with a new Bayesian statistical tool, I derived an overall binary fraction of $f_{\rm tot} = 8 \pm 6\%$ for these objects, with a peak in separation at $\sim$3 AU and a mass ratio distribution peaking strongly towards unity.

These results support the idea of a decreasing binary frequency with spectral type in the Galactic field, reinforcing the significance of a tighter and higher mass ratio companion population around lower-mass primaries. Trends seen in the binary statistics of stars are thus found to continue throughout the substellar regime, persisting down to the end of the T spectral sequence. The observed continuity between the multiplicity fractions and population distributions of stars and brown dwarfs argues for a common formation mechanism between the stellar and substellar regimes, providing valuable clues for formation models at the low-mass end of the substellar regime.

5.1.2 Chapter 3

Stellar multiplicity is believed to influence planetary formation and evolution, although the precise nature and extent of this role remain ambiguous. In Chapter 3, I presented a study aimed at testing the role of stellar multiplicity in the formation and/or evolution of the most massive, close-in planetary and substellar companions. From a robust statistical analysis, I derived a very high binary fraction peaking at $\sim$80% between 20$-$10,000 AU for these systems. This is twice as high as for field stars with a 3-σ significance.

With a significantly larger binary fraction for companion-bearing stars relative to the overall stellar population, these results demonstrate that binarity plays a crucial role in the existence of very massive short-period giant planets and brown dwarf desert inhabitants. These findings have crucial implications for formation and evolution theories for massive Jovian planets and brown dwarf companions to stars. The strong evidence that these systems are almost exclusively observed in multiple systems will allow for the development of new classes of planetary formation simulations involving binary systems.

5.1.3 Chapter 4

In Chapter 4, I introduced a new code, COPAINS (Code for Orbital Characterisation of Astrometrically Inferred New Systems), developed to identify new directly-imaged companions and characterise their orbits. Based on changes in stellar proper motions across multiple astrometric catalogues, this powerful tool allows for the computation of masses and separations of companions compatible with observed astrometric trends. This in turn enables me to sturdily select the most promising targets for direct imaging campaigns. This will significantly increase the current census of wide giant planets orbiting stars, which have an inherently low occurrence rate and remain extremely rare in the searches conducted so far, which mostly use uninformed target selection processes.

My innovative approach also allows for the parametrisation of orbital elements and the measurement of dynamical masses for identified systems. Validating the method with well-constrained targets, I found that COPAINS provides robust orbital and dynamical constraints with very limited orbital coverage, by combining data from a couple of direct imaging observations with proper motion measurements from several astrometric catalogues such as *Hipparcos* and *Gaia*. The calculation of model-independent masses for astrometric companions provides a very powerful way to circumvent the large uncertainties introduced by theoretical models in the substellar regime. Furthermore, obtaining larger samples of dynamical masses for such benchmark objects will substantially help the crucial calibration of evolutionary and atmospheric models for brown dwarfs and giant exoplanets.

5.2 Future Prospects

Deeper contrasts and smaller inner working angles will be achieved with the upcoming generation of telescopes, extending the scope of current capabilities to unexplored parts of the exoplanet population. High-contrast imaging and high-resolution spectroscopy with thirty meter-class telescopes, equipped with extreme AO systems, will enable a more complete understanding of the architectures and origin of exoplanets, at the individual and population levels. Ongoing and future projects with the current and next generations of space-based instruments are also critical to constrain the statistical distributions and fundamental properties of brown dwarfs, and to characterise their complex atmospheres.

5.2.1 Detecting and Monitoring Directly-Imaged Exoplanets

The new selection method from our COPAINS tool presented in Chapter 4 will be crucial to discover new directly-imaged companions in the coming years. Samples gathered with such an informed selection procedure are likely to considerably increase the very low detection rates from current imaging campaigns (Bowler 2016). The anticipated *James Webb Space Telescope* (*JWST*) will allow for unparalleled probes of planetary atmospheres, but will primarily serve as a characterisation mission. It is thus vital to identify new benchmark systems to follow-up with *JWST* in anticipation of its commissioning.

Null detections in such programs with current-generation facilities (e.g. VLT/ SPHERE, Gemini/GPI) would also allow us to rule out the presently-accessible part of the parameter space for these targets. With evidence of a perturbing body and no detection at currently-probed masses and separations, such results would yield excellent samples for ground-based direct imaging surveys with the upcoming Extremely Large Telescopes (ELTs), significantly reducing the risks of non-detections. Furthermore, the future Data Releases of the 5-yr *Gaia* mission will further increase the sensitivity of such an approach to fainter and closer-in companions, which will be within the reach of next-generation high-contrast imagers (see Perryman et al. 2014). Using our innovative COPAINS orbital characterisation procedure from Chapter 4, initial dynamical mass estimates and

orbital constraints will be attainable for these key systems within a couple of years only. Followed by extensive monitoring with *JWST* or the ELTs, these planets will serve as fundamental calibrators to test evolutionary and atmospheric models for giant planets.

The future generation of facilities will explore new ranges of planetary masses and separations, which remain inaccessible with direct imaging up to now. *JWST* will be sensitive to truly cold Jupiters and sub-Jovian planets that are only detectable through their thermal emission at infrared wavelengths (Danielski et al. 2018). The inner working angles of the ELTs will be ideal to study cool giant planets down to separations of a few AU from their stars (Quanz et al. 2015; Meyer et al. 2018). These new facilities will bridge for the first time the observational space probed by direct imaging and other detection methods like radial velocity. Extremely high angular resolution is also required to detect very young, hot planets in the process of forming, as accreting exoplanets embedded in their discs are not likely to be well-defined point sources (e.g. Quanz et al. 2013). The unprecedented spatial resolution of the ELTs will thus provide new opportunities to capture the birth of gas giant planets. This will allow for the measurement of initial entropies and accretion rates for protoplanets, as well as to connect the giant planet population to protoplanetary disc structures.

The remarkable spatial and spectral resolution of these future instruments will therefore complete our fragmented knowledge of exoplanet demographics, extending the range of the probed population and removing current biases towards the brightest, youngest and most massive systems. Direct photometry and spectroscopy with *JWST* and the ELTs will provide new clues on initial conditions, locations and timescales for giant planet formation. Results from upcoming surveys in the next decade will hence enable novel insights into formation mechanisms and provide fundamental constraints for theoretical simulations.

5.2.2 Characterising Ultracool Atmospheres

The next generation of telescopes will tremendously improve the atmospheric characterisation of extra-solar giant planets. This will again enhance our understanding of planet formation, allowing for new diagnostics of formation

pathways. For example, *JWST* will be able to measure relative abundances of deuterium to hydrogen for substellar objects. Molecular composition can distinguish between an accretion scenario, subject to evolving chemical processes within a disc, and a star-like fragmentation mechanism, preserving protostellar abundances (Morley et al. 2018). Similarly, C/O ratios are believed to be linked to a planet's formation location (Öberg et al. 2011), and can be used to trace formation and evolution processes (Mordasini et al. 2016). Transmission and emission spectra of hot Jupiters with *JWST* will yield robust measurements of C/O ratios, providing crucial information regarding formation and evolution histories for giant exoplanets (Greene et al. 2016).

Directly-imaged planets and ultracool brown dwarfs are brightest in the mid-infrared ($\sim$3$-$10 μm), where most of their flux is emitted through thermal radiation. Current ground-based facilities suffer from very high sky background levels at these wavelengths, due to the Earth's blackbody peak at $\sim$10 μm, while *HST* only covers the NIR range. As a result, very few planetary-mass objects have been characterised in spectral regions beyond 5 μm to date. With exquisite stability from space and powerful coronagraphic abilities, *JWST* will be capable of moderate-resolution spectroscopy over the 0.6$-$29 μm range, for both isolated ultracool Y dwarfs and wide planetary companions to stars (Boccaletti et al. 2015). Similarly, mid-IR instruments on the ELTs will enable extensive spectral characterisation, variability searches and even surface mapping for wide-orbit directly-imaged exoplanets like β Pic b (Snellen et al. 2014).

Spectral characterisation at previously-inaccessible wavelengths for T and Y dwarfs, as well as massive exoplanets, will revolutionise the study of planetary atmospheres. This will lead to a deeper understanding of the key atmospheric properties of these objects, from their chemical composition to their cloud or band features and photometric variability. As these next-generation facilities will be sensitive to fainter companions and smaller orbital separations than current instruments, these prospects will also be possible for lower-mass and cooler planets, closing the gap between giant exoplanets and the Solar system planets.

Combined with precise distances, the detailed atmospheric characterisation of brown dwarfs and giant planets will provide unique opportunities to calibrate atmospheric and evolutionary models in the substellar regime. While companions

to stars typically have good distance estimates from their host stars, distances to faint isolated brown dwarfs are particularly challenging to obtain. Bedin & Fontanive (2018) recently devised a new method to improve the astrometric precision of *HST* using the *Gaia* DR2 catalogue. Based on multiple epochs of *HST* observations, this robust approach allows for the determination of astrometric parameters (parallax and proper motion) for sources present in the *HST* fields, but too faint for *Gaia*. This provides a powerful procedure to infer highly-precise distances for extremely faint brown dwarfs, achieving precisions at the milli-arcsecond level on parallaxes. Improved distances for new ultracool brown dwarfs will be crucial to refine theoretical models and allow for precise calibrations in preparation of upcoming missions.

5.2.3 A Direct Imaging Search for Planets around Ultracool Brown Dwarfs

With a new *Hubble Space Telescope* program (GO 15201, PI Fontanive), I will conduct the first large-scale direct imaging search for planetary companions around ultracool, free-floating brown dwarfs. This survey will address outstanding questions in the study of brown dwarfs and giant planets, including the existence of planets around the coolest objects, formation and evolution processes, and key measurements of physical properties.

A number of planets have been identified around brown dwarfs in the last two decades, ranging from young and massive directly-imaged companions of a few Jupiter masses (e.g. Chauvin et al. 2005) to Earth-mass companions identified via microlensing (e.g. Shvartzvald et al. 2017). While such findings remain rare and their demographics poorly constrained, the discovery of circumstellar disks around very young brown dwarfs (e.g. Luhman & Muench 2008), together with the exoplanet statistics of M dwarfs (Howard et al. 2012), strongly motivates the study of planet populations around brown dwarfs.

Using 33 orbits of *HST* time from a dedicated high-resolution spectral differential imaging program (e.g. Stumpf et al. 2010), I will search for planetary companions to 33 of the coolest known late-T and Y brown dwarfs ($T_{\mathbf{eff}} < 500$ K), with estimated masses near or inside the planetary mass regime. With deeper

exposures than any previous study of the field population, this campaign will allow for the retrieval of extremely faint and cool Jovian companions of only a few Jupiter masses. With this survey, I will determine the planet occurrence rate around ultracool brown dwarfs, which will allow, for the first time, a probe of the mass-dependent trends of planet properties inside the substellar regime. Constraining the planetary populations around brown dwarfs will provide crucial observational constraints for planet formation models.

Any detection from this program will be a major scientific breakthrough, filling a crucial gap in mass and temperature between brown dwarfs and exoplanets, thus completing the bridge between the substellar and planetary populations. New systems discovered in this study will be analogous to cool giant planets orbiting main-sequence stars on wide orbits, providing unique opportunities to study and model exoplanetary atmospheres. Such discoveries will be transformative for brown dwarf and exoplanet research, allowing for the very first tests to evolutionary and atmospheric models at such cool temperatures.

In Chapter 2, I showed that the continuous trends in binary properties among stars and brown dwarfs are consistent with a common formation mechanism between the stellar and substellar regimes. However, it is not clear whether the observed trends continue at even lower masses or to what mass limit they hold. Isolated planetary-mass objects may represent lower-mass analogues of L and T dwarfs, or could predominantly consist of ejected companions to stars. Observed discrepancies in binary statistics between warmer brown dwarfs and the new Y-dwarf population would reflect different formation processes for different mass regimes. By disentangling two possibly distinct populations via robust population statistics, I will conduct an unprecedented test for formation theories of the lowest-mass brown dwarfs.

Using the new method devised in Bedin & Fontanive (2018), I will derive precise distances for the largest sample of ultracool Y dwarfs, taking advantage of the *Gaia* DR2 catalogue and several epochs *HST* observations. New or refined parallaxes for numerous ultracool brown dwarfs will vastly improve characterisation and modelling for planetary-mass objects and wide-orbit, directly-imaged exoplanets. This work will consequently be highly beneficial for future

investigations, allowing for precise calibrations of both theoretical models and individual archetypal systems.

Finally, this project will provide excellent benchmark targets for follow-up observations with the anticipated space-based *JWST*, and the European Extremely Large Telescope (E-ELT), Thirty Meter Telescope (TMT) and Giant Magellan Telescope (GMT) ground-based facilities. With the characterisation of new exoplanet proxies and insights into novel theories to be tested, this survey will result in new scientific opportunities to be exploited with the next generation of telescopes.

5.3 Closing Remarks

This is an exciting era in the field of brown dwarf and exoplanetary astronomy. With the advent of *JWST* and the ELTs, the next decade promises to transcend current limitations, and lead to unprecedented discoveries and new characterisation possibilities. These scientific findings will yield unparalleled information about intrinsic physical properties and atmospheric dynamics, enable robust constraints on system architectures and population demographics, and provide key probes into formation histories and dynamical evolution processes. This thesis presents work that contributes to our fundamental understanding of brown dwarfs and extra-solar giant planets, with an emphasis on creative pathways to overcome the dominant challenges encountered in the theoretical modelling of these objects. I hope that this work will inspire innovative theoretical studies in the complex framework of brown dwarfs and giant exoplanets, and make possible a new scope of science to be conducted at the dawn of next-generation instruments, with the aim to advance our knowledge on the worlds lying outside the Solar systems.

References

Aberasturi, M., Burgasser, A. J., Mora, A., Solano, E., Martín, E. L., Reid, I. N., & Looper, D. 2014, AJ, 148, 129

Adams, E. R., Ciardi, D. R., Dupree, A. K., Gautier, T. N., I., Kulesa, C., & McCarthy, D. 2012, AJ, 144, 42

Adams, E. R., Dupree, A. K., Kulesa, C., & McCarthy, D. 2013, AJ, 146, 9

Aguilera-Gómez, C., Ramírez, I., & Chanamé, J. 2018, A&A, 614, A55

Alibert, Y., Mordasini, C., & Benz, W. 2011, A&A, 526, A63

Alibert, Y., Mordasini, C., Benz, W., & Winisdoerffer, C. 2005, A&A, 434, 343

Allard, F., Hauschildt, P. H., Alexander, D. R., Tamanai, A., & Schweitzer, A. 2001, ApJ, 556, 357

Allard, F., Homeier, D., Freytag, B., & Sharp, C. M. 2012, in EAS Publications Series, Vol. 57, EAS Publications Series, ed. C. Reylé, C. Charbonnel, & M. Schultheis, 3–43

Allen, P. R. 2007, ApJ, 668, 492

Allen, P. R., Koerner, D. W., Reid, I. N., & Trilling, D. E. 2005, ApJ, 625, 385

Allers, K. N. 2012, in IAU Symposium, Vol. 282, From Interacting Binaries to Exoplanets: Essential Modeling Tools, ed. M. T. Richards & I. Hubeny, 105–110

Allers, K. N., & Liu, M. C. 2010, in Bulletin of the American Astronomical Society, Vol. 42, American Astronomical Society Meeting Abstracts #215, 335

Allers, K. N., Jaffe, D. T., Luhman, K. L., Liu, M. C., Wilson, J. C., Skrutskie, M. F., Nelson, M., Peterson, D. E., Smith, J. D., & Cushing, M. C. 2007, ApJ, 657, 511

ALMA Partnership, Brogan, C. L., Pérez, L. M., Hunter, T. R., Dent, W. R. F., et al. 2015, ApJ, 808, L3

Almeida, P. V., Gameiro, J. F., Petrov, P. P., Melo, C., Santos, N. C., Figueira, P., & Alencar, S. H. P. 2017, A&A, 600, A84

Andrews, J. J., Chanamé, J., & Agüeros, M. A. 2017, MNRAS, 472, 675

Andrews, S. M., & Williams, J. P. 2007, ApJ, 659, 705

Apai, D., Radigan, J., Buenzli, E., Burrows, A., Reid, I. N., & Jayawardhana, R. 2013, ApJ, 768, 121

Arenou, F., Luri, X., Babusiaux, C., Fabricius, C., Helmi, A., et al. 2018, A&A, 616, A17

Artigau, É., Bouchard, S., Doyon, R., & Lafrenière, D. 2009, ApJ, 701, 1534

Asensio-Torres, R., Janson, M., Bonavita, M., Desidera, S., Thalmann, C., Kuzuhara, M., Henning, T., Marzari, F., Meyer, M. R., Calissendorff, P., & Uyama, T. 2018, A&A, 619, A43

Augereau, J. C., & Papaloizou, J. C. B. 2004, A&A, 414, 1153

Bailer-Jones, C. A. L., Rybizki, J., Fouesneau, M., Mantelet, G., & Andrae, R. 2018, AJ, 156, 58

Bailey, J. 2014, PASA, 31, e043

Bakos, G. Á., Hartman, J., Torres, G., Latham, D. W., Kovács, G., et al. 2011, ApJ, 742, 116

Baraffe, I., Chabrier, G., Allard, F., & Hauschildt, P. 2003, in IAU Symposium, Vol. 211, Brown Dwarfs, ed. E. Martín, 41

Baranec, C., Ziegler, C., Law, N. M., Morton, T., Riddle, R., Atkinson, D., Schonhut, J., & Crepp, J. 2016, AJ, 152, 18

Bardalez Gagliuffi, D., Ward-Duong, K., Faherty, J., Greenbaum, A., Marocco, F., et al. 2019, arXiv e-prints, arXiv:1903.06699

Bardalez Gagliuffi, D. C., Gelino, C. R., & Burgasser, A. J. 2015, AJ, 150, 163

Barge, P., Baglin, A., Auvergne, M., & CoRoT Team. 2008, in IAU Symposium, Vol. 249, Exoplanets: Detection, Formation and Dynamics, ed. Y.-S. Sun, S. Ferraz-Mello, & J.-L. Zhou, 3–16

Basri, G., & Reiners, A. 2006, AJ, 132, 663

Bate, M. R. 2009, MNRAS, 392, 590

Bate, M. R., Bonnell, I. A., & Bromm, V. 2002, MNRAS, 332, L65

Bate, M. R., Bonnell, I. A., & Bromm, V. 2003, MNRAS, 339, 577

Batygin, K., Morbidelli, A., & Tsiganis, K. 2011, A&A, 533, A7

Becklin, E. E., & Zuckerman, B. 1988, Nature, 336, 656

Bedin, L. R., & Fontanive, C. 2018, MNRAS, 481, 5339

Beichman, C., Gelino, C. R., Kirkpatrick, J. D., Cushing, M. C., Dodson-Robinson, S., Marley, M. S., Morley, C. V., & Wright, E. L. 2014, ApJ, 783, 68

Bell, K. R., Cassen, P. M., Klahr, H. H., & Henning, T. 1997, ApJ, 486, 372

Bergfors, C., Brandner, W., Janson, M., Daemgen, S., Geissler, K., Henning, T., Hippler, S., Hormuth, F., Joergens, V., & Köhler, R. 2010, A&A, 520, A54

Bergfors, C., Brandner, W., Daemgen, S., Biller, B., Hippler, S., Janson, M., Kudryavtseva, N., Geißler, K., Henning, T., & Köhler, R. 2013, MNRAS, 428, 182

Beust, H., Augereau, J.-C., Bonsor, A., Graham, J. R., Kalas, P., Lebreton, J., Lagrange, A.-M., Ertel, S., Faramaz, V., & Thébault, P. 2014, A&A, 561, A43

Biller, B. 2014, in IAU Symposium, Vol. 299, Exploring the Formation and Evolution of Planetary Systems, ed. M. Booth, B. C. Matthews, & J. R. Graham, 1–11

Biller, B., Allers, K., Liu, M., Close, L. M., & Dupuy, T. 2011, ApJ, 730, 39

Biller, B. A., Close, L. M., Masciadri, E., Nielsen, E., Lenzen, R., et al. 2007, ApJS, 173, 143

Biller, B. A., Liu, M. C., Wahhaj, Z., Nielsen, E. L., Hayward, T. L., et al. 2013a, ApJ, 777, 160

Biller, B. A., Crossfield, I. J. M., Mancini, L., Ciceri, S., Southworth, J., et al. 2013b, ApJ, 778, L10

Biretta, J. 2014, Space Telescope WFC Instrument Science Report, 1, 10

Blake, C. H., Charbonneau, D., & White, R. J. 2010, ApJ, 723, 684

Boccaletti, A., Lagage, P.-O., Baudoz, P., Beichman, C., Bouchet, P., et al. 2015, PASP, 127, 633

Boeshaar, P. C. 1976, PhD thesis, Ohio State University, Columbus.

Bonavita, M., de Mooij, E. J. W., & Jayawardhana, R. 2013, PASP, 125, 849

Bond, I. A., Abe, F., Dodd, R. J., Hearnshaw, J. B., Honda, M., et al. 2001, MNRAS, 327, 868

Bonfanti, A., Ortolani, S., & Nascimbeni, V. 2016, A&A, 585, A5

Bonfils, X., Delfosse, X., Udry, S., Forveille, T., Mayor, M., et al. 2013, A&A, 549, A109

Bonnell, I. A., Clark, P., & Bate, M. R. 2008, MNRAS, 389, 1556

Bonomo, A. S., Desidera, S., Benatti, S., Borsa, F., Crespi, S., et al. 2017, A&A, 602, A107

Borucki, W. J., Koch, D., Basri, G., Batalha, N., Brown, T., et al. 2010, Science, 327, 977

Boss, A. P. 1997, Science, 276, 1836

Boss, A. P. 2001, ApJ, 551, L167

Boss, A. P. 2006, ApJ, 641, 1148

Bouy, H., Martín, E. L., Brandner, W., Zapatero-Osorio, M. R., Béjar, V. J. S., Schirmer, M., Huélamo, N., & Ghez, A. M. 2006, A&A, 451, 177

Bowler, B. P. 2016, Publications of the Astronomical Society of the Pacific, 128, 102001

Bowler, B. P., Liu, M. C., & Cushing, M. C. 2009, ApJ, 706, 1114

Bowler, B. P., Dupuy, T. J., Endl, M., Cochran, W. D., MacQueen, P. J., et al. 2018, AJ, 155, 159

Boyd, D. F. A., & Whitworth, A. P. 2005, A&A, 430, 1059

Brandeker, A., & Cataldi, G. 2019, A&A, 621, A86

Brandner, W., Zinnecker, H., Alcalá, J. M., Allard, F., Covino, E., Frink, S., Köhler, R., Kunkel, M., Moneti, A., & Schweitzer, A. 2000, AJ, 120, 950

Brandt, T. D. 2018, ApJS, 239, 31

Brandt, T. D., Dupuy, T. J., & Bowler, B. P. 2018, arXiv e-prints, arXiv:1811.07285

Burgasser, A. J. 2004, ApJS, 155, 191

Burgasser, A. J. 2007, AJ, 134, 1330

Burgasser, A. J., Cruz, K. L., Cushing, M., Gelino, C. R., Looper, D. L., Faherty, J. K., Kirkpatrick, J. D., & Reid, I. N. 2010, ApJ, 710, 1142

Burgasser, A. J., Geballe, T. R., Leggett, S. K., Kirkpatrick, J. D., & Golimowski, D. A. 2006a, ApJ, 637, 1067

Burgasser, A. J., Gelino, C. R., Cushing, M. C., & Kirkpatrick, J. D. 2012, ApJ, 745, 26

Burgasser, A. J., Kirkpatrick, J. D., Cruz, K. L., Reid, I. N., Leggett, S. K., Liebert, J., Burrows, A., & Brown, M. E. 2006b, ApJS, 166, 585

Burgasser, A. J., Kirkpatrick, J. D., Reid, I. N., Brown, M. E., Miskey, C. L., & Gizis, J. E. 2003, ApJ, 586, 512

Burgasser, A. J., Reid, I. N., Siegler, N., Close, L., Allen, P., Lowrance, P., & Gizis, J. 2007, Protostars and Planets V, 427

Burgasser, A. J., Wilson, J. C., Kirkpatrick, J. D., Skrutskie, M. F., Colonno, M. R., Enos, A. T., Smith, J. D., Henderson, C. P., Gizis, J. E., Brown, M. E., & Houck, J. R. 2000, AJ, 120, 1100

Burgasser, A. J., Kirkpatrick, J. D., Brown, M. E., Reid, I. N., Burrows, A., Liebert, J., Matthews, K., Gizis, J. E., Dahn, C. C., Monet, D. G., Cutri, R. M., & Skrutskie, M. F. 2002, ApJ, 564, 421

Burgasser, A. J., Cushing, M. C., Kirkpatrick, J. D., Gelino, C. R., Griffith, R. L., et al. 2011, ApJ, 735, 116

Burningham, B., Pinfield, D. J., Leggett, S. K., Tamura, M., Lucas, P. W., et al. 2008, MNRAS, 391, 320

Burningham, B., Cardoso, C. V., Smith, L., Leggett, S. K., Smart, R. L., et al. 2013, MNRAS, 433, 457

Burrows, A., Hubbard, W. B., Lunine, J. I., & Liebert, J. 2001, Reviews of Modern Physics, 73, 719

Burrows, A., & Sharp, C. M. 1999, ApJ, 512, 843

Burrows, A., Sudarsky, D., & Lunine, J. I. 2003, ApJ, 596, 587

Burrows, A., Marley, M., Hubbard, W. B., Lunine, J. I., Guillot, T., Saumon, D., Freedman, R., Sudarsky, D., & Sharp, C. 1997, ApJ, 491, 856

Butler, R. P., Marcy, G. W., Fischer, D. A., Brown, T. M., Contos, A. R., Korzennik, S. G., Nisenson, P., & Noyes, R. W. 1999, ApJ, 526, 916

Butler, R. P., Marcy, G. W., Williams, E., Hauser, H., & Shirts, P. 1997, ApJ, 474, L115

Butler, R. P., Wright, J. T., Marcy, G. W., Fischer, D. A., Vogt, S. S., Tinney, C. G., Jones, H. R. A., Carter, B. D., Johnson, J. A., McCarthy, C., & Penny, A. J. 2006, ApJ, 646, 505

Calissendorff, P., & Janson, M. 2018, A&A, 615, A149

Caloi, V., Cardini, D., D'Antona, F., Badiali, M., Emanuele, A., & Mazzitelli, I. 1999, A&A, 351, 925

Cameron, A. G. W. 1978, Moon and Planets, 18, 5

Cannon, A. J., & Pickering, E. C. 1901, Annals of Harvard College Observatory, 28, 129

Chabrier, G., Baraffe, I., Allard, F., & Hauschildt, P. 2000, ApJ, 542, 464

Chabrier, G., Baraffe, I., Allard, F., & Hauschildt, P. H. 2005, arXiv Astrophysics e-prints, astro-ph/0509798

Charbonneau, D., Brown, T. M., Burrows, A., & Laughlin, G. 2007, Protostars and Planets V, 701

Chauvin, G., Lagrange, A.-M., Dumas, C., Zuckerman, B., Mouillet, D., Song, I., Beuzit, J.-L., & Lowrance, P. 2004, A&A, 425, L29

Chauvin, G., Lagrange, A.-M., Dumas, C., Zuckerman, B., Mouillet, D., Song, I., Beuzit, J.-L., & Lowrance, P. 2005, A&A, 438, L25

Chauvin, G., Lagrange, A.-M., Udry, S., Fusco, T., Galland, F., Naef, D., Beuzit, J.-L., & Mayor, M. 2006, A&A, 456, 1165

Chauvin, G., Lagrange, A.-M., Beust, H., Bonnefoy, M., Boccaletti, A., Apai, D., Allard, F., Ehrenreich, D., Girard, J. H. V., Mouillet, D., & Rouan, D. 2012, A&A, 542, A41

Chauvin, G., Vigan, A., Bonnefoy, M., Desidera, S., Bonavita, M., et al. 2015, A&A, 573, A127

Chauvin, G., Desidera, S., Lagrange, A.-M., Vigan, A., Feldt, M., Gratton, R., Langlois, M., Cheetham, A., Bonnefoy, M., & Meyer, M. 2017, in SF2A-2017: Proceedings of the Annual meeting of the French Society of Astronomy and Astrophysics, ed. C. Reylé, P. Di Matteo, F. Herpin, E. Lagadec, A. Lançon, Z. Meliani, & F. Royer, 331–335

Chen, X. P., Henning, T., van Boekel, R., & Grady, C. A. 2006, A&A, 445, 331

Chiu, K., Fan, X., Leggett, S. K., Golimowski, D. A., Zheng, W., Geballe, T. R., Schneider, D. P., & Brinkmann, J. 2006, AJ, 131, 2722

Clarke, C. J., & Lodato, G. 2009, MNRAS, 398, L6

Close, L. M., Siegler, N., Freed, M., & Biller, B. 2003, ApJ, 587, 407

Close, L. M., Siegler, N., Potter, D., Brandner, W., & Liebert, J. 2002, ApJ, 567, L53

Close, L. M., Zuckerman, B., Song, I., Barman, T., Marois, C., et al. 2007, ApJ, 660, 1492

Coker, C. T., Gaudi, B. S., Pogge, R. W., & Horch, E. 2018, AJ, 155, 27

Crepp, J. R., Gonzales, E. J., Bechter, E. B., Montet, B. T., Johnson, J. A., Piskorz, D., Howard, A. W., & Isaacson, H. 2016, ApJ, 831, 136

Crepp, J. R., Johnson, J. A., Fischer, D. A., Howard, A. W., Marcy, G. W., et al. 2012a, ApJ, 751, 97

Crepp, J. R., Johnson, J. A., Howard, A. W., Marcy, G. W., Fischer, D. A., Hillenbrand, L. A., Yantek, S. M., Delaney, C. R., Wright, J. T., Isaacson, H. T., & Montet, B. T. 2012b, ApJ, 761, 39

Crepp, J. R., Principe, D. A., Wolff, S., Giorla Godfrey, P. A., Rice, E. L., Cieza, L., Pueyo, L., Bechter, E. B., & Gonzales, E. J. 2018, ApJ, 853, 192

Cruz, K. L., Kirkpatrick, J. D., & Burgasser, A. J. 2009, AJ, 137, 3345

Cruz, K. L., Reid, I. N., Kirkpatrick, J. D., Burgasser, A. J., Liebert, J., Solomon, A. R., Schmidt, S. J., Allen, P. R., Hawley, S. L., & Covey, K. R. 2007, AJ, 133, 439

Cumming, A., Butler, R. P., Marcy, G. W., Vogt, S. S., Wright, J. T., & Fischer, D. A. 2008, PASP, 120, 531

Curiel, S., Cantó, J., Georgiev, L., Chávez, C. E., & Poveda, A. 2011, A&A, 525, A78

Currie, T., Bailey, V., Fabrycky, D., Murray-Clay, R., Rodigas, T., & Hinz, P. 2010, ApJ, 721, L177

Curtis, J. L., Wolfgang, A., Wright, J. T., Brewer, J. M., & Johnson, J. A. 2013, AJ, 145, 134

Cushing, M. C., Kirkpatrick, J. D., Gelino, C. R., Griffith, R. L., Skrutskie, M. F., et al. 2011, ApJ, 743, 50

Daemgen, S., Bonavita, M., Jayawardhana, R., Lafrenière, D., & Janson, M. 2015, ApJ, 799, 155

Daemgen, S., Hormuth, F., Brandner, W., Bergfors, C., Janson, M., Hippler, S., & Henning, T. 2009, A&A, 498, 567

Danielski, C., Baudino, J.-L., Lagage, P.-O., Boccaletti, A., Gastaud, R., Coulais, A., & Bézard, B. 2018, AJ, 156, 276

Dawson, R. I., & Johnson, J. A. 2018, Annual Review of Astronomy and Astrophysics, 56, 175

Delfosse, X., Beuzit, J.-L., Marchal, L., Bonfils, X., Perrier, C., Ségransan, D., Udry, S., Mayor, M., & Forveille, T. 2004, in Astronomical Society of the Pacific Conference Series, Vol. 318, Spectroscopically and Spatially Resolving the Components of the Close Binary Stars, ed. R. W. Hilditch, H. Hensberge, & K. Pavlovski, 166–174

Desidera, S., & Barbieri, M. 2007, A&A, 462, 345

Desidera, S., Gratton, R. G., Claudi, R. U., Carretta, E., Lucatello, S., et al. 2004, in Astronomical Society of the Pacific Conference Series, Vol. 321, Extrasolar Planets: Today and Tomorrow, ed. J. Beaulieu, A. Lecavelier Des Etangs, & C. Terquem, 103

Díaz, R. F., Santerne, A., Sahlmann, J., Hébrard, G., Eggenberger, A., et al. 2012, A&A, 538, A113

Diolaiti, E., Bendinelli, O., Bonaccini, D., Close, L., Currie, D., & Parmeggiani, G. 2000, A&AS, 147, 335

Dipierro, G., Price, D., Laibe, G., Hirsh, K., Cerioli, A., & Lodato, G. 2015, MNRAS, 453, L73

Dobbs-Dixon, I., Lin, D. N. C., & Mardling, R. A. 2004, ApJ, 610, 464

Döllinger, M. P., Hatzes, A. P., Pasquini, L., Guenther, E. W., Hartmann, M., Girardi, L., & Esposito, M. 2007, A&A, 472, 649

Dommanget, J., & Nys, O. 2000, A&A, 363, 991

Dong, R., Zhu, Z., Fung, J., Rafikov, R., Chiang, E., & Wagner, K. 2016, ApJ, 816, L12

Dong, S., Katz, B., & Socrates, A. 2014, ApJ, 781, L5

Duchêne, G. 2010, ApJ, 709, L114

Duchêne, G., Bontemps, S., Bouvier, J., André, P., Djupvik, A. A., & Ghez, A. M. 2007, A&A, 476, 229

Duchêne, G., & Kraus, A. 2013, ARA&A, 51, 269

Dupuy, T. J., Brandt, T. D., Kratter, K. M., & Bowler, B. P. 2019, ApJ, 871, L4

Dupuy, T. J., & Kraus, A. L. 2013, Science, 341, 1492

Dupuy, T. J., & Liu, M. C. 2011, ApJ, 733, 122

Dupuy, T. J., & Liu, M. C. 2012, ApJS, 201, 19

Dupuy, T. J., & Liu, M. C. 2017, ApJS, 231, 15

Dupuy, T. J., Liu, M. C., & Bowler, B. P. 2009, ApJ, 706, 328

Dupuy, T. J., Liu, M. C., & Ireland, M. J. 2014, ApJ, 790, 133

Dupuy, T. J., Liu, M. C., & Leggett, S. K. 2015, ApJ, 803, 102

Duquennoy, A., & Mayor, M. 1991, A&A, 248, 485

Eggenberger, A., Udry, S., Chauvin, G., Beuzit, J.-L., Lagrange, A.-M., Ségransan, D., & Mayor, M. 2007, A&A, 474, 273

Eggenberger, A., Udry, S., Chauvin, G., Forveille, T., Beuzit, J.-L., Lagrange, A.-M., & Mayor, M. 2011, in IAU Symposium, Vol. 276, The Astrophysics of Planetary Systems: Formation, Structure, and Dynamical Evolution, ed. A. Sozzetti, M. G. Lattanzi, & A. P. Boss, 409–410

Eggenberger, A., Udry, S., & Mayor, M. 2004, A&A, 417, 353

Eggleton, P. P., Kiseleva, L. G., & Hut, P. 1998, ApJ, 499, 853

Eggleton, P. P., & Tokovinin, A. A. 2008, MNRAS, 389, 869

Einstein, A. 1936, Science, 84, 506

Eisner, J. A., Hillenbrand, L. A., White, R. J., Akeson, R. L., & Sargent, A. I. 2005, ApJ, 623, 952

Els, S. G., Sterzik, M. F., Marchis, F., Pantin, E., Endl, M., & Kürster, M. 2001, A&A, 370, L1

Epchtein, N., de Batz, B., Capoani, L., Chevallier, L., Copet, E., et al. 1997, The Messenger, 87, 27

ESA, ed. 1997, ESA Special Publication, Vol. 1200, The HIPPARCOS and TYCHO catalogues. Astrometric and photometric star catalogues derived from the ESA HIPPARCOS Space Astrometry Mission

Esteves, L. J., De Mooij, E. J. W., & Jayawardhana, R. 2015, ApJ, 804, 150

Evans, T. M., Sing, D. K., Kataria, T., Goyal, J., Nikolov, N., et al. 2017, Nature, 548, 58

Fabrycky, D., & Tremaine, S. 2007, ApJ, 669, 1298

Faherty, J. K., Burgasser, A. J., Cruz, K. L., Shara, M. M., Walter, F. M., & Gelino, C. R. 2009, AJ, 137, 1

Faherty, J. K., Rice, E. L., Cruz, K. L., Mamajek, E. E., & Núñez, A. 2013, AJ, 145, 2

Faherty, J. K., Burgasser, A. J., Walter, F. M., Van der Bliek, N., Shara, M. M., Cruz, K. L., West, A. A., Vrba, F. J., & Anglada-Escudé, G. 2012, ApJ, 752, 56

Farihi, J., Bond, H. E., Dufour, P., Haghighipour, N., Schaefer, G. H., Holberg, J. B., Barstow, M. A., & Burleigh, M. R. 2013, MNRAS, 430, 652

Filippazzo, J. C., Rice, E. L., Faherty, J., Cruz, K. L., Van Gordon, M. M., & Looper, D. L. 2015, ApJ, 810, 158

Fischer, D. A., & Marcy, G. W. 1992, ApJ, 396, 178

Fischer, D. A., & Valenti, J. 2005, ApJ, 622, 1102

Fischer, D. A., Gaidos, E., Howard, A. W., Giguere, M. J., Johnson, J. A., et al. 2012, ApJ, 745, 21

Fontanive, C., Biller, B., Bonavita, M., & Allers, K. 2018, MNRAS, 479, 2702

Fontanive, C., Rice, K., Bonavita, M., Lopez, E., Mužić, , K., & Biller, B. 2019, MNRAS, 485, 4967

Foreman-Mackey, D., Hogg, D. W., Lang, D., & Goodman, J. 2013, PASP, 125, 306

Forgan, D., & Rice, K. 2009, MNRAS, 400, 2022

Forgan, D., & Rice, K. 2011, MNRAS, 417, 1928

Forgan, D., & Rice, K. 2013, MNRAS, 432, 3168

Fortney, J. J., Marley, M. S., Saumon, D., & Lodders, K. 2008, ApJ, 683, 1104

Fruchter, A. S., & Hook, R. N. 2002, PASP, 114, 144

Fuhrmann, K., Chini, R., Buda, L.-S., & Pozo Nuñez, F. 2014, ApJ, 785, 68

Gagliuffi, D. C. B., Burgasser, A. J., Gelino, C. R., Looper, D. L., Nicholls, C. P., Schmidt, S. J., Cruz, K., West, A. A., Gizis, J. E., & Metchev, S. 2014, The Astrophysical Journal, 794, 143

Gaia Collaboration, Prusti, T., de Bruijne, J. H. J., Brown, A. G. A., Vallenari, A., Babusiaux, C., Bailer-Jones, C. A. L., Bastian, U., Biermann, M., Evans, D. W., & et al. 2016, A&A, 595, A1

Gaia Collaboration, Babusiaux, C., van Leeuwen, F., Barstow, M. A., Jordi, C., Vallenari, A., Bossini, D., Bressan, A., Cantat-Gaudin, T., van Leeuwen, M., & et al. 2018a, A&A, 616, A10

Gaia Collaboration, Brown, A. G. A., Vallenari, A., Prusti, T., de Bruijne, J. H. J., Babusiaux, C., Bailer-Jones, C. A. L., Biermann, M., Evans, D. W., Eyer, L., & et al. 2018b, A&A, 616, A1

Galicher, R., Marois, C., Macintosh, B., Zuckerman, B., Barman, T., Konopacky, Q., Song, I., Patience, J., Lafrenière, D., Doyon, R., & Nielsen, E. L. 2016, A&A, 594, A63

Galland, F., Lagrange, A.-M., Udry, S., Beuzit, J.-L., Pepe, F., & Mayor, M. 2006, A&A, 452, 709

Galland, F., Lagrange, A.-M., Udry, S., Chelli, A., Pepe, F., Beuzit, J.-L., & Mayor, M. 2005, A&A, 444, L21

Garcia, E. V., Dupuy, T. J., Allers, K. N., Liu, M. C., & Deacon, N. R. 2015, ApJ, 804, 65

Gauza, B., Béjar, V. J. S., Pérez-Garrido, A., Rosa Zapatero Osorio, M., Lodieu, N., Rebolo, R., Pallé, E., & Nowak, G. 2015, ApJ, 804, 96

Geballe, T. R., Knapp, G. R., Leggett, S. K., Fan, X., Golimowski, D. A., et al. 2002, ApJ, 564, 466

Gelino, C. R., Kirkpatrick, J. D., Cushing, M. C., Eisenhardt, P. R., Griffith, R. L., Mainzer, A. K., Marsh, K. A., Skrutskie, M. F., & Wright, E. L. 2011, AJ, 142, 57

Ghez, A. M., Neugebauer, G., & Matthews, K. 1993, AJ, 106, 2005

Gillon, M., Jehin, E., Lederer, S. M., Delrez, L., de Wit, J., et al. 2016, Nature, 533, 221

Gillon, M., Triaud, A. H. M. J., Demory, B.-O., Jehin, E., Agol, E., et al. 2017, Nature, 542, 456

Ginski, C., Mugrauer, M., Seeliger, M., & Eisenbeiss, T. 2012, MNRAS, 421, 2498

Ginski, C., Mugrauer, M., Seeliger, M., Buder, S., Errmann, R., Avenhaus, H., Mouillet, D., Maire, A.-L., & Raetz, S. 2016, MNRAS, 457, 2173

Gizis, J. E., Reid, I. N., Knapp, G. R., Liebert, J., Kirkpatrick, J. D., Koerner, D. W., & Burgasser, A. J. 2003, AJ, 125, 3302

Goodman, J., & Weare, J. 2010, Communications in applied mathematics and computational science, 5, 65

Goodwin, S. P., & Whitworth, A. 2007, A&A, 466, 943

Greene, T. P., Chu, L., Egami, E., Hodapp, K. W., Kelly, D. M., Leisenring, J., Rieke, M., Robberto, M., Schlawin, E., & Stansberry, J. 2016, in Proc. SPIE, Vol. 9904, Space Telescopes and Instrumentation 2016: Optical, Infrared, and Millimeter Wave, 99040E

Grether, D., & Lineweaver, C. H. 2006, The Astrophysical Journal, 640, 1051

Guenther, E. W., Hartmann, M., Esposito, M., Hatzes, A. P., Cusano, F., & Gandolfi, D. 2009, A&A, 507, 1659

Guilloteau, S., Simon, M., Piétu, V., Di Folco, E., Dutrey, A., Prato, L., & Chapillon, E. 2014, A&A, 567, A117

Haikala, L. K., Gahm, G. F., Grenman, T., Mäkelä, M. M., & Persson, C. M. 2017, A&A, 602, A61

Hall, C., Forgan, D., & Rice, K. 2017, MNRAS, 470, 2517

Han, C. 2005, ApJ, 633, 414

Hastings, W. 1970, Biometrika, 57, 97

Hayashi, C., & Nakano, T. 1963, Progress of Theoretical Physics, 30, 460

Heintz, W. D. 1978, Geophysics and Astrophysics Monographs, 15

Hellier, C., Anderson, D. R., Collier Cameron, A., Gillon, M., Hebb, L., et al. 2009, Nature, 460, 1098

Hennebelle, P., & Teyssier, R. 2008, A&A, 477, 25

Herriot, G., Morris, S., Anthony, A., Derdall, D., Duncan, D., et al. 2000, in Proc. SPIE, Vol. 4007, Adaptive Optical Systems Technology, ed. P. L. Wizinowich, 115–125

Hester, J. J., Scowen, P. A., Sankrit, R., Lauer, T. R., Ajhar, E. A., et al. 1996, AJ, 111, 2349

Hodapp, K. W., Jensen, J. B., Irwin, E. M., Yamada, H., Chung, R., et al. 2003, PASP, 115, 1388

Høg, E., Fabricius, C., Makarov, V. V., Urban, S., Corbin, T., Wycoff, G., Bastian, U., Schwekendiek, P., & Wicenec, A. 2000, A&A, 355, L27

Horch, E. P., Howell, S. B., Everett, M. E., & Ciardi, D. R. 2012, AJ, 144, 165

Horch, E. P., Veillette, D. R., Baena Gallé, R., Shah, S. C., O'Rielly, G. V., & van Altena, W. F. 2009, AJ, 137, 5057

Howard, A. W., Marcy, G. W., Johnson, J. A., Fischer, D. A., Wright, J. T., Isaacson, H., Valenti, J. A., Anderson, J., Lin, D. N. C., & Ida, S. 2010, Science, 330, 653

Howard, A. W., Marcy, G. W., Bryson, S. T., Jenkins, J. M., Rowe, J. F., et al. 2012, ApJS, 201, 15

Hoyle, F. 1953, ApJ, 118, 513

Huélamo, N., Ivanov, V. D., Kurtev, R., Girard, J. H., Borissova, J., Mawet, D., Mužić, K., Cáceres, C., Melo, C. H. F., Sterzik, M. F., & Minniti, D. 2015, A&A, 578, A1

Hunter, C. 1962, ApJ, 136, 594

Hußmann, B., Stolte, A., Brandner, W., Gennaro, M., & Liermann, A. 2012, A&A, 540, A57

Ida, S., & Lin, D. N. C. 2004, ApJ, 604, 388

Irwin, J., Buchhave, L., Berta, Z. K., Charbonneau, D., Latham, D. W., et al. 2010, ApJ, 718, 1353

Jang-Condell, H., Mugrauer, M., & Schmidt, T. 2008, ApJ, 683, L191

Janson, M., Bonavita, M., Klahr, H., & Lafrenière, D. 2012a, ApJ, 745, 4

Janson, M., Apai, D., Zechmeister, M., Brandner, W., Kürster, M., Kasper, M., Reffert, S., Endl, M., Lafrenière, D., Geißler, K., Hippler, S., & Henning, T. 2009, MNRAS, 399, 377

Janson, M., Carson, J., Thalmann, C., McElwain, M. W., Goto, M., et al. 2011, ApJ, 728, 85

Janson, M., Hormuth, F., Bergfors, C., Brandner, W., Hippler, S., Daemgen, S., Kudryavtseva, N., Schmalzl, E., Schnupp, C., & Henning, T. 2012b, ApJ, 754, 44

Jeans, J. H. 1902, Philosophical Transactions of the Royal Society of London Series A, 199, 1

Jeffries, R. D. 2014, in EAS Publications Series, Vol. 65, EAS Publications Series, 289–325

Jenkins, J. S., Jones, H. R. A., Tuomi, M., Díaz, M., Cordero, J. P., et al. 2017, MNRAS, 466, 443

Jensen, E. L. N., & Akeson, R. L. 2003, ApJ, 584, 875

Joergens, V. 2008, A&A, 492, 545

Jofré, E., Petrucci, R., Saffe, C., Saker, L., de la Villarmois, E. A., Chavero, C., Gómez, M., & Mauas, P. J. D. 2015, A&A, 574, A50

Johansen, A., Oishi, J. S., Mac Low, M.-M., Klahr, H., Henning, T., & Youdin, A. 2007, Nature, 448, 1022

Johns-Krull, C. M., McLane, J. N., Prato, L., Crockett, C. J., Jaffe, D. T., et al. 2016, ApJ, 826, 206

Johnson, J. A., Winn, J. N., Bakos, G. Á., Hartman, J. D., Morton, T. D., et al. 2011, ApJ, 735, 24

Johnson, M. C., Cochran, W. D., Albrecht, S., Dodson-Robinson, S. E., Winn, J. N., & Gullikson, K. 2014, ApJ, 790, 30

Jones, J., White, R. J., Boyajian, T., Schaefer, G., Baines, E., et al. 2015, ApJ, 813, 58

Jones, M. I., Jenkins, J. S., Bluhm, P., Rojo, P., & Melo, C. H. F. 2014, A&A, 566, A113

Jones, M. I., Jenkins, J. S., Rojo, P., Melo, C. H. F., & Bluhm, P. 2013, A&A, 556, A78

Kaib, N. A., Raymond, S. N., & Duncan, M. 2013, Nature, 493, 381

Kane, S. R., Henry, G. W., Dragomir, D., Fischer, D. A., Howard, A. W., Wang, X., & Wright, J. T. 2011a, ApJ, 735, L41

Kane, S. R., Howard, A. W., Pilyavsky, G., Mahadevan, S., Henry, G. W., et al. 2011b, ApJ, 733, 28

Kane, S. R., Barclay, T., Hartmann, M., Hatzes, A. P., Jensen, E. L. N., Ciardi, D. R., Huber, D., Wright, J. T., & Quintana, E. V. 2015, ApJ, 815, 32

Kasper, M., Apai, D., Janson, M., & Brandner, W. 2007, A&A, 472, 321

Kellogg, K., Metchev, S., Miles-Páez, P. A., & Tannock, M. E. 2017, AJ, 154, 112

Kennedy, G. M., & Kenyon, S. J. 2008, ApJ, 673, 502

Keppler, M., Benisty, M., Müller, A., Henning, T., van Boekel, R., et al. 2018, A&A, 617, A44

King, R. R., Parker, R. J., Patience, J., & Goodwin, S. P. 2012, MNRAS, 421, 2025

Kipping, D. M. 2013, MNRAS, 434, L51

Kirkpatrick, J. D. 2005, ARA&A, 43, 195

Kirkpatrick, J. D. 2008, in Astronomical Society of the Pacific Conference Series, Vol. 384, 14th Cambridge Workshop on Cool Stars, Stellar Systems, and the Sun, ed. G. van Belle, 85

Kirkpatrick, J. D., Henry, T. J., & Liebert, J. 1993, ApJ, 406, 701

Kirkpatrick, J. D., Henry, T. J., & McCarthy, Jr., D. W. 1991, ApJS, 77, 417

Kirkpatrick, J. D., Reid, I. N., Liebert, J., Cutri, R. M., Nelson, B., Beichman, C. A., Dahn, C. C., Monet, D. G., Gizis, J. E., & Skrutskie, M. F. 1999, ApJ, 519, 802

Kirkpatrick, J. D., Looper, D. L., Burgasser, A. J., Schurr, S. D., Cutri, R. M., et al. 2010, ApJS, 190, 100

Kirkpatrick, J. D., Cushing, M. C., Gelino, C. R., Griffith, R. L., Skrutskie, M. F., et al. 2011, ApJ, 197, 19

Kirkpatrick, J. D., Gelino, C. R., Cushing, M. C., Mace, G. N., Griffith, R. L., et al. 2012, ApJ, 753, 156

Kirkpatrick, J. D., Martin, E. C., Smart, R. L., Cayago, A. J., Beichman, C. A., et al. 2019, ApJS, 240, 19

Kley, W. 2001, in IAU Symposium, Vol. 200, The Formation of Binary Stars, ed. H. Zinnecker & R. Mathieu, 511

Knapp, G. R., Leggett, S. K., Fan, X., Marley, M. S., Geballe, T. R., et al. 2004, AJ, 127, 3553

Knutson, H. A., Fulton, B. J., Montet, B. T., Kao, M., Ngo, H., et al. 2014, ApJ, 785, 126

Konacki, M., & Wolszczan, A. 2003, ApJ, 591, L147

Konopacky, Q. M., Ghez, A. M., Barman, T. S., Rice, E. L., Bailey, III, J. I., White, R. J., McLean, I. S., & Duchêne, G. 2010, ApJ, 711, 1087

Konopacky, Q. M., Ghez, A. M., Rice, E. L., & Duchêne, G. 2007, ApJ, 663, 394

Kouwenhoven, M. B. N., Brown, A. G. A., Portegies Zwart, S. F., & Kaper, L. 2007, A&A, 474, 77

Kozai, Y. 1962, AJ, 67, 591

Kratter, K. M., Murray-Clay, R. A., & Youdin, A. N. 2010, ApJ, 710, 1375

Kraus, A. L., & Hillenbrand, L. A. 2012, ApJ, 757, 141

Kraus, A. L., Ireland, M. J., Hillenbrand, L. A., & Martinache, F. 2012, ApJ, 745, 19

Kraus, A. L., Ireland, M. J., Huber, D., Mann, A. W., & Dupuy, T. J. 2016, AJ, 152, 8

Kraus, A. L., White, R. J., & Hillenbrand, L. A. 2006, ApJ, 649, 306

Krist, J. 1995, in Astronomical Society of the Pacific Conference Series, Vol. 77, Astronomical Data Analysis Software and Systems IV, ed. R. A. Shaw, H. E. Payne, & J. J. E. Hayes, 349

Kumar, S. S. 1963, ApJ, 137, 1121

Kumar, S. S. 2003, in IAU Symposium, Vol. 211, Brown Dwarfs, ed. E. Martín, 3

Lachapelle, F.-R., Lafrenière, D., Gagné, J., Jayawardhana, R., Janson, M., Helling, C., & Witte, S. 2015, ApJ, 802, 61

Lada, C. J., & Lada, E. A. 2003, ARA&A, 41, 57

Lafrenière, D., Jayawardhana, R., & van Kerkwijk, M. H. 2008, ApJ, 689, L153

Lafrenière, D., Jayawardhana, R., van Kerkwijk, M. H., Brandeker, A., & Janson, M. 2014, ApJ, 785, 47

Lafrenière, D., Doyon, R., Marois, C., Nadeau, D., Oppenheimer, B. R., et al. 2007, ApJ, 670, 1367

Lagrange, A. M., Beust, H., Udry, S., Chauvin, G., & Mayor, M. 2006, A&A, 459, 955

Lagrange, A.-M., Bonnefoy, M., Chauvin, G., Apai, D., Ehrenreich, D., Boccaletti, A., Gratadour, D., Rouan, D., Mouillet, D., Lacour, S., & Kasper, M. 2010, Science, 329, 57

Lambrechts, M., & Johansen, A. 2012, A&A, 544, A32

Lambrechts, M., & Johansen, A. 2014, A&A, 572, A107

Law, N. M., Morton, T., Baranec, C., Riddle, R., Ravichandran, G., et al. 2014, ApJ, 791, 35

Leggett, S. K., Marley, M. S., Freedman, R., Saumon, D., Liu, M. C., Geballe, T. R., Golimowski, D. A., & Stephens, D. C. 2007, ApJ, 667, 537

Leggett, S. K., Morley, C. V., Marley, M. S., Saumon, D., Fortney, J. J., & Visscher, C. 2013, ApJ, 763, 130

Leggett, S. K., Tremblin, P., Esplin, T. L., Luhman, K. L., & Morley, C. V. 2017, ApJ, 842, 118

Lenzen, R., Hartung, M., Brandner, W., Finger, G., Hubin, N. N., Lacombe, F., Lagrange, A.-M., Lehnert, M. D., Moorwood, A. F. M., & Mouillet, D. 2003, in Proc. SPIE, Vol. 4841, Instrument Design and Performance for Optical/Infrared Ground-based Telescopes, ed. M. Iye & A. F. M. Moorwood, 944–952

Lewis, N. K., Knutson, H. A., Showman, A. P., Cowan, N. B., Laughlin, G., et al. 2013, ApJ, 766, 95

Lidov, M. L. 1962, Planet. Space Sci., 9, 719

Lindegren, L., Hernández, J., Bombrun, A., Klioner, S., Bastian, U., et al. 2018, A&A, 616, A2

Liu, M. C., Dupuy, T. J., & Allers, K. N. 2016, ApJ, 833, 96

Liu, M. C., Dupuy, T. J., Bowler, B. P., Leggett, S. K., & Best, W. M. J. 2012, ApJ, 758, 57

Liu, M. C., Dupuy, T. J., & Leggett, S. K. 2010, ApJ, 722, 311

Liu, M. C., Fischer, D. A., Graham, J. R., Lloyd, J. P., Marcy, G. W., & Butler, R. P. 2002, ApJ, 571, 519

Liu, M. C., Leggett, S. K., Golimowski, D. A., Chiu, K., Fan, X., Geballe, T. R., Schneider, D. P., & Brinkmann, J. 2006, ApJ, 647, 1393

Liu, M. C., Delorme, P., Dupuy, T. J., Bowler, B. P., Albert, L., Artigau, E., Reylé, C., Forveille, T., & Delfosse, X. 2011, ApJ, 740, 108

Liu, Y. J., Sato, B., Zhao, G., Noguchi, K., Wang, H., et al. 2008, ApJ, 672, 553

Lo Curto, G., Mayor, M., Benz, W., Bouchy, F., Hébrard, G., et al. 2013, A&A, 551, A59

Lodders, K. 2002, ApJ, 577, 974

Looper, D. L., Kirkpatrick, J. D., & Burgasser, A. J. 2007, AJ, 134, 1162

Lovis, C., Ségransan, D., Mayor, M., Udry, S., Benz, W., et al. 2011, A&A, 528, A112

Lowrance, P. J., Kirkpatrick, J. D., & Beichman, C. A. 2002, ApJ, 572, L79

Lucas, P. W., & Roche, P. F. 2000, MNRAS, 314, 858

Luhman, K. L. 2004, ApJ, 614, 398

Luhman, K. L. 2007, ApJS, 173, 104

Luhman, K. L. 2014, ApJ, 786, L18

Luhman, K. L., Burgasser, A. J., & Bochanski, J. J. 2011, ApJ, 730, L9

Luhman, K. L., Mamajek, E. E., Allen, P. R., Muench, A. A., & Finkbeiner, D. P. 2009, ApJ, 691, 1265

Luhman, K. L., Mamajek, E. E., Shukla, S. J., & Loutrel, N. P. 2017, AJ, 153, 46

Luhman, K. L., & Muench, A. A. 2008, ApJ, 684, 654

Ma, B., & Ge, J. 2014, Monthly Notices of the Royal Astronomical Society, 439, 2781

Ma, B., Ge, J., Wolszczan, A., Muterspaugh, M. W., Lee, B., et al. 2016, AJ, 152, 112

Mace, G. N., Kirkpatrick, J. D., Cushing, M. C., Gelino, C. R., Griffith, R. L., et al. 2013, ApJS, 205, 6

Macintosh, B., Graham, J. R., Ingraham, P., Konopacky, Q., Marois, C., et al. 2014, Proceedings of the National Academy of Science, 111, 12661

Maire, A.-L., Stolker, T., Messina, S., Müller, A., Biller, B. A., et al. 2017, A&A, 601, A134

Makarov, V. V., & Kaplan, G. H. 2005, AJ, 129, 2420

Malbet, F., & Sozzetti, A. 2018, Astrometry as an Exoplanet Discovery Method, 196

Maldonado, J., & Villaver, E. 2017, A&A, 602, A38

Manjavacas, E., Goldman, B., Reffert, S., & Henning, T. 2013, A&A, 560, A52

Manjavacas, E., Apai, D., Zhou, Y., Lew, B. W. P., Schneider, G., et al. 2019, AJ, 157, 101

Mann, R. K., & Williams, J. P. 2009, ApJ, 694, L36

Marcy, G. W., & Butler, R. P. 2000, Publications of the Astronomical Society of the Pacific, 112, 137

Marcy, G. W., Butler, R. P., Vogt, S. S., Fischer, D. A., Wright, J. T., Johnson, J. A., Tinney, C. G., Jones, H. R. A., Carter, B. D., Bailey, J., O'Toole, S. J., & Upadhyay, S. 2008, Physica Scripta Volume T, 130, 014001

Mardling, R. A., & Lin, D. N. C. 2002, ApJ, 573, 829

Marley, M. S., Fortney, J. J., Hubickyj, O., Bodenheimer, P., & Lissauer, J. J. 2007, ApJ, 655, 541

Marley, M. S., & Robinson, T. D. 2015, ARA&A, 53, 279

Marley, M. S., Saumon, D., Cushing, M., Ackerman, A. S., Fortney, J. J., & Freedman, R. 2012, ApJ, 754, 135

Marley, M. S., Seager, S., Saumon, D., Lodders, K., Ackerman, A. S., Freedman, R. S., & Fan, X. 2002, ApJ, 568, 335

Marois, C., Macintosh, B., Barman, T., Zuckerman, B., Song, I., Patience, J., Lafrenière, D., & Doyon, R. 2008, Science, 322, 1348

Marois, C., Zuckerman, B., Konopacky, Q. M., Macintosh, B., & Barman, T. 2010, Nature, 468, 1080

Martin, E. C., Kirkpatrick, J. D., Beichman, C. A., Smart, R. L., Faherty, J. K., et al. 2018, ApJ, 867, 109

Masana, E., Jordi, C., & Ribas, I. 2006, A&A, 450, 735

Mason, B. D., Wycoff, G. L., Hartkopf, W. I., Douglass, G. G., & Worley, C. E. 2001, AJ, 122, 3466

Matsuo, T., Shibai, H., Ootsubo, T., & Tamura, M. 2007, ApJ, 662, 1282

Mayer, L., Wadsley, J., Quinn, T., & Stadel, J. 2005, MNRAS, 363, 641

Mayor, M., & Queloz, D. 1995, Nature, 378, 355

Mayor, M., & Udry, S. 2008, Physica Scripta Volume T, 130, 014010

Mayor, M., Pepe, F., Queloz, D., Bouchy, F., Rupprecht, G., et al. 2003, The Messenger, 114, 20

Mayor, M., Marmier, M., Lovis, C., Udry, S., Ségransan, D., et al. 2011, arXiv e-prints, arXiv:1109.2497

McAlister, H. A., Hartkopf, W. I., Hutter, D. J., & Franz, O. G. 1987, AJ, 93, 688

McArthur, B. E., Benedict, G. F., Barnes, R., Martioli, E., Korzennik, S., Nelan, E., & Butler, R. P. 2010, ApJ, 715, 1203

McLean, I. S., McGovern, M. R., Burgasser, A. J., Kirkpatrick, J. D., Prato, L., & Kim, S. S. 2003, ApJ, 596, 561

Metchev, S. A., & Hillenbrand, L. A. 2009, ApJS, 181, 62

Metchev, S. A., Kirkpatrick, J. D., Berriman, G. B., & Looper, D. 2008, ApJ, 676, 1281

Metropolis, N., Rosenbluth, A. W., Rosenbluth, M. N., Teller, A. H., & Teller, E. 1953, J. Chem. Phys., 21, 1087

Meyer, M. R., Amara, A., Reggiani, M., & Quanz, S. P. 2018, A&A, 612, L3

Michalik, D., Lindegren, L., & Hobbs, D. 2015, A&A, 574, A115

Mitchell, D. S., Reffert, S., Trifonov, T., Quirrenbach, A., & Fischer, D. A. 2013, A&A, 555, A87

Morbey, C. L., & Brosterhus, E. B. 1974, PASP, 86, 455

Mordasini, C. 2018, Planetary Population Synthesis, 143

Mordasini, C., Alibert, Y., Benz, W., Klahr, H., & Henning, T. 2012, A&A, 541, A97

Mordasini, C., van Boekel, R., Mollière, P., Henning, T., & Benneke, B. 2016, ApJ, 832, 41

Morley, C. V., Fortney, J. J., Marley, M. S., Visscher, C., Saumon, D., & Leggett, S. K. 2012, ApJ, 756, 172

Morley, C. V., Skemer, A. J., Miles, B. E., Line, M. R., Lopez, E. D., Brogi, M., Freedman, R. S., & Marley, M. S. 2018, arXiv e-prints, arXiv:1810.04241

Morton, T. D., Bryson, S. T., Coughlin, J. L., Rowe, J. F., Ravichandran, G., Petigura, E. A., Haas, M. R., & Batalha, N. M. 2016, ApJ, 822, 86

Moutou, C., Vigan, A., Mesa, D., Desidera, S., Thébault, P., Zurlo, A., & Salter, G. 2017, A&A, 602, A87

Mróz, P., Ryu, Y. H., Skowron, J., Udalski, A., Gould, A., et al. 2018, AJ, 155, 121

Mugrauer, M., & Neuhäuser, R. 2005, MNRAS, 361, L15

Mugrauer, M., & Neuhäuser, R. 2009, A&A, 494, 373

Mugrauer, M., Neuhäuser, R., & Mazeh, T. 2007, A&A, 469, 755

Mugrauer, M., Neuhäuser, R., Mazeh, T., Guenther, E., & Fernández, M. 2004, Astronomische Nachrichten, 325, 718

Mugrauer, M., Neuhäuser, R., Mazeh, T., Guenther, E., Fernández, M., & Broeg, C. 2006, Astronomische Nachrichten, 327, 321

Müller, A., Keppler, M., Henning, T., Samland, M., Chauvin, G., et al. 2018, A&A, 617, L2

Muterspaugh, M. W., Lane, B. F., Kulkarni, S. R., Konacki, M., Burke, B. F., Colavita, M. M., Shao, M., Hartkopf, W. I., Boss, A. P., & Williamson, M. 2010, AJ, 140, 1657

Nakajima, T., Oppenheimer, B. R., Kulkarni, S. R., Golimowski, D. A., Matthews, K., & Durrance, S. T. 1995, Nature, 378, 463

Naoz, S., Farr, W. M., & Rasio, F. A. 2012, ApJ, 754, L36

Nayakshin, S. 2010, MNRAS, 408, L36

Ngo, H., Knutson, H. A., Hinkley, S., Crepp, J. R., Bechter, E. B., Batygin, K., Howard, A. W., Johnson, J. A., Morton, T. D., & Muirhead, P. S. 2015, ApJ, 800, 138

Ngo, H., Knutson, H. A., Hinkley, S., Bryan, M., Crepp, J. R., et al. 2016, ApJ, 827, 8

Nielsen, E. L., & Close, L. M. 2010, ApJ, 717, 878

Nielsen, E. L., Liu, M. C., Wahhaj, Z., Biller, B. A., Hayward, T. L., et al. 2013, ApJ, 776, 4

Nowak, G., Palle, E., Gandolfi, D., Dai, F., Lanza, A. F., et al. 2017, AJ, 153, 131

Öberg, K. I., Murray-Clay, R., & Bergin, E. A. 2011, ApJ, 743, L16

O'Donovan, F. T., Charbonneau, D., Torres, G., Mandushev, G., Dunham, E. W., Latham, D. W., Alonso, R., Brown, T. M., Esquerdo, G. A., Everett, M. E., & Creevey, O. L. 2006, ApJ, 644, 1237

Opitz, D., Tinney, C. G., Faherty, J. K., Sweet, S., Gelino, C. R., & Kirkpatrick, J. D. 2016, ApJ, 819, 17

Oppenheimer, B. R., Kulkarni, S. R., Matthews, K., & Nakajima, T. 1995, Science, 270, 1478

Padoan, P., & Nordlund, Å. 2002, ApJ, 576, 870

Padoan, P., & Nordlund, Å. 2004, ApJ, 617, 559

Pál, A., Bakos, G. Á., Torres, G., Noyes, R. W., Fischer, D. A., et al. 2010, MNRAS, 401, 2665

Patience, J., White, R. J., Ghez, A. M., McCabe, C., McLean, I. S., et al. 2002, ApJ, 581, 654

Peretti, S., Ségransan, D., Lavie, B., Desidera, S., Maire, A.-L., et al. 2018, arXiv e-prints, arXiv:1805.05645

Perryman, M., Hartman, J., Bakos, G. Á., & Lindegren, L. 2014, ApJ, 797, 14

Perryman, M. A. C., Lindegren, L., Kovalevsky, J., Hoeg, E., Bastian, U., et al. 1997, A&A, 323, L49

Peter, D., Feldt, M., Henning, T., & Hormuth, F. 2012, A&A, 538, A74

Petrovich, C. 2015, ApJ, 799, 27

Pichardo, B., Sparke, L. S., & Aguilar, L. A. 2005, MNRAS, 359, 521

Pinfield, D. J., Jones, H. R. A., Lucas, P. W., Kendall, T. R., Folkes, S. L., Day-Jones, A. C., Chappelle, R. J., & Steele, I. A. 2006, MNRAS, 368, 1281

Pinfield, D. J., Gromadzki, M., Leggett, S. K., Gomes, J., Lodieu, N., et al. 2014, MNRAS, 444, 1931

Piskorz, D., Knutson, H. A., Ngo, H., Muirhead, P. S., Batygin, K., Crepp, J. R., Hinkley, S., & Morton, T. D. 2015, ApJ, 814, 148

Pollacco, D. L., Skillen, I., Collier Cameron, A., Christian, D. J., Hellier, C., et al. 2006, PASP, 118, 1407

Pollack, J. B., Hubickyj, O., Bodenheimer, P., Lissauer, J. J., Podolak, M., & Greenzweig, Y. 1996, Icarus, 124, 62

Pourbaix, D., Tokovinin, A. A., Batten, A. H., Fekel, F. C., Hartkopf, W. I., Levato, H., Morell, N. I., Torres, G., & Udry, S. 2009, VizieR Online Data Catalog, 1

Pozio, F. 1991, Mem. Soc. Astron. Italiana, 62, 171

Prato, L., Greene, T. P., & Simon, M. 2003, ApJ, 584, 853

Preibisch, T., & Mamajek, E. 2008, The Nearest OB Association: Scorpius-Centaurus (Sco OB2), ed. B. Reipurth, 235

Price, D. J., & Bate, M. R. 2009, MNRAS, 398, 33

Quanz, S. P., Amara, A., Meyer, M. R., Kenworthy, M. A., Kasper, M., & Girard, J. H. 2013, ApJ, 766, L1

Quanz, S. P., Crossfield, I., Meyer, M. R., Schmalzl, E., & Held, J. 2015, International Journal of Astrobiology, 14, 279

Radigan, J., Jayawardhana, R., Lafrenière, D., Artigau, É., Marley, M., & Saumon, D. 2012, ApJ, 750, 105

Rafikov, R. R. 2005, ApJ, 621, L69

Rafikov, R. R. 2013, ApJ, 765, L8

Raghavan, D., Henry, T. J., Mason, B. D., Subasavage, J. P., Jao, W.-C., Beaulieu, T. D., & Hambly, N. C. 2006, ApJ, 646, 523

Raghavan, D., McAlister, H. A., Henry, T. J., Latham, D. W., Marcy, G. W., Mason, B. D., Gies, D. R., White, R. J., & ten Brummelaar, T. A. 2010, ApJS, 190, 1

Rameau, J., Chauvin, G., Lagrange, A.-M., Klahr, H., Bonnefoy, M., Mordasini, C., Bonavita, M., Desidera, S., Dumas, C., & Girard, J. H. 2013, A&A, 553, A60

Ranalli, P., Hobbs, D., & Lindegren, L. 2018, A&A, 614, A30

Reboussin, L., Guilloteau, S., Simon, M., Grosso, N., Wakelam, V., Di Folco, E., Dutrey, A., & Piétu, V. 2015, A&A, 578, A31

Reffert, S., Bergmann, C., Quirrenbach, A., Trifonov, T., & Künstler, A. 2015, A&A, 574, A116

Reid, I. N., Gizis, J. E., Kirkpatrick, J. D., & Koerner, D. W. 2001, AJ, 121, 489

Reid, I. N., Lewitus, E., Allen, P. R., Cruz, K. L., & Burgasser, A. J. 2006, AJ, 132, 891

Reipurth, B., & Clarke, C. 2001, AJ, 122, 432

Rice, K., Lopez, E., Forgan, D., & Biller, B. 2015, MNRAS, 454, 1940

Rice, W. K. M., & Armitage, P. J. 2009, MNRAS, 396, 2228

Rice, W. K. M., Veljanoski, J., & Collier Cameron, A. 2012, MNRAS, 425, 2567

Richert, A. J. W., Getman, K. V., Feigelson, E. D., Kuhn, M. A., Broos, P. S., Povich, M. S., Bate, M. R., & Garmire, G. P. 2018, MNRAS, 477, 5191

Ricker, G. R., Winn, J. N., Vanderspek, R., Latham, D. W., Bakos, G. Á., et al. 2015, Journal of Astronomical Telescopes, Instruments, and Systems, 1, 014003

Riddle, R. L., Tokovinin, A., Mason, B. D., Hartkopf, W. I., Roberts, Jr., L. C., et al. 2015, ApJ, 799, 4

Roberts, L. C., & Mason, B. D. 2018, MNRAS, 473, 4497

Roberts, Jr., L. C., Tokovinin, A., Mason, B. D., Riddle, R. L., Hartkopf, W. I., Law, N. M., & Baranec, C. 2015, AJ, 149, 118

Roberts, Jr., L. C., Turner, N. H., ten Brummelaar, T. A., Mason, B. D., & Hartkopf, W. I. 2011, AJ, 142, 175

Rodigas, T. J., Arriagada, P., Faherty, J., Anglada-Escudé, G., Kaib, N., et al. 2016, ApJ, 818, 106

Roell, T., Neuhäuser, R., Seifahrt, A., & Mugrauer, M. 2012, A&A, 542, A92

Rousset, G., Lacombe, F., Puget, P., Hubin, N. N., Gendron, E., et al. 2003, in Proc. SPIE, Vol. 4839, Adaptive Optical System Technologies II, ed. P. L. Wizinowich & D. Bonaccini, 140–149

Sahlmann, J., Lazorenko, P. F., Ségransan, D., Martín, E. L., Mayor, M., Queloz, D., & Udry, S. 2014, A&A, 565, A20

Sahlmann, J., Lovis, C., Queloz, D., & Ségransan, D. 2011, A&A, 528, L8

Santerne, A., Moutou, C., Barros, S. C. C., Damiani, C., Díaz, R. F., Almenara, J. M., Bonomo, A. S., Bouchy, F., Deleuil, M., & Hébrard, G. 2012, A&A, 544, L12

Santos, N. C., Israelian, G., & Mayor, M. 2004, A&A, 415, 1153

Santos, N. C., Mayor, M., Naef, D., Pepe, F., Queloz, D., Udry, S., Burnet, M., Clausen, J. V., Helt, B. E., Olsen, E. H., & Pritchard, J. D. 2002, A&A, 392, 215

Santos, N. C., Adibekyan, V., Figueira, P., Andreasen, D. T., Barros, S. C. C., Delgado-Mena, E., Demangeon, O., Faria, J. P., Oshagh, M., Sousa, S. G., Viana, P. T. P., & Ferreira, A. C. S. 2017, A&A, 603, A30

Sato, B., Izumiura, H., Toyota, E., Kambe, E., Ikoma, M., et al. 2008, Publications of the Astronomical Society of Japan, 60, 539

Sato, B., Omiya, M., Liu, Y., Harakawa, H., Izumiura, H., et al. 2010, Publications of the Astronomical Society of Japan, 62, 1063

Saumon, D., Hubbard, W. B., Burrows, A., Guillot, T., Lunine, J. I., & Chabrier, G. 1996, ApJ, 460, 993

Saumon, D., & Marley, M. S. 2008, ApJ, 689, 1327

Schlaufman, K. C. 2018, ApJ, 853, 37

Schmidt-Kaler, T. 1982, Bulletin d'Information du Centre de Donnees Stellaires, 23, 2

Schneider, A. C., Cushing, M. C., Kirkpatrick, J. D., & Gelino, C. R. 2016, ApJ, 823, L35

Schneider, A. C., Cushing, M. C., Kirkpatrick, J. D., Gelino, C. R., Mace, G. N., Wright, E. L., Eisenhardt, P. R., Skrutskie, M. F., Griffith, R. L., & Marsh, K. A. 2015, ApJ, 804, 92

Schönrich, R., McMillan, P., & Eyer, L. 2019, arXiv e-prints, arXiv:1902.02355

Scott, N. J., Howell, S. B., Horch, E. P., & Everett, M. E. 2018, PASP, 130, 054502

Seidelmann, P. K. 1992, Explanatory Supplement to the Astronomical Almanac. A revision to the Explanatory Supplement to the Astronomical Ephemeris and the American Ephemeris and Nautical Almanac.

Shatsky, N. 2001, A&A, 380, 238

Shaya, E. J., & Olling, R. P. 2011, ApJS, 192, 2

Shporer, A., O'Rourke, J. G., Knutson, H. A., Szabó, G. M., Zhao, M., et al. 2014, ApJ, 788, 92

Shvartzvald, Y., Yee, J. C., Calchi Novati, S., Gould, A., Lee, C.-U., et al. 2017, ApJ, 840, L3

Silk, J. 1977, ApJ, 214, 152

Sing, D. K., Wakeford, H. R., Showman, A. P., Nikolov, N., Fortney, J. J., et al. 2015, MNRAS, 446, 2428

Sing, D. K., Fortney, J. J., Nikolov, N., Wakeford, H. R., Kataria, T., et al. 2016, Nature, 529, 59

Siverd, R. J., Beatty, T. G., Pepper, J., Eastman, J. D., Collins, K., et al. 2012, ApJ, 761, 123

Skemer, A. J., Close, L. M., Szűcs, L., Apai, D., Pascucci, I., & Biller, B. A. 2011, ApJ, 732, 107

Skrutskie, M. F., Cutri, R. M., Stiening, R., Weinberg, M. D., Schneider, S., et al. 2006, AJ, 131, 1163

Snellen, I. A. G., Brandl, B. R., de Kok, R. J., Brogi, M., Birkby, J., & Schwarz, H. 2014, Nature, 509, 63

Snellen, I. A. G., & Brown, A. G. A. 2018, Nature Astronomy, 2, 883

Soderblom, D. R., Hillenbrand, L. A., Jeffries, R. D., Mamajek, E. E., & Naylor, T. 2014, Protostars and Planets VI, 219

Southworth, J. 2012, MNRAS, 426, 1291

Spiegel, D. S., & Burrows, A. 2012, ApJ, 745, 174

Stamatellos, D. 2013, in European Physical Journal Web of Conferences, Vol. 47, European Physical Journal Web of Conferences, 08001

Stamatellos, D., & Herczeg, G. J. 2015, MNRAS, 449, 3432

Stamatellos, D., & Whitworth, A. P. 2008, A&A, 480, 879

Stamatellos, D., & Whitworth, A. P. 2009, MNRAS, 392, 413

Stephens, D. C., & Leggett, S. K. 2004, PASP, 116, 9

Stumpf, M. B., Brandner, W., Joergens, V., Henning, T., Bouy, H., Köhler, R., & Kasper, M. 2010, ApJ, 724, 1

Szabó, G. M., Szabó, R., Benkó, J. M., Lehmann, H., Mezó, G., Simon, A. E., Kóvári, Z., Hodosán, G., Regály, Z., & Kiss, L. L. 2011, ApJ, 736, L4

Tamuz, O., Ségransan, D., Udry, S., Mayor, M., Eggenberger, A., et al. 2008, A&A, 480, L33

Thalmann, C., Carson, J., Janson, M., Goto, M., McElwain, M., et al. 2009, ApJ, 707, L123

Thebault, P., & Haghighipour, N. 2015, Planet Formation in Binaries, 309–340

Thiele, T. N. 1883, Astronomische Nachrichten, 104, 245

Tinney, C. G., Burgasser, A. J., Kirkpatrick, J. D., & McElwain, M. W. 2005, AJ, 130, 2326

Tinney, C. G., Faherty, J. K., Kirkpatrick, J. D., Cushing, M., Morley, C. V., & Wright, E. L. 2014, ApJ, 796, 39

Tinney, C. G., Faherty, J. K., Kirkpatrick, J. D., Wright, E. L., Gelino, C. R., Cushing, M. C., Griffith, R. L., & Salter, G. 2012, ApJ, 759, 60

Tinney, C. G., Kirkpatrick, J. D., Faherty, J. K., Mace, G. N., Cushing, M., Gelino, C. R., Burgasser, A. J., Sheppard, S. S., & Wright, E. L. 2018, ApJS, 236, 28

Todorov, K., Luhman, K. L., & McLeod, K. K. 2010, ApJ, 714, L84

Todorov, K. O., Luhman, K. L., Konopacky, Q. M., McLeod, K. K., Apai, D., Ghez, A. M., Pascucci, I., & Robberto, M. 2014, ApJ, 788, 40

Tokovinin, A., Hartung, M., & Hayward, T. L. 2013, AJ, 146, 8

Tokovinin, A., Hartung, M., Hayward, T. L., & Makarov, V. V. 2012, AJ, 144, 7

Tokovinin, A., Thomas, S., Sterzik, M., & Udry, S. 2006, A&A, 450, 681

Tokovinin, A. A., Griffin, R. F., Balega, Y. Y., Pluzhnik, E. A., & Udry, S. 2000, Astronomy Letters, 26, 116

Tsapras, Y. 2018, Geosciences, 8, 365

Turner, N., ten Brummelaar, T., Roberts, Jr., L., Gies, D., Mason, B., & Hartkopf, W. 2006, in The Advanced Maui Optical and Space Surveillance Technologies Conference, E104

Udalski, A. 2003, Acta Astron., 53, 291

Udry, S., Mayor, M., Naef, D., Pepe, F., Queloz, D., Santos, N. C., & Burnet, M. 2002, A&A, 390, 267

Uyama, T., Hashimoto, J., Kuzuhara, M., Mayama, S., Akiyama, E., et al. 2017, AJ, 153, 106

van Leeuwen, F. 2007, A&A, 474, 653

Vanhollebeke, E., Groenewegen, M. A. T., & Girardi, L. 2009, A&A, 498, 95

Vigan, A., Patience, J., Marois, C., Bonavita, M., De Rosa, R. J., Macintosh, B., Song, I., Doyon, R., Zuckerman, B., Lafrenière, D., & Barman, T. 2012, A&A, 544, A9

Vigan, A., Bonnefoy, M., Ginski, C., Beust, H., Galicher, R., et al. 2016, A&A, 587, A55

Vigan, A., Bonavita, M., Biller, B., Forgan, D., Rice, K., et al. 2017, A&A, 603, A3

Vos, J. M., Biller, B. A., Bonavita, M., Eriksson, S., Liu, M. C., et al. 2019, MNRAS, 483, 480

Vrba, F. J., Henden, A. A., Luginbuhl, C. B., Guetter, H. H., Munn, J. A., et al. 2004, AJ, 127, 2948

Wagner, K., Apai, D., Kasper, M., & Robberto, M. 2015, ApJ, 813, L2

Wang, J., Fischer, D. A., Horch, E. P., & Huang, X. 2015, ApJ, 799, 229

Wang, J., Fischer, D. A., Xie, J.-W., & Ciardi, D. R. 2014a, ApJ, 791, 111

Wang, J., Xie, J.-W., Barclay, T., & Fischer, D. A. 2014b, ApJ, 783, 4

Warren, S. J., Mortlock, D. J., Leggett, S. K., Pinfield, D. J., Homeier, D., et al. 2007, MNRAS, 381, 1400

White, R. J., & Ghez, A. M. 2001, ApJ, 556, 265

Whitworth, A., Bate, M. R., Nordlund, Å., Reipurth, B., & Zinnecker, H. 2007, Protostars and Planets V, 459

Whitworth, A. P., & Goodwin, S. P. 2005, Astronomische Nachrichten, 326, 899

Whitworth, A. P., & Zinnecker, H. 2004, A&A, 427, 299

Wilson, J. C., Kirkpatrick, J. D., Gizis, J. E., Skrutskie, M. F., Monet, D. G., & Houck, J. R. 2001, AJ, 122, 1989

Wilson, P. A., Hébrard, G., Santos, N. C., Sahlmann, J., Montagnier, G., et al. 2016, A&A, 588, A144

Winn, J. N., Holman, M. J., Torres, G., McCullough, P., Johns-Krull, C., Latham, D. W., Shporer, A., Mazeh, T., Garcia- Melendo, E., Foote, C., Esquerdo, G., & Everett, M. 2008, ApJ, 683, 1076

Wittenmyer, R. A., Endl, M., & Cochran, W. D. 2007, ApJ, 654, 625

Wittenmyer, R. A., Endl, M., Cochran, W. D., Levison, H. F., & Henry, G. W. 2009, ApJS, 182, 97

Wizinowich, P. L., Le Mignant, D., Bouchez, A., Chin, J., Contos, A., Hartman, S., Johansson, E., Lafon, R., Neyman, C., Stomski, P., Summers, D., & van Dam, M. A. 2004, in Proc. SPIE, Vol. 5490, Advancements in Adaptive Optics, ed. D. Bonaccini Calia, B. L. Ellerbroek, & R. Ragazzoni, 1–11

Wöllert, M., & Brandner, W. 2015, A&A, 579, A129

Wöllert, M., Brandner, W., Bergfors, C., & Henning, T. 2015, A&A, 575, A23

Wolszczan, A., & Frail, D. A. 1992, Nature, 355, 145

Wong, I., Knutson, H. A., Lewis, N. K., Kataria, T., Burrows, A., et al. 2015, ApJ, 811, 122

Wright, E. L., Eisenhardt, P. R. M., Mainzer, A. K., Ressler, M. E., Cutri, R. M., et al. 2010, AJ, 140, 1868

Wu, Y., Murray, N. W., & Ramsahai, J. M. 2007, ApJ, 670, 820

York, D. G., Adelman, J., Anderson, Jr., J. E., Anderson, S. F., Annis, J., et al. 2000, AJ, 120, 1579

Youdin, A. N., & Goodman, J. 2005, ApJ, 620, 459

Zacharias, N., Monet, D. G., Levine, S. E., Urban, S. E., Gaume, R., & Wycoff, G. L. 2004, in Bulletin of the American Astronomical Society, Vol. 36, American Astronomical Society Meeting Abstracts, 1418

Zapatero Osorio, M. R., Martín, E. L., Béjar, V. J. S., Bouy, H., Deshpande, R., & Wainscoat, R. J. 2007, ApJ, 666, 1205

Ziegler, C., Law, N. M., Morton, T., Baranec, C., Riddle, R., Atkinson, D., Baker, A., Roberts, S., & Ciardi, D. R. 2017, AJ, 153, 66

Ziegler, C., Law, N. M., Baranec, C., Morton, T., Riddle, R., De Lee, N., Huber, D., Mahadevan, S., & Pepper, J. 2018, AJ, 156, 259

Zucker, S., & Mazeh, T. 2002, ApJ, 568, L113

Zucker, S., Mazeh, T., Santos, N. C., Udry, S., & Mayor, M. 2003, A&A, 404, 775

Zucker, S., Mazeh, T., Santos, N. C., Udry, S., & Mayor, M. 2004, A&A, 426, 695

Zuckerman, B. 2014, ApJ, 791, L27